Institut für Erd- und Umweltwissenschaften
Universität Potsdam
Sektion 3.3: Geochemie der Erdoberfläche
Deutsches GeoForschungsZentrum GFZ

Dissertation

zur Erlangung des akademischen Grades

"doctor rerum naturalium"
(Dr. rer. nat.)

in der Wissenschaftsdisziplin "Geowissenschaften"

Causes for slow weathering and erosion in the steep, warm, monsoon-subjected Highlands of Sri Lanka

---

von

Ricarda Behrens

eingereicht an der
Mathematisch-Naturwissenschaftlichen Fakultät
der Universität Potsdam

Ort und Tag der Disputation: Potsdam, den 06.02.2018

Betreuer: Prof. Dr. Manfred Strecker
Prof. Dr. Friedhelm von Blanckenburg

Published online at the
Institutional Repository of the University of Potsdam:
URN urn:nbn:de:kobv:517-opus4-408503
http://nbn-resolving.de/urn:nbn:de:kobv:517-opus4-408503

Hiermit erkläre ich, dass die Arbeit an keiner anderen Hochschule eingereicht sowie selbständig von mir und nur mit den angegebenen Mitteln angefertigt wurde.

Potsdam, den _____

Unterschrift der Doktorandin/des Doktoranden

Summary

In the Highlands of Sri Lanka, erosion and chemical weathering rates are among the lowest for global mountain denudation. In this tropical humid setting, highly weathered deep saprolite profiles have developed from high-grade metamorphic charnockite during spheroidal weathering of the bedrock. The spheroidal weathering produces rounded corestones and spalled rindlets at the rock-saprolite interface. I used detailed textural, mineralogical, chemical, and electron-microscopic (SEM, FIB, TEM) analyses to identify the factors limiting the rate of weathering front advance in the profile, the sequence of weathering reactions, and the underlying mechanisms. The first mineral attacked by weathering was found to be pyroxene initiated by *in situ* Fe oxidation, followed by *in situ* biotite oxidation. Bulk dissolution of the primary minerals is best described with a dissolution – re-precipitation process, as no chemical gradients towards the mineral surface and sharp structural boundaries are observed at the nm scale. Only the local oxidation in pyroxene and biotite is better described with an ion by ion process. The first secondary phases are oxides and amorphous precipitates from which secondary minerals (mainly smectite and kaolinite) form. Only for biotite direct solid state transformation to kaolinite is likely. The initial oxidation of pyroxene and biotite takes place in locally restricted areas and is relatively fast: log J = -11 $mol_{min}/(m^2$ s). However, calculated corestone-scale mineral oxidation rates are comparable to corestone-scale mineral dissolution rates: log R = -13 $mol_{px}/(m^2$ s) and log R = -15 $mol_{bt}/(m^2$ s). The oxidation reaction results in a volume increase. Volumetric calculations suggest that this observed oxidation leads to the generation of porosity due to the formation of micro-fractures in the minerals and the bedrock allowing for fluid transport and subsequent dissolution of plagioclase. At the scale of the corestone, this fracture reaction is responsible for the larger fractures that lead to spheroidal weathering and to the formation of rindlets. Since these fractures have their origin from the initial oxidational induced volume increase, oxidation is the rate limiting parameter for weathering to take place. The ensuing plagioclase weathering leads to formation of high secondary porosity in the corestone over a distance of only a few cm and eventually to the final disaggregation of bedrock to saprolite. As oxidation is the first weathering reaction, the supply of O_2 is a rate-limiting factor for chemical weathering. Hence, the supply of O_2 and its consumption at depth connects processes at the weathering front with erosion at the surface in a feedback mechanism. The strength of the feedback depends on the relative weight of advective *versus* diffusive transport of O_2 through the weathering profile. The feedback will be stronger with dominating diffusive transport. The low weathering rate ultimately depends on the transport of O_2 through the whole regolith, and on lithological factors such as low bedrock porosity and the amount of Fe-bearing primary minerals. In this regard the low-porosity charnockite with its low content of Fe(II) bearing minerals impedes fast weathering reactions. Fresh weatherable surfaces are a pre-requisite for chemical weathering. However, in the case of the charnockite found in the Sri Lankan Highlands, the only process that generates these surfaces is the fracturing induced by oxidation. Tectonic

quiescence in this region and low pre-anthropogenic erosion rate (attributed to a dense vegetation cover) minimize the rejuvenation of the thick and cohesive regolith column, and lowers weathering through the feedback with erosion.

Zusammenfassung

Erosions- und chemische Verwitterungsraten im srilankischen Hochland gehören zu den langsamsten der globalen Gebirgsdenudationsraten. In diesem tropischen, humiden Gebiet entwickelten sich mächtige Verwitterungsprofile – sogenannte Saprolite – auf spheroidal verwittertem, hochgradig metamorphen Charnockit. Spheroidale Verwitterung führt zu abgerundeten „corestones“ mit abgesplitterten Rinden („rindlets“) an der Gesteins – Saprolit Grenze. Zur Identifizierung der ratenlimitierenden Faktoren des Fortschreiten der Verwitterungsfront, der Sequenz der Verwitterungsreaktionen und der dahinterliegenden Mechanismen nutzte ich detaillierte gesteinsstrukturelle, mineralogische, chemische und elektronenmikroskopische (SEM, FIB, TEM) Analysemethoden. Die initiale Verwitterung beginnt mit lokal begrenzter *in situ* Oxidation in Pyroxen, gefolgt von *in situ* Oxidation von Biotit. Die Auflösung der Minerale wird am besten durch einen Auflöse – Wiederausfällungs-prozess beschrieben, da zur Mineralgrenze hin keine chemischen Gradienten, dafür aber auf der nm-Skala scharfe strukturelle Grenzen zu beobachten sind. Die ersten ausfallenden Sekundärphasen sind Oxide und amorphe Phasen aus denen sich Sekundärmineral (hauptsächlich Smectit und Kaolinit) bilden. Für Biotit ist auch eine direkte Umwandlung im Festzustand zu Kaolinit möglich. Die initiale Pyroxen- und Biotitoxidation ist relativ schnell: $\log J = -11\ mol_{min}/(m^2\ s)$. Berechnete Oxidationsraten auf der corestone-Skala (cm) sind vergleichbar zu Auflöseraten auf derselben Skala: $\log R = -13\ mol_{px}/(m^2\ s)$ und $\log R = -15\ mol_{bt}/(m^2\ s)$. Volumetrische Berechnungen führen zum Schluss, dass die Oxidation mit einhergehender Volumenzunahme zur Entwicklung von Mikrofrakturen in den Mineralen und dem Gesamtgestein führt. Diese begünstigen Fluidtransport und damit einhergehende Plagioklasverwitterung. Des Weiteren ist diese Oxidationsreaktion verantwortlich für die Entstehung der Frakturen bei spheroidaler Verwitterung des Gesteins, welche die „rindlets“ vom „corestone“ abgrenzen. Daraus kann geschlossen werden, dass *in situ* Oxidation der ratenlimitierende Prozess bei der Verwitterung ist. Plagioklasverwitterung führt zu einer hohen Porositätszunahme und der endgültigen Umwandlung von Gestein zu Saprolit. Da Oxidation die erste Verwitterungsreaktion ist, verbinden die Zuführung und der Verbrauch von O_2 zur, beziehungsweise an die Verwitterungsfront Erosion an der Oberfläche mit Prozessen an der Verwitterungsfront über einen Feedbackmechanismus. Daher hängt die langsame Verwitterungsrate letztlich vom Sauerstofftransport durch das Verwitterungsprofil und von lithologischen Faktoren des Charnockit wie zum Beispiel geringe Gesteinsporosität und/oder wenige Fe(II)-haltige Primärminerale ab. Des Weiteren ist der einzige Prozess im Charnockit der frische verwitterbare Oberflächen (eine Voraussetzung für chemische Verwitterung) generiert die oxidations-induzierte Frakturierung. Darüber hinaus minimieren die Abwesenheit von tektonischer Aktivität und geringe prä-anthropogene Erosionsraten in dieser Region den Abtrag des mächtigen und kohäsiven Verwitterungsprofils und somit über den beschriebenen Feedback auch die chemische Verwitterungsrate.

Contents

List of Figures

List of Tables

1 Motivation, aim and objectives

In times of climate change and increasing intensity of land use, it is crucial to understand the controls on rock conversion into loose soil material and how humans are changing this system. However, the processes and the driving factors that influence the chemical alteration of bedrock which finally leads to the formation of soils are still not well understood. The fact that most of the continental areas are covered by regolith (composed of the mobile soil layer overlying the *in situ* weathered saprolite) suggests that over millennial time scales removal of regolith material by erosion is mostly balanced by its production through bedrock weathering. This observation hints at the existence of a feedback between regolith depth and rates of weathering and erosion processes that produce and destroy regolith, respectively (Carson and Kirkby, 1972; Heimsath et al., 1997). Furthermore, the existence of this feedback is also suggested by the empirical negative relationship between soil production and soil thickness, the so-called "soil production function" (*e.g.,* Heimsath et al. (1997) and Heimsath et al. (2009)). The “soil production function” has been established for the mobile soil layer. Models for regolith development have suggested that this relationship might extend through the entire regolith (Lebedeva et al., 2010). The fact that a negative feedback between regolith thickness and weathering rate exists is an implicit conclusion of the observation that weathering rates are generally low where thick regolith prevails – a phenomenon commonly lumped into the term “soil shielding” (Goddéris et al., 2008; Hartmann et al., 2014; Stallard, 1995). However, alternative views suggest that in tectonically quiescent cratons, this feedback is absent such that regolith production outpaces erosion, leading to continuously thickening weathering profiles (Lebedeva et al., 2010). Furthermore, beside the tectonic regime, other factors such as lithology, mineralogy, vegetation and climate play a fundamental role for such feedbacks. To be explicit, on a global scale feedback mechanisms or the strength of the feedback may differ depending on the pre-conditions of the host-rock, like for example porosity and mineralogical composition. The mechanisms may also depend on climatic impacts or the geomorphic regime. For example Maher and Chamberlain (2014) suggested that the strength of the feedback between climate and weathering, through the removal of CO_2, depends on the tectonic regime, with the feedback being stronger in tectonically active regions.

In order to develop an improved understanding of the mechanisms leading to the above mentioned relationships, it is critical (i) to explore the mechanism leading to primary mineral dissolution; (ii) to identify the chemical agents (O_2, protons, acids, complexing agents) that limit the rate of these mineralogical transformations; (iii) to examine in detail the mineralogical transformations occurring at the “weathering front”, where rock is converted into saprolite; and (iv) to characterize the formation of pathways, such as fractures and macro-cracks or connected pore spaces that support transport of the chemical agents to the weathering front. In particular and addressing the lithological and mineralogical control on feedbacks, an oxidative process for spheroidal fracturing was proposed by Buss et al. (2008), Fletcher et al. (2006), and Lebedeva et al. (2007), where Fe(II) in bedrock minerals is

oxidized after O_2 transport from the soil surface into the rock. Oxidative weathering produces an increase in the specific volume of the primary minerals and thus builds up strain that fractures the rock. Similarly, precipitation of secondary clay minerals following dissolution of primary minerals was proposed to result in strain build-up and rock fracturing (Jamtveit et al., 2011; Jamtveit et al., 2009; Røyne et al., 2008; Rudge et al., 2010). In contrast to pathways that require the generation of strain, the transport of chemical agents from the surface to the weathering front might also be promoted by the formation of secondary porosity by primary mineral dissolution and precipitation of secondary minerals with a lower molar volume (Lebedeva et al., 2007; Navarre-Sitchler et al., 2011; Sak et al., 2010; Velbel, 1993). All these models imply that the supply of a reactive compound from the atmosphere (*e.g.,* O_2) or from the upper regolith layers (*e.g.*, organic acids) is necessary to the downward propagation of the weathering front, thereby providing a negative feedback between the regolith thickness and mineral dissolution taking place at depth (Fletcher et al., 2006). Alternative models addressing the tectonic or geomorphological control on landscape processes suggest that the lowering of the water table induced by channel incision promotes the downward propagation of the weathering front (Edmond et al., 1995; Rempe and Dietrich, 2014). Such a mechanism also requires the formation of fractures and open pore spaces for corrosive fluids to reach unweathered minerals in low-porosity bedrocks. Where tectonic forces were insufficient to produce fractures before the bedrock entered the weathering zone, such a mechanism was lumped into the term "geomorphic fracturing" by Clarke and Burbank (2011). This term describes any mechanism that produces "surface-down" fractures. These are for example thermal, chemical or biotic processes (such as biota-induced oxidation and fracturing). Even topographic relief or surface curvature may lead to fracturing by generation of internal stresses. However, robust evidence is still lacking about the processes that generate these fluid pathways and about their relative contribution to the advance of the weathering front. But active tectonics is thought to be a key driver. As an example, in actively uplifting regions tectonic processes fractures the rock before it reaches depth which are accessible by surface processes (Molnar et al., 2007). As a result, erosional processes that further disaggregate the rock are facilitated in these fractured rocks and fresh weatherable surfaces are produced at high rates. Finally, a series of studies emphasize the potential role of biota and organic acids on incipient weathering (Bonneville et al., 2011; Bonneville et al., 2009; Gorbushina, 2007; Landeweert et al., 2001; Leake et al., 2008; Smits et al., 2005). The biotic effect on mineral weathering will not be explored in this thesis.

Embedded into the different processes is a possibility for an influence of processes at the top of a weathering profile (erosion or biological activity) on mineral dissolution at the weathering front, although the consequence in terms of soil stability was stated explicitly only by Fletcher et al. (2006). Exploring the way in which fluid and gas pathways through the regolith are generated is important because their understanding is fundamental to quantitative models of the advance of the weathering front (Bazilevskaya et al., 2013; Bazilevskaya et al., 2014; Brantley et al., 2008; Fletcher et al., 2006; Goddéris et al., 2006; Lebedeva et al., 2007; Lebedeva et al., 2010; Moore et al., 2012; Navarre-Sitchler et al., 2011). These models essentially characterize the transport of solutes and gases through regolith profiles and the participating weathering reactions. The successful application of these models relies on an accurate knowledge of the weathering system's transport properties (*e.g.*, soil and saprolite

permeability) and chemical parameters (*e.g.*, kinetics of dissolution and precipitation, or equilibrium constants). Most of these recent model concepts rely on simplified mineral reaction pathways, whereas, the nature and properties of the secondary precipitates formed during weathering (*i.e.*, their mineralogy, crystallinity, or ability to form aggregates) exert a strong control on the outputs of such models (Maher et al., 2009). In particular, many weathering reactions have been reported to produce amorphous intermediate phases rather than forming crystalline clays directly from primary minerals (Chadwick and Chorover, 2001; Dahlgren et al., 1997; Hellmann et al., 2012; Steefel and van Cappellen, 1990).

The relevance of these weathering model predictions needs to be evaluated against field observations across a range of different lithological and geomorphological contexts and different scales. In this regard, there exists a large data set from studies that focused (i) on weathering and erosion via mass balances on a regional or global scale (*e.g.*: Dixon and von Blanckenburg (2012); Gabet and Mudd (2009); Gaillardet et al. (1999); Gislason et al. (2009); Godsey et al. (2009); Locsey et al. (2011); Moon et al. (2014); Summerfield and Hulton (1994); West et al. (2005); White and Blum (1995); and references therein) on one hand and on the other hand (ii) on mineral reactions during weathering and mechanisms of weathering reactions on the small scale (nm to µm) (*e.g.*: Banfield and Barker (1994); Delvigne (1983); Hellmann et al. (2012); Maher et al. (2016); Merino et al. (1993); Noack et al. (1993); and references therein). However, a link between small scale processes and regional scale processes is rarely found. In particular, mineral dissolution processes at the nm to µm scale (*e.g.* leached layer formation, dissolution – re-precipitation model or ion-by-ion dissolution) are highly debated (Daval et al., 2013; Hellmann et al., 2015; Reis, 2015; Ruiz-Agudo et al., 2016; Ruiz-Agudo et al., 2014; Ruiz-Agudo et al., 2012). The prevailing process will have strong effects on *e.g.* the dissolution rate, preferential mobility of elements against others, formation kinetics of secondary precipitates, or the control of primary minerals on secondary minerals (degree of crystallinity, lattice orientation, *etc.*). To identify the rate-limiting process during chemical weathering it is crucial to determine important profile and bedrock parameters that support slow or fast weathering regimes. Only few studies seeked to close the gap between small scale processes and large-scale weathering. For example and similar to this thesis, Goodfellow et al. (2016) used the model presented in Fletcher et al. (2006) to calculate how strain formation during biotite oxidation fractures intact bedrock to promote initial weathering.

A weathering profile at Hakgala in the Central Highlands of Sri Lanka offers the opportunity to explore in detail the sequence of weathering processes from coherent bedrock to loose soil in a tropical mountain environment that is not currently subject to significant tectonic activity. Weathering and erosion rates, and the degree of chemical weathering have been quantified in great detail (Gunnell and Louchet, 2000; Hewawasam et al., 2013; Hewawasam et al., 2003; Vanacker et al., 2007b; von Blanckenburg et al., 2004), providing boundary conditions on the relevant mass fluxes across the weathering system. Hewawasam et al. (2013) showed that in this setting weathering along hill slopes is slow, and operates at a steady state, *i.e.,* regolith removal by erosion balances regolith production by downward propagation of the weathering front. Such steady state is indicated by finding roughly similar weathering rates over two different time scales. The rates calculated from river dissolved loads (time scale ca. 10 years)

agree with those from cosmogenic nuclides that are combined with chemical weathering indices in the profile (time scale ca. 10^4 years). Because the Hakgala weathering profile is a well-characterized, thick regolith profile representative of slow denudation-tropical settings that prevail on a large portion of the continental surface (Braun et al., 2009; Braun et al., 2012; Dequincey et al., 1999; Edmond et al., 1995; Hewawasam et al., 2013), it provides a perfect field site to study in detail the links between regolith properties and weathering at depth. In particular, the Hakgala weathering profile features corestones consisting of bedrock fragments remaining in the regolith that are progressively spheroidally weathered. Corestones comprise a core of bedrock and several layers around this core with increasing weathering intensities outward. They serve as small natural laboratories on which incipient weathering can be studied in detail (Buss et al., 2008; Ma et al., 2012; Sak et al., 2004; Sak et al., 2010). In fact, as the fronts of the respective weathering reactions move inwards with time, the spatial alignment also represents the state of weathering at different times, with outer layers having been exposed to weathering for longer times than inner layers. Therefore, primary mineral weathering reactions during different weathering extends can be studied, and reaction pathways, kinetics and products can be determined. Furthermore, the study of corestones also allows deriving links between the overall profile weathering mechanisms to incipient primary mineral weathering reactions.

In the present study, I build upon chemical and mineralogical analyses conducted by Hewawasam et al. (2013) who derived chemical mass fluxes, weathering degree, and the weathering front advance rate. Here, I further (i) trace the initiation of weathering of primary minerals and mechanisms and processes leading to primary mineral dissolution and secondary phase formation (including amorphous phases and secondary clays), (ii) derive oxidation and dissolution rates for primary minerals at different scales (*in situ* and bulk rock rates), (iii) identify the chemical reaction mechanisms and show the significance of amorphous secondary phases for the conversion of bedrock to loose material; (iv) identify textural changes between the compartments of the weathering profile; (v) discuss reactions that involve element fluxes and volume changes driving chemical weathering and the nature of the feedbacks between regolith thickness and propagation of the weathering front, and (vi) discuss how regional scale observations can be linked to processes that are observed at the mineral scale (nm to μm). With these new results I address the following questions: What are the mechanisms responsible for the slow propagation of the weathering front in deep regoliths under tropical climate? What are the rate limiting parameters? How is the propagation rate of the weathering front influenced by transport properties in the regolith? How and by which process is weathering initiated at depth and can this process serve as a model to explain other low-weathering rate profiles? Why are low weathering rates in tropical mountain regions often associated with a thick regolith cover?

1.1 Structure, contributions and acknowledgements

The project was conducted in the frame of the Graduate School GRK1364 funded by the German Science Foundation (DFG), co-financed by GFZ Potsdam, and the University of Potsdam. At this point I would like to thank my supervisors Friedhelm von Blanckenburg and

Manfred Strecker for giving me the opportunity to deal with such a great project. I appreciate Friedhelms openness to my own ideas with respect to research questions that I wanted to address during this project and the techniques to apply. Furthermore, as member of the Graduate School I was allowed to take part in the field courses to Kenya and the Himalaya that were a great experience and inspired me in many ways. The dissertation can be divided into two parts based on the spatial scales they encompass:

(1) One part considers the macro-scale bulk measurements and results (cm to m, result sections 3.1 to 3.4). They provide the basis for the discussion of the conversion of bedrock to soil in the profile (section 4.1). Furthermore, the bulk analyses set the background and input data for the oxidative fracture model (section 4.4) and the feedback model in section 4.5. These parts and the corresponding figures have been peer-reviewed and published as: *Behrens, R., Bouchez, J., Schuessler, J.A., Dultz, S., Hewawasam, T., von Blanckenburg, F., 2015. Mineralogical transformations set slow weathering rates in low-porosity metamorphic bedrock on mountain slopes in a tropical climate. Chemical Geology, vol. 411, pp 283-298.* For this part of my thesis, I would like to thank my Co-authors Julien Bouchez, Jan Schüssler, Stefan Dultz, Tilak Hewawasam and Friedhelm von Blanckenburg for their work on the manuscript and the helpful discussions we had. I would like to especially thank Julien Bouchez for his help of the formulation of the feedback model and the numerous discussions about the Fletcher model and how it can be applied to the Sri Lankan setting. Furthermore, I greatly acknowledge the previous work by Tilak Hewawasam, Julien Bouchez, Jean L. Dixon, Jan Schüssler and Friedhelm von Blanckenburg with respect to the design of the study within the framework of the Graduate School GRK1364 at the University of Potsdam, field sampling and initial work on the samples. This previous work provided me an excellent framework for my thesis project. In addition, Stefan Gehrmann and Otto Diedrich are thanked for preparation of cylindrical samples from the corestone, and Tobias Meier and Eric Rybacki for their guidance with the He-pycnometry measurements. Thanks also go to Michael Klatt for support of laboratory work in Hannover, to Franziska Adams for help with Fe-redox analyses. Except for the XRD measurements all experiments and measurements were conducted by myself. The XRD measurements were performed by Michael Klatt but peak interpretation and interpretation of all bulk results are my own work. Furthermore, Geerke Floor and anonymous reviewers improved the manuscript in form and content.

(2) After having performed the bulk measurements it was obvious to down-scale the analytical methods to the mineral scale. Hence, a second part encompasses the nm to µm mineral scale analyzed by electron microscopy on thin sections. The results of these measurements are discussed in section 4.2 to infer the dissolution mechanisms and in section 4.3 were the *in situ* measurements are used to derive nm-scale oxidation and dissolution rates of the Fe-bearing minerals. The preparation of the foils for transmission electron microscopy (TEM) was done by Anja Schreiber. Her great expertise in TEM sample preparation guaranteed the success of the TEM work. The High Resolution TEM (HRTEM) and selected area electron diffraction (SAED) work was performed with help from Richard Wirth, the FIB measurements with help from Luiz Fernando Morales and the microprobe work with help from Dieter Rhede. Additionally, I acknowledge the help of Monika Koch-Müller for her help in interpreting the EELS measurements with respect to the Fe-redox state. The discussion of

these measurements was supported by Richard Wirth who gave me insights into the state of the art of interface geochemistry and its application to natural settings. The discussion and a manuscript in progress about this part benefited a lot from his expertise.

Last, I would like to thank my PhD student colleges from section 3.3 at the GFZ and from the Graduate School for their support, the lively discussions and the great time we had. I really appreciated it.

1.2 Study site and sampling

The Hakgala weathering profile (06.92923° N, 80.81834° E) is located on a fresh road cut along the road from Nuwara Eliya to Welimada near the Hakgala Botanical Garden in the Central Highlands of Sri Lanka and is bordered by a mature and stable nature reserve (Fig. 1.1A). The initial investigation of the profile that this thesis is based on was reported by Hewawasam et al. (2013). The central Sri Lankan Highlands depict a hilly to mountainous landscape which is surrounded by an escarpment zone. This zone divides the Central Sri Lankan Highlands from the low laying coastal plain. The hillslope angles encompass a range of 10 – 30° with higher angles in the escarpment zone. Hillslopes are covered with a thick regolith. Bedrock outcrops are found on very steep hillslopes in the escarpment zone and on hilltops. The underlying bedrock in the Central Sri Lankan Highlands is a Precambrian crystalline metamorphic rock and belongs to the Highland complex of Sri Lanka (Fig. 1.1B). The profile site is exposed to two monsoon seasons, the mean annual precipitation is 2013 mm, and the mean annual temperature is 16 °C. The vegetation is comprised of upper montane rainforest with a canopy height of up to 20 m (Hewawasam et al., 2013).

An approximately 10 m-thick regolith profile (including a zone with corestones at the bottom, a deeply weathered saprolite layer, and 60 cm of soil on top, Figure 1.2A and B) developed over a charnockitic bedrock lithology, with plagioclase (An25), K-feldspar, and quartz as major mineral components and minor amounts of biotite and orthopyroxene. The weathering of the bedrock is initiated along large conjugated fractures dividing the bedrock into blocks. The separated blocks of charnockite weather spheroidally resulting in an approximately 3 m thick transition zone in the weathering profile featuring rounded corestones between coherent bedrock and deeply weathered saprolite. Due to the inward advance of weathering, corestones are surrounded by spheroidally spalled “rindlets” (Buss et al., 2008). These spheroidally weathered corestones feature several weathering fronts on a cm- to dm-scale, separating a virtually unweathered core from saprolite-like material in the outer rindlets. Despite humid, tropical climate and high relief the chemical weathering (chemically removed material) and total denudation (sum of chemical weathering and physical erosion) rates were calculated to be as low as 22 t km^{-2} y^{-1} and 42 t km^{-2} y^{-1}, respectively (Hewawasam et al., 2013).

Samples from the profile (Figure 1.2A) were taken in October 2010 from the bedrock to the soil layer (Hewawasam et al., 2013). A corestone from 8.30 m depth was sampled and visually divided into several zones of different weathering degree, which were then characterized microscopically and chemically by Hewawasam et al. (2013). These different corestone zones are shown in Figure 1.2C: the dark, visually unweathered core, termed zone

1; a light gray layer surrounding the core, termed zone 2; a yellow rim, termed zone 3; and successive "rindlets", termed zone 4 (4a and 4c were studied). From these different zones, samples were taken for bulk and *in situ* measurements. The samples for the bulk measurements are drilled from the corestone with a 5 mm drill in diameter and from 4 cm thick slices from the different zones as further described in more detail in section 2 (Fig 2.1). For *in situ* microscope work, thin sections were made in such a way that they cover the entire corestone zones as depicted in section 2.5 (Fig. 2.2). The minerals first affected by weathering are successively pyroxene, biotite and plagioclase, as shown by a mineralogical investigation of the corestone (Hewawasam et al., 2013). Plagioclase is the first mineral dissolved to completion at the corestone-saprolite boundary as indicated by the full removal of Na and Ca at this depth, while biotite and pyroxene continue to weather further up in the saprolite profile. The saprolite itself is highly weathered, as half of the mass of the parent material is lost by weathering by the time material reaches the top of the saprolite, as indicated by a chemical depletion fraction, CDF (Riebe et al., 2003), of 0.5 (Hewawasam et al., 2013).

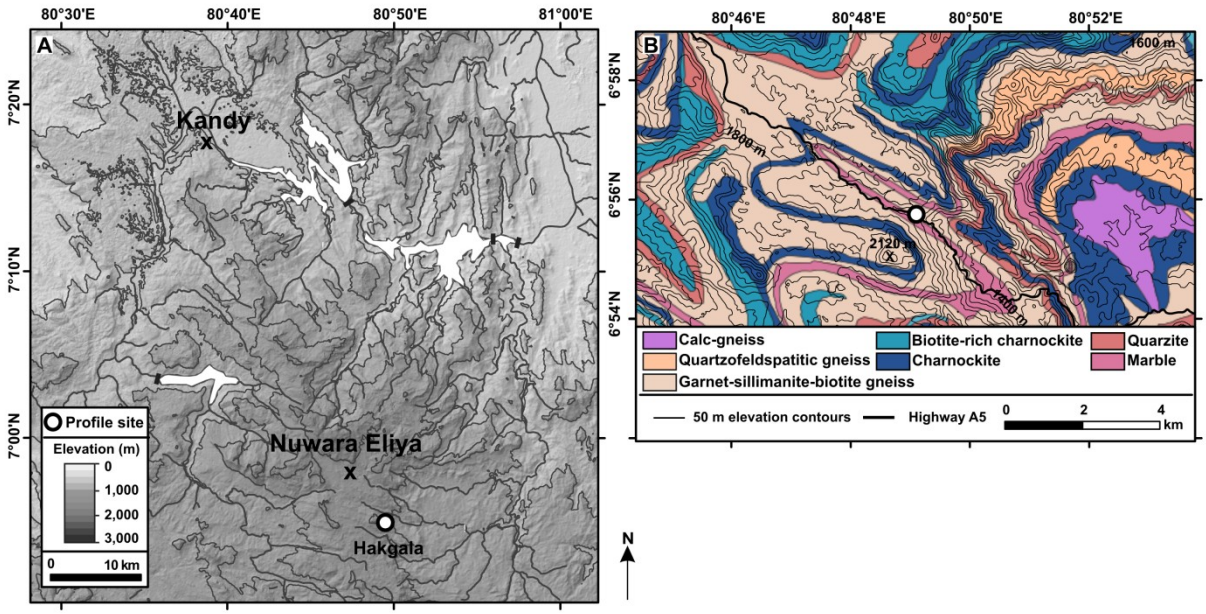

Figure 1.1 Profile location and geological setting (after Hewawasam et al. (2013)). Panel (A) is a topographic map of the Sri Lankan Highlands showing the location of the Hakgala weathering profile, white circle. The geological map in (B) depicts the underlying lithology in the study catchment of the Hakgala weathering profile. *Source*: Geological Survey and Mines Bureau, Sri Lanka. The rock types are intercalated at smaller scale than represented on this map. Therefore the profile appears to be located over garnet-sillimanite–biotite gneiss, although the local rock is a charnockite.

Detailed textural, chemical and mineralogical analyses were performed on samples from the whole weathering profile of Hewawasam et al. (2013) (Figure 1.2A and C). In addition, I characterized an extensive set of samples from the spheroidally weathered corestone of Hewawasam et al. (2013). As these samples were used for bulk measurements I will refer to the bulk sample set throughout this thesis. The bulk sample set includes samples from the corestone (zone 1 to zone 4, Figure 1.2 C), from the lower saprolite (samples SL 25 to SL 21),

from the transition zone between the lower and upper saprolite (sample SL 17), from the upper saprolite (samples SL 14 to SL 8), and from the soil layer (sample SL 6). Thus, this sample set covers the whole profile scale of a few cm to 10 m. A compilation of these samples is provided in the results section 3, table 3.1. Detailed *in situ* electron microscopic work was only performed on thin sections from the corestone and the rindlets and focused on the textural, chemical and mineralogical changes during incipient weathering at the nm to µm scale. The samples for detailed electron microscope work are visualized in Fig. 2.2, in part 2.5, where a detailed sampling description is provided.

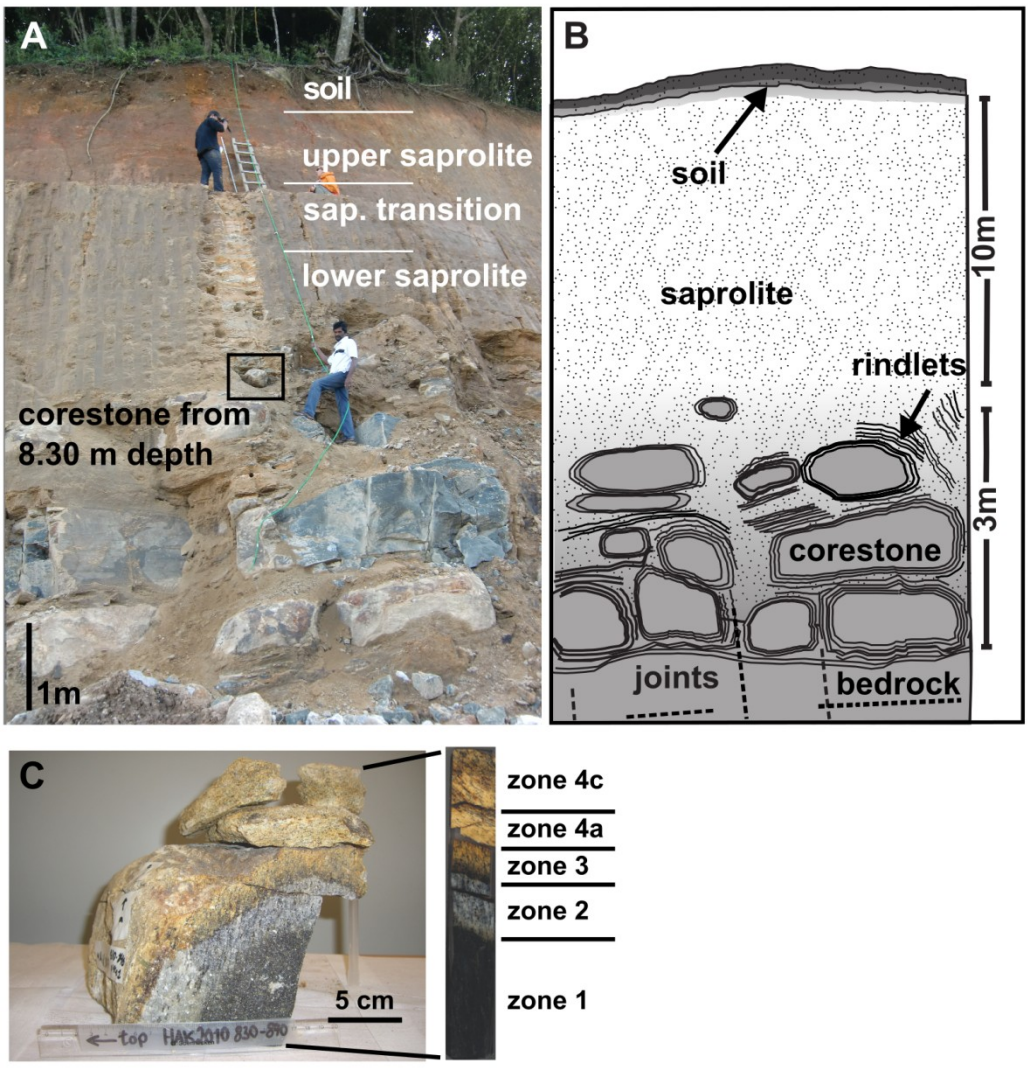

Figure 1.2 Study site. Photographs of the weathering profile near Hakgala (A) and the investigated corestone from 830 cm depth (C). (B) shows schematically how bedrock is first divided into larger blocks along large scale joints which are then progressively weathered to corestones and eventually saprolite and soil. This schematic sketch was first published by Hewawasam et al. (2013) and is provided in a modified way. The corestone in picture C was sampled from the approximately 3 m-thick corestone zone in the lower part of the profile. The polished section to the right was prepared from this corestone and shows the different weathered zones from which thin sections were made.

2. Methods

The following analyses were performed to identify the transformation pathways during the weathering reactions in the Hakgala profile. Textural and porosity changes were determined by analyses of particle size distribution, BET-specific surface area measurements (SSA) and He-pycnometry. Crystalline and amorphous secondary phases were identified and quantified by selective extraction of (non)crystalline Al- and Fe-(oxy)(hydr)oxides with dithionite and NaOH, FTIR spectroscopy, X-ray powder diffraction, electron microprobe, FIB, TEM, and Fe-redox analyses. The TEM and Fe redox analyses were used to derive dissolution and oxidation rates of Fe-bearing primary minerals. The methods are divided into bulk analyses (section 2.1 – 2.4) and microscope work on thin sections from the corestone (section 2.5). For bulk measurements on corestone samples, cylinder shaped samples were drilled from the corestone for further treatment. These corestone sample locations are given in Fig. 2.1.

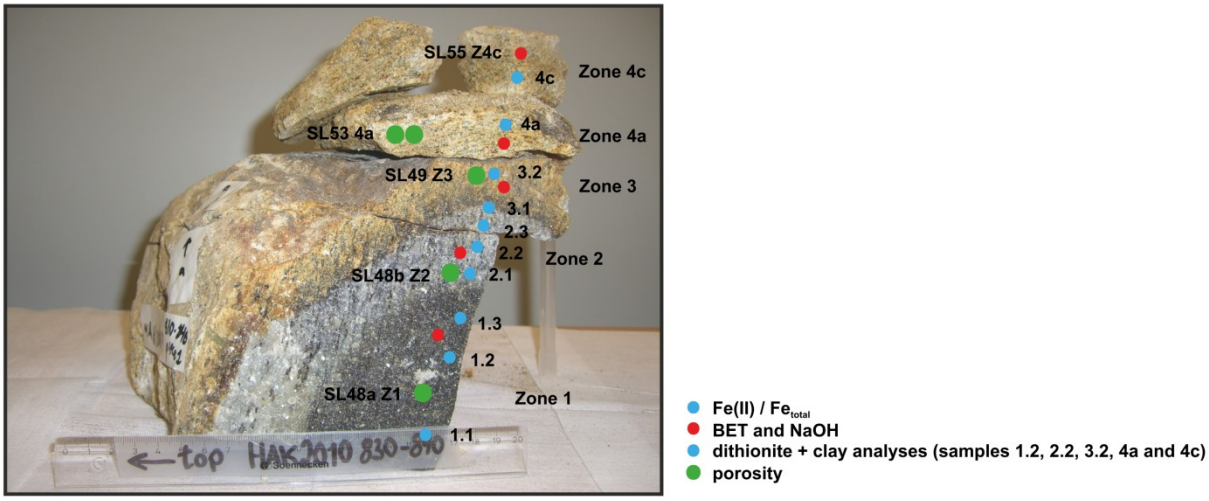

Figure 2.1 Corestone sample locations for bulk measurements.

2.1 Textural characterization

2.1.1 Particle size determination

Samples, previously sieved to < 2 mm, were gently crushed using a hand mortar to break up large aggregates (saprolite and soil samples) and solid corestone samples (cylinders obtained by drilling). After removal of Fe-(oxy)(hydr)oxides with dithionite (see section 2.3), the samples were separated into three particle size fractions (sand: 2000 µm – 63 µm, silt: 63 – 2 µm, and clay: < 2 µm) by gravitational settling in a water column of the clay-sized minerals and wet sieving of particles > 63 µm at the Institute of Soil Science, Leibniz Universität Hannover, Germany. The amounts of silt- and sand-sized fractions were determined by direct

weighing after drying, and the weight difference to the bulk sample weight was attributed to the clay-sized fraction. Hence, the size fractions for sand and silt are minimum values, while those for the clay-sized fractions are maximum values. Moreover, I acknowledge that the initial gentle crushing of solid corestone samples can slightly bias the particle size distribution towards finer grain sizes. However, from visual observations during crushing this effect is most likely small (< 5% relative) as compared to the overall estimated uncertainty of the method (< 15% relative), especially regarding the uncertainty in determination of the clay-sized fraction by difference (< 20% relative).

2.1.2 Specific surface area (SSA) – BET analyses

About 1 g of sample (loose saprolite, and cylindric drill cores from the corestone and the rindlets) was left to degas in a FlowVag Degasser from Quantachrome Instruments. After complete degassing, the specific surface area was measured with a NOVA 4000e surface area & pore size analyzer from Quantachrome Instruments using N_2 and the BET method (Brunauer et al., 1938) at the Institute of Soil Science, Universität Hannover. The uncertainty and the smallest detectable SSA are ±0.01% and 0.01 m^2/g (detection limit), respectively (Quantachrome Instruments). Because the sample volume is small, I emphasize that there is an important difference between the detection limit and the limit for properly quantifying SSA. As corestone samples are cylindric drill cores and not powders, for these samples the specific surface area rather describes a connected internal surface area of N_2 accessible grain boundaries, and micro-fractures.

2.1.3 Porosity – He-pycnometry measurements

He-pycnometry measurements were performed to quantify the connected porosity. Cylinder-shaped samples with a defined volume V_{sample} (diameter 1 cm, height 2.0 to 2.5 cm) were drilled from the corestone and its first rindlet (outer rindlets were too friable to obtain a sample with a precise volume), and polished afterwards to obtain an even surface. Prior to measurements, cylinders were dried and weighed. After weighing they were exposed to a pressure of 19 kbar in a AccuPyc 1330 He-pycnometer (Micromeritics) at GFZ Potsdam. The measurement of the volume of gas V_{pore} that is displaced provides a quantification of the connected porosity. The porosity ϕ [vol%] can be determined with the following equation (Palacio et al., 1999):

$$\phi = \left[1 - \left(\frac{V_{total} - V_{empty}}{V_{sample}}\right)\right] * 100 = \left[1 - \left(\frac{V_{pore}}{V_{sample}}\right)\right] * 100 \qquad (2.1)$$

V_{empty} is the volume of displaced gas in the empty sample holder. V_{total} is the volume of displaced gas in the sample holder containing the sample. The repeatability (five repeats) of sample volumes is 0.02%, and the accuracy is within 0.03% of gas displacement reading plus

0.03% of the sample chamber volume. Relative uncertainty on the measured porosity results is estimated to be < 2.3%.

2.2 Clay mineralogy – FTIR and XRD

The primary minerals in the Hakgala rock and in regolith bulk material are reported in Hewawasam et al. (2013). In order to identify the crystalline weathering products, I separated the clay-sized fractions of the samples and analyzed them using X-ray powder diffraction (XRD) and Fourier transformed infrared (FTIR) spectroscopy at the Institute of Soil Science, Universität Hannover. For XRD measurements, binding sites for exchangeable cations of the clay fraction were saturated with Mg^{2+} (Moore and Reynolds, 1997). The aliquots for Mg^{2+} saturation were taken from the clay suspension after dithionite extraction (see section 2.3) and separation of the clay sized fraction (see section 2.1.1). The Mg^{2+}-saturated suspension was transferred to a glass slide and left to dry at room temperature to obtain oriented samples. As the clay-sized fraction of corestone zones 1 and 2 is dominated by fragments of primary minerals rather than by secondary weathering products, I do not report the XRD and IR patterns of these two samples. X-ray diffraction patterns were acquired using a Siemens D 500 diffractometer, with Cu-Kα radiation, and a resolution of about 0.01° 2 Theta. Peak maxima were identified using the PowDLL software (Kourkoumelis, 2013). Infrared spectroscopy measurements were performed on clay-sized fractions in transmission mode using KBr pellets (*e.g.,* Balan (2006); van der Marel and Beutelspacher (1976)). About 1 mg of each dried clay separated fraction of the samples (treated previously with dithionite, see section 2.3) and 300 mg KBr were gently homogenized in a mortar and pressed to transparent pellets. Transmission spectra were recorded with a Bruker Tensor 27 FTIR spectrometer in a wavelength range from 400 to 4000 cm^{-1}, at a resolution better than 1 cm^{-1}, and a wavelength accuracy of 0.01 cm^{-1}. The spectra were evaluated using the OPUS software (Bruker).

2.3 Selective extraction of amorphous phases and oxides using dithionite and NaOH

Extractions of secondary oxides from the samples were performed using (a) sodium dithionite ($Na_2S_2O_4$) to release chemical elements from (non)crystalline Fe-(oxy)(hydr)oxides (mostly containing Fe, Al, Mn, and Si); and (b) NaOH to extract chemical elements from amorphous phases (mostly containing Al and Si). Corestone samples were gently crushed using a hand mortar prior to the treatment. Dithionite extractions were conducted on bulk samples following Mehra and Jackson (1960) and Schwertmann (1964). The two-step extraction procedure involved 3 h leaching at 72 °C in dithionite solution buffered with citrate bicarbonate, followed by another 30 min leaching after fresh dithionite addition. After sampling of an aliquot from the solution for chemical analyses of dissolved elements, the remaining suspension was used for grain size analysis, FTIR and XRD measurements of the clay sized fraction (< 2 µm). Extractions with 0.5M NaOH were performed for 4 h in a boiling steam bath on bulk samples following Foster (1953) and Sauer et al. (2006). The

chemical composition of the leachates was measured in 0.15M HNO_3 with a Varian ICP-OES at the Institute of Soil Science, Universität Hannover, with a relative analytical uncertainty of 5% (estimated from repeat measurements on reference materials).

2.4 Bulk Fe(II)/Fe_{total} ratios

$Fe(II)/Fe_{total}$ ratios on bulk samples were measured following the method described in Schuessler et al. (2008) at the Institute of Mineralogy, Universität Hannover. About 15 to 20 mg (corestone) or 5 to 20 mg (saprolite and soil) powdered sample aliquots (depending on the expected Fe(II), Fe(III) and total Fe concentration) were digested in a HF-vanadate mixture using V(VI) as a carrier for Fe(II). The Fe(II) concentrations were measured with an UV/VIS spectrometer (UV-1800, Shimadzu). The amount of Fe_{total} was determined on the same analyte solution after Fe(III) reduction with hydroxylamine hydrochloride. The measurement sequence included a procedure blank (< 3% of processed Fe and therefore considered insignificant) and the USGS BIR-1 basalt and ANRT GS-N granite reference materials for data quality control. Uncertainty in $Fe(II)/Fe_{total}$ ratios is ±0.03 (2SD), based on repeat measurements of certified reference materials (Schuessler et al., 2008).

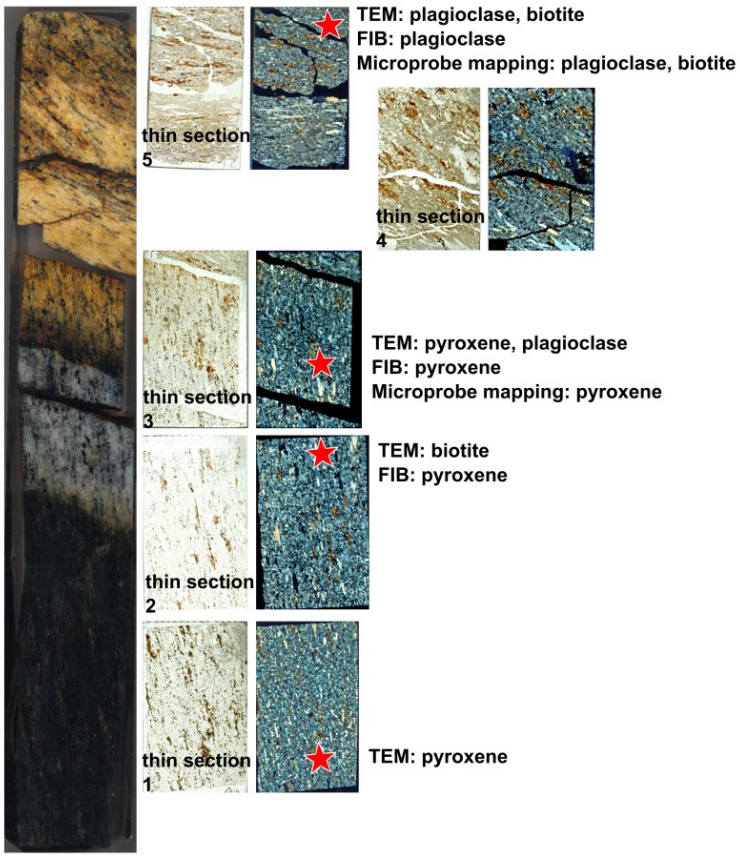

Figure 2.2 Electron microscope sample locations. The figure shows a slab from the corestone with the associating thin sections. Electron microscope investigations were performed on these thin sections (marked with a red star) according to the specific locations: TEM: Transmission Electron Microscope, FIB: Focused Ion Beam. The locations of the element maps shown in Fig. 2.3 are from thin sections 5 (plagioclase and biotite) and 3 (pyroxene) within the star-marked areas.

2.5 Electron microscope analyses of weathering features in the corestone and the rindlets

A slab was prepared from the corestone, ranging from the center of the corestone (zone 1) to the outer rindlet (zone 4). Five thin sections were produced from this slab to study the weathering features and mineralogical changes in the primary minerals in the corestone and the rindlets with different microscope techniques (Fig. 2.2).

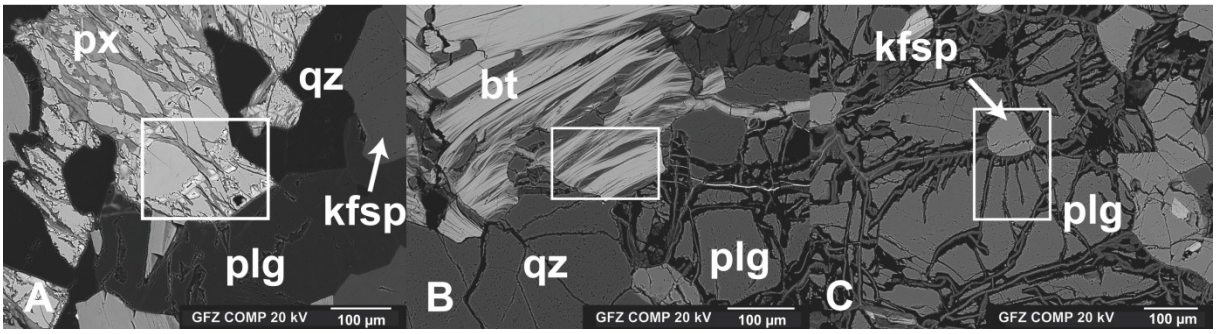

Figure 2.3 Back scatter detector electron microscope images. White boxes show the locations of the element maps performed by electron microprobe. Picture A shows a pyroxene from corestone zone 3, with its weathering features that include the grey and bright secondary precipitates. Picture B provides the element map location from a biotite from zone 4c, the outer rindlet. The maps include the biotite and the open spacings in between. Picture C shows a plagioclase from zone 4c. The mapping was performed on the K-feldspar and the plagioclase with the weathering features penetrating into the mineral.

2.5.1 Microprobe investigations

Electron microprobe analyses on primary minerals were done on four polished thin sections, which together represent the whole corestone weathering sequence. The measurements were performed with a JEOL JXA 8500F field emission electron probe micro analyzer at GFZ Potsdam. Multi-element measurements (beam size 0.04 – 20 µm) were carried out on unweathered parts in pyroxene, biotite and plagioclase grains from corestone zone 1 to zone 4. Furthermore, element maps of unweathered and weathered parts in pyroxene, biotite and plagioclase were produced. The areas selected for the element maps are shown in Fig. 2.2 and 2.3. The pyroxene sample is situated in zone 3, the yellow-brown rim of the corestone, and the biotite and plagioclase samples are from the outermost rindlet. The microprobe is equipped with 5 spectrometers and a Schottky-field emitter as electron gun. It was operated at 20 kV accelerating voltage and 20 nA beam current in WDS mode (wavelength dispersive spectra). The beam diameter was 1 µm (pyroxene), 5 µm (biotite), and 10 µm (plagioclase). The detection limit is 40 – 215 ppm (Ca and Ti, respectively). Peak counting times were 20 – 30 s, and background counting times were always set to half of the respective peak counting times. The CITZAF routine in the JEOL software, which is based on the $\Phi(\rho Z)$ method

(Armstrong, 1995), was used as matrix correction algorithm. The relative 2SD for major constituents of the minerals is <5.5%, and for minor components <38% (except for Na in biotite with 75% 2SD).

2.5.2 Visualization of weathering interfaces in 3D with focused ion beam (FIB)

The focused ion beam (FIB) nanotomography was performed with a FEI Quanta 3D FEG Dual Beam machine. This machine combines traditional thermal emission scanning electron microscopy (SEM) with focused ion beam (FIB) and allows the characterization of materials in 3D. The sample preparation was performed on the aforementioned thin sections (sample locations are given in Fig. 2.2 and 2.6). Prior to measurements three trenches (one frontal, two lateral) were produced normal to the surface of the thin section, enveloping the area of interest (Fig. 2.4). The trenches were created by sputtering material out from the sample using a Ga ion source with accelerating voltage of 30 kV and a beam current of 30 nA. Afterwards, material from the frontal trench was removed by sputtering using the same accelerating voltage, but with a beam current of 3 nA, to make the surface very flat and clean. Then, the "slice and view" process was applied, where thin slices of 50 nm were progressively removed from the frontal surface (accelerating voltage: 30 kV, beam current: 3 nA) and normal to the surface of the thin section. After each slice removed, an image was generated by using the electron source with backscattered detector, using 15 kV accelerating voltage and 8 nA beam current. The whole process took about 20 hours. The "slice and view" process is described in Wirth and Morales (2012) and schematically depicted in Fig. 2.5. The amount of the different slices (each 50 nm thick) varies from 200 to 640 for the different samples, hence 200 to 640 pictures were obtained. The pictures can then be combined in a movie, or treated with the Avizo Fire software for 3D visualization.

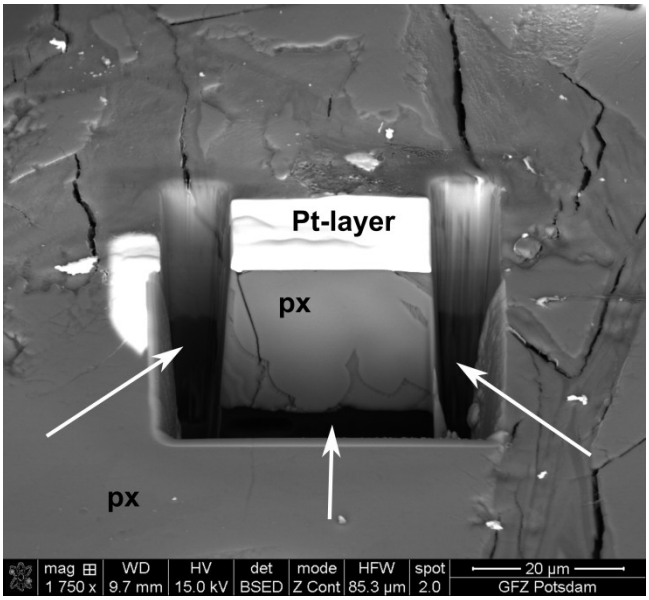

Figure 2.4 Example of the preparation of the sampling area for the FIB "slice and view" procedure and the TEM sample foil. The BSE image shows a pyroxene in a thin section from corestone zone 3. The bright phase on top of the sampling area is a protective Pt – layer. The three trenches are marked with white arrows.

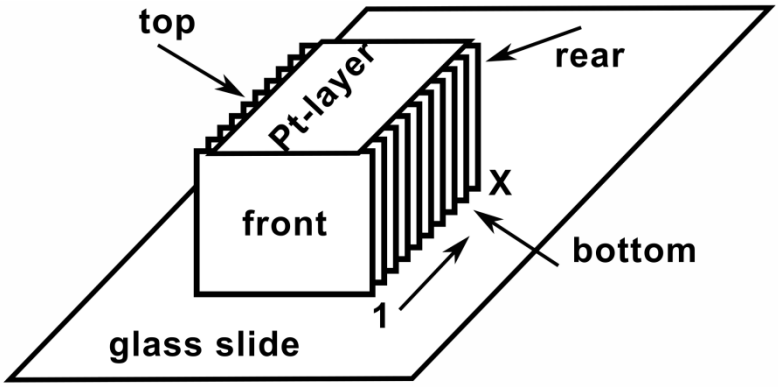

Figure 2.5 Schematic sketch of the "slice and view" procedure. Top refers to the surface of the thin section and bottom to the bottom of the thin section in contact with the glass slide. The surface of the thin section is coated with a protective Pt-layer. The first slice produced (number 1, normal to the surface of the thin section) is labeled as front, while the last slice "X" is labeled as rear. The arrow from 1 to X depicts the direction of the removal of the slices. The whole "slice and view" process is similar with cutting a loaf of bread into "X" slices. A picture is generated from each slice which are 50 nm thick. The pictures can then be combined for a 3D visualization.

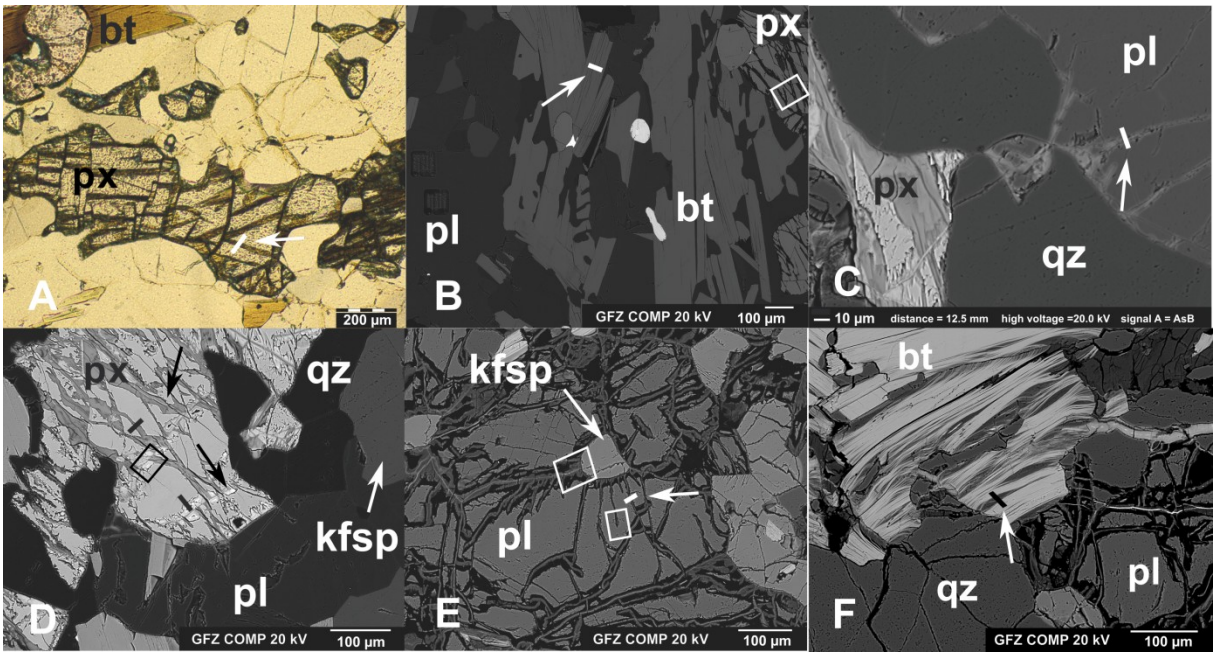

Figure 2.6 Overview of minerals investigated with TEM and FIB. Pictures A – F show pyroxene, biotite and plagioclase from different zones in the corestone sampled for analyses done with TEM and FIB. Bars (white and black) indicate the sampling location for the TEM foils and rectangles the sampling locations for FIB. Picture A depicts an optical microscope image of a pyroxene from zone 2, where a TEM foil was cut across a crack in the pyroxene, sample 3452. The back scatter electron (BSE) image in B provides the TEM sampling locality of a biotite from zone 2 and the location of FIB investigation of pyroxene. The TEM foil was sampled perpendicular to the biotite layers, sample 3396. Picture C shows a BSE image of an investigated plagioclase from zone 3 adjacent to a dissolving pyroxene, sample 3314. BSE image D depicts two sampling locations in a pyroxene from zone 3. Two TEM foils were cut across a grey band of secondary minerals (Al-phase) and the surrounding pyroxene, samples 3321 (thinner for EELS measurements) and 3300. The other foil was cut across the bright secondary phase (Fe-phase) and the surrounding pyroxene, sample 3307. The black rectangle depicts the FIB investigation area. Picture E shows a BSE image of plagioclase and K-feldspar from zone 4c, the outer rindlet. A TEM sample was cut crossing the secondary phase and the interface with the plagioclase on both sides, sample 3320. The white rectangles show the sample location for FIB measurements in plagioclase and K-feldspar, respectively. Picture F shows a BSE image of an investigated biotite from zone 4c. A foil was sampled perpendicular to the biotite layers and including the secondary phase, sample 3313.

2.5.3 Transmission electron microscopy (TEM)

To analyze in detail the weathering features in pyroxene, plagioclase, and biotite that were previously observed with optical microscopy, transmission electron microscopy (TEM) measurements included: Electron Dispersive X-ray (EDX) measurements for chemistry, Electron Energy Loss Spectroscopy (EELS) for Fe-redox analyses and High Resolution TEM (HRTEM) together with Selected Area Electron Diffraction measurements (SAED) for crystallographic analyses. For sampling, electron transparent foils were cut from thin sections with a Ga focused ion beam (FIB) (Fig. 2.4) following the foil preparation techniques described in detail in Wirth (2004) and (2009). All foils were cut in such a way that both the primary mineral and secondary precipitates could be investigated (mostly perpendicular to dissolution features, the boundary between primary and secondary phase, layering) and were selected based on optical and electron microscope investigations. Pyroxenes were sampled from zone 1 and zone 3, Fig. 2.6A and 2.6D. As can be seen in Fig. 2.6D, two different kinds of phases are observed in a crack (see section 3.5.1.2 in the results for detailed description). One phase forms darker gray bands (upper black arrow in Fig. 2.6D), and another (lower black arrow in Fig. 2.6D) shows bright contrast in backscatter electron images (BSE) in SEM (brightness depends on the atomic number, hence the chemical composition of the phases). Both were sampled for TEM investigations. Biotites were sampled from zone 2 and zone 4c, Fig. 2.6B and 2.6F. The foils crosscut the boundary between the biotite and the secondary precipitate in the spacing between the layers. Plagioclases were sampled from zone 3 and zone 4c, Fig. 2.6C and 2.6F to analyze dissolution features and secondary precipitates. Transmission electron microscopy (TEM) was performed with a FEI Tecnai™ G2 F20 X-Twin (200kV) equipped with an FEG electron source and a Gatan Tridiem energy filter with 1 eV energy resolution. Overview information of the samples were collected in scanning transmission electron microscopy (STEM) mode using the high-angle annular dark field (HAADF) detector, and with bright and dark field imaging. Chemical analyses included analytical electron microscopy (AEM) with electron dispersive X-rays (EDX), and electron energy loss spectroscopy (EELS). The condition for the EDX measurements are as follows: spot size 8, an acquisition time of 60 or 120 sec and windows of 60 – 400 nm (pyroxene), 92 – 375 nm (plagioclase) and 180 – 1000 nm (biotite) thickness for better count statistics and to reduce beam damage. The detection limit is of 0.2 – 1.0 wt%. Structural information was gained from high resolution transmission electron microscopy (HRTEM) and subsequent fast Fourier transforms (FFT), and selected area electron diffraction (SAED). Fe(III) contents were determined with EELS measurements. The settings for the EELS measurements are: 0.1 and 0.2 eV/channel dispersion, 1 second exposure time, sum of 10 and 20 spectra, 700 and 770 mm camera length, 2.0 mrad Y convergence angle, and 6 mrad collection semi-angle. To calculate the Fe(III) / Fe_{total} ratio, the recorded EEL spectra were treated afterwards with a program written by C. Petrick (Helmholtz-Zentrum Potsdam, Deutsches GeoForschungsZentrum-GFZ, Potsdam, Germany) following the analytical method described in van Aken and Liebscher (2002) and van Aken et al. (1998) using peak shifts between the $L_{2,3}$ –edge specific peaks for Fe(II) and Fe(III), respectively. By applying the technique of the modified integral Fe $L_{2,3}$ white-line intensity ratio (van Aken and Liebscher, 2002), the background was fitted to a double arctan function with its height scaled to the minima behind

the Fe *L*3- and *L*2-edges and fixed inflection points at 708.65 and 721.65 eV, respectively. Two integration windows of 2 eV width each were positioned around 709.5 and 720.7 eV for *L*3Fe(III) and *L*2Fe(II), respectively, after subtraction of the background. To calculate the final Fe(III) / Fe_{total} ratio the following calibration curve was applied (van Aken and Liebscher, 2002)

$$\frac{I(L3)}{I(L2)_{mod}} = \frac{1}{ax^2 + bc + c} - 1$$

With a = 0.193 (7), b = –0.465 (9), c = 0.366 (3). This technique was previously successfully applied by *e.g.* Koch-Müller et al. (2009) or Mrosko et al. (2013) and yields absolute errors of 0.04 of Fe(III) / Fe_{total} ratio.

3. Results

The presentation of the results is organized along the two spatial scales they address. Sections 3.1 to 3.4 cover the corestone to the profile scale (cm). These results include bulk measurements of samples from the corestone, the saprolite and the soil. Fig. 2.1 in the methods section shows the sample locations in the corestone for bulk measurements. Section 3.5 encompasses the micro scale (nm to µm) and covers the electron microscopic work on thin sections from the corestone.

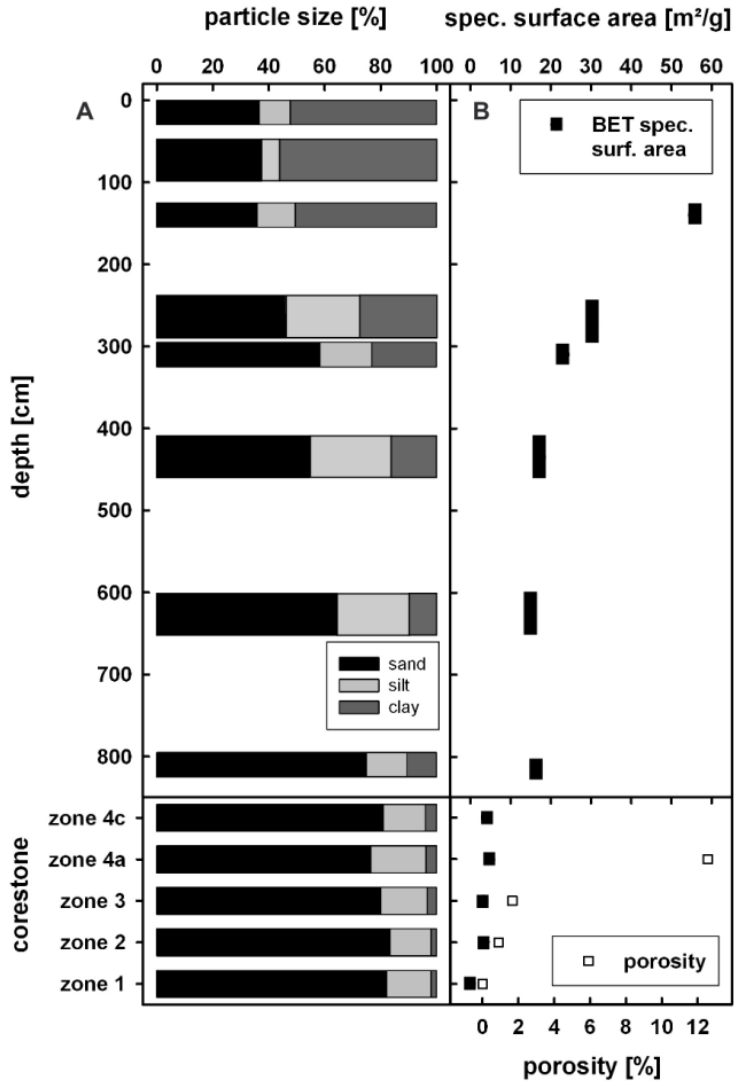

Figure 3.1 Results of texture analyses from the Hakgala profile. (A) particle size analyses. (B) specific surface area (SSA, upper axis) analysed by the N_2 adsorption method, and porosity (lower axis). The upper section represents the saprolite and soil and the lower section the different corestone zones. Note that in the dense corestone the BET method gives the connected internal surface area, which is below detection limit for corestone zone 1 (Table 1). Porosity measurements were conducted for the corestone only. Error bars are smaller than the symbols.

Table 3.1 Compilation of measurement results in corestone and regolith samples

sample[a]		depth	particle size distrib.			SSA[b]	porosity	selective extractions[c]							Fe(II)/Fe_{total}
			sand	silt	clay			Fe_d/Fe_{total}	Mn_d/Mn_{total}	Al_d/Al_{total}	Al_{NaOH}/Al_{total}	Si_d/Si_{total}	Si_{NaOH}/Si_{total}	Σ_{d+NaOH}	
		[cm]	[%]	[%]	[%]	[m^2/g]	[vol%]	[%]	[%]	[%]	[%]	[%]	[%]	[wt%]	[%]
soil															
	SL6	0 – 30	36.6	11.1	52.3			37.8	25.7	8.6	14.6	0.3	2.7	9.7	44
upper saprolite															
	SL8	60 – 100	37.4	6.6	56.0			47.9	36.2	8.8	20.1	0.1	2.3	13.6	15
	SL 10	125 – 150	35.9	13.7	50.4	55.6		31.5	87.4	5.0	14.8	0.1	5.1	13.6	6
	SL 13	250 – 300	46.1	26.7	27.2	30.2		19.3	69.6	2.3	10.6	0.1	4.0	8.4	3
	SL 14	300 – 320	58.2	18.7	23.2	23.2		16.2	57.4	2.6	15.1	0.1	3.0	6.6	1
transition zone															
	SL 17	410 – 460	54.7	29.3	16.0	17.3		32.0	61.7	1.6	11.7	0.1	3.3	7.2	6
lower saprolite															
	SL 21	600 – 650	64.4	26.1	9.6	15.1		18.8	60.1	1.2	11.9	0.1	3.8	6.5	20
	SL 25	800 – 820	74.8	14.7	10.5	16.6		15.3	83.8	1.4		0.1			44
corestone															
zone 4	4c	corestone from 830 cm depth	80.9	15.2	3.9	4.0		9.2	< 0.05 [d]	1.5	14.2	0.2	3.2	5.3	70
	4a		76.6	19.6	3.8	4.7	12.6	11.8	< 0.05 [d]	0.9	8.1	0.2	2.2	3.6	68
zone 3	3.2		80.1	16.6	3.3	3.1	1.66	11.2	< 0.05 [d]	0.4	1.8	0.3	0.9	1.5	79
	3.1														78
zone 2	2.3		83.4	14.7	2.0	3.4	0.89	0.6	< 0.05 [d]	0.1	0.5	0.2	0.6	0.6	94
	2.2														94
	2.1														93
zone 1	1.3		82.2	15.9	2.0	< 0.01 [d]	ϕ_{pore} < He [d]	1.5	< 0.05 [d]	0.1	0.5	0.1	0.5	0.6	93
	1.2														93
	1.1														94

[a]See figure 1 for sampling in the regolith profile and corestone.
[b]SSA is the specific surface area of bulk samples determined from N_2 adsorption. For the corestone this represents the connected internal surface area.
[c]Extractions were performed on bulk samples using dithionite (d) and NaOH to release elements from Fe-amorphous phases, (Fe-hydr)oxides and Al-Si-amorphous phases, respectively. Leached element fractions are reported relative to the total element concentration in the bulk sample in percent. The sum of the dithionite- and NaOH-extractable phases given in oxide wt% of the bulk sample gives an upper limit as both leaching methods (dithionite and NaOH) partly extract both (Fe- and Al-) phases.
[d]below detection limit

3.1 Textural characterization

The range of the clay-sized fraction (< 2 μm) is maximum 2 – 4% in the corestone, and increases to 56% in the upper saprolite (Fig. 3.1A, Table 3.1). It becomes the dominant size fraction at about 150 cm depth. However, the clay-sized fraction is slightly lower in the soil than in the upper saprolite. The silt-sized fraction ranges from 14.7 to 16.6% in the corestone. In the regolith, the silt-sized fraction ranges between 6.6 and 29.3% with lower values towards the top. The fraction of sand-sized minerals is 80.1 – 83.4% in the corestone. In the regolith its contribution decreases from 74.8% in the lower saprolite to 36.6% in the soil.

Porosity is below the detection limit of the He-pycnometry method in corestone zone 1 (pores are too small to be entered by He atoms). In corestone zone 2 the porosity is 0.89 ±0.02 vol.% and increases in corestone zone 3 to 1.66 ±0.04 vol.% and to 12.57 ±0.28 vol.% in corestone zone 4 (Fig. 3.2B, Table 3.1, uncertainties are absolute values and are based on measurement, volumetric and mass uncertainties, the relative uncertainty is < 2.3% of porosity). Additionally, the internal surface area of grain boundaries and micro-fractures that are connected and hence accessible with N_2 is below the detection limit of the BET method (< 0.01 m^2/g using N_2) in corestone zone 1, but zone 2 has a connected internal surface area of about 3 m^2/g, similar to zone 3. The connected internal surface area then increases towards the rindlets in zone 4 to 4.6 m^2/g. In the saprolite, specific surface area (SSA) increases from 15.1 m^2/g above the corestone to 55.6 m^2/g in the upper saprolite (Table 3.1). Please note that as already explained in the method section (2.1.2), I refer to connected internal surface area for the corestone samples because they are cylindric drill cores and not powders like the regolith samples.

3.2 Clay mineralogy

The clay mineral assemblages were identified from FTIR and XRD analyses by comparison to published reference data (Balan, 2006; Gustafsson et al., 1999; Hong et al., 2012; Moore and Reynolds, 1997; van der Marel and Beutelspacher, 1976) and results are compiled in Table 3.2 and Fig. 3.2. Note that due to the dithionite treatment prior to the grain size separation Fe-(oxy)(hydr)oxides do not appear in FTIR spectra and XRD pattern. The FTIR spectra are shown only in the range of 3800 – 3300 cm^{-1} (Fig. 3.2A), where peaks specific of clay minerals are located. Because the clay-sized fraction in corestone zones 1 and 2 is dominated by primary minerals, the results for these corestone zones are not reported in Fig. 3.2. Importantly, and in contrast to the extractions of the (non)crystalline (oxy)(hydr)oxides, the clay mineralogical analyses were only performed on the clay-sized fraction separates.

Characteristic peaks for clay minerals in the spectra are close to background level for corestone samples, but clearly detectable in saprolite and soil samples. Combining results from both analytical techniques (XRD and FTIR), kaolinite can be identified as the major secondary clay mineral throughout the regolith, followed by gibbsite. In the lowest saprolite sample SL 25 and in the upper soil sample SL 6 quartz and feldspars are detected in the clay-sized fraction, combined to primary minerals in Fig. 3.2B. The broadening of the strong XRD

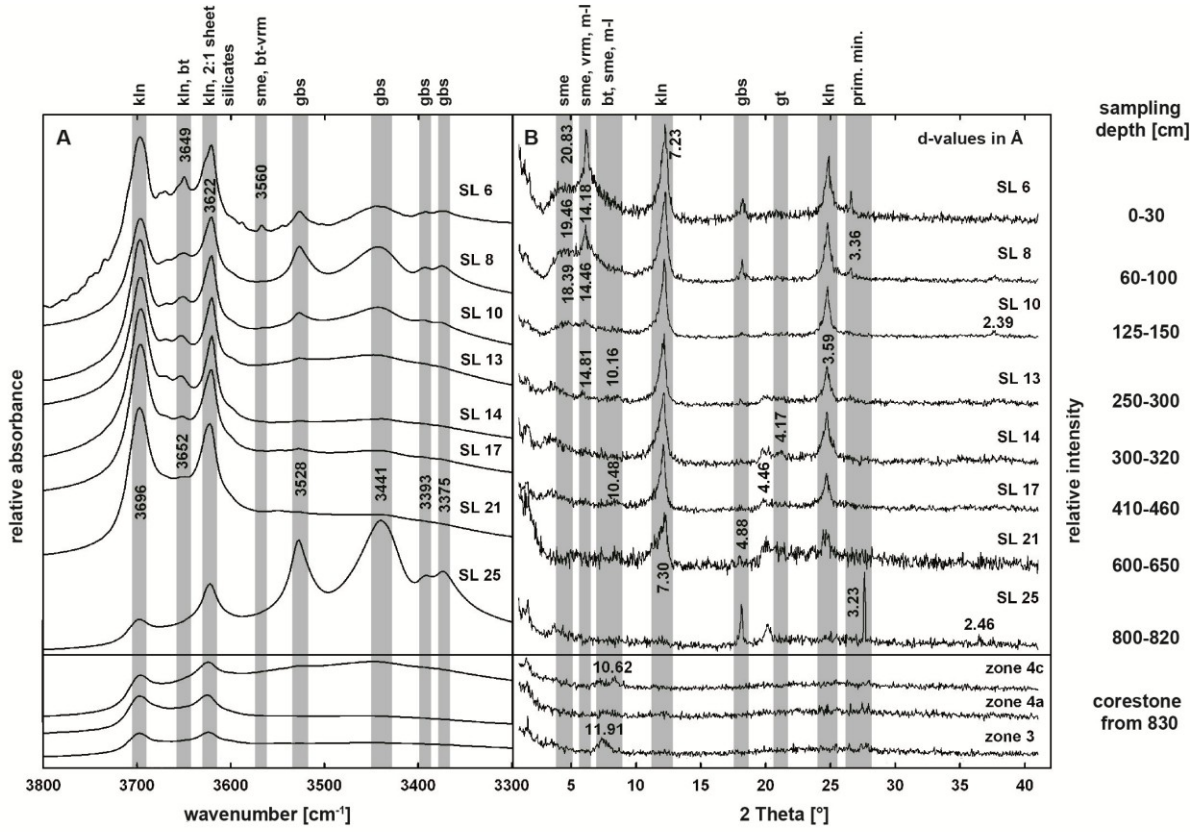

Figure 3.2 Results of IR spectroscopy (A) and X-ray diffraction (B) measurements on clay-sized fractions separated from the regolith samples and the corestone. Because the clay-sized fractions of corestone zones 1 and 2 are dominated by primary minerals spectra for these zones are not shown. The IR spectra in (A) are only shown from 3800 to 3300 cm^{-1} to facilitate the identification of secondary minerals according to their OH-stretching vibrations. The labeled d-spacing values in the XRD pattern (B) are reported in Å units. The primary mineral peaks at 3.36 and 3.23 Å are quartz and feldspar, respectively. bt: biotite, gbs: gibbsite, gt: goethite, kln: kaolinite, m-l: mixed-layer clays, sme: smectite, vrm: vermiculite.

kaolinite peak at 7.3 Å towards higher values (hence lower 2 Theta angles, *e.g.,* SL 21, Fig. 3.2B) can be explained by inter-stratification of halloysite or smectite layers, but for simplification I do not differentiate between "pure" kaolinite and mixed-layer kaolinite minerals, and in the following the term kaolinite is used interchangeably. Minor peaks in the region 10 – 20 Å can be attributed collectively to a group of 2:1 sheet silicates (biotite) and the clay minerals smectite, vermiculite, illite, and chlorite. Distinguishing between these minerals and potentially mixed-layer minerals is more challenging. However, I first note that in most samples (except in the upper saprolite and soil) these peaks are relatively small, suggesting that their contribution to the mineral assemblage is almost negligible. Second, although mixed-layer clay minerals with a high biotite component can produce the XRD peaks observed around 10 Å (Fig. 3.2B), the XRD peak at 12 Å might rather reflect a regularly interstratified phase containing alternating14 Å and 10 Å layers, *i.e.*, 2:1 clay layers within the biotite minerals (mixed layer clays), or poorly hydrated smectites. Expansion of the biotite layers, due to hydration (hydrobiotite), oxidation, or replacement of K by other cations could also shift the 10 Å biotite peak to higher values (Kalinowski and Schweda, 1996; Malmström and Banwart, 1997). The presence of 2:1 clay minerals can also result in XRD

peaks such as those observed at 14 Å and the broad XRD peaks between 18 and 20 Å. No further analyses were carried out to distinguish between the different secondary 2:1 clay minerals, as the peak intensities are too low for an identification of the individual minerals. Nevertheless, as Na and Ca are almost entirely solubilized from the whole regolith at Hakgala (Hewawasam et al., 2013) montmorillionite- or nontronite-like smectites are unlikely to be present, as well as illite and chlorite as this highly weathered profile has developed under tropical climate (Hong et al., 2009; Robert and Kennett, 1994). Hence, I infer that these 2:1 clay minerals are most likely smectite and vermiculite. In addition, I would like to point out that these minerals are most likely of Fe-rich chemical composition, as Fe is supplied through pyroxene and biotite weathering (see section 3.5) and is not removed from the system (Hewawasam et al., 2013).

Table 3.2 Secondary mineral associations of the < 2 µm fraction in the regolith profile and corestone

zone	sample	depth [cm]	minerals in < 2 µm size fraction
soil	SL 6	0 – 30	kaolinite, 2:1 clays, gibbsite
upper saprolite	SL 8	60 – 100	kaolinite, 2:1 clays, gibbsite,
	SL 10	125 – 150	kaolinite, gibbsite, (2:1 clays)
	SL 13	250 – 300	kaolinite, gibbsite, (2:1 clays)
	SL 14	300 – 320	kaolinite, goethite
transition zone	SL 17	410 – 460	kaolinite, goethite
lower saprolite	SL 21	600 – 650	kaolinite, gibbsite, goethite
	SL 25	800 – 820	kaolinite, gibbsite, goethite
corestone			
zone 4c	SL 55	corestone from 830 cm depth	kaolinite, gibbsite, 2:1 clays, goethite
zone 4a	SL 53		kaolinite, goethite, 2:1 clays
zone 3	SL 49		kaolinite, biotite, 2:1 clays, goethite
zone 2	SL 48b		(primary minerals), biotite, goethite, (2:1 clays)
zone 1	SL 48a		(primary minerals)

3.3 Selectively extracted (non)crystalline (oxy)(hydr)oxides

The dithionite-soluble Fe (Fe_d) ranges from 0.01 to 4.1 wt.% over the entire profile. Normalizing the concentration of Fe_d to total Fe concentration from bulk XRF analyses (Hewawasam et al., 2013) yields the fraction of Fe that is carried by (non)crystalline Fe-(oxy)(hydr)oxides. The Fe_d/Fe_{total} ratio is 1.5% in corestone zone 1, 0.6% in zone 2, 11.2% in zone 3, 11.8% in zone 4a and 9.2% in zone 4c (Fig. 3.3A, Table 3.1). In the saprolite the Fe_d/Fe_{total} ratio increases to 32.0%, from the corestone to the transition zone in the saprolite at 435 cm depth, and increases again to 47.9% in the upper saprolite. The soil exhibits a Fe_d /

Fe_{total} ratio of 37.8%. The dithionite-soluble Mn (Mn_d) in the corestone was too low for quantitative determination by ICP-OES in the extracts (*i.e.,* indistinguishable from blank level concentrations). In the saprolite, the Mn_d/Mn_{total} ratio is relatively consistent in the lower and the upper saprolite with values between 57.4% and 87.4%. However, towards the soil Mn_d/Mn_{total} decreases to 36.2%. The soil exhibits a Mn_d/Mn_{total} ratio of 25.7% (Fig. 3.3B). The concentration of Al contained in dithionite-soluble phases (Al_d) ranges from 0.01 wt.% to 1.0 wt.%, corresponding to a dithionite-soluble Al fraction (Al_d/Al_{total}) of 0.1% in zone 1 to 1.5% in zone 4c. In the saprolite profile, the Al_d/Al_{total} ratio increases from about 1% in the lower saprolite to 8.6% in the soil (Figure 3.3C). Only a small amount of Si is extracted by dithionite (Si_d), ranging from 0.02 to 0.1 wt.%, and Si_d/Si_{total} is < 0.3% throughout the profile (Fig. 3.3D).

Aluminum and silicon contained in NaOH-soluble phases (amorphous Si and Al phases, Al_{NaOH} and Si_{NaOH}) show the same trends in the corestone but differ in the upper saprolite. The Al_{NaOH} increases from 0.04 wt.% in the corestone to 2.3 wt.% in the saprolite; Al_{NaOH} / Al_{total} in the corestone is between 0.5% and 14.2% (Fig. 3.3E, Table 3.1). In the saprolite and the soil the fraction Al_{NaOH}/Al_{total} ranges from 10.6% to 20.1% with no clear trend. The measured Si_{NaOH} concentrations range between 0.2 and 1.3 wt.%. This corresponds to Si_{NaOH}/Si_{total} ratios of 0.5% to 3.2% in the corestone and 2.3% to 5.1% in the saprolite and soil (Fig. 3.3F).

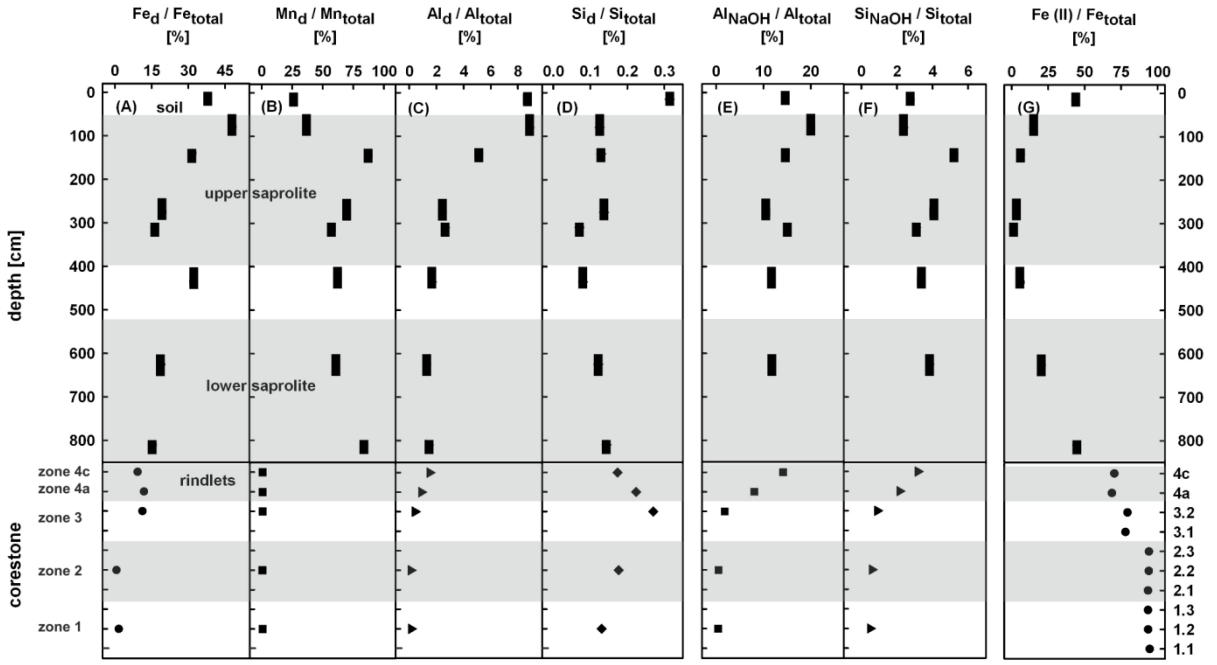

Figure 3.3 Results of the selective extractions. (A-D) Fractions [%] of Fe, Mn, Al, and Si contained in Fe-amorphous phases and Fe-(oxy)(hydr)oxides (extracted using dithionite). (E, F) Fractions [%] of Al and Si contained in Al-amorphous phases (extracted using NaOH). The total concentration of each element in the bulk sample was measured by XRF (data from Hewawasam et al., 2013). (G) Fe(II) / Fe_{total} ratio. The grey horizontal bands indicate different zones in the saprolite and the corestone. Error bars are smaller than the symbols. The Mn_d contents in the corestone dithionite extractions were below detection limit (Table 1) and hence Mn_d / Mn_{total} are plotted close to zero in the lower section of panel B for illustrative purposes.

The contribution of (non)crystalline Al- and Fe(oxy)(hydr)oxides (Σ_{d+NaOH}, in oxide %wt., Table 3.1) to the bulk sample mass was calculated assuming that the amorphous phases are fully oxidized (*i.e.*, Fe is present as Fe(III) and Mn as Mn(IV)). Σ_{d+NaOH} ranges from 0.6% in corestone zone 1 to 5.3% in corestone zone 4, and increases to 6.5% in the lower saprolite. In the upper saprolite, Σ_{d+NaOH} is in the range of 6.6% and 13.6% and decreases to 9.7% in the soil.

3.4 Fe(II)/Fe_{total}

The corestone samples from zone 1 (samples 1.1 to 1.3) and the samples from zone 2 (light grey part in the corestone, samples 2.1 to 2.3) show no significant change in the Fe(II)/Fe_{total} ratio (93 – 94%, Fig. 3.3G, Table 3.1). Changes occur at the boundary from zone 2 to zone 3. This transition is macroscopically distinct as a darker band between the light gray zone 2 and the yellow zone 3 (Fig. 1.2C). Values in zone 3 show no trend and are in the range 78 – 79%. The two rindlets around the corestone are slightly more oxidized, with ratios of 68% and 70% for samples 4a and 4c, respectively. The lower saprolite samples depict a strong decrease in Fe(II) content, with a Fe(II)/Fe_{total} ratio changing from 44% above the corestone to 1% at a depth of about 300 cm. The Fe(II)/Fe_{total} ratio increases again in the upper saprolite towards the top from 3% to 44% in the soil sample.

3.5 Micro-scale investigations on primary minerals/weathering features in the corestone and the rindlets

3.5.1 Microprobe investigations

All microprobe measurements are compiled in Appendix A. Measurements include plagioclase, K-feldspar, pyroxene and biotite and the accessory minerals zircon, ilmenite, apatite and monazite. Quartz was excluded for the analyses, since it does not show significant weathering. The minerals that were observed to weather in the corestone are pyroxene, plagioclase, and biotite (Hewawasam et al., 2013), and therefore the main analyses focus on those minerals. Four main results can be gained from the electron microprobe analyses: (1) The mineral formula of the primary minerals, Tables 3.3 to 3.6. The mineral formulas given below present the mean mineral chemistry of the unweathered (pristine) minerals. (2) Primary and secondary textures in the minerals. (3) Element maps from which transport of elements during weathering can be derived (Fig. 3.6). (4) Identification of the composition of secondary precipitates.

Investigations of the minerals in the "virtually" unweathered parts of the rock as *e.g.* corestone zone 1, show that already there several reactions alter the rock. Some of the features have their origin in metamorphic processes but others stem from weathering. Throughout the different zones, the chemical compositions of the pristine primary minerals do not show significant changes.

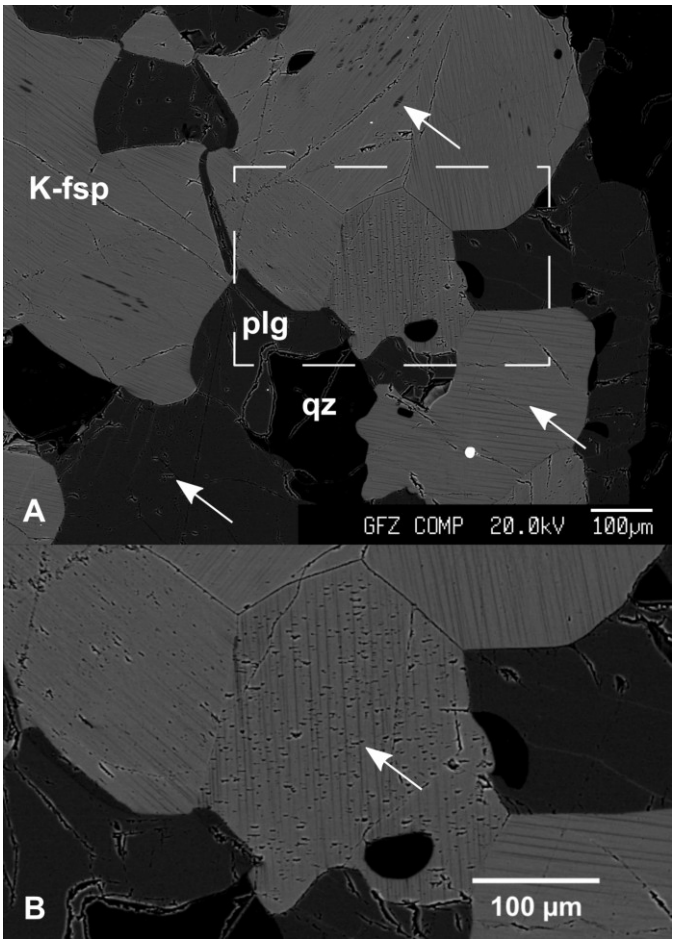

Figure 3.4 Features in feldspars from the "virtually" unweathered rock. The back scatter electron (BSE) image A, acquired with the microprobe, illustrates features observed in feldspars from zone 1. The K-feldspars show lamellae with plagioclase. Both patch and film lamellae are observed (white arrows in the right part). The plagioclase shows intra minerals fractures already in corestone zone 1. Panel B is a close up of the film lamellae in the K-fsp as indicated with the white box in Panel A. The white arrow shows nano-tubes that have been generated in the K-fsp connecting the film lamellae of plagioclase composition.

3.5.1.1 Feldspars

K-feldspars investigated in corestone zone 1 and 3 show exsolution lamellae. Although compositional analyses of the lamellae were not performed, they are most likely of the same composition as the Na- plagioclase. These exsolution lamellae were formerly described as film- or patch/spindle-perthite, depending on the form of the lamellae (Evangelakakis et al., 1993; Lee and Parsons, 1995; Parsons and Lee, 2009). Those that show lense-shaped or elongated lamellae are called patch/spindle-perthite, while K-feldspars that exhibit lamellae that are straight and < 1-2 µm in thickness are termed film-perthite. Even in corestone zone 1 but more pronounced in corestone zone 3, the lamellae are often associated with etches and rough feldspar surfaces. Fig. 3.4A and 3.4B show K-feldspars and plagioclase from zone 1 and corestone zone 3, respectively. Clearly visible are darker lense-shaped and straight lamellae in the K-feldspar (arrows in Fig. 3.4A and 3.4B). The plagioclases do not show exsolution lamellae but exhibit etches and intra mineral cracks, already in corestone zone 1. These are more pronounced in the outer corestone zones. In the rindlets (corestone zone 4) these cracks form a network in and around the plagioclase and are filled with secondary phases (overview pictures in Fig. 3.10 and 3.11, sample overview picture Fig. 2.3C in methods section 2.5).

Table 3.3 K-feldspar. Element-oxides in weight % ± 2SD, mean concentration data for each corestone zone

	Sample-1-Z1, n=16	**Sample-2-Z2, n=11**	**Sample-3-Z3, n=16**	**Sample-3-Z4a, n=5**	**Sample-5-Z4c, n=4**
SiO_2	64.55±0.34	64.50±0.30	64.53±0.45	63.65±0.52	63.82±0.21
TiO_2	bdl *	0.01±0.04	bdl *	bdl *	bdl *
Al_2O_3	18.55±0.18	18.64±0.18	18.69±0.23	18.84±0.11	18.63±0.07
FeO	0.04±0.11	0.01±0.03	0.13±0.29	0.03±0.04	0.02±0.02
MnO	bdl *	bdl *	bdl *	bdl *	bdl *
CaO	0.05±0.05	0.07±0.05	0.07±0.08	0.04±0.06	0.09±0.04
Na_2O	1.63±0.26	1.78±0.36	1.53±0.77	1.80±0.24	2.15±0.19
K_2O	14.13±0.41	13.91±0.47	14.19±1.05	13.90±0.40	13.44±0.30
Total	98.96	98.92	99.14	98.28	98.15

bdl *: below detection limit

Molar chemical formula based on O = 8				
Si	**Al**	**Ca**	**Na**	**K**
2.98	**1.02**	**0.00**	**0.16**	**0.82**

$$(Na_{0.16}Ca_{0.00}K_{0.82})Al_{1.02}Si_{2.98}O_8$$

Table 3.4 Plagioclase. Element-oxides in weight % ± 2SD, mean concentration data for each corestone zone

	Sample-1-Z1, n=13	**Sample-2-Z2, n=10**	**Sample-3-Z3, n=13**	**Sample-3-Z4a, n=5**	**Sample-5-Z4c, n=6**
SiO_2	61.81±0.50	61.80±0.69	61.91±0.39	61.21±0.33	60.90±0.71
TiO_2	0.02±0.04	0.01±0.02	0.02±0.03	0.01±0.03	0.02±0.04
Al_2O_3	23.54±0.23	23.65±0.16	23.79±0.25	23.82±0.14	23.59±0.19
FeO	0.08±0.13	0.05±0.03	0.06±0.07	0.05±0.04	0.05±0.02
MnO	0.01±0.02	0.01±0.02	0.01±0.02	bdl *	0.01±0.02
CaO	5.27±0.12	5.25±0.07	5.31±0.14	5.18±0.07	5.21±0.12
Na_2O	8.45±0.15	8.57±0.18	8.50±0.25	8.61±0.23	8.48±0.21
K_2O	0.27±0.10	0.24±0.06	0.27±0.09	0.26±0.09	0.35±0.08
Total	99.45	99.57	99.86	99.13	98.60

bdl *: below detection limit

Molar chemical formula based on O = 8				
Si	**Al**	**Ca**	**Na**	**K**
2.75	**1.25**	**0.25**	**0.74**	**0.02**

$$(Na_{0.74}Ca_{0.25}K_{0.02})Al_{1.25}Si_{2.75}O_8$$

While K-feldspars show no weathering in the corestone and the rindlets, significant weathering of plagioclase starts in zone 3 along grain boundaries and inner-mineral cracks. However, the pristine plagioclase retain their original composition on all corestone zones

(Table 3.4). Pronounced precipitation of secondary phases is observed in zone 4. The weathered plagioclases have open veins in which secondary phases precipitate. The element maps show that Ca and Na are not detectable, while Si and Al precipitate in the secondary phases (detection limits as mentioned in the method section 2.5.1). Compared to the plagioclase, less Si, and more Al are present. Moreover, in the secondary phases also Fe was detected (Fig. 3.6C).

3.5.1.2 Pyroxene

All pyroxenes are highly fractured and exhibit rough surfaces with etch pits, even in corestone zone 1. Also the minerals in direct vicinity of pyroxenes show fracturing. Significant pyroxene weathering features with precipitation of secondary phases are prominent in zone 3, but the high resolution analyses show the initiation of weathering in zone 1 (section 3.5.3). Dissolution of pyroxene proceeds along pre-existing cracks, on the one to tens of µm scale (section 3.5.3). In these cavities two kinds of secondary phases could be recognized (overview picture in Fig. 3.9, sample overview picture Fig. 2.3A in methods section 2.5). The first phase, here called the Al-phase, is precipitated in the former crack network and is really prominent. The second phase, here termed Fe-phase, forms smaller spots in the first secondary phase and is much brighter in backscatter images (due to higher amounts of elements with higher atomic number). In the weathering products of pyroxene no Mg and Mn are detected. The Al-phases contain less Fe compared to the pyroxene, but more Ca. Phosphorous and Al were also abundant in detectable amounts. The Fe- phase revealed much higher Fe and higher Ca concentrations compared to the pyroxene. Moreover, P was determined with higher amounts compared to the Al-phase (Fig. 3.6A). Silicon was not investigated with the mapping but single point electron microprobe measurements revealed that this phase is mainly composed of Al, Si, and Fe. Furthermore, during TEM analyses it was shown that both phases contain Si (see section 3.5.3).

Table 3.5 Pyroxene. Element-oxides in weight % ± 2SD, mean concentration data for each corestone zone

	Sample-1-Z1, n =20	**Sample-2-Z2, n=20**	**Sample-3-Z3, n=23**	**sample-3-Z4a, n=5**	**Sample-5-Z4c, n=7**
SiO_2	50.56±0.38	50.57±0.56	50.64±0.66	50.65±0.58	50.28±0.63
TiO_2	0.08±0.04	0.08±.0.6	0.07±0.5	0.05±0.04	0.08±0.08
Al_2O_3	0.62±0.17	0.62±0.22	0.61±0.19	0.62±0.19	0.79±0.19
Cr_2O_3	0.01±0.02	0.01±0.02	0.01±0.02	bdl *	0.01±0.02
FeO	33.19±0.64	33.36±0.39	33.13±0.55	33.34±0.25	33.53±0.68
MnO	0.65±0.05	0.62±0.04	0.60±0.04	0.62±0.06	0.57±0.06
MgO	14.45±0.34	14.24±0.22	14.56±0.42	14.30±0.13	14.18±0.49
CaO	0.53±0.06	0.52±0.06	0.49±0.07	0.47±0.04	0.47±0.06
Na_2O	0.01±0.02	0.02±0.02	0.02±0.04	0.02±0.03	0.02±0.03
K_2O	bdl *	bdl *	0.01±0.04	bdl *	0.01±0.01
Total	100.09	100.09	100.14	100.07	99.94

bdl *: below detection limit

Molar chemical formula based on O = 6					
Si	**Al**	**Fe**	**Mn**	**Mg**	**Ca**
1.97	**0.03**	**1.09**	**0.02**	**0.83**	**0.08**

$$(Fe_{1.09}Mg_{0.83}Ca_{0.08}Al_{0.03}Mn_{0.02})Si_{1.97}O_6$$

3.5.1.3 Biotite

The Ti-rich biotite does not show any alteration features in the innermost corestone zone. However expansion of layers are observed in zone 2. Significant weathering features are observable in zone 4. From this zone element maps in biotite were produced (Fig. 3.6B, sample overview picture Fig. 2.3B, methods section 2.5). The layers of biotite show expansion from each other and secondary phases precipitate in these cavities. No Fe, K, and Ti and nearly no Mg are contained in theses phases. Compared to biotite, Si is not significantly increasing, but Al is highly enriched. In some parts (veins) higher concentrations of Fe and Ca are observed (Fig. 3.6B). Adjacent minerals show intra-mineral fracturing.

Table 3.6 Biotite. Element-oxides in weight % ± 2SD, mean concentration data for each corestone zone

	Sample-1-Z1, n=18	**Sample-2-Z2, n=15**	**Sample-3-Z2, n=7**	**Sample-3-Z3, n=11**	**Sample-3-Z4a, n=6**	**Sample-5-Z4c, n=6**
SiO_2	37.45±0.55	37.42±0.57	37.53±0.30	37.25±1.32	37.18±0.37	37.39±0.28
TiO_2	5.69±0.51	5.31±0.38	5.80±0.32	5.16±0.23	5.25±0.12	5.46±0.40
Al_2O_3	13.58±0.49	13.68±0.34	13.78±0.18	13.94±0.63	13.86±0.20	13.75±0.32
SrO	0.13±0.03	0.14±0.03	0.14±0.03	0.13±0.02	0.13±0.03	0.13±0.02
FeO	19.63±0.71	19.77±0.47	19.42±0.46	19.94±0.38	19.73±0.60	19.94±0.26
MnO	0.08±0.02	0.07±0.04	0.07±0.04	0.06±0.04	0.05±0.02	0.06±0.03
MgO	10.88±0.36	11.16±0.39	11.03±0.31	11.39±0.59	11.21±0.24	10.84±0.48
CaO	bdl *	bdl *	bdl *	bdl *	bdl *	bdl *
Na_2O	0.06±0.04	0.04±0.03	0.05±0.03	0.07±0.03	0.06±0.04	0.09±0.05
K_2O	9.13±0.60	9.19±0.18	9.15±0.13	9.01±0.23	9.16±0.12	9.28±0.12
Cl	0.11±0.02	0.11±0.01	0.11 ±0.01	0.11±0.02	0.11 ±0.01	0.11 ±0.01
Total	96.75	96.89	97.07	97.08	96.75	97.04

bdl *: below detection limit

Molar chemical formula based on O = 12								
Si	**Ti**	**Al**	**Sr**	**Fe**	**Mg**	**Na**	**K**	**Cl**
3.06	**0.34**	**1.33**	**0.01**	**1.35**	**1.35**	**0.01**	**0.96**	**0.02**

$$(K_{0.96}Na_{0.01})(Fe_{1.35}Mg_{1.35}Ti_{0.34}Sr_{0.01})(Al_{1.33}Si_{3.06})O_{10}((OH)_2Cl_{0.02})$$

3.5.1.4 Accessory minerals

Results are reported for apatite, monazite, ilmenite, and zircon. Their chemical composition is tabulated in Appendix A. Apatites in corestone zone 1 already show rough surfaces, etch pits, and intra mineral fractures (Fig. 3.5B). Approximately 4 wt% F are incorporated in the apatite but minimal Cl was analyzed, hence I refer to a Fluor-apatite. Furthermore impurities of Ce were detected. In many occurrences, the apatite is accompanied by small monazite crystals, predominantly at the grain boundary or in cracks in the apatite (Fig. 3.5B). Monazite also occurs as single crystals in the rock matrix (Fig. 3.5A). Cerium is the major light rare earth element (LREE) component in the monazite, but also thorium is included in high amounts (up to 18 wt%). The single monazite crystals show a zoning with areas that appear brighter in BSE images according to higher amounts of elements with higher atomic number (Fig. 3.5C). The darker areas, as compared to the brighter parts show strong depletion of Th, and a slight depletion of Si and Ca, while the LREE (Ce, La) and P show higher concentrations. Praseodym, Nd, and Sm show no significant differences in both parts, while the Heavy Rare Earth Element (HREE) Gd is slightly enriched in the darker areas. The monazites depict rough surfaces with etch pits and intra mineral fractures already in the inner most part of the corestone (Fig. 3.5C). Like the aforementioned minerals, zircon and ilmenite appear with rough surfaces and etches already in corestone zone 1 (Fig. 3.5D). The analyzed zircons contain impurities of Hf of 1.0 – 2.6 wt%. Very rarely, a Th-oxide could be found.

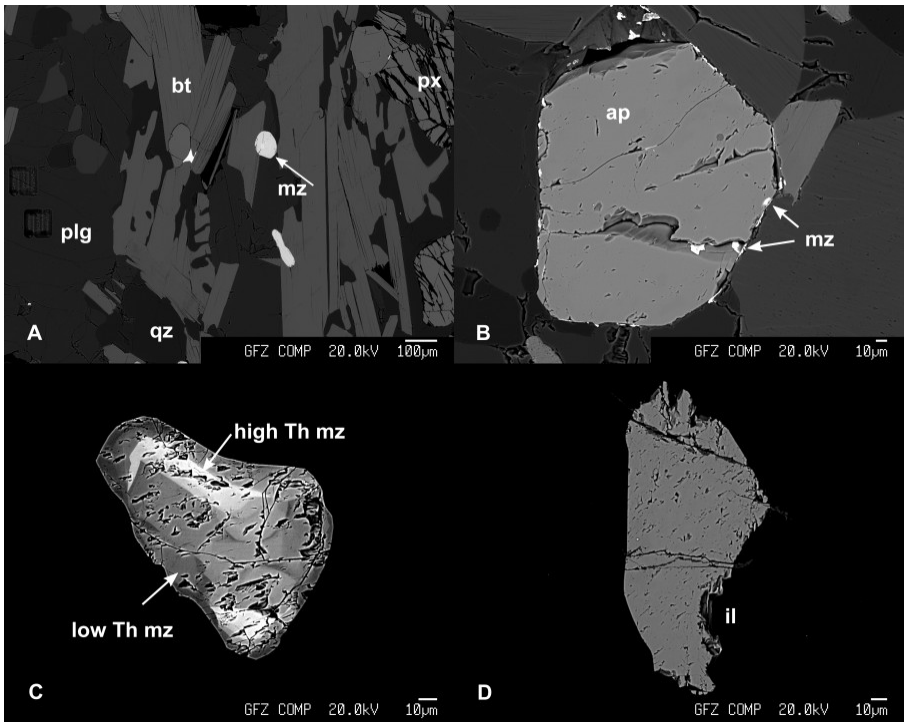

Figure 3.5 Features observed in primary minerals from the "virtually" unweathered rock and during incipient weathering. The pictures are acquired with the microprobe in BSE modes. (A) was taken in corestone zone 2 and shows a fractured pyroxene in the right upper corner, and single monazite crystals unassociated with apatite. (B) shows an apatite mineral from zone 1 with small monazite precipitated at the apatite grain boundary or in cavities and fractures inside the mineral. (C) depicts a single monazite mineral from zone 2 with brighter and darker areas that hold higher and lower Th concentrations, respectively. (D) shows an ilmenite from zone 1, which exhibits a rough surface with deep etches and intra minerals fractures. The abbreviations for the minerals are as follows: px: pyroxene, bt: biotite, plg: plagioclase, qz: quartz, mz: monazite, ap: apatite, il: ilmenite.

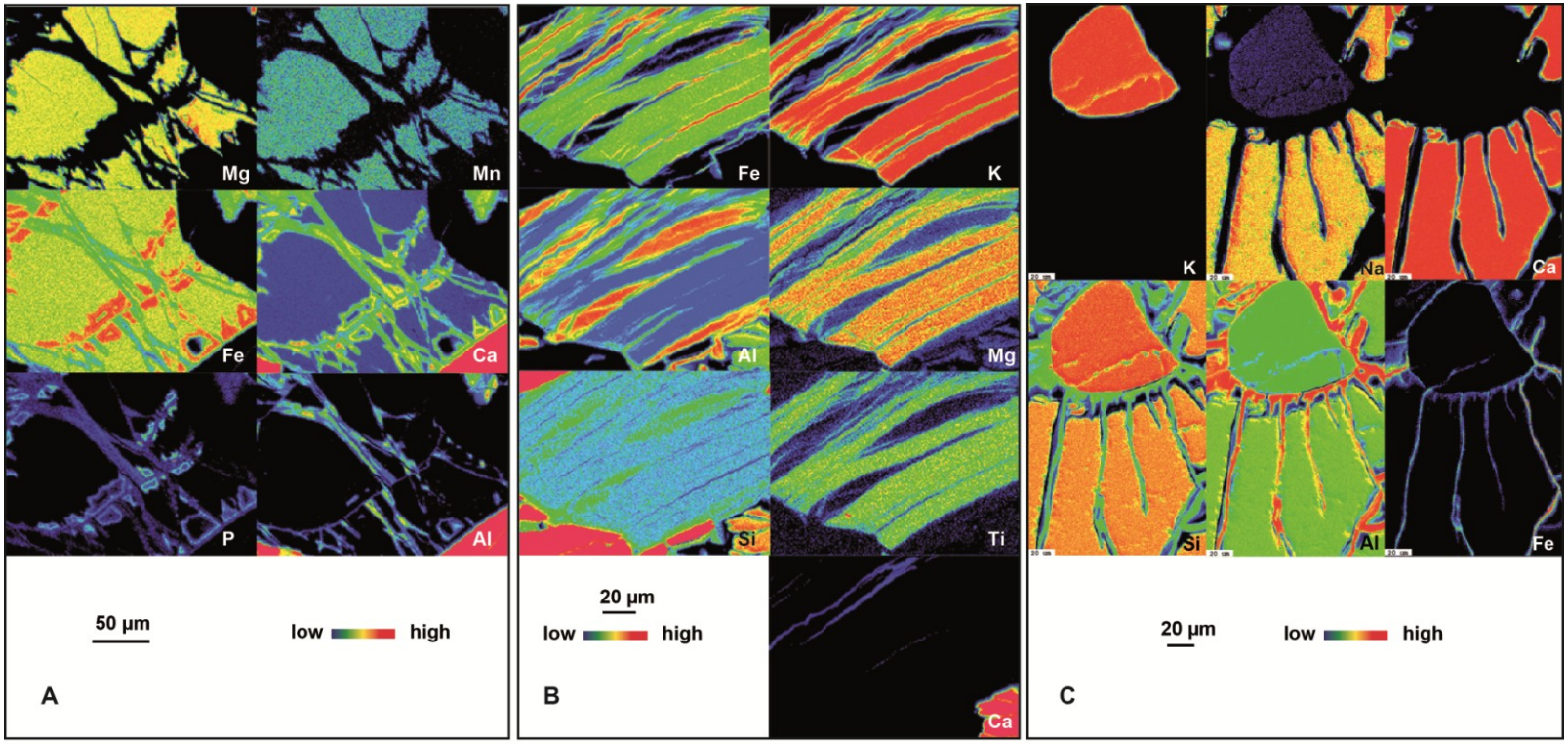

Figure 3.6 The microprobe element maps of weathered pyroxene, biotite and plagioclase. (A) shows the distribution of Mg, Mn, Fe, Ca, P, and Al in a weathered pyroxene and two weathering products from zone 3. The scale bar is 50 µm and the color coding shows higher concentrations towards red and lower concentrations towards blue. The mapping revealed depletion of Mg and Mn and enrichment of Ca, and P in the secondary precipitates. Fe is enriched in some but depleted in other phases and Al is only enriched in one phase. Si was not investigated but is thought to be present in both phases and was determined with TEM measurements. (B) shows the concentrations of Fe, K, Al, Mg, Si, Ti, and Ca in a biotite and its weathering products from zone 4c, the outermost rindlet. The scale is 20 µm, and the color coding is the same as for the pyroxene mapping. During weathering, Fe, K, Mg, and Ti are removed, whereas Al and Si added to the secondary precipitate. In some parts, also Ca is precipitating. (C) presents the element maps of a plagioclase and its weathering products again from zone 4c. Concentrations of K, Na, Ca, Si, Al, and Fe were determined. While the K-feldspar stays intact, the plagioclase weathers along voids. During weathering Na, Ca, and some Si are lost and Al and Fe are added to the secondary phases.

3.5.1.5 Pore fillings

As already described while presenting the microprobe results for pyroxene, biotite and plagioclase, pore fillings are mainly composed of either Al and Si or Fe, Al, and Si. Minor amounts are P, Ca and Mg are present. Even in corestone zone 1, intra mineral fractures are occasionally filled with Fe rich precipitates. In the corestone parts that are subject to significant weathering, hollow spaces that were previously occupied by primary minerals might be completely filled with secondary phases. However, these phases contain high internal porosity as exemplarily shown in Fig. 3.7 which depicts such a space filled with secondary precipitates. Most strikingly is the partitioning into two distinct phases: the darker Al-bearing phase and the bright Fe-rich phase. The Al-bearing phase contains many disruptions perpendicular to the course of the phase. In contrast, the Fe-rich phase shows rosette-like features and evolves into the open void. The microprobe analyses revealed 70 wt% Fe, 23 wt% Si and 5 wt% Al and with minor contributions of Ca and K.

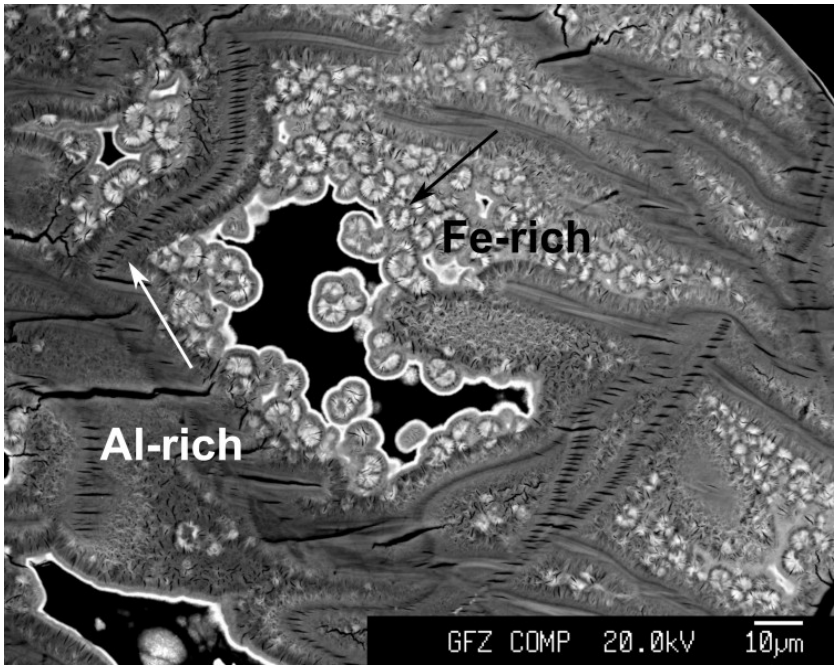

Figure 3.7 Pore fillings in corestone zone 4c. This BSE picture nicely illustrates an open space, formerly occupied by a primary mineral, which is now nearly completely filled with secondary precipitates. Only the dark area in the center of the void is left open. White parts are Fe-rich and contain rosette-like features (dark arrow), while darker parts reveal higher Al concentrations. The Al-rich parts contain many traversing fractures (white arrow).

3.5.2 Weathering features in 3D derived from FIB imaging

Weathered pyroxenes and plagioclases were investigated by FIB imaging to characterize the interface between primary and secondary phases. The “slice and view” procedure (Wirth and Morales, 2012) was applied for 3D visualization (see method section 2.5.2, Fig. 2.5). Due to low contrast differences between the different secondary phases and the primary mineral within the images it was only possible to produce a 3D visualization of the investigated pyroxene from zone 2.

In an early stage of weathering (sample from zone 2, Fig. 3.8), the fractured pyroxene show precipitation along the cracks. The secondary phases are much darker than the pyroxene, which indicate higher abundance of elements with lower atomic number than the pyroxene. The cracks form a connected network within the pyroxene, whereas the surrounding minerals show no fracturing. Additionally, the pyroxene fragments show micro-cracking (Fig. 3.8C). The 3D-model of the weathered pyroxene from zone 2 is provided in Fig. 3.8D and Fig. 3.8E. Fig. 3.8D illustrates the model from the rear view which is the last slice that has been removed during FIB investigation (see Fig. 2.5 in the method section 2.5.2 for explanation). The bottom of the thin section points towards the top of the image. Fig. 3.8E presents the first slice that has been cut and the surface of the thin section points to the top of the image. A narrow fracture of a few µm plunges downward (as seen from the surface) into the pyroxene, dividing the pyroxene in an “upper” and a “lower” part. From this fracture, a number of smaller but wider fractures further disintegrate the mineral. Along these smaller fractures high amounts of secondary phases precipitated. Due to low contrast in the images, the open fractures and the secondary precipitates appear as open voids in the 3D model (as well as the plagioclase in the lower right corner). Based on the 3D model illustrating the open space in the pyroxene, one can estimate that up to 20 % of the pyroxene might have been dissolved. With further weathering (results from corestone zone 3, Fig. 3.9), pyroxenes dissolve preferentially along the crystal lattice producing the Fe- phase. High micro-scale porosity is generated directly in contact with the dissolving surface, Fig. 3.9C. The Al-containing phase precipitates along the primary cracks. During incipient weathering in the more inward corestone zone 2, these cracks are ca. 1µm in diameter. In corestone zone 3 cracks extend to a width of ca. 10 µm and bigger. Larger pores occur in the Al-containing phase. From these, a network of smaller pores branch off, and the clear division into two distinguish phases disappears. The total porosity seems to be higher in the Al-containing phase (Fig. 3.9E and 3.9F).

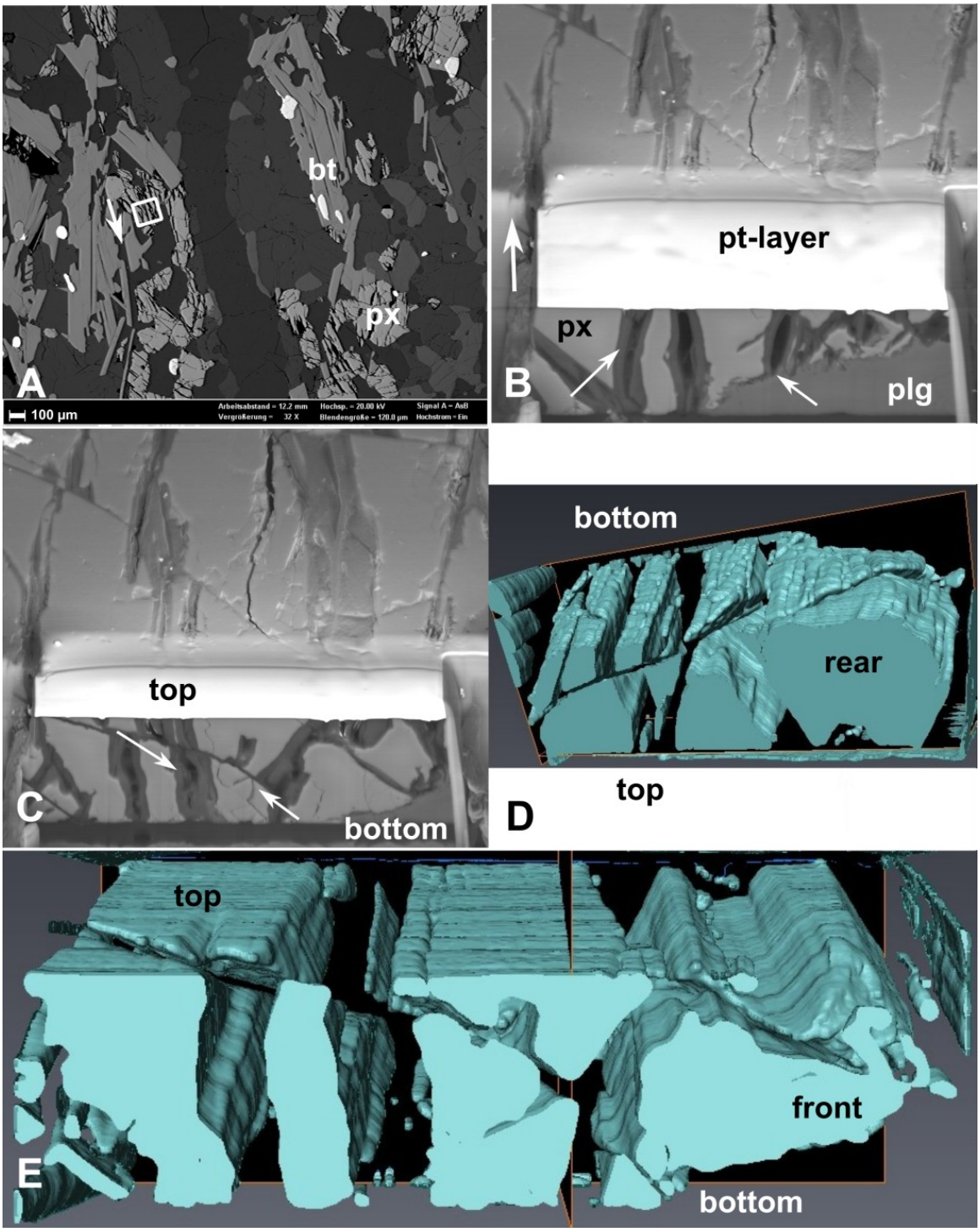

Figure 3.8 FIB mapping of pre-existing internal porosity in pyroxenes from zone 2. The overview panel in A shows the location of the FIB investigation (white rectangle). The arrow depicts the direction of removal of the slices. Panel B shows the highly cracked and weathered pyroxene (px) in contact to a plagioclase (plg). No dissolution of plg is observed (arrow). The black parts are filled with epoxy. Secondary phases precipitated along the crack walls, *e. g.*, left arrows in panels B and C. Internal cracking of the pyroxene during weathering is attributed to the volume change during *in situ* Fe oxidation, right arrow in panel C. Panels D and E show a 3D model of the pyroxene (green areas) and internal porosity resulting from the fracture network distribution within the pyroxene. Panel D shows a rear view of the 3D model, while panel E gives a front view of the 3D model similar to the stage in panel C. The labels "rear" refers to the rear view of the model, hence the last slice, while "front" refers to the first slice. Bottom refers to the bottom of the thin section (in contact to the glass slide and top is the surface of the thin section (with the protective Pt-layer, see Fig. 2.5 in method section 2.5.2 for explanation of orientation).

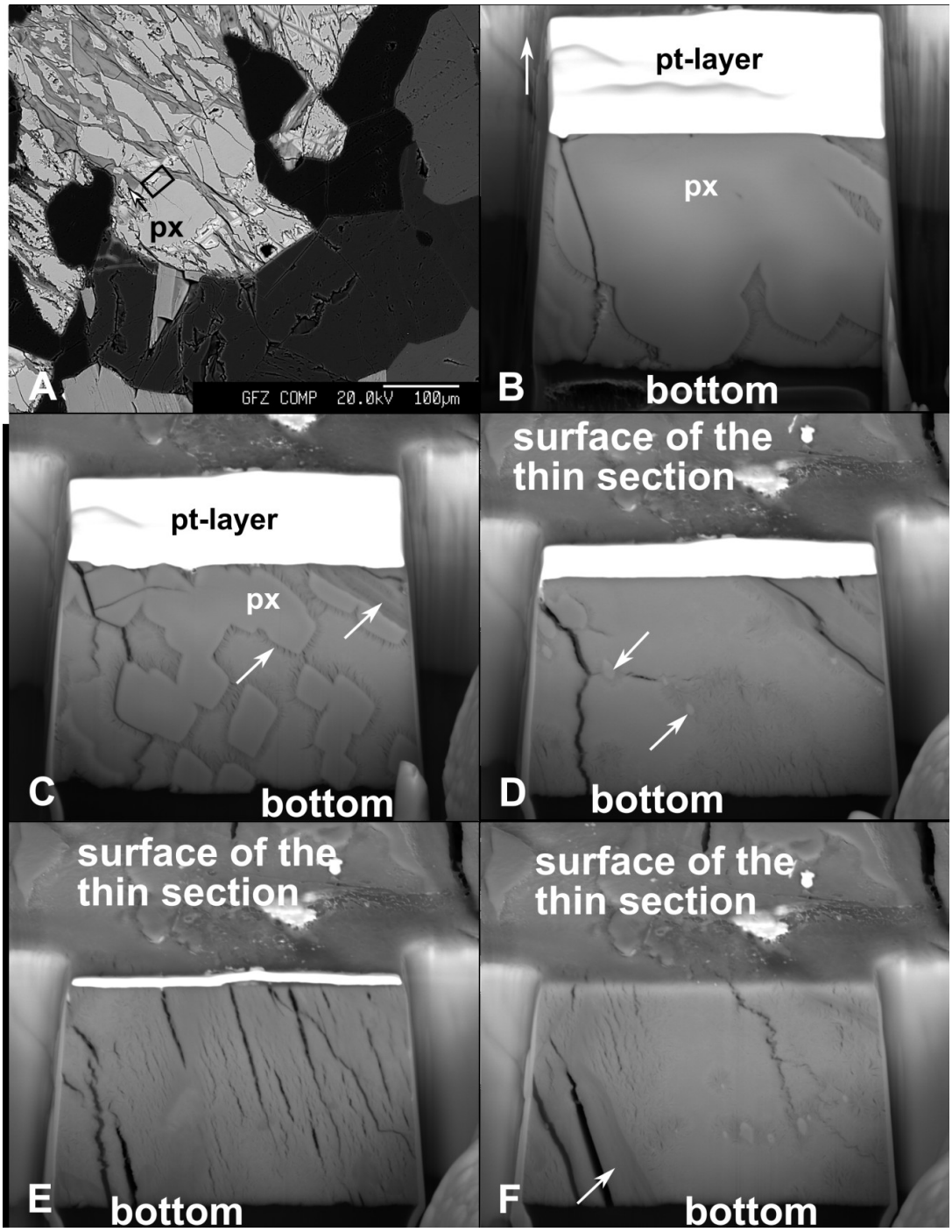

Figure 3.9 FIB mapping of weathering features in pyroxene, zone 3. Panel A is an overview image of the pyroxene and provides the location of the FIB investigation (black rectangle). The arrow depicts the direction of removal of the slices (see Fig. 2.5 in method section 2.5.2 for explanation of orientation). Panel B shows the front of the investigation. The center part is filled with pyroxene which is surrounded by secondary phases. The white arrow shows the direction of removal. Panel C shows how the weathered pyroxene disaggregates into smaller pieces. Weathering occurs preferentially along lattice structure. During weathering, high internal porosity is formed as shown by the open pores in contact to the pyroxene (left arrow). Along larger pores, elements are transported to the secondary phases (darker parts in the upper right corner, right arrow). As revealed by the TEM measurements, this element is mainly Al. In Panel D, the pyroxene is almost entirely replaced by secondary phases and pyroxene remnants appear as islands in the secondary phases (white arrows). Panel E shows high internal porosity within the secondary phases. All pores are arranged in the same direction. Panel F (the last slice of the investigation) depicts the difference between parts with larger pores to those with less or smaller pores. The darker color along the pores (arrow) is caused by a higher Al content compared to the phases in the center, where Fe is the major phase.

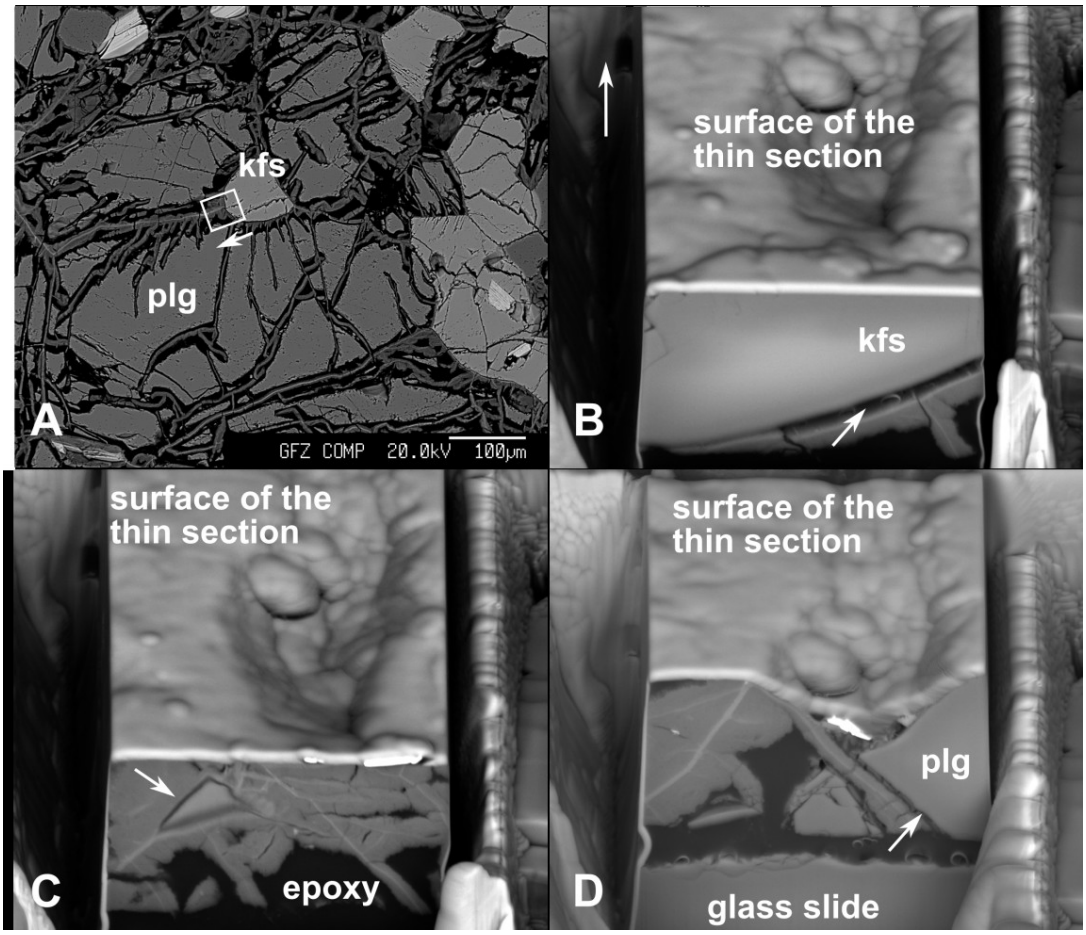

Figure 3.10 FIB mapping of K-feldspar (kfs) and plagioclase (plg) weathering. Panel A provides an overview of the FIB investigation. The arrow depicts the direction of removal of the slices (see Fig. 2.5 in method section 2.5.2 for explanation of orientation). Panel B and C show the interface between K-feldspar (kfs) and the products of plagioclase weathering. The left white arrow in B illustrates the direction of removal of the slices. The embedded K-feldspar is separated from the secondary phases by open pore space (arrows). Further along the direction of removal of the slices, the K-feldspar disappears; Panel C. Panel D shows the extensive secondary products of plagioclase weathering. The light grey veins are the Fe-rich centers described with the TEM measurements. The white arrow marks the Al-amorphous phase investigated in detail with TEM (section 3.5.3, Fig. 3.20 and 3.23).

The 3D models for the plagioclase show the weathering structures resulting from plagioclase dissolution, further analyzed with microprobe and TEM (see sections 3.5.1 and 3.5.3). Similar structures are not apparent for the K-feldspars. Additionally, open voids are observed between the K-feldspar and the secondary phases from plagioclase weathering without precipitation of an amorphous layer onto the grain boundary. In this specific 3D model (Fig. 3.10), the central Fe-amorphous phase from the plagioclase weathering surrounds the visually intact and unweathered K-feldspar. The second model was produced to investigate the spatial structure of the precipitating phases, especially the tip in the specific sample. Due to high re-deposition of material during the start of the measurement, the tip as it is situated at the thin section surface could not be imaged. However, the FIB slices show that the precipitates shape a plain that plunges into the plagioclase (normal to the surface of the thin section, Fig. 3.11). Three different phases are observed which are analyzed in detail with TEM (section 3.5.3). Despite

some disturbances during sample preparation, the Al-amorphous layer seems to precipitate on the plagioclase grain boundary. The void is filled with the Al-Si phase and the Si-Al-Fe phase in the center. Dark grey areas depict filling by epoxy, while black parts are empty. The 3D model beautifully shows the generation of a pore in the center of this set of secondary phases (white arrow in Fig. 3.11D). However, it is not clear if this is situated in the Si-Al-Fe phase or between that and the Al-Si phase. To summarize, a network of secondary precipitates from plagioclase weathering developed without impact on adjacent K-feldspars. Porosity is formed between the Al-amorphous layer precipitated on the plagioclase surfaces and the voids-filling precipitates and inside of the Al-Si and Si-Al-Fe phases.

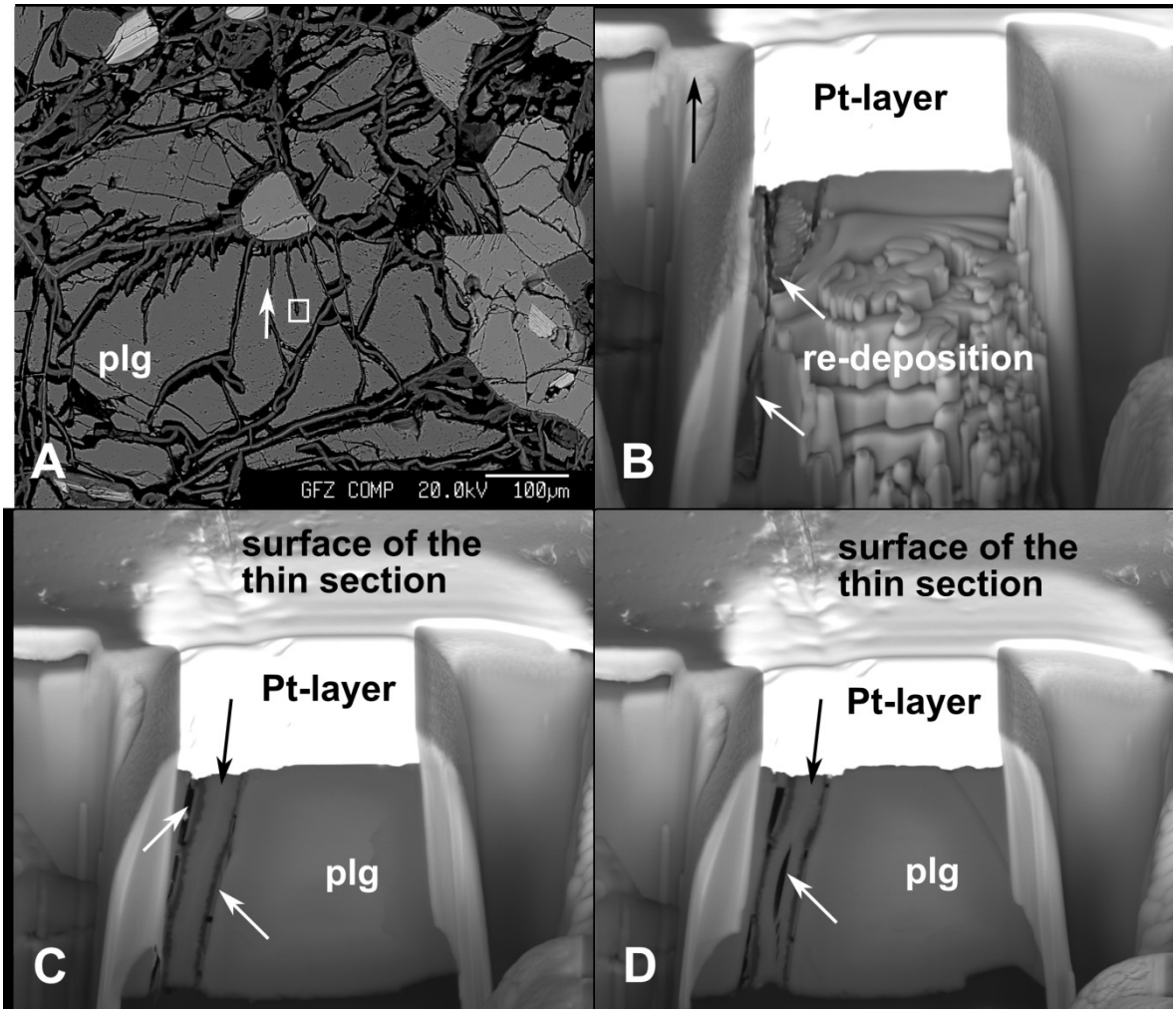

Figure 3.11 FIB mapping of weathering features in plagioclase, zone 4c. An overview where the FIB slices were cut is provided in SEM image A (white rectangle). The white arrow depicts the direction of removal of the slices. Panel B shows the tip of the secondary phase in the plagioclase (upper white arrow) and how the plane forming phase plunges into the plagioclase mineral (lower white arrow). On the right part of the plagioclase sputtered material was re-deposited. The black arrow indicates the direction of the FIB slices. Panel C shows the secondary phase in the plagioclase (black arrow in C and D). Dark parts are open pore space (left white arrow). The right white arrow marks the Al-rich amorphous phase which is in contact with the plagioclase (further described with the TEM measurements). Open pores appear in the center of the void filling secondary phase, as depicted in Panel D (white arrow).

3.5.3 TEM investigations of pyroxene, biotite and plagioclase

To analyze in detail the weathering processes at the micro-scale, transmission electron microscopy (TEM) measurements included: Electron Dispersive X-ray (EDX) measurements for chemistry, Electron Energy Loss Spectroscopy (EELS) for Fe-redox analyses and High Resolution TEM (HRTEM) together with Selected Area Electron Diffraction measurements (SAED) for crystallographic analyses. All EDX measurement results are compiled in the Appendix, as well as overview images of the different samples (Appendix B).

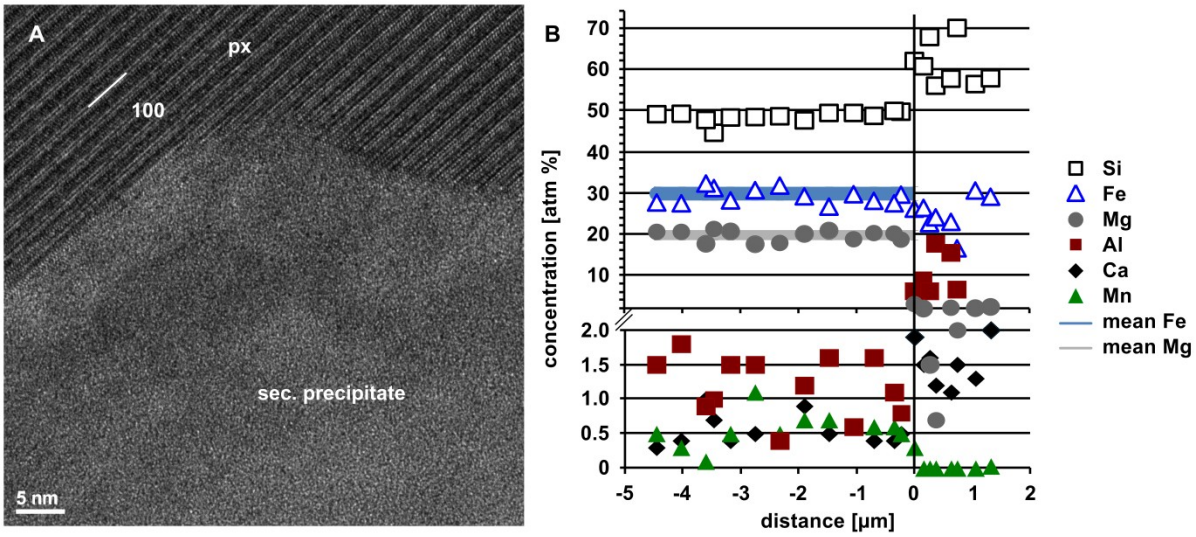

Figure 3.12 Interface of pyroxene and its weathering product from corestone zone 3. Panel A is a high-resolution TEM (HR-TEM) image and shows the pyroxene with 100 basal planes in contact with a non-crystalline precipitate. Panel B shows a transect of the chemical composition from the pristine pyroxene towards the interface and across in the secondary precipitate. The perpendicular line at 0 µm represents the location of the interface. Mean Fe and Mg values are shown as blue and gray bar, respectively, where their width corresponds to 1 SD.

The investigated pyroxene samples from zone 1 and zone 3 show similar weathering features which are more pronounced in the outer corestone zone 3. In the studies of Hewawasam et al. (2013) and Behrens et al. (2015) it was assumed that the onset of pyroxene weathering is detectable in corestone zone 2. However, the high resolution electron microscopic investigations presented here show pyroxene weathering along pre-existing cracks in the minerals already in zone 1. The contact between the primary pyroxene and the secondary precipitates is characterized by a sharp boundary on the atomic scale (Fig. 3.12A). No change in chemical composition is observed with EDX measurements from the pristine pyroxene towards the interface (Fig. 3.12B). However, parts of the pyroxenes from both zones sampled in the corestone show local *in situ* oxidation of structural Fe(II) as revealed by EELS measurements and further peak shift analyses following van Aken and Liebscher (2002), Fig. 3.13. Higher Fe(III) concentration causes peaks shifted to higher energies. The oxidation of Fe(II) in pyroxene does not form an oxidized layer but rather occurs locally as these zones occur adjacent to unoxidized areas. The spatial extent of oxidation varies from 0 to 950 nm into the mineral, and produces up to 24% Fe(III) at the interface. The pristine pyroxene hosts

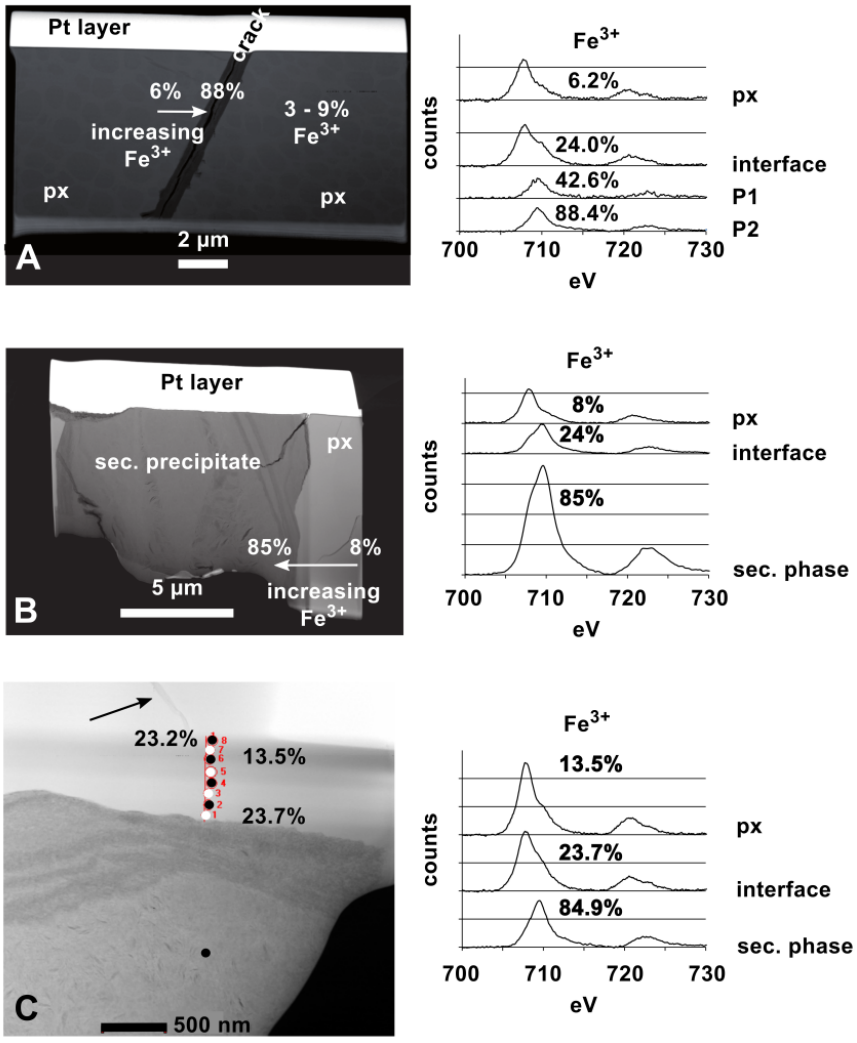

Figure 3.13 Oxidation in pyroxene. Panel A represents measurements from corestone zone 1 that were chosen to show an example of the change of oxidation from the pristine pyroxene (px), at the interface and in the two secondary phases P1 and P2 that precipitated in the crack. These two phases are described in detail in the text and Fig. 3.14. Measurements in the px cover a range of 900 nm from the interface into px. Panel B shows the state of the calculated oxidation from EELS at three different locations in the px sample from corestone 3: in the px, at the interface and in the secondary product. Panel C shows oxidation measurements from the same sample as in B. Here, a range of approximately 700 nm into the mineral was investigated. One EELS measurement was performed in the secondary precipitate. In this sample, the influence of intra mineral cracks is observed. Similar to the other samples, 24% Fe^{3+} was calculated at the interface and decreases with distance to the interface. However, it increases again with proximity to a crack (black arrow in C). Peaks shifted to higher eV depict higher Fe^{+3} concentrations. Peak maxima range from 700 counts to 35000 counts.

approximately 6% Fe(III) (mean value). As can be seen from Fig. 3.13C, close to internal cracks the oxidation can be increased as well. The only differences between the samples of the different zones are differences in the secondary phases. In zone 1, two highly porous secondary phases are recognized in approximately 1 µm-wide cracks (Fig. 3.14A). Secondary phase 1 (P1) exhibits a constant thickness of about 130 nm. Compared to the pyroxene, Al and Ca are enriched in the secondary phases while Mn is absent, Fe shows a decreasing trend through the two phases towards the crack and Mg is only slightly lower in the inner secondary phase 1 (Fig. 3.14B). Both layers exhibit an amorphous matrix in which nm-sized secondary and poorly crystalline clay minerals with 10 Å lattice distances have formed (Fig. 3.16A).

They are more distinct in the outer layer of the secondary phase 2 (P2). In zone 3, with ongoing weathering, the different secondary phases are less distinguishable at the nm scale, but merge to one highly porous Fe-Al-Si amorphous precursor phase with varying Fe and Al concentrations (Fig. 3.12B and 3.13C). This is contrary to the microprobe measurements which revealed a clear distinction between two different phases. Compared to the pyroxene, this phase exhibits less Mg and Mn but more Si, Al and Ca (Fig. 3.12B). Additionally, P was recognized with the microprobe analyses. Also in the samples from the outer corestone zone 3, secondary clay minerals occur in the non-crystalline matrix and show lattice distances of 10 Å (Fig. 3.16B). They are less common and distinct than in the previous secondary phase 2. Aluminum is enriched along pores, as seen in Fig. 3.15, where the carbon mapping revealed a void filled with epoxy in an environment with higher Al concentrations in the secondary precipitate.

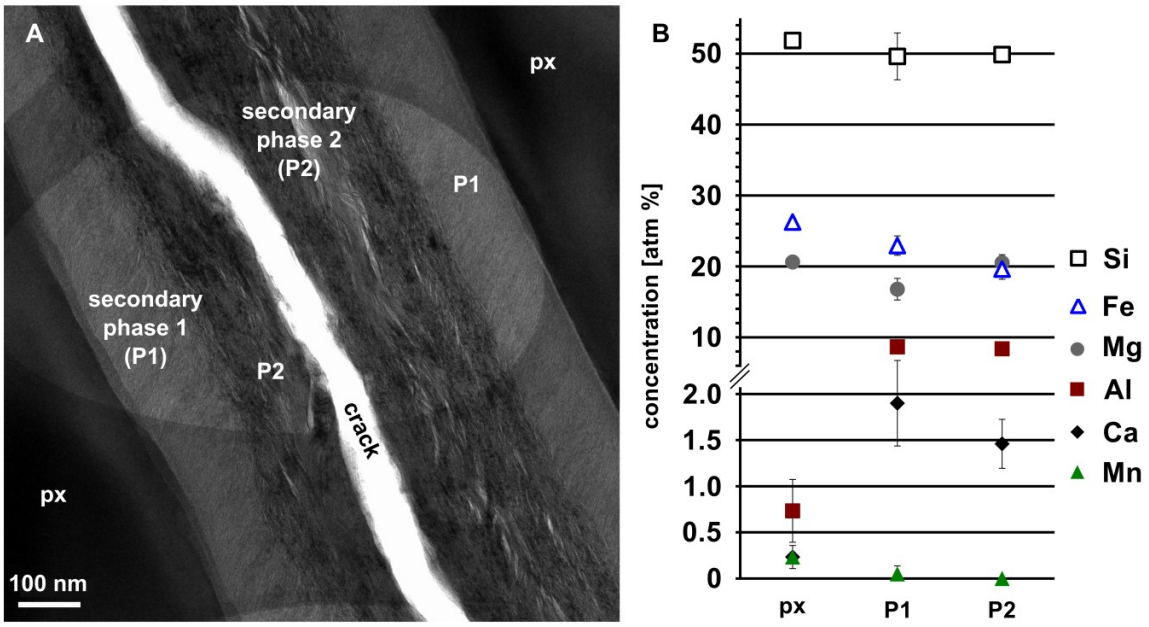

Figure 3.14 Chemical composition of pyroxene and secondary phases in corestone zone 1. Panel A shows a close-up of the crack in the pyroxene from zone 1 (from overview image in Fig. 3.13A). The secondary precipitates can be divided into two distinguish phases P1 in direct contact to the pyroxene and P2 towards (in contact with P1) the open crack. Panel B shows the chemical composition of pyroxene (px) and the secondary precipitates (P1, P2) from corestone zone 1. Values are mean values in atom percent (atm %) with 1 SD. In some cases errors are smaller than the symbols.

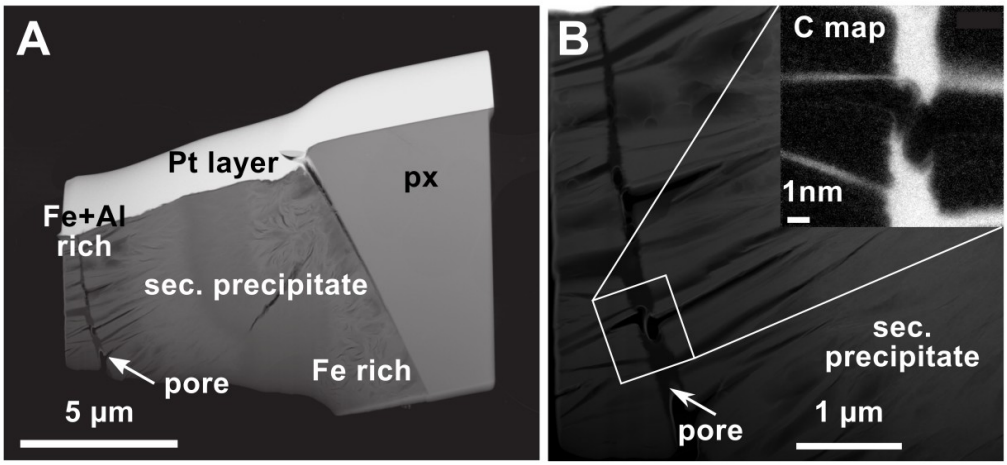

Figure 3.15 Investigated pyroxene from zone 3. Panel A gives an overview of the weathered pyroxene and a pore within the secondary precipitate (white arrow). Panel B is a close-up of the pore presented in panel A. Carbon mapping of the pore revealed high concentrations of C in the pore (insect in panel B), pointing to the presence of epoxy. The open pores found in the secondary phases show enrichment of Al in the secondary phases along these pores.

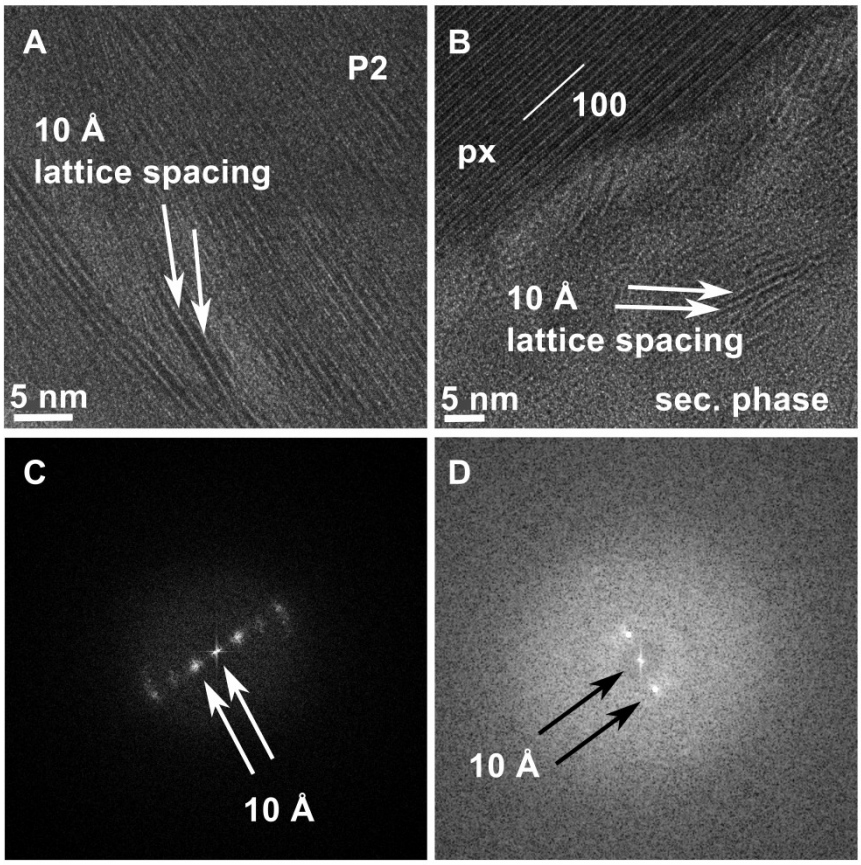

Figure 3.16 Secondary precipitates from pyroxene weathering. Panel A shows HR-TEM investigations of the secondary precipitate P2 found in pyroxene from corestone zone 1. The corresponding diffraction patterns are given in panel C. Panel B shows a HR-TEM image of the secondary phase found in pyroxene from corestone zone 3. The corresponding diffraction patterns are given in panel D. In both cases, nm-sized and poorly crystalline phases with 10 Å lattice spacings were observed.

Biotite weathering is detectable in zone 2, more towards the corestones center than previously thought (Hewawasam et al., 2013). Similar to the pyroxenes, no chemical changes are observed from the pristine mineral towards open spaces between different layers (Fig. 3.17). This might be due to the fact that EDX measurements had to be performed on larger area to integrate the chemical analyses and to avoid beam damage. Hence, the spatial scale on which such chemical differences occur might be smaller than the analyzed scale. Likewise to the pyroxene results, local *in situ* oxidation of structural Fe(II) in the biotite could be observed with EELS (Fig. 3.18) which also does not form a layer. The extent of oxidation in the biotite is up to 700 nm (Fig. 3.18B). At the biotite boundary, 68% Fe(III) is measured, while the pristine biotite contains 30% Fe(III) (Fig. 3.18C). This value might be biased towards higher values due to another open void from which oxidation might also occur (Fig. 3.18B). Secondary precipitates are observed in open voids. The boundary between biotite and secondary precipitates is atomically sharp (no distorted lattice fringes). At the boundary an approximately 10 nm thick layer of another mineral with 7 Å lattice spacing is observed (Fig. 3.19). This layer is discontinuous and consists mostly of Si and Al with minor amounts of Mg (Fig. 3.17B). The biotite and the secondary phase show in part identical crystallographic orientation (Fig. 3.19A and 3.19B, respectively). Furthermore, the HRTEM analyses revealed distorted lattice spacings in the biotite (Fig. 3.19A). Inside of the void, secondary precipitates are non-crystalline with nm-sized and poorly crystalline secondary precipitates. The chemical composition and lattice spacings are the same as the layer in contact with the biotite (Fig. 3.19C).

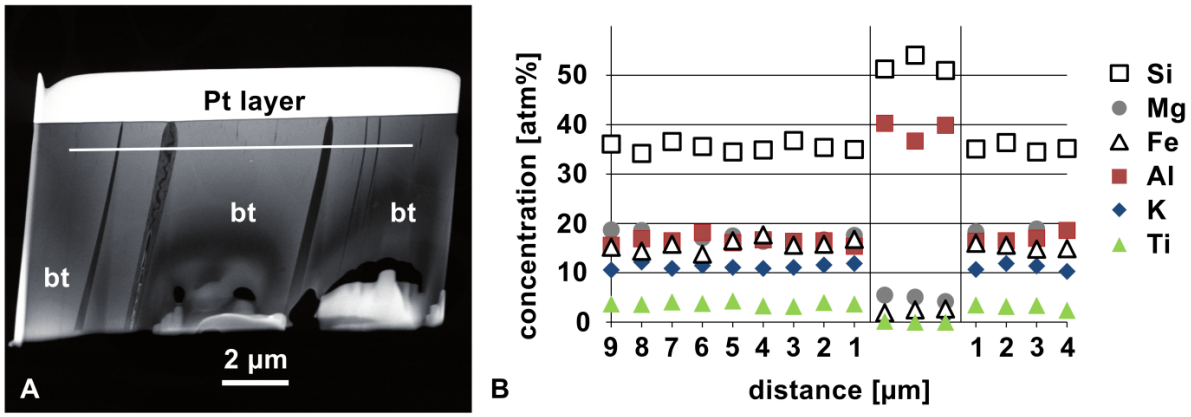

Figure 3.17 Chemical composition of biotite and secondary phases in corestone zone 2. Panel A is an overview image of the investigated biotite sample from corestone zone 2. The white line represents the transect for chemical analyses with EDX. Panel B shows the chemical composition of biotite and the secondary phase found in the largest void in panel A. The transect traverses the biotite, the secondary phase (delimited by the two lines in panel B) and biotite again. The secondary phase consists mainly of Al and Si.

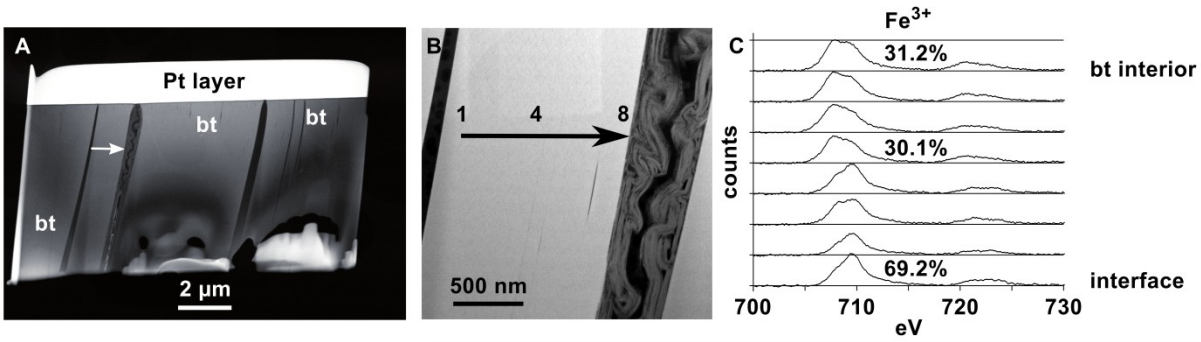

Figure 3.18 Oxidation in biotite. Panel A provides an overview of the biotite sample from corestone zone 2. The white arrow shows the direction of EELS measurements for Fe redox determination. Panel B is a close-up of the investigated area. Number 1 marks the first point of measurement in the biotite and number 8 the last point of measurement at the biotite interface. Panel C shows the characteristic Fe peaks from EELS measurements. Peaks shifted towards higher eV depict higher Fe^{+3} concentrations. Peak maxima are around 10000 counts. The lowest Fe^{3+} concentration was determined at approximately 700 nm from the interface into the mineral (point 4 in panel B). It increases towards the voids in the biotite (point 1 and 8 in panel B). The highest Fe^{3+} concentrations in biotite were found at the interface (point 8 in panel B). EELS measurements in the secondary precipitate were not successful due to the low Fe concentration.

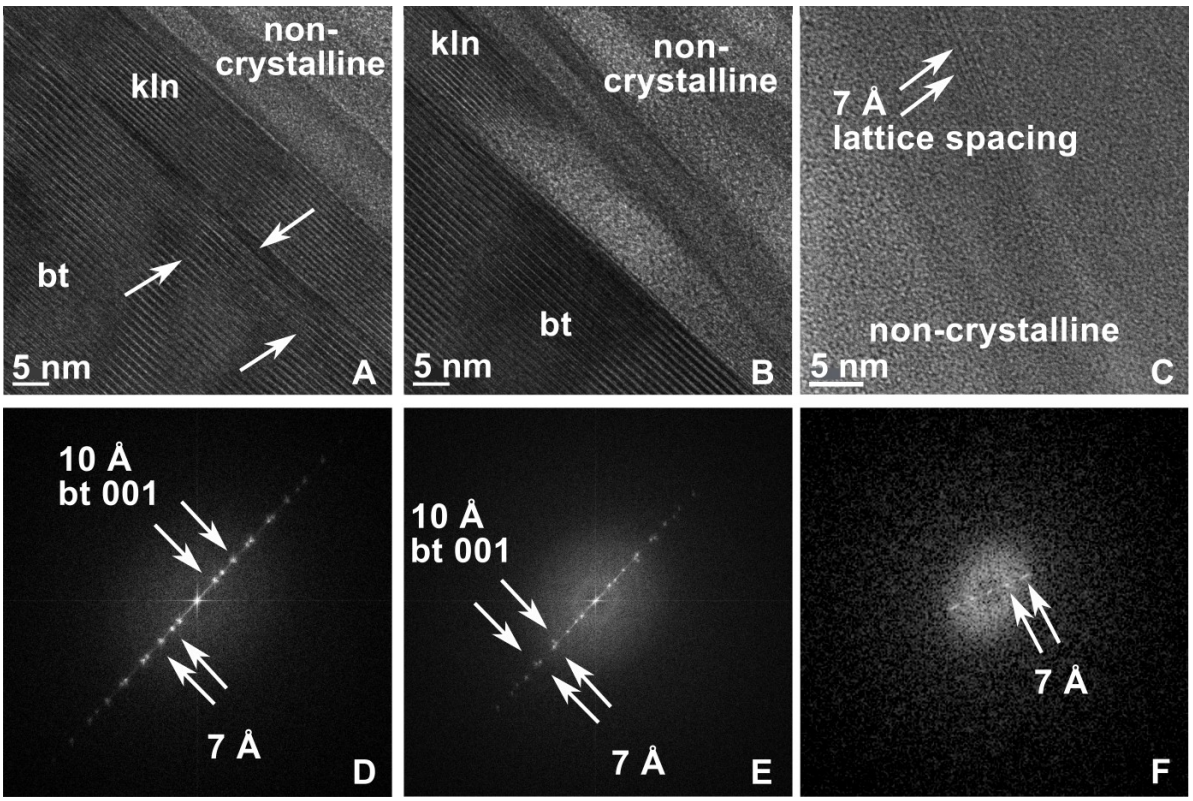

Figure 3.19 Interface between biotite and secondary precipitates from corestone zone 2. Panels A, B and C show HR-TEM images of the interface between biotite and the secondary precipitate (A and B) and the interior of the secondary precipitate (C). Panels D, E and F show the associated diffraction patterns. In all cases diffraction patterns of the secondary phases revealed 7 Å lattice spacings (with 10 Å lattice spacings for biotite). The biotite interface is atomically sharp and a secondary precipitate with 10 nm thickness is observed (panel A). However, this phase does not form a continuous layer at the biotite interface but contains interruptions (panel B). The crystalline precipitate at the biotite interface shows partly the same crystallographic orientation like biotite (in panel A) since both diffraction patterns are in line with each other. But elsewhere, the diffraction patterns are slightly tilted to each other showing different crystallographic orientation of the two phases (panel B).

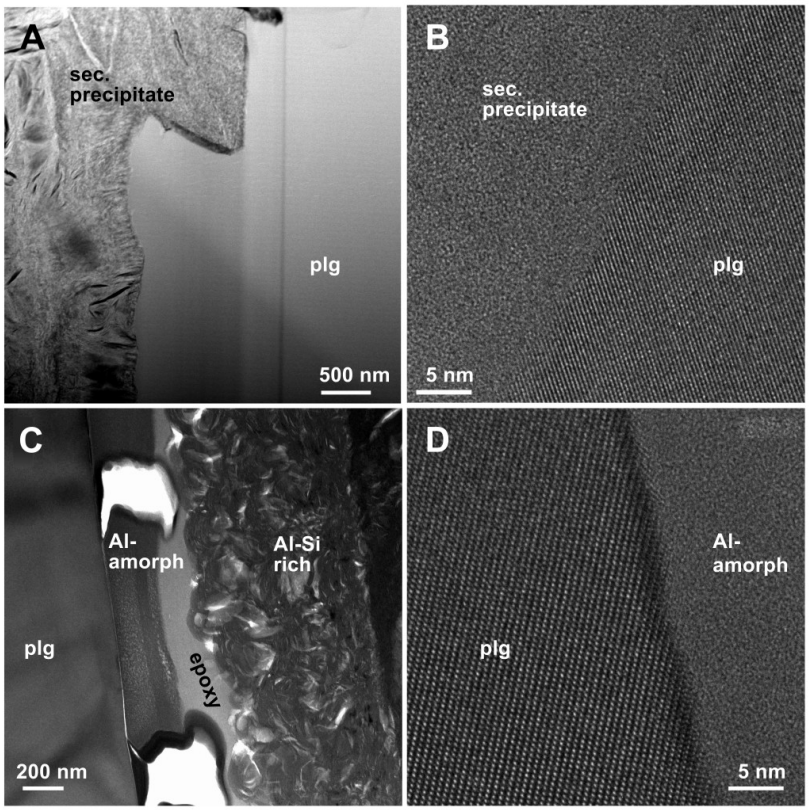

Figure 3.20 Interface of the plagioclase from corestone zone 3 and 4 (panels A+B and C+D, respectively). Compared to the other minerals, the interface is not that sharp and shows distorted lattices for 1 to 2 nm (B and D). In corestone zone 3, a secondary precipitate is found with changing composition. Whereas in corestone zone 4, an approximately 200 – 300 nm thick layer of a purely non-crystalline and highly porous Al-Si phase was observed (Al-amorph in panel C and D).

Dissolution of plagioclase is initiated along grain boundaries, micro-cracks and cleavages in the mineral. All samples have in common that the interface between the plagioclase and secondary precipitates is not as sharp as that observed for pyroxene and biotite. In contrast, distorted lattice fringes are observed in the first nm into the mineral (Fig. 3.20). No chemical gradients towards the grain boundary are observed. However, the secondary precipitates are different between corestone zone 3 and corestone 4. The investigated sample from zone 3 exhibits a secondary precipitate composed of varying amounts of Si, Al and Fe (Fig. 3.21). In this porous and non-crystalline phase, nm-sized clay minerals are observed of poor crystallinity and with lattice distances of 10 Å (Fig. 3.22). The sample from corestone zone 4, influenced by intensified weathering (Behrens et al., 2015) (section 3.2 and 3.3), exhibits three different and distinct secondary precipitates filling a void in the plagioclase (Fig. 3.23). Directly in contact to the plagioclase is a ca. 200 – 300 nm thick layer of a secondary phase with high and variable porosity (Fig. 3.20C). This phase, here termed Al-amorph, is disturbed and partly removed on the right sight of the sample due to sample preparation. It contains high amounts of Al and Si and minor contributions of Ca and P (Fig. 3.23B). No crystalline products were observed. Further away from the plagioclase grain boundary, epoxy was found that filled open pore space during sample preparation. The next secondary precipitate in the void is composed of Al and Si and Fe in minor amounts (Fig. 3.23). This phase revealed a

non-crystalline matrix in which nm-sized secondary clay minerals with 7 Å lattice distances are observed (Fig. 3.24B). The secondary precipitate in the center contains Si, Al and Fe, with impurities of Ca and P (Fig. 3.23B). It exhibits a non-crystalline matrix in which secondary clay minerals with 14 Å lattice distances of nm-size and poor crystallinity are found (Fig. 3.24C). Since I investigated a pore in the plagioclase I found a concentric structure where the central Fe-rich secondary phase is rimmed subsequently by the Al-Si rich phase, open pore space, the Al-amorphous phase and plagioclase.

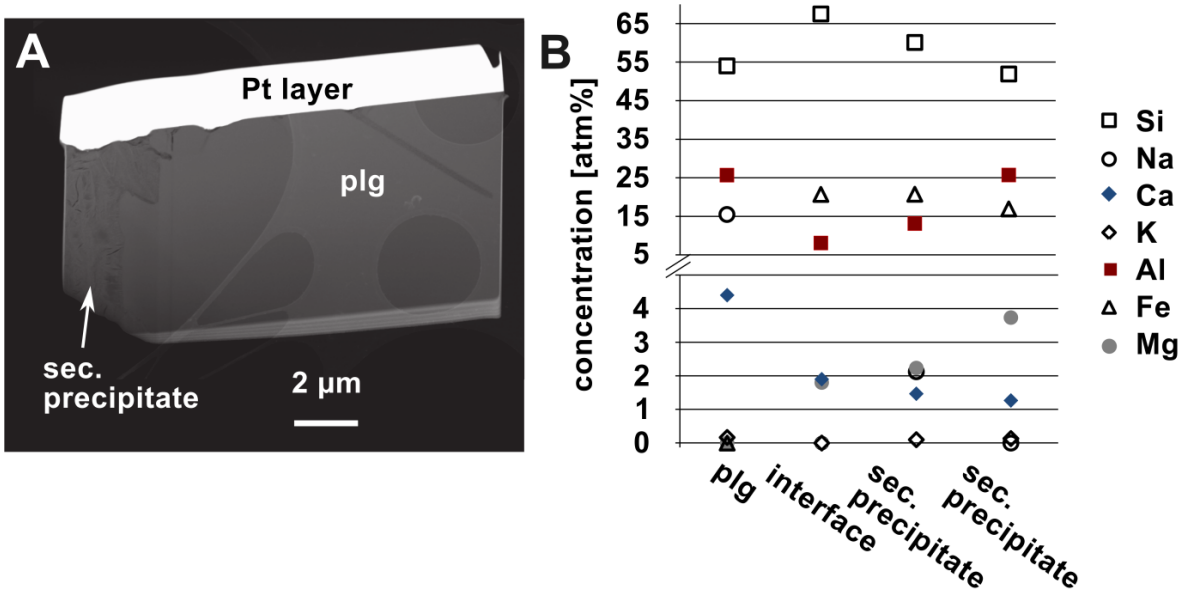

Figure 3.21 Chemical composition of plagioclase and secondary phases in corestone zone 3. Panel A gives an overview of the investigated plagioclase (plg). Panel B shows the chemical composition of the plagioclase and the secondary phase. Because of the changing chemical composition of the secondary phases, two different plots are provided. Variations are found mainly in Al, Fe, Si and Mg concentrations.

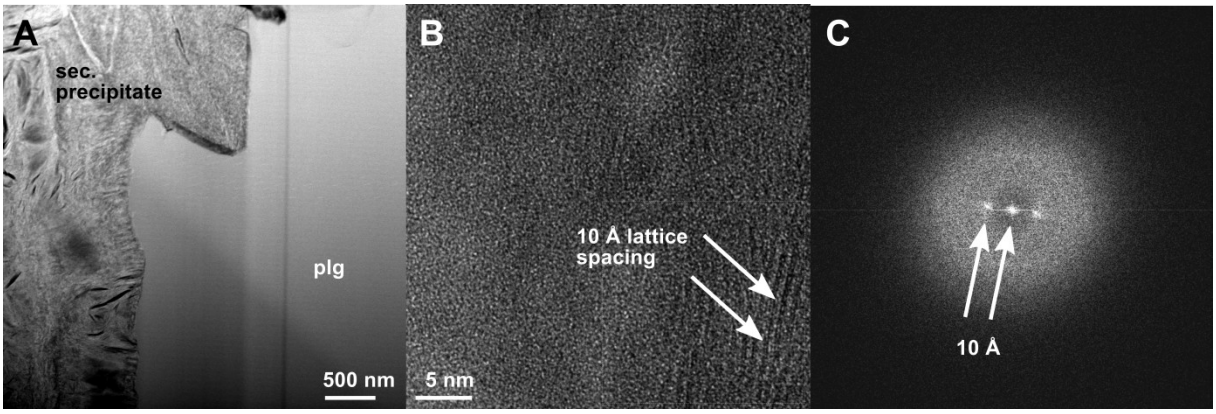

Figure 3.22 HR-TEM investigation of the secondary precipitates from corestone zone 3. Panel A gives an overview of the investigated secondary precipitate from plagioclase weathering. Panel B shows a nm-sized and poorly crystalline secondary mineral in an amorphous matrix. The crystalline secondary phases show 10 Å lattice spacings. Panel C shows the associated diffraction patterns.

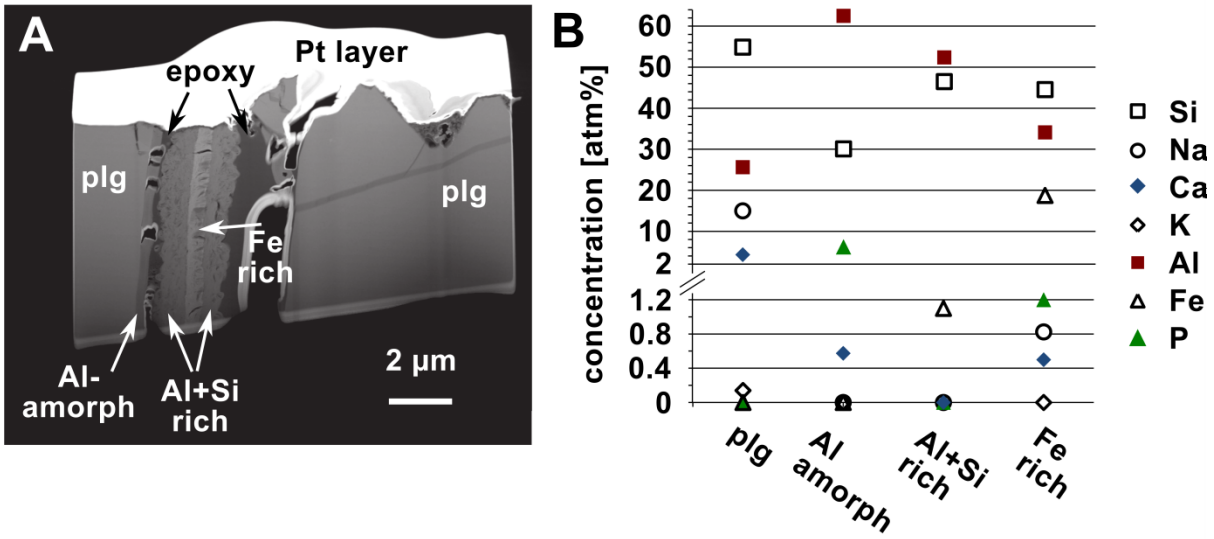

Figure 3.23 Chemical composition of plagioclase and secondary phases in corestone zone 4. Panel A gives an overview of the plagioclase and the different weathering products. Four different phases were observed: the plagioclase itself (plg), an highly amorphous and purely non-crystalline Al-rich phases (Al-amorph), an Al and Si rich phases and a Fe rich phase. The chemical composition determined with EDX is shown in Panel B.

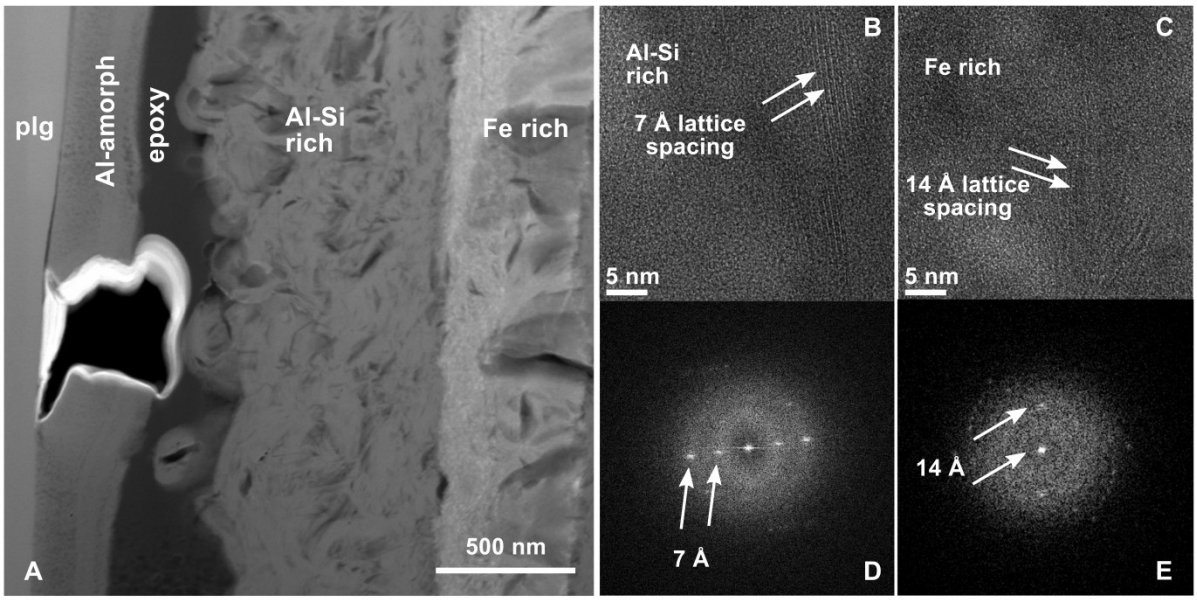

Figure 3.24 HR-TEM investigation of the secondary precipitates from corestone zone 4. Panel A is provided as an overview image and shows the plagioclase (plg) and the different weathering products as described in the text and in Fig. 3.23. Crystalline precipitates were observed only in the Al+Si rich and the Fe-rich matrix phases. Panels B and C show HR-TEM images of the Al-Si rich phase and the Fe rich phase, respectively. The associated diffraction patterns in are given in panel D for the Al-Si rich phase and E for the Fe rich phase.

4. Discussion

4.1 The sequence of weathering reactions according to bulk rock measurements

In the first section of the discussion, the results from bulk rock measurements are interpreted to derive the sequence of reactions leading to the overall conversion of bedrock into saprolite and soil. In this respect, the spatial sequence of samples, investigated from the center of the corestone towards the rindlets and saprolite, directly corresponds to the progress of weathering with time. In the second part, a detailed discussion about reaction mechanisms is provided in order to derive weathering processes that can produce the observations on the mineral scale. The mechanisms of primary mineral dissolution and secondary phase formation will be worked out in great detail. Furthermore, dissolution and oxidation rates for different scales will be calculated to determine the rate-limiting reaction for chemical weathering in the Sri Lankan profile. The third part of the discussion will show how these findings from the small scale can help to find factors that drive the overall conversion of bedrock to soil via fracture and porosity formation during spheroidal weathering. A feedback model suited to explain how the profiles' surface is connected to the weathering front will be postulated. The last part provides a view on the findings from the Sri Lanka profile with respect to factors that set slow rates of weathering and denudation.

4.1.1 Corestone zone 1: virtually unweathered bedrock

Detailed textural characterization neither reveals any measurable connected porosity nor connected internal surface area of grain boundaries and micro-fractures, as their values are below the detection limit. Besides fracturing into and around pyroxenes, electron microscope observations from Hewawasam et al. (2013) suggested that all minerals in zone 1 are unweathered. However, the TEM results show that pyroxene already starts to weather in zone 1. A detailed discussion of the mineral scale is provided in section 4.2 and 4.3. Since the reactions at the mineral scale are not intense the discussion of bulk observations based on bulk rock measurements considers that corestone zone 1 is the starting material of the whole weathering sequence. Accordingly, only a small contribution of amorphous secondary phases was detected (< 0.6 wt.% of total mass, as calculated from the sum of dithionite- and NaOH-soluble major elements) showing only minor alteration of bedrock in zone 1 (Fig. 3.3, Table 3.1).

4.1.2 Corestone zone 2: onset of weathering processes with pyroxene weathering

Corestone zone 2 shows strong evidence for weathering: (a) connected internal surface area of grain boundaries and micro-fractures measured by the BET method and porosity become detectable (Fig. 3.1); (b) dithionite- and NaOH-soluble secondary phases are present (< 1%, Table 3.1, Fig. 3.3); and (c) microscopic observations reveal additional weathering of biotite (*e.g.,* oxidation of biotite and lattice expansion), while plagioclase remains unaltered (Hewawasam et al., 2013). The selective extraction experiments show that Fe-(oxy)(hydr)oxides form (Fig. 3.3A), most likely as a result of pyroxene and biotite weathering. Weathering of pyroxene to goethite was also reported by Colin et al. (1990), Delvigne (1983), Merino et al. (1993), and Noack et al. (1993).

4.1.3 Corestone zone 3: sharp plagioclase weathering front and significant increase in porosity

Compared to the innermost layers, corestone zone 3 exhibits higher porosity (Fig. 3.1), presence of kaolinite and 2:1 sheet silicates (Fig. 3.2), higher concentration of dithionite- and NaOH-soluble phases, and larger extent of Fe oxidation (Fig. 3.3). In addition to pyroxene and biotite, plagioclase also shows weathering features in this zone (dissolution along grain boundaries and cracks in plagioclase). Ongoing biotite and pyroxene weathering contribute to the decreasing $Fe(II)/Fe_{total}$ and to the Fe-(oxy)(hydr)oxides observed there.

4.1.4 Corestone zone 4: Rindlet formation

Zone 4 is characterized by a high porosity and slightly higher connected internal surface area values than in zone 3. Here, secondary crystalline products (2:1 clay minerals and gibbsite) are still close to the detection limit of XRD and FTIR (Fig. 3.2), whereas large fractions of element contents (*e.g.,* Fe, Al, Si) are hosted by amorphous phases (Fig. 3.3). Note that the specific clay mineral analyses were carried out on the clay-sized fraction separates only, which make up 4% of the bulk sample (Table 3.1), whereas the non-crystalline phases were extracted from bulk samples. Therefore, I can infer that in this zone weathering products are still mainly of amorphous character. That was also revealed by the TEM analyses. The incipient gibbsite precipitation most likely results from crystallization of the Al-amorphous precursor produced after plagioclase dissolution (Balan, 2006; Dahlgren et al., 1997; Merino et al., 1993). Additionally, the decreasing amount of Fe(II), inferred from the $Fe(II)/Fe_{total}$ ratio of 68 – 70% is an indicator for ongoing weathering of pyroxene and biotite (Fig. 3.3).

4.1.5 The rindlet-saprolite boundary

Saprolite is formed at the rindlet-to-saprolite boundary. At this boundary the content of clay-sized minerals and the specific surface area (SSA) increase sharply (Fig. 3.1). While the

rindlets exhibit a $Fe(II)/Fe_{total}$ ratio of 68%, the lower saprolite shows a significantly higher degree of oxidation of the Fe-bearing primary minerals ($Fe(II)/Fe_{total}$ < 44%, Fig. 3.3). Presumably this oxidation can be attributed to biotite and minor amounts of pyroxene still remaining unweathered at the rindlet-saprolite boundary. As shown by electron microprobe analyses, Mn is mostly hosted in pyroxenes and thus can be used as a proxy for pyroxene content. Furthermore, no secondary crystalline Mn-bearing phases could be detected by TEM, XRD or FTIR in the corestone and the rindlets. Therefore, Mn is soluble in the corestone and the rindlets. However, Mn is incorporated into secondary phases in the regolith, as revealed by the Mn_d/Mn_{total} ratio. As a loss of 75% Mn is shown by the mass transfer coefficient τ of Mn (τ_{Mn}) in the outermost rindlet (Hewawasam et al., 2013), I can infer that at least 75% of the pyroxene is dissolved before the solid material enters the saprolite *per se*. However, small amounts of Mn-bearing secondary precipitates might remain undetected, thus leading to an underestimation of this pyroxene loss.

4.1.6 The saprolite and the formation of kaolinite

Throughout the lower saprolite the parameters showing the most striking changes are particle size distribution, SSA (Fig. 3.1), and the $Fe(II)/Fe_{total}$ ratio decreasing to near zero at approximately 3 m depth in the upper saprolite (Figure 4). Therefore, all Fe-bearing primary minerals are weathered to completion at this depth. As the amount of gibbsite decreases upward in the profile and as 2:1 clay minerals were not found in the saprolite, kaolinite appears to be the final weathering product. The formation of kaolinite is confirmed by the amounts of clay-sized particles that strongly increase towards the top of the profile and from the XRD and FTIR patterns. The formation of kaolinite in the saprolite requires a source for Si, which could be the weathering of K-feldspar and the decomposition of the secondary 2:1 clays. Furthermore, the continuous increase of the contribution of dithionite-soluble phases reveals increasing amounts of Fe-(oxy)(hydr)oxides towards the top.

4.1.7 The formation of soil from saprolite

In contrast to the saprolite, where kaolinite and Fe-(oxy)(hydr)oxides are the major secondary minerals, secondary 2:1 clay minerals are abundant in the soil. Like gibbsite, the abundance of secondary 2:1 clay minerals and the $Fe(II)/Fe_{total}$ ratio are increasing towards the top. I contend that mineralogical and chemical transformations within the soil layer are disconnected from those in the saprolite beneath it. Chemical reactions within the soil system can be influenced and altered by redox processes, pH changes, clay translocation, biological activity and external inputs, for example. In particular, dust can add primary and secondary minerals to the system and dust dissolution can in turn impact the pore-water chemistry. Evidence for dust input to the Hakgala soil was found using mass transfer coefficients and radiogenic Sr isotope analyses (Hewawasam et al., 2013).

4.2 Mechanisms of primary mineral dissolution and precipitation processes of secondary phases

The bulk measurements discussed above helped in discussing mineralogical, textural and chemical changes in the entire weathering profile from bottom to the top and illustrate the conversion of bedrock to soil. However, the starting process that drives chemical weathering at the nm scale remains unknown. Therefore, this part of the discussion only considers the measurements on the micr-scale, which are the TEM, FIB and microprobe measurements with which I will present possible mechanisms for the dissolution of primary minerals and the precipitation of (non-)crystalline secondary phases. In this regard, I will use chemical and structural (crystallographic orientation, lattice spacings, crystallinity or non-crystallinity) changes to identify the different phases. The TEM and microprobe results are partly discussed together since both techniques obtain similar results on different spatial scales.

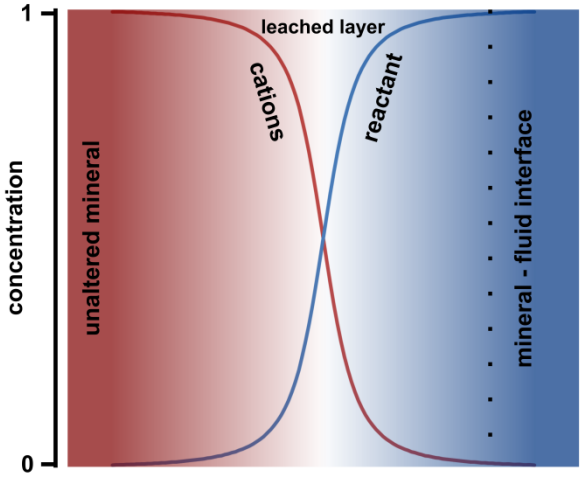

Figure 4.1 Leached layer model (after Hellmann et al. (2012)). Leached layers exhibit element gradients that result in depletion profiles of cations towards the mineral boundary (red curve) together with increasing concentrations of reactants (blue curve). Reactants may be H^+ or other cations that exchange with cations from the primary minerals (*e.g.* cation exchange in sheet silicates).

One important aspect in discussing primary mineral dissolution is the question of a slow diffusion versus a fast dissolution – re-precipitation process. In the first case, the surface of the minerals interacts with the fluid and cations may be preferentially lost or replaced by other cations from the fluid. Due to the incongruent dissolution and preferential release of certain elements sigmoidal cation depletion profiles in the mineral can establish. This process leads to the formation of a leached layer in the mineral (Fig. 4.1, Hellmann et al. (2012)). During a dissolution – re-precipitation process (DR process) no preferential release of elements occurs in the mineral. In contrast, total release of all elements is observed at the interface leading to total dissolution of the mineral. The mineral dissolves layer by layer and no elemental gradient in the primary mineral towards the mineral grain boundary develops (Fig. 4.2). Some elements may re-precipitate immediately after dissolution. As a result, sharp crystallographic

and chemical interfaces at a nm scale develop caused by congruent dissolution and a highly porous and amorphous surface layer will be expected (Chardon et al., 2006; Hellmann et al., 2012; Putnis, 2009; Putnis and Austrheim, 2010). Nevertheless, preferential release of elements may occur but is restricted to the first monolayer of the mineral (Hellmann et al., 2012). In this DR process, the amorphous surface layers are not passivating and element gradients may establish, similar to the leached layer process. However, these gradients are restricted to the amorphous surface layers (Fig. 4.2A). Furthermore, cations may be partial incorporated or enriched in the surface layer depending on the solubility and fluid composition (Fig. 4.2B). A third process of mineral dissolution is an ion by ion process (Fig. 4.3, Nielsen et al. (2012)). During this process, ions may attach and detach separately and with different rates at site defects at the mineral surface (Maher et al., 2016; Nielsen et al., 2012; Stack et al., 2012; Watkins et al., 2013). The difference in the forward (attachment) to backward (detachment) rate determines growth or dissolution of the mineral. Such process was found during the early stages of mineral growth and dissolution experiments before the reaction can reach steady state congruent dissolution (Maher et al., 2016; Nielsen et al., 2012). In the study of Nielsen et al. (2012) it was explicitly mentioned that this process is not compatible with the occurrence of an amorphous layer, while in the study of Maher et al. (2016), the ion by ion process was used to calculate ion dissolution rates for olivine in the presence of an amorphous active layer attached to the mineral surface. The ion by ion dissolution process might also be the process leading to leached layer formation or dissolution – re-precipitation since, depending on the magnitude, it may produce sharp interfaces or larger chemical gradients.

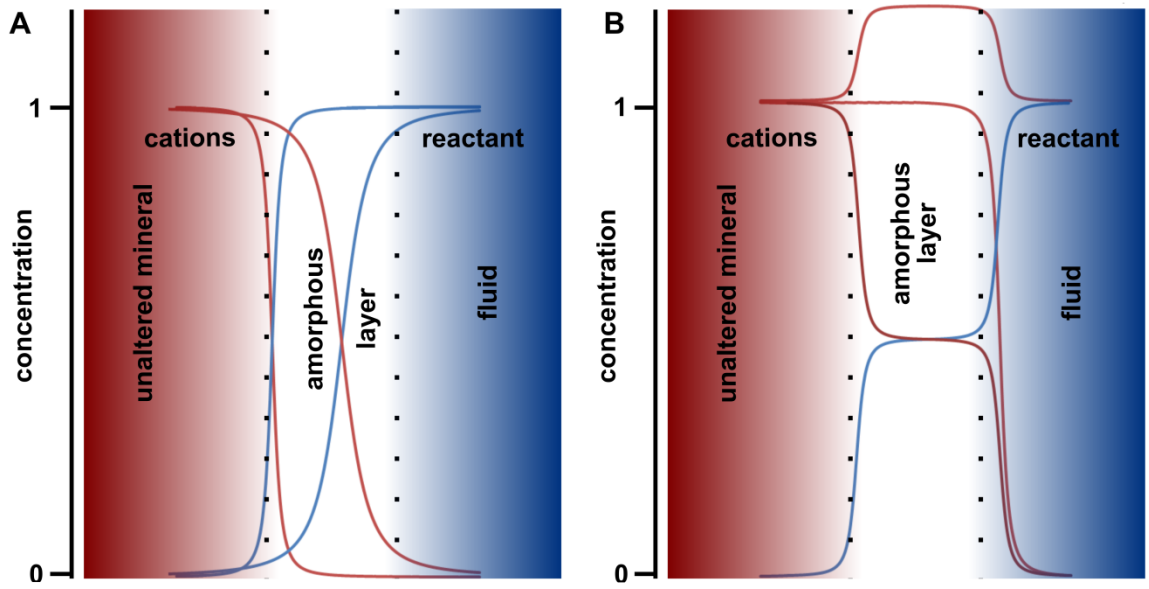

Figure 4.2 Dissolution – re-precipitation model (after Hellman et al. (2012))**.** All reaction interfaces exhibit atomically sharp gradients at the mineral boundary. A highly amorphous layer precipitates in direct contact to the primary mineral. In this layer depletion profiles due to elemental loss can establish which are similar to leached layers (A). However, elements may also be incorporated in the same amounts, in higher amounts or less compared to the primary mineral (B). Reactants may be H^+ or other cations that exchange with cations from the primary minerals.

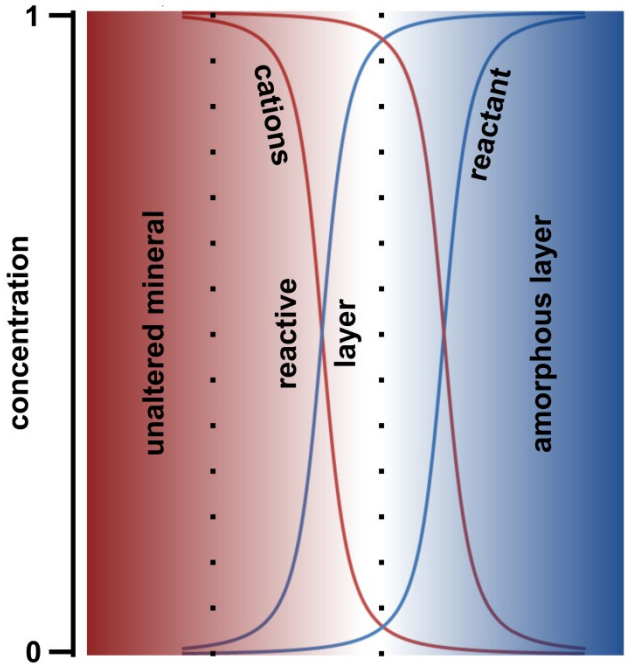

Figure 4.3 Ion by ion model (after Nielsen et al. (2012))**.** In this model ions are detached (dissolution) or attached (precipitation) at different rates and a reactive layer might occur in the primary mineral where gradients of certain elements establish. These layers are similar to the leached layers explained above and were termed active layer in Maher et al. (2016). However, also sharp chemical interfaces might occur, as described in a dissolution – re-precipitation process. Reactants may be H^+ or other cations that exchange with cations from the primary minerals (*e.g.* cation exchange in sheet silicates).

4.2.1 The primary mineral boundary: initiation of chemical weathering

The interface of and the vicinity in the pristine minerals was structurally and chemically analyzed in great detail by TEM. The sample set contains pyroxene samples from corestone zone 1 and 3, biotite samples from corestone zone 2 and 4c (the outer rindlet) and plagioclase samples from zone 3 and 4c. The investigated mineral surfaces are along intra mineral cracks in pyroxene and plagioclase and basal planes (001) in biotite. The formation or occurrence of such fresh and reactive surfaces is a pre-requisite for weathering to take place.

All interfaces have in common that they show sharp crystallographic boundaries at the atomic scale. This is especially true for the pyroxenes were an atomically sharp boundary is in direct contact with an amorphous phase and only surface steps occur (Fig. 3.12A). In the plagioclase a narrow zone of 1 to 2 nm at the grain boundary is observed which shows distorted lattice fringes (Fig. 3.20B and D). This feature could be caused by preferential leaching of certain elements in the first few mono layers or an inclined interface. Only for biotite some parts show diffuse basal planes (001) (Fig. 3.19A). Two explanations are possible: (1) expansion of the layers caused by Fe(II) oxidation (Buss et al., 2008); or (2) re-distribution of biotite layers to one kaolinite layer. This re-distribution implies replacement of the Fe-Mg rich tri-

octahedral sheets with Al di-octahedral sheets, inversion of one biotite-tetrahedral sheet, and replacement of all tetrahedral Al with Si (Dong et al., 1998; Murphy et al., 1998). Nevertheless, the basal planes at the interface show sharp transitions. While pyroxene and plagioclase are in contact with a highly porous amorphous phase of constant thickness (pyroxene: 130 nm and plagioclase: 200 – 300 nm), biotite weathering leads to precipitation of kaolinite with a constant thickness of about 10 nm (Fig. 3.19A). Only some gaps occur in the kaolinite where a highly porous amorphous phase precipitated (Fig. 3.19B). These amorphous phases with high porosity together with a structurally sharp interface are commonly observed in DR processes (dissolution – re-precipitation process; Hellmann et al. (2012) and Putnis (2009)). They are comparable to the amorphous surface layers as described in Hellmann et al. (2012) (amorphous layers in Fig. 4.2). The Al-rich amorphous layer at the plagioclase interface shows a constant thickness of about 200-300 nm (Fig. 3.24A), while Hellmann et al. (2012) reported thinner thicknesses of such amorphous surface layers on feldspar of about 50 nm but noted that they were thicker at lower pH. In the Hellmann et al. (2012) study, the natural weathered feldspar are K-feldspars from a glacial erratic boulder from the Mt. Blanc (France) and were exposed to the surface or from beneath a thin soil cover, while the feldspars in this study are Na-rich and from the bottom of a thick, slowly weathering profile in the tropics. At these depths the fluid flow rate can be considerably lower thus favoring the formation of thicker surface layers because of higher fluid residence time and therefore higher Si saturation (Hellmann et al., 2012). For pyroxene, two distinct amorphous phases were observed in the innermost sample only (Fig. 3.14). Phase 1, in direct contact to the pyroxene shows a constant thickness of about 130 nm, exhibits high porosity and a noncrystalline matrix with only minimal secondary clay formation, and is comparable to the amorphous surface layers described in Hellmann et al. (2012), too. The second phase, Phase 2, is delimited by an open pore and does not show the same thickness on both pore walls but exhibits slightly more secondary clay formation. This layer might be more comparable to the thick over layers described in Hellmann et al. (2012). With ongoing weathering they seem to mingle with each other and can not be distinguished (Fig. 3.12A). The secondary phases are discussed in more detail in section 4.2.2.

A second important parameter in discussing different dissolution mechanisms is the chemical composition in the mineral towards the interface. For all samples no preferential release of elements could be observed on the nm scale (≥ 50 nm, Appendix B). However, for biotite and plagioclase I had to choose broader EDX windows and chemical changes might have remained un-resolvable. Nevertheless, preferential leaching would exhibit element depleted layers of 100 – 1000 nm (Hellmann et al., 2012). Hence, these observations further strengthen the DR process.

Fe redox changes were found in pyroxene and biotite with areas of oxidation within the minerals of up to 900 nm in pyroxene (Fig. 3.13) and 700 nm in biotite (Fig. 3.18). This finding is at odds with a DR process. Furthermore, the oxidized areas do not form a continuous layer, which does not support the leached layer model either. Oxidation rather takes place along intra mineral cracks, cleavage planes and lattice defects. For oxidation to take place, O_2 needs to be transported to the reactive sites. Since the pristine rock does not exhibit significant porosity this transport must occur along grain boundaries or along

dislocation cores. Kruhl et al. (2013) showed that grain boundaries exhibit partially open voids that enhance the transport. The microprobe investigations show that for example the pyroxenes themselves are already fractured in the corestone center and exhibit rough surfaces (Fig. A1, Appendix A), hence they provide a number of reactive surfaces for oxidative attack. Additionally and discussed in detail in section 4.4.1, the *in situ* oxidation induces a positive volume change (Bonneville et al., 2016; Buss et al., 2008; Fletcher et al., 2006; Goodfellow et al., 2016) which causes micro-fracturing in the host mineral and the surrounding minerals. These micro-fractures were observed during microprobe investigations and are able to enhance the O_2 transport within the mineral and the environment. The oxidation of structural Fe(II) causes a charge imbalance which was previously reported to lead to preferential release of cations from biotite (Bonneville et al., 2011; Buss et al., 2008; Shelobolina et al., 2012). That this kind of leaching was not observed in this study might be due to the case that elemental loss was un-resolvable with the applied techniques since only partial oxidation of the minerals occurred. As already mentioned above, the oxidation may cause expansion of basal planes in biotite which leads to the distorted lattices observed with HRTEM (Fig. 3.19A). Furthermore, Shelobolina et al. (2012) reported that the increase in Fe(III) during oxidation produces a stacking disorder and the Fe-Mg-trioctahedral sheets are gradually transformed into Al-dioctahedral sheets to form kaolinite.

To conclude, the leached layer model can be ruled out as a mechanism leading to primary mineral dissolution. Rather a combination of ion by ion and dissolution – re-precipitation (DR) model is likely. The *in situ* oxidation of structural Fe(II) occurs with the ion by ion process along lattice defects and intra mineral cracks. This process is dependent on the intra mineral diffusion of O_2 and is further discussed in section 4.3. However, the overall mineral dissolves layer by layer and is hence best described with the DR model explained in detail in Hellmann et al. (2012), which is in agreement with sharp interfaces (Fig. 4.2) and precipitation of distinct secondary phases (highly porous amorphous surface layers and crystalline phyllosilicates). Nevertheless, Hellmann et al. (2012) also mentioned that preferential release of cations may take place as long as it is restricted to the first monolayer, therefore, an ion by ion dissolution process might be un-resolvable and may lead to overall layer by layer dissolution.

4.2.2 Element transport and formation of secondary phases

Formation of secondary phases often requires the supply of dissolved species to the site of their formation. Besides protons, O_2, water, and soluble elements released by mineral dissolution, these "required" dissolved species can be fairly insoluble elements transported over reasonably short distances. Whether and what secondary phases form depends on the prerequisites potentially limiting the weathering reactions: (1) the dissolution of primary minerals by under-saturated fluids, hence the release and transport of elements; (2) the supply of fluids that contain dissolved species required for precipitation of the product; and (3) the volume available for precipitation of the product. I can identify two types of limiting factors for weathering reactions that will influence conversion of bedrock to loose material. Firstly, in a relatively closed system like a corestone, the availability of dissolved species, such as

protons, or cations like Al^{3+}, can become reaction rate limiting. Aluminum is mentioned here in particular, since for the weathering reactions from pyroxene and biotite to form secondary clay minerals Al-import is needed to maintain stoichiometry. Furthermore, from the TEM – EDX measurements it was found that Al import occurs, while most of the other elements are lost (sections 3.5.1 and 3.5.3, Fig. 3.6, 3.12B, 3.14B, 3.17B, 3.21B and Tables in Appendix B). Secondly, the available space can limit the formation of secondary precipitates, regardless of the availability of their constituents. The reaction ceases when all the void space is occupied by secondary minerals. However, since formation of high internal porosity is observed, most reactions can be explained by element-limiting conditions and are most likely dependent on Al^{3+} transport and incorporation into secondary minerals (see discussion about reactions below, equations (4.1) to (4.5)).

The TEM results (section 3.5.3) let me conclude the following sequence of pyroxene weathering: (1) *in situ* oxidation of structural Fe(II); (2) dissolution of pyroxene layers; (3) precipitation of amorphous secondary phases and goethite; and (4) formation of smectite in the amorphous matrix. For several reasons the two distinct amorphous layers that form during incipient weathering (Fig. 3.12B) differ from the amorphous "active layer" and the amorphous "precipitated layer" described in Maher et al. (2016) (compiled in Fig. 4.3, section 4.2): Maher et al. (2016) reported constant thicknesses for both layers. The inner "active layer" in contact to their dissolving olivine exhibits decreasing Mg concentrations while Si remains unchanged. Hence this layer was not considered to be a new precipitate. The outer "precipitated layer" was only observed where saturation of SiO_2(am) was reached and exhibit low Mg/Si ratios throughout. For the Sri Lanka pyroxene only the inner layer (phase 1 in contact to the pyroxene, Fig. 3.14) exhibits a constant thickness but no significant preferential loss of elements inside the layers is observed. Although there are changing concentrations of Mg and Fe between the two different layers, no gradual change in concentration as described in Maher et al. (2016) could be observed. In contrast, import of Al was inferred (Fig. 3.15). The two different layers rather depict stages of different weathering extent, where the outer layer experienced longer exposure time to weathering. This is inferred from the facts that weathering of primary minerals proceeds inwards from the crack into the minerals and (although still minor) secondary minerals are more abundant, larger in size and stronger ordered in the outer layer. Hence, the findings of the different layers presented in Maher et al. (2016) may only be observable in controlled and time-resolvable lab experiments, whereas in nature the weathering features are more complex and depict just one stage adjusted to the environmental conditions. Nevertheless, with ongoing weathering (samples from outer corestone layers) loss of Mn and Mg is detected (section 3.5.3) and import of Al and Ca to the reaction sites takes place along pores (section 3.5.3, Fig 3.15). Considering the elements available in the amorphous phase for incorporation into the secondary minerals, and the observed lattice distances of 10 Å (Fig. 3.16), smectite is the most likely secondary mineral to form in both zone 1 and zone 3 from the amorphous precursor. Even where the smectites are in direct contact with the pyroxene, they are randomly oriented. However, Velbel and Barker (2008) suggested a re-arrangement of the tetrahedral chains of pyroxene to tetrahedral sheets of 2:1 layer silicates. The exact composition of the smectites could not be analyzed because of their small size (a few nm), but the loss of Mg in the amorphous phase detected with EDX (Appendix B, Tables B1 to B4) might not only be caused by transport of Mg into solution, but

also by incorporation of Mg into the smectite. This incorporation is feasible as described above: Mg is first retained in phase 1 and phase 2 (Fig. 3.14B; Appendix B Table B3) but with further weathering (zone 3) it is also lost from the amorphous phase (Fig. 3.12B). Depending on the composition of the crystalline product, a possible (approximately isovolumetric) stoichiometric weathering reaction of pyroxene weathering to Fe-rich smectite is:

$$3(Fe_{1.0}Mg_{0.8}Ca_{0.1}Mn_{0.1})Si_{1.8}O_8 + 2Al^{2+} + 9.4H^+ + 7.6H_2O \rightarrow \quad (4.1)$$

$$Ca_{0.3}(FeMg)_3(AlSi)_4O_{10}(OH)_2{*}4H_2O + FeO(OH) + 1.4Mg^{2+} + 0.3Mn^{2+} + 3.4H_4SiO_4$$

It is even more likely that during incipient weathering, more pyroxene weathers than would be required to form the smectite, because only low amounts of 2:1 clay minerals are observed (see section 4.1.4). This observation was also made by Banfield and Barker (1994) and was called non-stoichiometric weathering, with stoichiometric dissolution of pyroxene and non-stoichiometric precipitation of smectite. With ongoing ageing of the intermediate amorphous phase during further weathering, this reaction eventually becomes stoichiometric. If more dilute fluids drive the reaction (more H_2O, less H^+), OH^- is produced (equation (4.2) which can act as charge balancing phase at the pyroxene interface. Equation (4.1) can then be rewritten for example to:

$$3(Fe_{1.0}Mg_{0.8}Ca_{0.1}Mn_{0.1})Si_{1.8}O_8 + 2Al^{2+} + 8.4H^+ + 8.6H_2O \rightarrow \quad (4.2)$$

$$Ca_{0.3}(FeMg)_3(AlSi)_4O_{10}(OH)_2{*}4H_2O + FeO(OH) + 1.4Mg^{2+} + 0.3Mn^{2+} + 3.4H_4SiO_4 + OH^-$$

However, since pyroxene weathering and formation of smectite is the first process and already occurs in corestone zone 1, this reaction requires mobility of Al throughout the corestone zones. As I will show below, the source of Al is most likely from plagioclase weathering in zone 3 and the rindlets. Furthermore, in the amorphous matrix certain amounts of P and Ca were observed. Excess phosphorous and calcium may have their source from apatite dissolution. As it was shown by the microprobe investigations, apatites depict rough surfaces and etch pits and show reformation to Ce-bearing monazite during a metamorphic event (discussed in section 4.2.4). Hence, the Ca-bearing apatites might be less resistant to weathering. Another Ca source might also be the weathering of plagioclase. However, Hewawasam et al. (2013) demonstrated that Ca is lost in great amounts from corestone zone 3 (where plagioclase starts to weather) and the rindlets. Weathering to completion of plagioclase is only observed over the small corestone – rindlet zone and occurs apparently rapid. They argued that this Ca is exported in solution and eventually taken up by plants.

The biotite TEM analyses point to the following weathering sequence: (1) oxidation of structural Fe(II); (2) dissolution of biotite layers; and (3) precipitation of kaolinite and amorphous Al-Si-Fe phases (section 3.5.3, Appendix B Tables B5 and B6). That kaolinite is formed is concluded from the chemical composition of the secondary phase that is mainly composed of Al and Si (Fig. 3.17B), and the lattice spacing of 7 Å (Fig. 3.19). For step (2)

and (3) a direct solid state transformation of biotite to kaolinite might also be possible. This would require the re-arrangement of two layers of biotite to form one layer of kaolinite to maintain the stoichiometry of Al. In this scenario, weathering of biotite may exhibit the following different temporal reaction sequences: (1) dissolution of biotite – precipitation of an Al-Si-Fe amorphous phase – formation of kaolinite by re-arrangement of Al-Si tetrahedra; (2) dissolution of biotite – precipitation of / or solid state transformation to kaolinite – dissolution of kaolinite and precipitation of an Al-Si-Fe amorphous phase; or (3) dissolution of biotite – precipitation of / or solid state transformation to kaolinite contemporaneously with amorphous Al-Si-Fe precipitation. Unfortunately, whether the phase in direct contact to the biotite is originally non-crystalline or kaolinite cannot be clearly determined. Therefore, I can only discuss factors to distinguish between direct transformation of biotite to kaolinite versus dissolution of biotite and precipitation of kaolinite on the surface. Supporting observations for the direct transformation are the partially identical crystallographic orientation of biotite and kaolinite (Fig. 3.19A), distorted lattices in biotite (Fig. 3.19A), and a constant kaolinite layer thickness of 10 nm (Fig. 3.19A). The direct transformation of biotite to kaolinite requires the redistribution of the former biotite tetra- and octahedrons. As reported in Shelobolina et al. (2012), the increase in Fe(III) during oxidation produces a stacking disorder and the Fe-Mg-trioctahedral sheets are gradually transformed into Al-dioctahedral sheets. This stacking disorder produces differences in lattice distances. The constant thickness of the kaolinite layer implies that both the biotite and the kaolinite weathering reaction fronts move at the same rate. The kaolinite is then consumed to form the amorphous Al-Si phase in which remnants of kaolinite are still present. On the other hand, the kaolinite in contact with the biotite is partly oriented in another direction (Fig. 3.19B) which is not in agreement with a direct transformation to kaolinite but with a dissolution and re-precipitation process. If this is the case, the formation and the thickness of the kaolinite layer is a direct process and only restricted by the availability of Al. Furthermore, *e. g.* Putnis (2002) or Wilson (2004) reported that lattice parameters might be maintained in non-direct transformation dissolution – re-precipitation reactions, if both minerals have similar crystallographic properties and if the educt serves as nucleation surface. In this regard, the distorted lattices in the biotite may be caused by expansion of the layer due to charge imbalance after *in situ* oxidation, which would explain the rare occurrence of theses distorted lattices, because only small areas are oxidized. A possible biotite weathering reaction to form kaolinite assuming a conservative behavior of Al, regardless whether the reaction occurs directly or via an amorphous precursor, is:

$$2K_{0.7}(Fe_{1.0}Mg_{0.8}Ti_{0.2})(Al_{1.1}Si_{2.7}O_{10})(OH)_2+9.6H^+ +3.4H_2O\rightarrow \quad (4.3)$$

$$Al_{2.2}Si_{1.8}O_5(OH)_4+2FeO(OH)+1.4K^+ +1.6Mg^{2+}+0.4Ti^+ +3.6H_4SiO_4$$

However, Murphy et al. (1998) reported weathering of biotite to kaolinite where only one layer of biotite is consumed to form two layers of kaolinite or, with an intermediate halloysite, consumption of one layer of biotite to eventually form one layer of kaolinite. Moreover, it was already shown that transport of Al occurs to the reaction sites, which is also likely available for biotite weathering reactions. Hence, import of Al can maintain the stoichiometry to form kaolinite. Gaps occurring in the kaolinite layers as well as the center of the open space

in the biotite are filled with Al-Si rich non-crystalline material. Since this matrix is highly porous it can serve as pathways for reactive fluids. With import of Al a following reaction may apply:

$$1K_{0.7}(Fe_{1.0}Mg_{0.8}Ti_{0.2})(Al_{1.1}Si_{2.7}O_{10})(OH)_2 + 0.9Al^{2+} + 2.2H^+ + 1.8H_2O \rightarrow \quad (4.4)$$
$$Al_2Si_2O_5(OH)_4 + 1FeO(OH) + 0.7K^+ + 0.8Mg^{2+} + 0.2Ti^+ + 0.7H_4SiO_4$$

Similar to the pyroxene weathering reaction the Al source is the plagioclase weathering. Because both TEM and microprobe measurements revealed higher Al concentrations over other elements in the secondary precipitates the second equation is favored over the first one. In section 4.3.2, bulk weathering reactions are formulated from bulk measurements for the weathering profile as a whole. In these reactions goethite and secondary 2:1 clay minerals appear in the weathering sequence of biotite because goethite and secondary 2:1 clay minerals were unambiguously detected in the saprolite with XRD and IR spectroscopy. Hence, with intensified weathering, different weathering products and re-formation to other clay minerals can occur due to changes in the weathering environment such as availability of elements (other primary minerals take part in weathering), pH regime or fluid composition.

Plagioclase weathering products exhibit the strongest differences between early and late stage weathering reactions. During incipient weathering stages in intra mineral cracks and grain boundaries, the precipitates experience a strong control from other mineral dissolution and mixing of reagents takes place. Hence the first phase that precipitates contains Si, Al and Fe and features an amorphous matrix from which smectites form, according to lattice distances of 10 Å (Fig. 3.20 to 3.22 and Table B8 in Appendix B). With ongoing weathering and accompanying mineral retreat due to dissolution, this phase remains in the center of open pores. With ageing of the precipitate the amorphous matrix contains secondary clay minerals with increasing distances of the frayed lattices to approximately 14 Å (Fig. 3.23, 3.24C). The chemical composition and the (Mg+Fe+Al+Ca)/Si ratios between 1 – 1.5 indicate vermiculite-like clay minerals or hydrated smectites (*e.g.* Murphy et al. (1998) and reference therein). Nevertheless, Mg is absent in this phase. At the same time, dissolution of plagioclase produces a highly porous and entire amorphous Al-Si layer as already described in the previous section (Fig. 3.23 and 3.24A). The porous structure allows for transport of reactants to the dissolving plagioclase and loss of Na and Ca. With ongoing weathering, this phase ages and re-ordering of Al-Si tetrahedra leads to nucleation of kaolinite clay minerals with 7 Å lattice spacings (Fig. 3.24B). Gibbsite, which was detected with IR spectroscopy (section 4.1.4) was not observed with TEM analyses. Therefore, I conclude that at the initial stage of weathering, gibbsite is not stable but with intensified weathering it becomes stable in the lower saprolite. This is similar to the possible formation of smectite from biotite weathering (see above). The observation of different shells of secondary phases that represent different weathering stages and formation of open voids surrounding the primary minerals was already described by Merino et al. (1993). Due to volume differences and densification of the secondary phases open voids develop and a new shell precipitates in contact with the dissolving primary mineral. This formation of shells that form a “septa”-like network

perfectly matches with the observations from Sri Lanka. The first stage is represented with the central Fe-rich amorphous phase with vermiculite/smectite. This central phase in the void formed along the former grain boundary/internal fracture, where first dissolution of plagioclase and mixing with other weathering products occurs. The second stage is characterized by the Al-Si phase containing kaolinite. The third stage is depicted by the Al-Si amorphous layer attached to the plagioclase. A possible ideal weathering reaction of plagioclase to form kaolinite is given below:

$$2(Na_{0.74}Ca_{0.25}K_{0.016})Al_{1.25}Si_{2.75}O_8 + 7H_2O + 4H^+ \rightarrow \quad (4.5)$$
$$Al_2Si_2O_5(OH)_4 + 1.48Na^+ + 0.50Ca^{2+} + 0.50Al^{2+} + 0.032K^+ + 3.5H_4SiO_4$$

Since the reaction to vermiculite only occurs during initial weathering along grain boundaries and were pyroxene is present, hence is not significant and representative for bulk rock reactions as discussed in section 4.4.2, I just present the weathering reaction to kaolinite. From this equation it is clearly visible that Al is not totally consumed during kaolinite formation. However this reaction is reasonable to occur as only minor amounts of kaolinite were observed in the amorphous matrix of the Al-Si rich phase.

Please note that all the reactions presented above are ideal reactions that include the total weathering of a primary mineral to a secondary clay mineral. But secondary 2:1 and 1:1 clay minerals at the weathering front are only observed in low amounts and are poorly crystalline, which made it impossible to measure their actual composition. Hence, not all available elements might be incorporated into the secondary minerals right at the beginning and can be transported to other weathering sites. With this in mind, and as was also shown by Merino et al. (1993), plagioclase weathering further up in a weathering profile is a considerable source for Al to form Al-bearing secondary clay minerals downwards to the weathering front (for the case of a corestone: inwards to the weathering front). For example, Hewawasam et al. (2013) showed that at the bulk scale Al is not lost by export in solution but stays in the profile. These facts strengthen the assumption that Al, Ca and P are soluble in the corestone and at least limited transport between the different zones of the corestone occurs. Furthermore, as already mentioned above, the weathering environments change in space and time with ongoing and intensified weathering. Thus, other secondary minerals may become stable as other conditions (element-availability, pH, fluid composition, weathering of more stable primary minerals) favor other weathering end-products. Finally, I would like to mention that if weathering reactions are considered to be isovolumetric, the formation of porosity has to be taken into account for reactions with a negative volume change according to the molar volume changes of the participating minerals. A discussion about the implications these weathering reactions at the micro-scale will follow for the bulk conversion of rock to soil during spheroidal weathering and a discussion about formation of strain and porosity during all these reactions based on volume changes is presented in section 4.4.

4.2.3 Pre-conditioning of the K-feldspar for weathering in the saprolite

As I could show with the TEM results, plagioclase and K-feldspar remain unweathered until corestone zone 3 and the rindlet-saprolite boundary, respectively. The pristine K-feldspar perthites from corestone zones 1 to 4, investigated with the microprobe, show nano-tubes (Results Fig. 3.4) in the plagioclase film-lamellae (Lee et al., 1998; Lee and Parsons, 1995). This observation was also previously made by Evangelakakis et al. (1993) from metamorphic rocks from the Central Sri Lankan Highlands. In their study, they argue that the film perthite might have formed below 350 – 500 °C and cooled under dry conditions. There is no evidence for a late stage hydrothermal event. However, plagioclase lamellae in K-feldspar might serve as preferential locations for dissolution (Lee et al., 1998; Lee and Parsons, 1995), because plagioclase show less resistivity to weathering compared to K-feldspar (Nesbitt et al., 1997). With preferential dissolution of plagioclase from the film and patch lamellae during the beginning of the weathering, secondary internal porosity in the K-feldspar may be generated, increasing small-scale connected pathways for reactive fluids and the reactive surface of the K-feldspar. Nevertheless, the K-feldspars remain unweathered in the corestone and the rindlets. Once entering the saprolite weathering begins. I call this observation pre-conditioning for weathering because the K-feldspar itself is not affected by dissolution but the plagioclase in the lamellae. Thus, they are viewed as two separate minerals.

4.2.4 Accessory minerals

The most striking and possibly most relevant observations from accessory minerals for weathering reactions stem from the microprobe analyses of apatite and monazite. The larger single monazite grains show areas of re-crystallization, as indicated by zones with low-Th and high-Th concentrations (Harlov et al., 2005). While this feature might not be relevant for weathering reactions, the apatite-monazite paragenesis could provide a source of elements observed in the secondary phases. The apatites contain Ce-impurities. To charge balance these, Si is substituted for P (Harlov and Förster, 2003). During metasomatism, preferential removal of Si might occur (Harlov and Förster, 2003; Harlov et al., 2005) which leads to a charge imbalance and subsequent release of Ce, or other REE elements incorporated into apatite. Harlov et al. (2005) reported formation of monazite from apatite. They observed a reacted apatite depleted in REEs and Si with high internal porosity. Monazite was observed in direct vicinity of these reacted apatites. Hence, I conclude that the apatite-monazite assemblage might have formed in a similar way. The reacted apatites with their high internal porosity exhibit many reactive surfaces and, for this reason, are weak with respect to weathering. Therefore, dissolution of apatites can be a considerable source of Ca and P incorporated into secondary phases observed during weathering reactions of pyroxene.

4.3 Dissolution and oxidation rates for pyroxene and biotite

The TEM investigations unambiguously show that oxidation is the first weathering process in the Sri Lanka charnockite. As this oxidation reaction invokes a volume increase eventually resulting in fracture formation, as well as *in situ* (intra-mineral) but also at the bulk rock scale, it is an important process for the formation of fresh weatherable surfaces and for the formation of pathways for fluids. But is this oxidation process rate determining for weathering? This question will be addressed in the following three paragraphs by calculating and comparing oxidation and dissolution rates for different scales. Corestone-scale dissolution and oxidation rates encompass the entire corestone of a few cm and the *in situ* oxidation rates are calculated for the micro-scale of a few hundred nm. Here, I would like to note that oxidation of the minerals is also dependent on the supply and availability of oxygen. This relationship is further explored in section 4.5.

4.3.1 Corestone-scale dissolution and oxidation rates

The first approach to calculate dissolution and oxidation rates averages over the entire mineral and the corestone scale. The rate is normalized to the specific surface area of the mineral and the gradient of the Fe(II) / Fe_{total} ratio throughout the different corestone zones measured on bulk corestone samples is used. I call these rates corestone-scale dissolution and oxidation rates. The idea behind this approach is that if oxidation is the rate-limiting parameter it will influence the dissolution rate of pyroxene and biotite by providing mineral surfaces that are susceptible to weathering due to oxidation induced mineral defects and *in situ* fracturing. Hence, on the broad corestone scale these rates should be similar to each other, if steady state is assumed. This assumption will be tested with this approach. On the other hand, this steady state assumption implies that oxidation and subsequent dissolution of the Fe(II)-bearing minerals should be in agreement with the profile weathering front advance rate. The steady state assumption was also considered in Hewawasam et al. (2013) to derive chemical weathering rates based on K- feldspar, plagioclase and biotite dissolution rates. They showed that mineral dissolution is in agreement with the weathering front advance rate for the Sri Lankan weathering profile. Here, I extend the calculation to derive pyroxene dissolution rates based on Mn loss as a proxy for pyroxene weathering over the corestone zones. Pyroxene is the only Mn-containing primary mineral. The loss is expressed as the mass transfer coefficient (Brimhall and Dietrich, 1987) of Mn, τ_{Mn}, and was calculated in Hewawasam et al. (2013). Furthermore, by using the bulk Fe(II) / Fe_{total} ratio changes measured over the entire corestone range I am able to derive oxidation rates. This approach was shown to be applicable by Buss et al. (2008) for oxidation of biotite in a weathering profile from Puerto Rico. The mineral dissolution rate equation used in Hewawasam et al. (2013) and Buss et al. (2008) is given in White (2002):

$$R_{min} = \frac{\omega}{SSA_{min} * x_{min} * \beta} * \frac{\Delta[X]}{\Delta z} \qquad (4.6)$$

Table 4.1 Parameters for corestone-scale mineral dissolution and oxidation rates, approach 1

$R_{px, Mn}$ [a]			
	ω [b]	6 – 14	mm/ky
	SSA_{px} [c]	80	m^2/kg_{px}
	x_{px} [b]	0.04	kg_{px}/kg_{rock}
	β	0.02	mol_{Mn}/mol_{px}
	C_{Mn} zone 1	7.28×10^{-3}	mol_{Mn}/kg_{rock}
	C_{Mn} zone 4	1.82×10^{-3}	mol_{Mn}/kg_{rock}
	Δx	5.46×10^{-3}	mol_{Mn}/kg_{rock}
	Δz	0.163	m
$R_{px, ox}$ [a]		zone 3	
	ω [b]	6 – 14	mm/ky
	SSA_{px} [c]	80	m^2/kg_{px}
	x_{px} [b]	0.04	kg_{px}/kg_{rock}
	β	1.02	$mol_{Fe(II)}/mol_{px}$
	$C_{Fe(II)}$ px centre	43.46	$mol_{Fe(II)}/kg_{px}$
	$C_{Fe(II)}$ px rim	38.08	$mol_{Fe(II)}/kg_{px}$
	Δx	0.22	$mol_{Fe(II)}/kg_{rock}$
	Δz	0.163	m
$R_{bt, ox}$ [a]			
	ω [b]	6 – 14	mm/ky
	SSA_{bt} [c]	5000	m^2/kg_{bt}
	x_{bt} [b]	0.07 – 0 015	kg_{bt}/kg_{rock}
	β	1.27	$mol_{Fe(II)}/mol_{bt}$
	$C_{Fe(II)}$ bt centre	25.76	$mol_{Fe(II)}/kg_{bt}$
	$C_{Fe(II)}$ bt rim	20.18	$mol_{Fe(II)}/kg_{ht}$
	Δx	0.39	$mol_{Fe(II)}/kg_{rock}$
	Δz	0.163	m

[a] dissolution rate based on Mn concentration in px (Behrens et al., 2015), and oxidation of Fe(II) in px and bt, respectively, from bulk measurements.
[b] values from Hewawasam et al. (2013).
[c] values from Oelkers and Schott (2001) and Brantley and White (2003).

where ω is the weathering front advance rate [m/s] (Hewawasam et al., 2013), SSA_{min} is the specific surface area [m^2/kg], and x_{min} is the mass proportion of biotite and pyroxene in the bedrock [kg_{px}/kg_{rock}] and [kg_{bt}/kg_{rock}], respectively. β is the stoichiometric coefficient of Mn in pyroxene [mol_{Mn}/mol_{px}] and Fe(II) in biotite and pyroxene [$mol_{Fe(II)}/mol_{px}$] and [$mol_{Fe(II)}/mol_{bt}$], respectively. Δ[X] is the change in Fe(II) (proportional to the contribution of pyroxene and biotite) and Mn concentration in the corestone [$mol_{Fe(II)}/kg_{rock}$] and [mol_{Mn}/kg_{rock}], respectively, and Δz is the distance [m] between the corestone center and the measurement point. The parameters, used for the calculation are summarized in Table 4.1. The weathering front advance rates (ω) and the mass proportion of the minerals (x_{min}) are taken from Hewawasam et al. (2013). The calculation is performed for both, the upper and the lower rate ω of 6 to 14 mm/kyr. The only unknown value in this calculation is the specific surface area SSA_{min} since the surface areas determined in this study with BET were performed on bulk rock samples and hence represent surfaces of open pores and fractures. For pyroxene, I used a SSA_{min} value from Oelkers and Schott (2001) reported for enstatite that is most similar to the Sri Lankan pyroxene (Mg-opx with considerable amounts of Fe from a charnockite-gneiss host rock). The parameters considered during literature research were: natural versus synthetic sample, crystallography and lithology. The biotite specific surface

area is, for consistency, the same as used for the weathering rate calculation for the Sri Lankan weathering profile given in Hewawasam et al. (2013). This value is based on data of White and Brantley (2003).

The calculation with the parameters presented in Table 4.1 revealed a corestone scale pyroxene dissolution rate based on the Mn concentration of log R_{Mn} = -13.24 $mol_{px}/(m^2\ s)$ with ω = 6 mm/ky and a log R_{Mn} = -12.87 $mol_{px}/(m^2\ s)$ for ω = 14 mm/ky. The oxidation rates of pyroxene are log $R_{px\text{-}ox}$ = -13.36 $mol_{px}/(m^2\ s)$ for ω = 6 mm/ky and a log $R_{px\text{-}ox}$ = -12.99 $mol_{px}/(m^2\ s)$ for ω = 14 mm/ky. Compared to literature data of laboratory-derived pyroxene (opx and cpx) dissolution rates at ambient temperatures and acidic to neutral pH of -9.8 to -12.4 $mol_{px}/(m^2\ s)$ (Brantley and Chen (1995), Bandstra et al. (2008) and references therein) the corestone-scale oxidation and dissolution rates are well within reported values (Fig. 4.4A, Table 4.3). However, since the specific surface area SSA_{min} is not known, the same calculation is provided for minimum and maximum SSA_{min} values of natural pyroxenes reported in literature (28 – 550 m^2/kg_{px}, Brantley and Chen (1995), Bandstra et al. (2008) and references therein, Daval et al. (2010)) to test the sensitivity of the analyses. This calculation gives a range of possible corestone-scale pyroxene dissolution rates (Fig 4.4B, Table 4.3) of log R_{Mn} = -12.79 $mol_{px}/(m^2\ s)$ to log R_{Mn} = -14.08 $mol_{px}/(m^2\ s)$ for ω = 6 mm/ky and log R_{Mn} = -12.42 $mol_{px}/(m^2\ s)$ to log R_{Mn} = -13.61 $mol_{px}/(m^2\ s)$ for ω = 14 mm/ky based on Mn as a proxy. For the corestone-scale pyroxene oxidation rate the SSA_{min} range results in log $R_{px\text{-}ox}$ = -12.90 $mol_{px}/(m^2\ s)$ to log $R_{px\text{-}ox}$ = -14.19 $mol_{px}/(m^2\ s)$ for ω = 6 mm/ky and a pyroxene oxidation rate range of log $R_{px\text{-}ox}$ = -12.53 $mol_{px}/(m^2\ s)$ to log $R_{px\text{-}ox}$ = -13.83 $mol_{px}/(m^2\ s)$ for ω = 14 mm/ky.

For biotite, the calculated oxidation rates are log $R_{bt\text{-}ox}$ = -15.12 $mol_{bt}/(m^2\ s)$ and log $R_{bt\text{-}ox}$ = -14.76 $mol_{bt}/(m^2\ s)$ for ω = 6 mm/ky and ω = 14 mm/ky, respectively. In comparison, reported laboratory-derived and calculated mineral dissolution rates (log R) of natural biotites at ambient temperatures and acidic to neutral pH range from -9.2 to -16 $mol_{bt}/(m^2\ s)$ for biotite (Acker and Bricker, 1992; Buss et al., 2008; Kalinowski and Schweda, 1996; Malmström and Banwart, 1997; Murphy et al., 1998; Taylor et al., 2000; Turpault and Trotignon, 1994; White and Brantley, 2003) which covers the rates reported here (Fig. 4.4A, Table 4.3). Likewise to the pyroxene sensitivity analysis calculation a range of corestone-scale biotite oxidation rates is obtained (Fig 4.3B, Table 4.3) based on minimum and maximum SSA_{min} (240 – 13000 m^2/kg_{bt}, Acker and Bricker (1992), Bonneville et al. (2011), Bray et al. (2014), Kalinowski and Schweda (1996), Malmström and Banwart (1997), Murphy et al. (1998), Taylor et al. (2000), Turpault and Trotignon (1994), White and Brantley (2003)). These are log $R_{bt\text{-}ox}$ = -13.53 $mol_{bt}/(m^2\ s)$ to log $R_{bt\text{-}ox}$ = -15.91 $mol_{bt}/(m^2\ s)$ for ω = 6 mm/ky and log $R_{bt\text{-}ox}$ = -13.16 $mol_{bt}/(m^2\ s)$ to log $R_{bt\text{-}ox}$ = -15.54 $mol_{bt}/(m^2\ s)$ for ω = 14 mm/ky. For both minerals a specific surface area SSA_{min} (Table 4.1) most appropriate to the Sri Lanka setting was chosen, based on crystallographic and external parameter like the climate, lithology and weathering regime. However, the biotite oxidation rate calculated here is about one order of magnitude faster than the biotite dissolution rate presented in Hewawasam et al. (2013), log R = -16 $mol_{bt}/(m^2\ s)$ for the same SSA.

4.3.2 *In situ* oxidation rates based on intra-mineral diffusion of O_2

The second approach follows the dissolution model of biotite during biotic weathering provided in Bonneville et al. (2011). In their study, the weathering rate of biotite is based on the diffusion of elements out of the mineral through an altered layer and the pristine mineral. Importantly, with this method the oxidation rates can be calculated on the mineral scale (nm – µm), whereas the other method covers a broader scale (cm – m). In the following, these oxidation rates at the mineral scale will be called as *in situ* oxidation rates. In the case of this study, oxidated areas in the pyroxene and the biotite (as discussed in section 4.2.1) are comparable to the altered layer as described in Bonneville et al. (2011). Hence, the calculation of the flux of an element through the altered layer can be applied to the Sri Lanka samples. In this regard, the calculated flux J_{min} [$mol_{FeIII}/(m^2\ s)$] is the rate of *in situ* oxidation of structural Fe(II) which is dependent on the diffusion of oxygen into the mineral. The rate J [$mol_{min}/(m^2\ s)$] is calculated as follows:

$$J_{min} = -D * \left(\frac{Fe(III)_{min} - Fe(III)_{alt}}{x}\right) \quad (4.7)$$

Here, $Fe(III)_{min}$ [$mol_{Fe(III)}/m^3_{min}$] is the concentration of Fe(III) in the pristine mineral, where the subscript *min* stands for *px* (pyroxene) and *bt* (biotite). $Fe(III)_{alt}$ [$mol_{Fe(III)}/m^3_{min}$] is the concentration of Fe(III) at the surface of the oxidized part towards the secondary precipitate. x [m] is the depth of the oxidized area and D is the diffusion coefficient of iron. In lack of precise data of O_2 diffusion coefficients in natural minerals at ambient temperatures, for calculation purpose I assume that oxidation of structural Fe(II) is in steady state with loss of Fe due to dissolution of the mineral and therefore comparable to the diffusion of Fe out of the mineral. In this regard, the diffusion coefficient of Fe as given in Bonneville et al. (2011) can be used. This assumption of coupled diffusion is well constrained since this process is in principle observed with K-loss during oxidation (Bonneville et al., 2011; Buss et al., 2008; Shelobolina et al., 2012). However, this coupled diffusion between inward O_2 transport and Fe oxidation was not put in relation before.

Iron redox measurements were performed on two pyroxenes (zone 1 and zone 3) and one biotite TEM sample (zone 2) with EELS. These $Fe(III)/Fe_{total}$ ratios can be used for the calculation of oxidation driven mineral dissolution. The parameters for the calculation are listed in Table 4.2. All values are measured values except for the diffusion coefficient of O_2 which was chosen as explained above.

For the pyroxene sample from corestone zone 1 the calculation yields an oxidation rate of log J_{px} = -11.69 $mol_{px}/(m^2\ s)$ as well as log J_{px} = -11.69 $mol_{px}/(m^2\ s)$ for the sample from corestone zone 3 (Fig. 4.4B). This shows that *in situ* oxidation rates are the same in different zones, hence different weathering stages. The calculation for the biotite sample from zone 2 yields log J_{bt} = -11.6 $mol_{bt}/(m^2\ s)$, (Fig. 4.4B, Table 4.3). Compared to literature data the *in situ* derived oxidation rates $J_{px,\ bt}$ lay well within reported natural dissolution rates at room temperature as reported above (Fig. 4.4A, Table 4.3). This comparison is crucial in

determining if it is in principle possible that oxidation is in steady state with and thus driving mineral dissolution. Compared to the corestone-scale oxidation rates, the *in situ* oxidation rates are more than one order of magnitude faster for pyroxene and more than 3 orders of magnitude faster for biotite (Fig. 4.4B, Table 4.3). A large uncertainty may arise with respect to the diffusion coefficient of Fe. For example, the diffusion rate may change after initial oxidation. Such a chance was observed by Bonneville et al. (2011) in an altered biotite layer underneath a hyphae and is about one magnitude faster ($D = 6.00*10^{-22}$) compared to the pristine mineral. Hence the oxidation rates will be one magnitude faster as well (J_{bt} = -10.5 $mol_{bt}/(m^2\ s)$ for biotite and J_{px} = -10.7 $mol_{px}/(m^2\ s)$ for pyroxene). Furthermore, the Fe diffusion may not be the relevant counterpart in a coupled diffusion process, but for example for biotite K- diffusion and for pyroxene Mg- diffusion better describes the coupled diffusion with O_2. However, this will only marginally change the oxidation rates to J_{bt} = -11.7 $mol_{bt}/(m^2\ s)$ for biotite and J_{px} = -12.0 $mol_{px}/(m^2\ s)$ for pyroxene as compared to J_{bt} = -11.6 $mol_{bt}/(m^2\ s)$ and J_{px} = -11.7 $mol_{px}/(m^2\ s)$, Table 4.3. A more detailed discussion about this is provided in section 4.3.3.

Table 4.2 Parameters for *in situ* mineral oxidation rates, approach 2

	nFe	0.056		kg/mol
	Fe diffusion coefficient [b]	**$5.6*10^{-23}$**		m^2/s
$J_{px,\ ox}$ [a]		zone 1	zone 3	
	FeO_{px} [c]	33.31		wt %
	Fe_{px}	258922		ppm
	$Fe(III)/Fe_{total}$ centre [d]	0.062	0.135	
	$Fe(III)/Fe_{total}$ rim [d]	0.24	0.237	
	$C_{Fe(III)}$ px centre, **$Fe(III)_{px}$**	$1.15*10^4$	$2.50*10^4$	$mol_{Fe(III)}/m^3_{px}$
	$C_{Fe(III)}$ px rim, **$Fe(III)_{alt}$**	$4.44*10^4$	$4.38*10^4$	$mol_{Fe(III)}/m^3_{px}$
	x	$9.00*10^{-7}$	$5.18*10^{-7}$	m
	px density [e]	3998		kg/m^3
$J_{bt,\ ox}$ [a]				
	FeO_{bt} [c]	19.74		wt %
	Fe_{bt}	153441		ppm
	$Fe(III)/Fe_{total}$ centre [d]	0.303		
	$Fe(III)/Fe_{total}$ rim [d]	0.68		
	$C_{Fe(III)}$ bt centre, **$Fe(III)_{bt}$**	$2.75*10^4$		$mol_{Fe(III)}/m^3_{px}$
	$C_{Fe(III)}$ bt rim, **$Fe(III)_{alt}$**	$6.18*10^4$		$mol_{Fe(III)}/m^3_{px}$
	x	$7.11*10^{-7}$		m
	bt density [e]	3317		kg/m^3

[a] dissolution rate based on oxidation of Fe(II) in px and bt, respectively
[b] taken from Bonneville et al. (2011)
[c] microprobe measurements
[d] $Fe(III)/Fe_{total}$ ratio derived from EELS
[e] from Robie and Hemingway (1995)

4.3.3 Corestone-scale rates versus *in situ* rates

The calculation results for both minerals, biotite and pyroxene, revealed a discrepancy between corestone-scale mineral oxidation and dissolution rates and the *in situ* derived oxidation rates. These differences are independent of the specific surface area SSA_{min} for corestone-scale oxidation and dissolution and independent of the diffusion coefficient for *in situ* oxidation. This is demonstrated by testing the uncertainties in specific surface area and diffusion coefficient. The analyses showed that for corestone-scale pyroxene dissolution and oxidation rates a range between -12.4 to -14.1 $mol_{px}/(m^2\ s)$ for dissolution based on Mn and a range between -12.5 to 14.2 $mol_{px}/(m^2\ s)$ for oxidation is obtained. *In situ* oxidation rates range between -10.7 to -11.7 $mol_{px}/(m^2\ s)$ and are thus considerably higher. This holds also true for biotite where a range of -13.2 to -15.9 for corestone-scale oxidation was calculated that contrasts with a range of -10.5 to -11.6 for *in situ* oxidation. On the other hand, the corestone-scale oxidation and dissolution rates for pyroxene, $R_{px\text{-}ox}$ and $R_{px\text{-}Mn}$, yield almost the same values. This implies that corestone-scale oxidation rates are in steady state with the corestone-scale mineral dissolution rates.

The differences between corestone-scale and *in situ* derived rates may have several reasons. One important aspect is the fact that oxidation is not observed to occur in a continuous layer but rather occurs locally, whereas calculated corestone-scale oxidation rates averages over the entire mineral. Therefore, the *in situ* oxidation rates only apply locally and oxidation is more likely to take place at crystal lattice defects and along intra-mineral cracks, rather than layer by layer. The oxidation rate will thus depend on the occurrence and density of these defects and preferential pathways. For example, in the pyroxene from zone 3 a nearby crack was observed (black arrow in 3.13C) and in the investigated biotite sample another expansion between basal planes was observed. These two features represent reactive surfaces that serve to facilitate oxidation within the minerals. Therefore it is possible that due to the increased occurrence of lattice expansion and intra-mineral cracks, the spatial extent of *in situ* oxidation is enhanced. Hence, the calculated *in situ* oxidation rates might be too high and do not represent incipient *in situ* oxidation rates. Moreover, the oxidation process itself results in a volume increase. This volume increase leads to fracture formation, as will be discussed and calculated in more detail in section 4.4. The formation of fractures is an important process in providing fresh weatherable surfaces; *in situ* but also at the corestone scale. Furthermore, the volume increase may cause *e.g.* expansion of biotite layers thus increasing the site defect density and accelerating the weathering. These findings are supported by the observation of Bonneville et al. (2011), were increased diffusion rates are modeled in altered biotite layers during hyphae-induced oxidative dissolution. Additionally, Shelobolina et al. (2012) reported the appearance of stacking disorder during oxidation of biotite which enhances total mineral dissolution or re-formation. Both, fracturing in and around the minerals and distorted lattices in biotite, were observed with microprobe and TEM measurements. Another aspect is that rates might differ with respect to the crystal lattice direction. Iron redox measurements were conducted only perpendicular to the 100 lattice axis of pyroxene and the 001 lattice axis of biotite. However, Banfield and Barker (1994) reported faster weathering at 110 interfaces. Such factors will only show up in the *in situ* calculated oxidation rates, while the corestone-scale oxidation rates average over the entire mineral. Taken together, I conclude that *in situ*

oxidation, which is dependent on the O_2 grain boundary diffusion, is a relatively fast process at mineral defects (crystal lattice site defects, intra mineral cracks etc.) and is a key driver for the corestone-scale overall mineral dissolution of Fe(II) bearing minerals for the following reasons: The oxidation of pyroxene and biotite leads to lattice defects and fractures in the minerals and the surrounding bulk rock. These site defects weakens the mineral with respect to dissolution and the fractures serve as newly created fresh weatherable surfaces that allow for further oxidation. In addition, the fractures in the bulk rock provide pathways for reactive fluids that drive mineral dissolution. Hence, the faster the oxidation of minerals the more site defects and fractures develop which make the minerals more prone to weathering. Furthermore, because corestone-scale dissolution and oxidation rates agree well with each other, too, the relatively fast but local *in situ* oxidation of the minerals is indeed the rate limiting factor for overall chemical weathering in the Sri Lankan weathering profile by providing more mineral defects to enhance the primary mineral dissolution.

Table 4.3 Pyroxene and biotite oxidation and dissolution rates

	pyroxene		**biotite**	
corestone scale [1]				
weathering front advance rate ω [2]	6 mm/ky	14 mm/ky	6 mm/ky	14 mm/ky
dissolution rate $\log R_{Mn}$ [mol/(m² s)]	-13.24	-12.87	-	-
Range for min and max SSA [3] [mol/(m² s)]	-14.08 to -12.79	-13.61 to -12.42	-	-
literature data [4] [mol/(m² s)]	-12.4 to -9.8		-16 to -9.2	
oxidation rate $\log R_{min\text{-}ox}$ [mol/(m² s)]	-13.36	-12.99	-15.12	-14.76
Range for min and max SSA [3] [mol/(m² s)]	-14.19 to -12.90	-13.83 to -12.53	-15.91 to -13.53	-15.54 to -13.16
***in situ* scale** [5]				
oxidation rate $\log J_{min}$ [6] [mol/(m² s)]	-11.69		-11.6	
for higher D_{Fe} [6] [mol/(m² s)]	-10.7		-10.5	
oxidation rate (D_{Mg}) [6] [mol/(m² s)]	-12.0		-	
oxidation rate (D_K) [6] [mol/(m² s)]	-		-11.7	

[1] Approach 1

[2] from Hewawasam et al. (2013)

[3] Minimum and maximum SSA_{px}: 28 – 550 m^2/kg_{px}, Brantley and Chen (1995), Bandstra et al. (2008) and references therein, Daval et al. (2010) and minimum and maximum SSA_{bt}: 240 – 13000 m^2/kg_{bt}, Acker and Bricker (1992), Bonneville et al. (2011), Bray et al. (2014), Kalinowski and Schweda (1996), Malmström and Banwart (1997), Murphy et al. (1998), Taylor et al. (2000), Turpault and Trotignon (1994), White and Brantley (2003).

[4] Literature data for pyroxene: Brantley and Chen (1995), Bandstra et al. (2008) and references therein and for biotite: (Acker and Bricker, 1992; Buss et al., 2008; Kalinowski and Schweda, 1996; Malmström and Banwart, 1997; Murphy et al., 1998; Taylor et al., 2000; Turpault and Trotignon, 1994; White and Brantley, 2003

[5] Approach 2

[6] based on intra diffusion of D_{O2} coupled to D_{Fe}. Oxidation rates are also provided in case of higher D_{Fe} = $6.00*10^{-22}$ m²/s, D_{O2} coupled to D_{Mg} = $2.6 *10^{-23}$ m²/s for pyroxene and D_K = $3.8*10^{-23}$ m²/s for biotite as explained in the text. Values are from Bonneville et al. (2011).

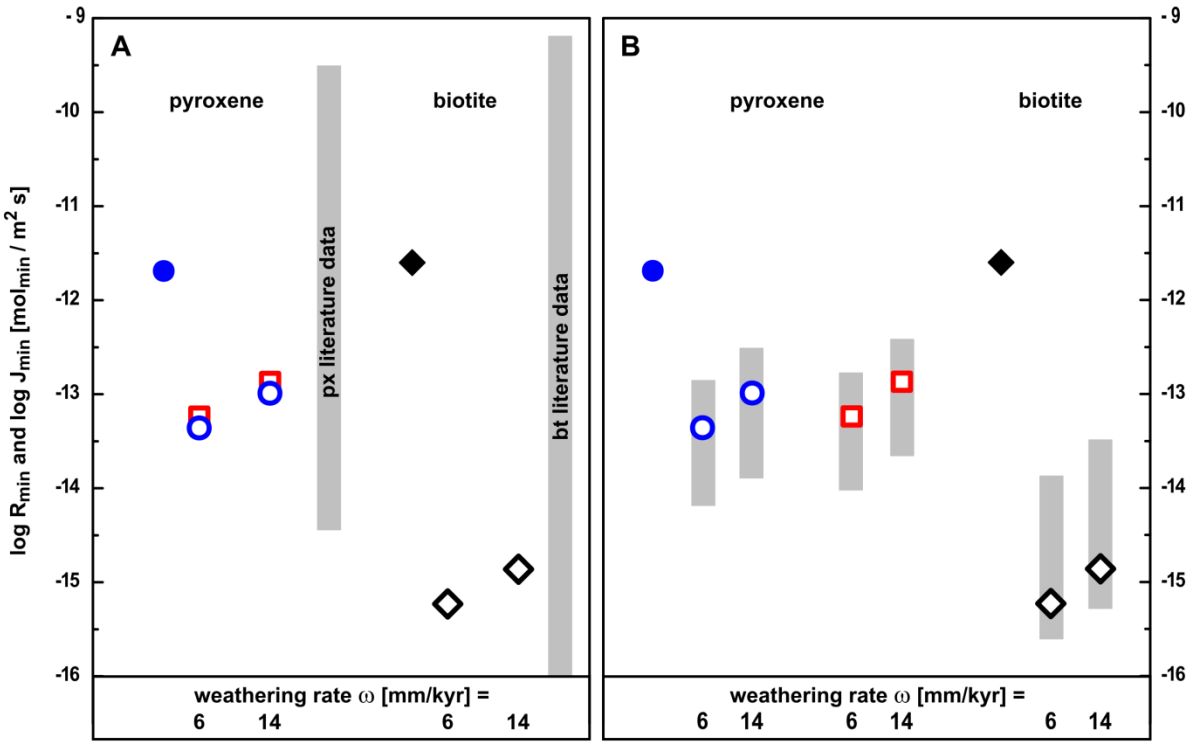

Figure 4.4 Compilation of the dissolution and oxidation rates of pyroxene and biotite for different scales and two different weathering rates. Black symbols are for biotite oxidation rates, blue symbols for pyroxene oxidation rates and red symbols for pyroxene dissolution rates based on Mn loss occurring in the corestone. Open symbols represent bulk oxidation and dissolution rates (corestone scale), while closed symbols stand for *in situ* oxidation rates (mineral scale). Panel A shows the bulk oxidation rates of biotite and pyroxene ($R_{bt\text{-}ox}$ and $R_{px\text{-}ox}$), the *in situ* oxidation rates of biotite and pyroxene (J_{bt} and J_{px}) and the bulk dissolution rate of pyroxene based on Mn loss over the corestone ($R_{px\text{-}Mn}$) in comparison to literature data. In panel B, the calculated rates are compared to the calculated range of oxidation and dissolution rates using a range of different specific surface areas (SSA_{min}) as found in literature, since this causes the highest uncertainty in this calculation.

Although oxidation of Fe(II)-bearing primary minerals is the first and rate limiting weathering process in the corestone, the final conversion of bedrock to saprolite at the rindlet-saprolite boundary occurs by plagioclase weathering due to major mass loss and mineralogical transformation and the accompanying formation of porosity in the rindlets. A detailed discussion about the interplay of fracture formation and formation of porosity during conversion of bedrock to saprolite is provided in section 4.4. This assumption is strengthened by the fact that plagioclase is weathered to completion over the entire corestone, while pyroxene and biotite were still found in the saprolite. However, since the abundance of biotite and pyroxene in the bulk rock are minor (7 and 4 vol%, Hewawasam et al. (2013)), the contribution of *in situ* oxidation to bulk rock weathering might be as low as 2 %. This assumption is based on mass balances and considers the amount of Fe(II) in the minerals and the mineral concentration of pyroxene and biotite in the bedrock. But on the other hand, without oxidation-induced fracturing no fresh weatherable surfaces are generated and no additional pathways for other weathering reactions like plagioclase dissolution are provided.

Hence, the bulk rock porosity would remain low, as well, and this would decrease the bulk rock weathering ability and lowers the rate of conversion of bedrock to soil. Therefore, the impact of oxidation is fundamental for chemical weathering reactions, and will be discussed in detail in the following section 4.4 and 4.5 were the oxidative fracturing is determined and a weathering feedback dependent on O_2 transport through the regolith will be postulated.

4.4 Fracture versus porosity formation across the corestone and the rindlets

Now that I discussed the initiating processes of chemical weathering at the micro-scale, I can upscale my findings further to discuss how these processes will affect the bedrock to produce the spheroidal weathered corestones and the conversion to soil. To do so, I will turn back to the profile scale (cm to m) and discuss how bulk chemical and mineralogical changes are important for the formation of fluid pathways. Especially the transport of O_2 is important as the oxidation is the rate-limiting weathering process.

Within the regolith column, fluids can circulate relatively easily because of the fragmented fabric and the high porosity, as indicated by the large specific surface area (SSA) values (Fig. 3.1). Throughout the corestone, microscopic observations together with connected internal surface area and porosity measurements suggest that an initial network of fluid pathways has developed in the form of connected pores and fractures, similar to the pathways described in Buss et al. (2008), Fletcher et al. (2006), or Navarre-Sitchler et al. (2013). However, these pathways are absent in corestone zone 1, *i.e.,* during incipient weathering, where porosity was below the detection limit. Therefore, reactive phases (*e.g.*, O_2, protons) can reach minerals only through (i) fractures of a scale larger than our observational scale of a few cm, followed by (ii) migration along grain boundaries. In corestone zone 2 and further outwards, porosity and connected internal surface area of grain boundaries and micro-fractures reach measurable values (Fig. 3.1), suggesting that reactive phases (including fluids) can percolate through connected pore spaces or a network of fractures. In particular, the formation of rindlets separated from each other by macroscopic fractures suggests that specific volume changes induced by mineral reactions build up sufficient strain to produce fracturing.

In the following section I discuss how such secondary porosity by fractures and open pore space might form in each zone of the corestone to promote mobility of reactive phases. In this regard it is important to note that formation of fractures requires the build-up of strain during reactions with a positive volume change, while open pore space is formed during reactions with a negative volume change. It should also be noted that both processes (fracture formation following a positive volume change and formation of open pore space during a negative volume change) ultimately produce porosity.

4.4.1. Strain formation by *in situ* Fe oxidation in pyroxene and biotite

In situ Fe oxidation (meaning oxidation of structural Fe(II) within the mineral lattice without inducing mineralogical phase transformations, *e.g.,* see Buss et al. (2008)) in pyroxene and biotite is the first weathering mechanism occurring in the corestone, implying that O_2 is the reactive phase driving the onset of weathering and is the rate limiting process as discussed above. As this process produces strain, following Fletcher et al. (2006) I hypothesize that this Fe(II) oxidation eventually leads to the formation of macro-fractures separating the rindlets from the corestone during spheroidal weathering. Because the porosity is low in the corestone center and fractures are not observed at the scale of our sample I assume that oxygen is transported along grain boundaries. Hence, below I consider the transport of O_2 in the gaseous

form. To test the hypothesis, I calculate the relative volume increase, and elastic strain ε, due to the iron oxidation reaction:

$$FeO + \frac{3}{2}H_2O + \frac{1}{4}O_2 = Fe(OH)_3 \quad (4.8)$$

Fracturing will occur if the elastic strain ε caused by *in situ* oxidation during chemical weathering overcomes the fracture surface energy Γ, following the fracture criterion:

$$2\Gamma = \frac{E\varepsilon^2}{1-\nu} = U \quad (4.9)$$

Where E is Young's Modulus, ν is Poisson's ratio (values are listed in Table 4.3) and U is the strain energy density that must overcome 2Γ in order to fracture the rock. This fracture criterion can be tested for each layer of the corestone, using elastic strain values calculated as:

Table 4.4 Parameters for oxidation model calculations

parameter	value	unit
$V_{Fe(OH)3}$	1.92 x 10^{-4}	m^3/kg
V_{FeO}	1.75 x 10^{-4}	m^3/kg
ρ_{rock}	2700	kg/m^3
$[px]_{rock}$	4	vol%
$[bt]_{rock}$	7	vol%
$[Fe]_{rock}$	0.0316	kg/kg_{rock}
$[FeO]_{px}$	0.33	kg/kg_{px}
$[FeO]_{bt}$	0.20	kg/kg_{bt}
$[Fe]_{px}$	0.020	kg/kg_{rock}
$[Fe]_{bt}$	0.014 – 0.017	kg/kg_{rock}
$[px]_0$	0.059	kg/kg_{rock}
$[bt]_0$	0.072 – 0.086	kg/kg_{rock}
$[Fe(OH)_3]_0$	0	kg/kg_{rock}
E	1.0 x 10^{12}	dyn/cm^2
ν	0.25	-
2Γ	4.0 x 10^5	dyn/cm^2

The rock parameters are taken from Hewawasam et al. (2013). E, ν and 2Γ are from Fletcher et al. (2006). $[Fe]_{px}$, $[Fe]_{bt}$, $[px]_0$, and $[bt]_0$ are calculated as explained in Appendix C. The values for $[bt]_0$, and $[Fe]_{bt}$, depend on the biotite density, therefore a range is calculated using an annite and a phlogopite specific density. Molar volumes of FeO and $Fe(OH)_3$ [m^3/mol] from Robie and Hemingway (1995) were converted to [m^3/kg].

$$\varepsilon = \frac{1}{3} * \frac{\Delta V_{rock}/M_{rock}}{V_{rock}/M_{rock}} = \frac{1}{3} * \Delta\tilde{V} * \rho_{rock} \quad (4.10)$$

Where M_{rock}, V_{rock}, and ρ_{rock} are the mass, volume, and density of rock being subjected to weathering, respectively [kg_{rock}, m^3, and kg_{rock}/m^3, respectively]. ΔV_{rock} is the volume change of this rock mass during oxidation of pyroxene and biotite [m^3]. $\Delta\tilde{V}$ is the corresponding volume change relative to mass rock unit [m^3/kg_{rock}], which can be calculated as:

$$\Delta\tilde{V} = \frac{\Delta V_{rock}}{M_{rock}} = V_{FeO} * \left([Fe]_{bt,0} * \left(1 + \tau_{bt,j}\right) - [Fe]_{bt,0}\right) + V_{FeO} * \left([Fe]_{px,0} * \left(1 + \tau_{px,j}\right) - [Fe]_{px,0}\right) + V_{Fe(OH)_3} * \left([Fe(OH)_3]_j - [Fe(OH)_3]_0\right) \quad (4.11)$$

$V_{Fe(OH)3}$ and V_{FeO} [m^3/kg] are the specific volumes of $Fe(OH)_3$ and FeO, respectively (Robie and Hemingway (1995), Tables 4.4 and 4.5). $[Fe]_{(bt,px),0}$ [in kg/kg_{rock}] represents the concentration of biotite (bt)- and pyroxene (px)-borne Fe in the rock, respectively (Appendix C). $\tau_{(bt,px),j}$ (Table 4.6) is the mass transfer coefficient (Brimhall and Dietrich, 1987) of biotite and pyroxene in weathered layers j, respectively (*i.e.,* minus the fraction of initial biotite and pyroxene weathered). $[Fe(OH)_3]_j$ is the $Fe(OH)_3$ concentration in the weathered layer j. $[Fe(OH)_3]_0$, the initial $Fe(OH)_3$ concentration in the rock, is set to be zero. In the corestone center only 5% of total Fe is ferric (as measured with bulk rock analyses) and is most likely of primary bedrock origin. Hence, it does not result from oxidation reactions and therefore can be neglected for this purpose. The values of these parameters are listed in Tables 4.4 and 4.5. Precipitation of clay minerals, another mechanism entailing a volume increase, was hypothesized by Jamtveit et al. (2011), Jamtveit et al. (2009), Røyne et al. (2008), and Rudge et al. (2010) to produce hierarchical fractures. However, in the corestone clay mineral precipitation is first initiated in zone 3 and even there the amount of clay minerals formed is not of significance. Therefore, I do not quantify the strain build-up during formation of clay minerals, which is unlikely to affect the volume budget near the weathering front.

Table 4.5 Mineral-specific molar weight, molar volume, and density

	molar weight [kg/mol]	molar volume [m^3/mol]	density [kg/m^3]
px (ferrosilite)	2.64×10^{-1}	6.60×10^{-5}	4.00×10^{3}
bt (annite)	5.12×10^{-1}	1.54×10^{-4}	3.32×10^{3}
bt (phlogopite)	4.17×10^{-1}	1.50×10^{-4}	2.79×10^{3}
FeO (wustite)	6.89×10^{-2}	1.20×10^{-5}	5.72×10^{3}
$Fe(OH)_3$	1.07×10^{-1}	2.05×10^{-5}	5.22×10^{3}
Fe	5.59×10^{-2}	-	-

The mineral specific values used to calculate the amount of iron bearing mineral $[x]_0$ (equation S2, Appendix C) were taken from Robie and Hemingway (1995). The pyroxene specific parameters are given for a mineral formula with 6 O atoms.

Table 4.6 Mass transfer coefficients for pyroxene (τ_{px}) and biotite (τ_{bt})

corestone	min τ_{bt}	max τ_{bt}	τ_{px}
zone 1	0.00	0.00	0.00
zone 2	0.00	0.00	-0.17
zone 3	-0.02	-0.13	-0.30
zone 4	-0.03	-0.17	-0.75

Mass transfer coefficients τ are used to calculate the extent of weathering for pyroxene and biotite ($[x]_j$ in equation S4, Appendix C) and is used for calculation of $FeO_{lost,\,j}$ (equation S5, Appendix C) and the total volume change $\Delta\tilde{V}$ (equation 4.11). τ_{px} was inferred from τ_{Mn} (Hewawasam et al., 2013). No single element is specific for biotite weathering, therefore the calculated minimum and maximum biotite depletion in the different zones is used (from Hewawasam et al., 2013).

Furthermore, I would like to stress out that this approach considers bulk rock reactions, hence the oxidation in pyroxene and biotite observed at the nm-scale, can be neglected. Therefore, corestone zone 1 is taken as the "un-reacted" reference rock.

To fulfill Eq. (4.9), I calculate that 7.71 x 10^{-3} kg/kg_{rock} (7.22 x 10^{-2} mol/kg_{rock}) FeO needs to be oxidized, corresponding to approximately τ_{px} = -0.25 or τ_{bt} = -0.34 (25% pyroxene or 34% biotite oxidation). The boundary at which this criterion is attained is the first point at which the strain increase overcomes the resistance of the rock to fracture.

A worked example of this calculation is provided in Appendix C. The outermost position at which such degree of oxidation (combining biotite and pyroxene oxidation) is reached, is between zone 2 and zone 3 (Table 4.7). However, in contrast to this prediction the innermost macroscopic fracture (fractures separating the rindlets from the corestone) is detected more outwards, at the boundary between zone 3 and zone 4. I note that the predicted position of fracturing is a conservative estimate, *i.e.*, based on the lowest biotite weathering intensity proposed by Hewawasam et al. (2013) and the smaller value for the biotite-specific molar volume (phlogopite, Table 4.5; Robie and Hemingway (1995)). Using a higher biotite weathering rate for a biotite molar volume of annite would result in a predicted position of fracturing that is even more inward. I also note that τ_{px} and τ_{bt} (tracked by the loss of Mn and Sr, respectively; Hewawasam et al. (2013)) could be underestimated: as the *in situ* oxidation occurs before the dissolution of mineral crystal lattice, oxidation of pyroxene and biotite is most likely faster than the release of Mn and Sr. However, a more accurate prediction of the position of the first fracture would also be closer to the core, hence even further from the observed position of fracturing. I can attribute the apparent discrepancy between the predicted and observed positions of fracturing to two factors that are not mutually exclusive:

(1) The increasing strain due to Fe(II) oxidation is compensated by the production of additional open pore space during plagioclase dissolution and replacement by clay minerals with lower specific molar volume such as kaolinite in corestone zone 3. However, I note that

in zone 2, plagioclase remains virtually unweathered. In zone 3 the strong increase in porosity (Fig. 3.1), and thus compensation of elastic strain, can be attributed to plagioclase weathering.

(2) Micro- rather than macro-fractures (as hypothesized by Fletcher et al. (2006)) are formed following strain build-up. In this case, the micro-fractures that I infer from the measurable porosity in zone 2 form in the direct vicinity of the oxidized minerals, where they accommodate the strain generated by Fe(II) oxidation. Only when a certain size and density of these micro-fractures is reached do they merge to form the macroscopic fractures separating the rindlets (Navarre-Sitchler et al., 2013). At Hakgala, I suggest that the macroscopic fractures form only in zones 3 and 4. The increase in porosity and connected internal surface area of grain boundaries and micro-fractures in corestone zone 2 supports the micro-fracture formation hypothesis. Bazilevskaya et al. (2014) also report that oxidation of biotite is the first weathering process causing micro-fracture formation, with these micro-fractures allowing then for fluid infiltration and hence dissolution of plagioclase. This finding is consistent with the observations for the Hakgala site, where the dissolution front of plagioclase (consumption of protons, zone 3) lies higher than the O_2 consumption front (zone 2).

In this regard, I note that my observations differ from the multi-mineral model of Lebedeva et al. (2007), which predicts (a) a zone of reduced porosity immediately surrounding unweathered rock that is caused by oxidation of Fe-bearing primary minerals and (b) an outer zone with higher porosity following plagioclase dissolution. In contrast, in the Hakgala corestone the Fe(II) oxidation zone is characterized by an increase in porosity (actually due to fracturing following Fe(II) oxidation). I note that this discrepancy might be ultimately due to the fact that the bedrock in the study of Lebedeva et al. (2007) already exhibits some connected porosity, while the bedrock in Sri Lanka does not. Although Lebedeva et al. (2007) acknowledge that this low-porosity layer could be a locus of fracturing in any case, their model does not take into account the fluid pathway provided by fractures. My findings indicate that such pathways are important and that in multi-mineral weathering systems the importance of strain *versus* secondary porosity budget has to be taken into account.

Goodfellow et al. (2016) provided a similar calculation for biotite oxidation in granodiorite in marine terraces, Monterey Peninsula (California). The main differences between the study by Goodfellow et al. (2016) and this thesis is that they focused on how the fracture formation will affect the direct vicinity of the oxidated minerals, rather than on corestone formation. That study also did not evaluate possible feedbacks with the profile surface (section 4.5) and whether the process of *in situ* oxidation is indeed rate limiting (section 4.3). Although there are differences in the setting (Mediterranean climate, granodiorite, shallow weathering profile of a few meters, plagioclase not weathered to completion, active tectonic region) this study supports my results shown here and published in Behrens et al. (2015): oxidation of Fe(II)-bearing minerals or reactions that produce a positive volume change are important processes in bedrock-weathering.

Table 4.7 Evolution of volume changes ΔV, elastic strain ε, and strain energy density U in the corestone zones for different biotite compositions

	corestone zone	U [dyn/cm²]	ε	$\Delta\tilde{V}$ [m³/kg$_{rock}$]	ΔV^{px} [m³/kg$_{rock}$]	ΔV^{bt} [m³/kg$_{rock}$]	$\Delta V^{Fe(OH)3}$ [m³/kg$_{rock}$]
bt (annite)	zone 1	0	0	0	0	0	0
	zone 2	1.78×10^{5}	3.66×10^{-4}	4.06×10^{-7}	-5.80×10^{-7}	0	9.87×10^{-7}
	zone 3	6.22×10^{5} to 1.06×10^{6}	6.83×10^{-4} to 8.91×10^{-4}	7.59×10^{-7} to 9.90×10^{-7}	-1.02×10^{-6}	-5.99×10^{-8} to -3.90×10^{-7}	1.84×10^{-6} to 2.40×10^{-6}
	zone 4	3.72×10^{6} to 1.56×10^{7}	1.67×10^{-3} to 3.42×10^{-3}	1.86×10^{-6} to 3.81×10^{-6}	-2.56×10^{-6}	-8.99×10^{-8} to -5.10×10^{-7}	4.51×10^{-6} to 5.22×10^{-6}
bt (phlogopite) min	zone 1	0	0	0	0	0	0
	zone 2	1.78×10^{5}	3.66×10^{-4}	4.06×10^{-7}	-5.80×10^{-7}	0	9.87×10^{-7}
	zone 3	6.11×10^{5} to 9.67×10^{5}	6.77×10^{-4} to 8.52×10^{-4}	7.52×10^{-7} to 9.46×10^{-7}	-1.02×10^{-6}	-5.04×10^{-8} to -3.28×10^{-7}	1.83×10^{-6} to 2.30×10^{-6}
	zone 4	3.68×10^{6} to 1.50×10^{7}	1.66×10^{-3} to 3.36×10^{-3}	1.85×10^{-6} to 3.73×10^{-6}	-2.56×10^{-6}	-7.56×10^{-8} to -4.28×10^{-7}	4.48×10^{-6} to 5.08×10^{-6}

U is the strain energy density. U must overcome the fracture surface energy 2Γ to fracture the rock, which is calculated according to equation 3. $\Delta\tilde{V}$ is the total volume change during oxidation of Fe(II) relative to the unweathered (un-oxidized) bedrock. This $\Delta\tilde{V}$ can be separated in the contribution of FeO oxidation from pyroxene (ΔV^{px}), biotite (ΔV^{bt}), and precipitation ($\Delta V^{Fe(OH)3}$). bt is calculated for different molar volumes of biotite: in lack of precise volumes for biotite present in the corestone, molar volumes of annite and phlogopite were taken from Robie and Hemingway (1995) to calculate a range of volume increase by biotite Fe oxidation. The range of values given for zone 3 and 4 is due to different τ, as calculated in Hewawasam et al. 2013.

4.4.2 Bulk rock weathering pathways and associated volume changes for the entire profile

I have shown that the competition between volume increase and formation of secondary porosity at the bulk rock scale generates fluid pathways. Therefore, I combine the results from porosity measurements and bulk analyses of the secondary phases (the leaching experiments, XRD and IR spectroscopy on clay separates) to reconstruct mineral-specific weathering pathways (for pyroxene, biotite, and plagioclase) in the corestone. I develop these reactions for the bulk rock as these reaction pathways are important to explore the final overall conversion of bulk rock to soil. The weathering pathways are depicted schematically in Fig. 4.5 and listed in Table 4.8. An important constraint in this reconstruction is the fact that amorphous phases are present deeper in the corestone (*i.e.*, appear earlier in time) than secondary clay minerals. This is shown in particular by the observation that in bulk samples amorphous phases were detected in the corestone, whereas clay minerals were barely detectable even in the separated clay-sized fraction. This can be interpreted in two ways. First, the solid products of weathering reactions might differ depending on where they occur in the regolith profile (*e.g.*, corestone *vs*. saprolite), as permeability, porosity, and chemical composition of reactive phases (including fluids) vary with depth within the regolith. Second, many weathering reactions have been shown to involve an amorphous precursor (Chadwick and Chorover, 2001; Dahlgren et al., 1997; Hellmann et al., 2012; Steefel and van Cappellen, 1990), which is the preferred interpretation here. Therefore, for a given primary mineral, I suggest that a distinction should be made between the "primary mineral dissolution front" and the “secondary clay crystallization front” (Fig. 4.5, the only exception at Hakgala might be weathering of biotite to kaolinite by direct transformation or dissolution and re-precipitation; Dong et al. (1998); Murphy et al. (1998)).

To briefly recapitulate: Pyroxene weathering starts in zone 1 with *in situ* oxidation and leads to the formation of an Fe-bearing amorphous precursor and Fe-(oxy)(hydr)oxides (goethite was identified with XRD) as revealed by the dithionite extraction. In zone 3, most likely Fe-rich smectite-like intermediate clay minerals form in higher amounts, which are eventually transformed to crystalline Fe-(oxy)(hydr)oxides and kaolinite in the saprolite (Fig. 4.5). Biotite weathering (after oxidation) produces an Fe- and Al-bearing amorphous precursor along with Fe-(oxy)(hydr)oxides and kaolinite, eventually leading to the formation of Fe-(oxy)(hydr)oxides and kaolinite (Fig. 4.5). I acknowledge that I do not distinguish between abiotic or biotic induced weathering reactions (Bonneville et al., 2009; Shelobolina et al., 2012). In addition, I note that oxidation of biotite might be accompanied by K-loss from the interlayer and expansion of the layers, forming an altered biotite layer (Bonneville et al., 2011; Bonneville et al., 2009; Bray et al., 2014; Buss et al., 2008; Kalinowski and Schweda, 1996; Malmström and Banwart, 1997). Furthermore, I would like to acknowledge that only kaolinite minerals were found in the Fe-Al amorphous matrix, however, 2:1 secondary clay minerals like smectite are possible to form with further weathering. Plagioclase weathering is also initiated in zone 3 and contributes to the formation of the Al-amorphous precursor, as kaolinite is barely detected. This amorphous precursor is converted into crystalline gibbsite and kaolinite in the rindlets where plagioclase weathering is intense (Fig. 4.5). Please note, that Fig. 4.5 is a simplified sketch of the bulk rock mineral reactions, but the important point

is that at the bulk scale most reactions exhibit a negative volume budget, hence, formation of high internal porosity. How this formation of porosity will affect the conversion of bedrock to soil is discussed in the next section.

Table 4.8 End members of schematic mineral weathering pathways in the corestone

primary mineral		secondary mineral
pyroxene (orthopyroxene)[1] $(Fe_{1.0}Mg_{0.8}Ca_{0.1})Si_{1.8}O_6$ molar volume[2]: 66.00 cm³/mol	→	**goethite** FeOOH molar volume[2]: 20.82 cm³/mol **2:1 clay minerals** $X(Y)_3(AlSi)_4O_{10}(OH)_2$ molar volume[2,3]: >150 cm³/mol
biotite[1] $K_{0.7}(Fe_{1.0}Mg_{0.8}Ti_{0.2})(Al_{1.1}Si_{2.7})O_{10}(OH)_2$ molar volume[2]: 149.65 – 154.30 cm³/mol	→	**goethite** FeOOH molar volume[2]: 20.82 cm³/mol **2:1 clay minerals** $X_{0.3}(Y)_3(AlSi)_4O_{10}(OH)_2$ molar volume[2,3]: 150 – 577 cm³/mol **kaolinite** $Al_2Si_2O_5(OH)_4$ molar volume[2]: 98.56 - 99.34 cm³/mol
plagioclase (albite)[1] $Na_{0.74}Ca_{0.25}K_{0.016}Al_{1.25}Si_{2.75}O_8$ molar volume[2]: 100.07 cm³/mol	→	**kaolinite** $Al_2Si_2O_5(OH)_4$ molar volume[2]: 98.56 - 99.34 cm³/mol **gibbsite** $Al(OH)_3$ molar volume[2]: 31.96 cm³/mol

The mineral specific molar volumes of the educts and products and their chemical compositions depict where negative or positive volume budgets and element import or removal can occur.

[1] mineral composition determined by electron microprobe analyses.

[2] molar volumes from Robie and Hemingway (1995).

[3] molar volumes depend on the hydration state and must be higher than the biotite molar volume (*e.g.* a molar volume of 577 m³/mol is reported for illite in Robie and Hemingway (1995)).

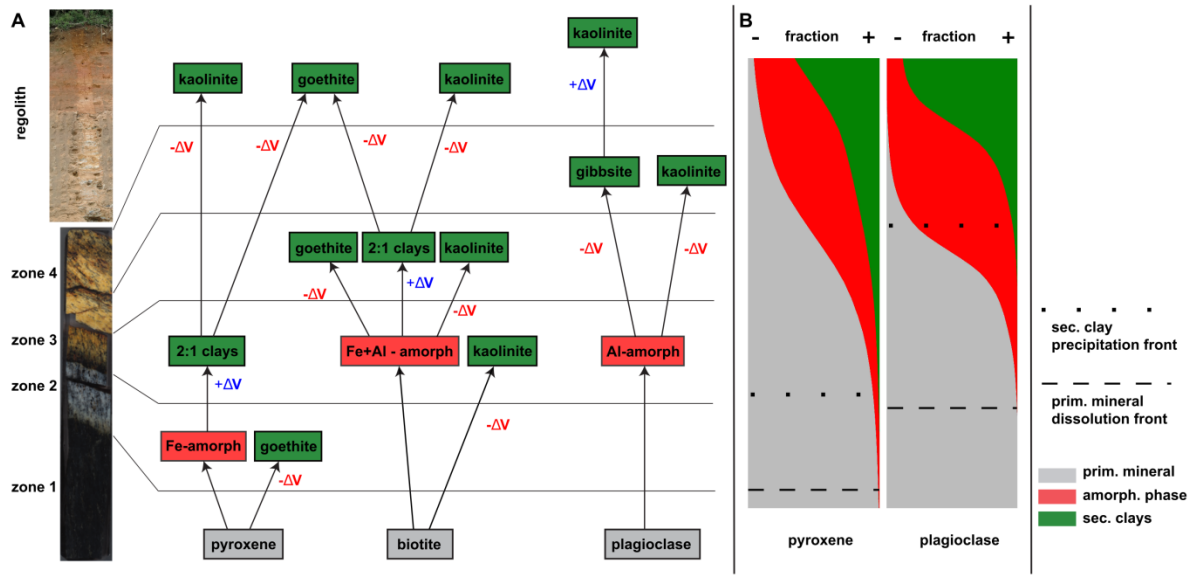

Figure 4.5 Schematic sketch of the pathways of mineral reactions during weathering of pyroxene, biotite, and plagioclase (A). Specific volume increase is presented in blue (+ΔV), and decreasing volume is presented in red (-ΔV). Volume changes during these reactions are associated with conversion to crystalline secondary products (green boxes). Meta-stable amorphous precursors are indicated by red boxes. For some reactions, especially those involving amorphous secondary phases, specific volume changes are not known. Fe-(oxy)(hydr)oxides are indicated as goethite, which was identified by XRD. Panel B schematically shows the onset of weathering for pyroxene and plagioclase at the weathering front (dashed horizontal line: primary mineral dissolution front) and the conversion of amorphous secondary phases to crystalline secondary clay minerals (dotted horizontal line: secondary clay crystallization front) in the corestone and the lower saprolite. As the reactions shown in panel A are continuously taking place in the corestone and the rindlets, (non)crystalline Fe- Al-(oxy)(hydr)oxides appear also in the upper part of the graph in panel B.

4.4.3 Spatial sequence of strain and porosity formation

Due to gaseous O_2 transport along grain boundaries and subsequent *in situ* Fe oxidation in pyroxenes in zone 1 the sequence starts with the build-up of strain in and around the oxidizing mineral. As stated previously, and importantly, such *in situ* Fe oxidation does not entail mineralogical phase transformations (see section 4.2.1). Rather, this strain increase induces micro-fractures in the minerals within the vicinity of the oxidized minerals, as already reported by Bazilevskaya et al. (2014). The micro-fractures are measurable as porosity increases in this zone, and serve as pathways for reactive phases (e.g., O_2, protons) and promote the weathering of the primary minerals. The first mineral transformation observed in zone 1 is the conversion of pyroxene to Fe-(oxy)(hydr)oxides that also contributes to porosity increase in corestone zone 2 because this reaction involves a negative volume budget and hence formation of pore spaces. The onset of biotite weathering could not be unequivocally detected, but starts with *in situ* Fe oxidation between zones 2 and 3, adding to the strain and triggering further micro-fracture formation. The porosity increase is then sufficient enough to allow for efficient transport of reactive phases (including aqueous fluids) leading to

plagioclase dissolution in zone 3. In this zone formation of pore spaces increases dramatically and compensates for the strain caused by Fe oxidation. Therefore, the macro-fractures that separate the rindlets occur later than expected and separate zone 4 from zone 3. At this point, the micro-fractures and the pore spaces merge together to form the macro-fractures and production of rindlets. Within the rindlets, the weathering of plagioclase to kaolinite increases dramatically, producing many pore spaces. Therefore, the combination of fracture formation due to *in situ* Fe oxidation and the formation of pore spaces during weathering reactions that exhibit a negative volume budget leads to the conversion of bedrock to saprolite via spheroidal weathering.

Most of the reactions reveal an amorphous precursor (including Fe-(oxy)(hydr)oxides) that forms deeper in space, hence earlier in time, than secondary minerals (Fig. 4.5). This observation is relevant for models showing that the fluid flow rate and the net precipitation rate of secondary minerals exert a substantial control over reaction rates, mass depletion and weathering advance rate (Maher et al., 2009). For example, it is expected that both the rate constants and the equilibria between fluids and secondary solids differ between amorphous and crystalline precipitates.

4.5 The role of O_2 transport in the feedback between erosion and weathering

I have shown that oxidation of Fe-bearing minerals is the limiting factor for the onset of the chemical weathering reactions at Hakgala and provides a possible feedback mechanism between erosion at the top of the profile and weathering at the bottom of the profile. This hypothesis is contrary to the suggestion given by Goodfellow et al. (2016). These authors suggest that feedback mechanisms are fundamentally different in different rock types and climatic regions. As I will show below (this section and section 4.6), these differences only affect the strength of the feedback, but do not affect the mechanism.

The oxidative weathering process requires the transport of O_2 from the surface where it is supplied in virtually unlimited amounts through the regolith to the weathering front, hence O_2 is the rate-limiting phase. I will now discuss how the relative importance of the type of O_2 transport (*i.e.*, diffusion *vs*. advection) through the Hakgala weathering profile influences the strength of this feedback. In a weathering system, where oxidative weathering is the process limiting the rate of regolith production, the strength of such a feedback can be envisaged by a simple scenario in which an erosion event removes an infinitely small layer of topsoil, that I call *dz* (Fig. 4.6A). As a result, regolith thickness decreases, and the weathering front comes closer to the surface, and hence to the atmosphere, by a distance equal to *dz*. As O_2 is consumed at depth and is supplied at the top, its concentration increases upward, and this lower distance between the weathering front and the surface results transiently in higher O_2 concentration (here called c_{wf}) at the weathering front. As a result, oxidative weathering will be enhanced and the weathering front will propagate further away from the surface, thereby increasing regolith thickness. The strength of this feedback mechanism is therefore dependent on the gradient of O_2 concentration, *dc/dz*, in the lowest part of the regolith, as suggested by Fletcher et al. (2006).

To explore these dependencies I developed a model in which transport of O_2 through a steady-state weathering profile occurs through both diffusion and advection. Advection can occur in regolith through macro-pores and fractures, while diffusion is more typical of transport through micro-pore networks prevailing near the weathering front or through clay layers in the regolith (Bazilevskaya et al., 2014; Brady and Weil, 2007). In this model, the boundary conditions are constant, meaning that erosion and regolith production are constant and balance each other, such that regolith thickness remains constant (such steady state condition applies to Hakgala, as shown by Hewawasam et al. (2013)), and that the bedrock is homogenous with uniform amounts of Fe(II)-bearing primary minerals. For the sake of simplicity, and although O_2 is obviously consumed in the saprolite (as shown by $Fe(II)/Fe_{total}$ profiles, Fig. 3.3), I assume that all O_2 is only consumed in a zone confined to the weathering front. Given these assumptions, the steady-state partial derivative equation for non-reactive transport of O_2 is:

$$\phi \frac{\partial c}{\partial t} = -v \frac{\partial c}{\partial z} + \phi D \frac{\partial^2 c}{\partial z^2} = 0 \qquad (4.12)$$

Where ν is the advective velocity [m/s], D is the diffusion coefficient [m²/s], ϕ is the porosity, c is the concentration [mol/kg], z the depth [m], and t is time [s]. The first boundary condition is given by the atmospheric O_2 concentration, c_0, at the surface (z = 0) and the secondary boundary condition is given by the gradient of O_2, f [mol_{O2}/m^3*m] over a distance of about 3 m (defined by the corestone zone), which is located at about 8.3 m depth in the Hakgala weathering profile at the saprolite-corestone transition. For calculation purposes, I use non-dimensional variables:

$$C = c/c_0 \tag{4.13}$$

$$F = f * H/c_0 \tag{4.14}$$

$$Z = z/H \tag{4.15}$$

with c_0 the atmospheric O_2 concentration, and H the depth of the weathering profile. F is the non-dimensional flux of O_2 consumption at the lower boundary. The calculation of F for the Hakgala weathering profile is shown further down. The steady-state solution of equation 4.12 and of the associated boundary and initial conditions is:

$$C = 1 + \frac{F}{Pe} * [exp^{-Pe} - exp^{-Pe(1-Z)}] \tag{4.16}$$

The Péclet number, *Pe*, expresses the competition between advection and diffusion and is defined as:

$$Pe = \frac{advective\ transport}{diffusive\ transport} = \frac{-vH}{\phi D} \tag{4.17}$$

with v for velocity, H as a length scale, ϕ the porosity, and D the diffusion coefficient. Higher *Pe* numbers describe advection-dominated systems, whereas lower *Pe* numbers represent diffusion-dominated transport. In a natural system it is unlikely that only one *Pe* number characterizes the entire profile. However, for the purpose of this simple model, I neglect these variations and use a "profile-averaged" *Pe* number. In soils, the transport conditions can vary over a wide range in small spatial distances. Previous studies show that *Pe* numbers cover a wide range of values across different soils (*e.g.*, 5 to 69; Mayes et al. (2003)). The relatively high *Pe* values indicate the importance of advection, although diffusion has been assumed to be the main mode of transport in weathering models (Brantley and Lebedeva, 2011; Lebedeva et al., 2010; Navarre-Sitchler et al., 2013). Bazilevskaya et al. (2014) found that in a supply-limited weathering regime, a combined transport of advection and diffusion will lead to thick weathering profiles, whereas transport only by diffusion will lead to thin weathering profiles. These authors also suggest that the oxidation-induced fracturing provides the condition for the combined diffusion-advection transport. I do not have any constraint on the *Pe* number of the Hakgala weathering profile, but as this is the only free parameter (F is constrained by the data,

see below), I can perform a sensitivity analysis of the model output as a function of the *Pe* value.

The O_2 gradient f resulting from O_2 consumption at depth due to Fe oxidation can be determined by calculating the mass transfer coefficient τ of Fe(II) normalized to Zr (which was shown to be immobile by Hewawasam et al. (2013)):

$$\tau_{Fe(II)} = \frac{[Fe(II)]_{weathered}}{[Fe(II)]_{parent}} * \frac{[Zr]_{parent}}{[Zr]_{weathered}} - 1 \quad (4.18)$$

I calculate the gradient for the entire approximately 3 m-thick corestone zone between the bedrock and the saprolite (over which corestones occur in the weathering profile). I assume that O_2 consumption in this entire zone occurs over an infinitely small layer at the lower boundary of the Hakgala weathering profile, comparable to the corestone zone. I use the change in Fe concentration and in $Fe(II)/Fe_{total}$ ratio from the corestone center to the outermost rindlet to calculate τ_{Fe}. With equation 4.18 I derive 28% oxidation of Fe(II) to Fe(III) (in total 6.62 x 10^{-3} kg_{Fe}/kg_{rock}, calculated with the average Fe concentration in the rock). If every mol Fe(II) consumes 0.25 mol O_2 (equation 4.8), the amount of O_2 per kg rock consumed during oxidation is about 2.95 x 10^{-2} mol_{O2}/kg_{rock}. The gradient of O_2 is f = 2.63 x 10^{-2} [mol_{O2}/m^3*m] at the saprolite-corestone transition in the Hakgala weathering profile. For this 3 m-thick corestone zone with an inferred porosity of 10% I calculate a non-dimensional gradient F = 2.42 x 10^{-1}. With this lower boundary condition, I can model the O_2 profile in the Hakgala regolith profile for different *Pe* numbers (Fig. 4.6B, Table 4.9). Diffusion-dominated transport of O_2 results in a steeper O_2 gradient in the lowest part of the saprolite than in the case of transport dominated by advection. Therefore, following the scenario developed above, diffusive O_2 transport will lead to stronger feedbacks between erosion at the top and weathering at depth. Diffusion-dominated transport likely also leads to low weathering front advance rates (Brantley and Lebedeva, 2011) and would be comparable to the model of Fletcher et al. (2006). However, as shown by Lebedeva et al. (2010), natural systems with thick weathering profiles are typically characterized by combined diffusive-advective transport. In such systems a feedback will be weakened, for example, if there is a thick, purely advective layer at the top where atmospheric concentrations prevail throughout the depth profile, or if consumption of O_2 is not the rate limiting factor, and excess of O_2 prevails at the weathering front (*e.g.*, when Fe(II)-bearing minerals are absent). Then, both boundaries might act independently and the weathering profile can thicken or thin as no feedback is in operation.

Similar conditions as described in Navarre-Sitchler et al. (2013) may exist in the Hakgala profile, where dominating advective transport (higher *Pe* numbers) is proposed to occur in the upper saprolite, along preferential pathways (like pore networks, pre-existing joints and cracks), and diffusion (lower *Pe* numbers) dominates the transport in the rock, the center of the separated rindlets and the lower saprolite. Because I used "profile-averaged" *Pe* numbers, lower *Pe* numbers may be most appropriate for the investigated profile to produce such a thick regolith as further discussed in the following section 4.6.

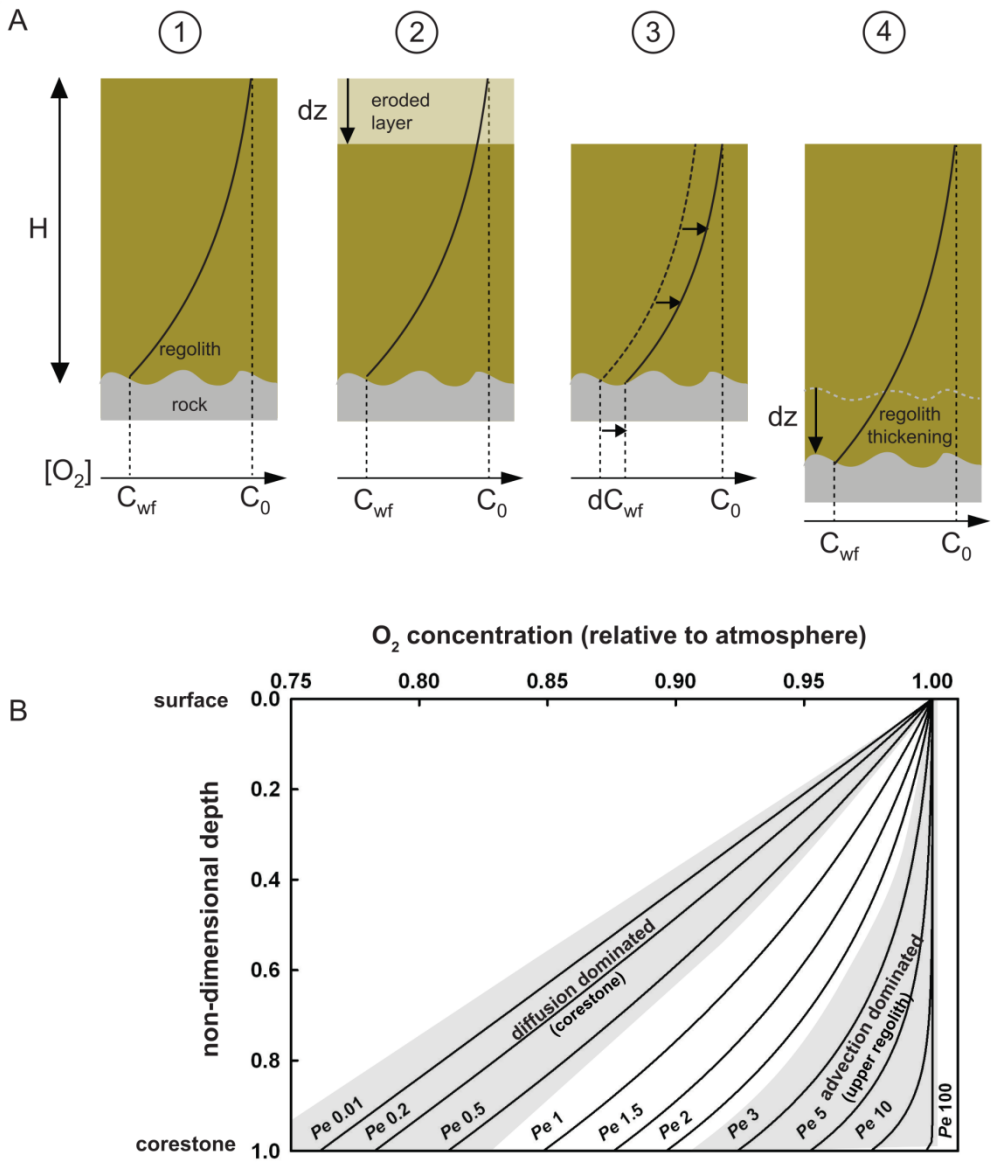

Figure 4.6 O_2 - driven weathering feedback. (A) Conceptual sketch showing how the coupling between regolith thickness and transport properties can be linked with the propagation of the weathering front through a feedback (Fletcher et al., 2006) for a given O_2 concentration profile. The O_2 profiles are modeled with respect to the consumption of O_2 due to oxidation of pyroxene and biotite at depth in the Hakgala weathering profile. (1) Initial steady state: the regolith thickness is H, the O_2 concentration in the pore and fracture network is C_0 (atmospheric concentration) at the surface and C_{wf} at the weathering front, with $C_{wf} < C_0$ as O_2 is consumed by oxidative weathering reactions at the weathering front. (2) An infinitesimal erosion event removes a layer of thickness dz at the regolith surface, which pushes the system out of steady state. (3) Re-equilibration of O_2 at the surface with the atmosphere results in an increase of O_2. As the transport properties of the regolith are not modified by the erosion event itself, the O_2 gradient throughout the regolith remains the same, such that C_{wf} increases too by an infinitesimal amount dC_{wf}. (4) The increase in C_{wf} enhances the kinetics of oxidative weathering reactions, ensuing fracturing and downward propagation of the weathering front by a distance dz, resulting in regolith thickening until the concentration of O_2 at the weathering front is C_{wf} again. The system is back at steady state. The "speed" at which the downward propagation of the weathering front occurs after the erosion event, which reflects the "strength" of the feedback, is set by the value of dC_{wf} for a given dz, *i.e.* by the gradient of O_2 concentration in the lowest part of the regolith (Fletcher et al., 2006), which is in turn dependent on the type of transport prevailing in the regolith (advective *vs.* diffusive). (B) Modeled O_2 concentration profiles as a function of the Péclet number (Pe): normalized O_2 concentrations in the profile versus normalized depth at different Péclet numbers. The O_2 concentration profiles are directly related to the consumption of O_2 at depth, calculated here using the data from the Hakgala weathering profile. The O_2 consumption depends on the oxidation of pyroxene and biotite in the corestone and the rindlets, which is quantified for the 3-m-thick corestone zone. Although for this simple model I assumed that one Pe number applies to the whole weathering profiles, low Pe numbers might be characteristic of transport in the corestone, and high Pe numbers characteristic of transport in the saprolite.

Table 4.9 Parameters for O_2 depth profile calculations

[Fe] average rock	24872	ppm
[Zr] average rock	226	ppm
Fe(II) / Fe_{total} zone 4c	0.68	
Fe(II) / Fe_{total} zone 1	0.95	
mol O_2 used	0.25	mol
mol H_2O used	0.75	mol
n Fe	0.056	kg/mol
corestone zone thickness	3	m
rock density	2.675	kg/m^3
rock porosity	0.1	
O_2 atmosphere	9.02	mol O_2/m^3
profile depth	8.3	m

Zr and Fe concentrations, the profile depth, and the corestone zone thickness are from Hewawasam et al. (2013). Fe(II) / Fe_{total} ratios are from Table 3.1. The rock density and the porosity are inferred from the He-pycnometry measurements. For calculation purposes, the O_2 concentration is converted from mol O_2/mol air into mol O_2/m^3 air.

4.6 Implications and outlook: Controls on weathering rates and evolution of thick weathering profiles

In the previous sections, I found that the oxidation and the supply of O_2 to the weathering front is the rate limiting parameter in the Sri Lankan weathering profile. Hence, fracture formation by oxidation is an important process to provide fresh weatherable surfaces. The importance of fracture formation was also hypothesized by Kim et al. (2017) and Brantley et al. (2017). But how can these two parameters (oxidation rate, supply of O_2) be influenced by external conditions (*e.g.* lithology, tectonics, climate, hydrology, or biota) on a regional scale? In this section I discuss some of these factors that lead to landscapes in which slow weathering and thick regolith profiles prevail. In this regard identifying the processes that connect the surface with the weathering front is an important issue for explaining the coupling between weathering and erosion. In recent years several studies have addressed similar questions in filling the knowledge-gap (Bazilevskaya et al., 2013; Bazilevskaya et al., 2014; Goodfellow et al., 2016; Rempe and Dietrich, 2014; Yesavage et al., 2016). Some of these studies came to similar results; others differed substantially in their conclusions. A principle observation of many weathering studies is that slow chemical weathering occurs where tectonic activity is absent and production of thick regolith occurs over granitic bedrock (Bazilevskaya et al., 2013; Brantley and Lebedeva, 2011; Brantley et al., 2017; Dixon and von Blanckenburg, 2012; Navarre-Sitchler et al., 2013).

The setting in Sri Lanka is representative of a supply-limited weathering end member, where the mineral dissolution kinetics are faster than the supply of fresh material into the weathering reactor. Here, a thick saprolite profile prevails, where plagioclase is completely dissolved in the lower part, as also reported by Navarre-Sitchler et al. (2013). However, unlike the weathering profile (featuring corestones) discussed in Navarre-Sitchler et al. (2013), the Sri Lankan weathering rate is at the lower end of global weathering rates (5 – 60 t km^{-2} y^{-1}, Dixon and von Blanckenburg (2012)). Two observations confirm that these rates represent a complete quantification of the total weathering flux. These rates are based on *in situ* cosmogenic nuclides measured in quartz sampled in top soil. As these rates detect denudation from the surface layer they were corrected for solute loss at greater depth (Hewawasam et al., 2013). That these local rates are representative for the landscape scale was demonstrated by the similar rates derived from solute concentrations in streams (Hewawasam et al., 2013). Hence, I regard the processes derived from the detailed investigation of the weathering profile in this thesis as those that govern weathering in the entire landscape.

At this point, I would like to stress why I consider the "top down" control over the weathering-erosion feedback illustrated and quantified in detail in this thesis rather than exploring the approach of Rempe and Dietrich (2014). In this alternative model the advance of the weathering front is driven by fluid flow when bedrock enters the saturated zone as driven by channel incision. A requirement is that the bedrock entering the weathering zone features porosity that provides pathways for reacting fluids. However, the bedrock at the Hakgala regolith profile in Sri Lanka is relatively compact and does not show any connected

porosity. Hence, porosity and fractures must first be produced to provide the hydraulic conductivity required to saturate the bedrock with fluids. Therefore, I consider surface-controlled O_2 driven fracturing to be the rate-limiting step that results in a connection between erosion at the surface and weathering at depth. I next discuss possible pre-requisites for the establishment of settings with low weathering rates as observed in Sri Lanka. My hypotheses for such low rates are: (1) the absence of a fast process that produces fresh weatherable surfaces and pathways for fluids in general, which would enhance chemical weathering reactions; (2) the occurrence of minerals unaffected by weathering that stabilize the bedrock and the regolith against weathering and erosional surface effects. A minor contribution might be the dilution of pore water due to different precipitation regimes. To test this hypothesis I evaluate the role of tectonic setting, lithology and mineralogy, pre-fracturing, soil shielding, and climate in the following paragraphs.

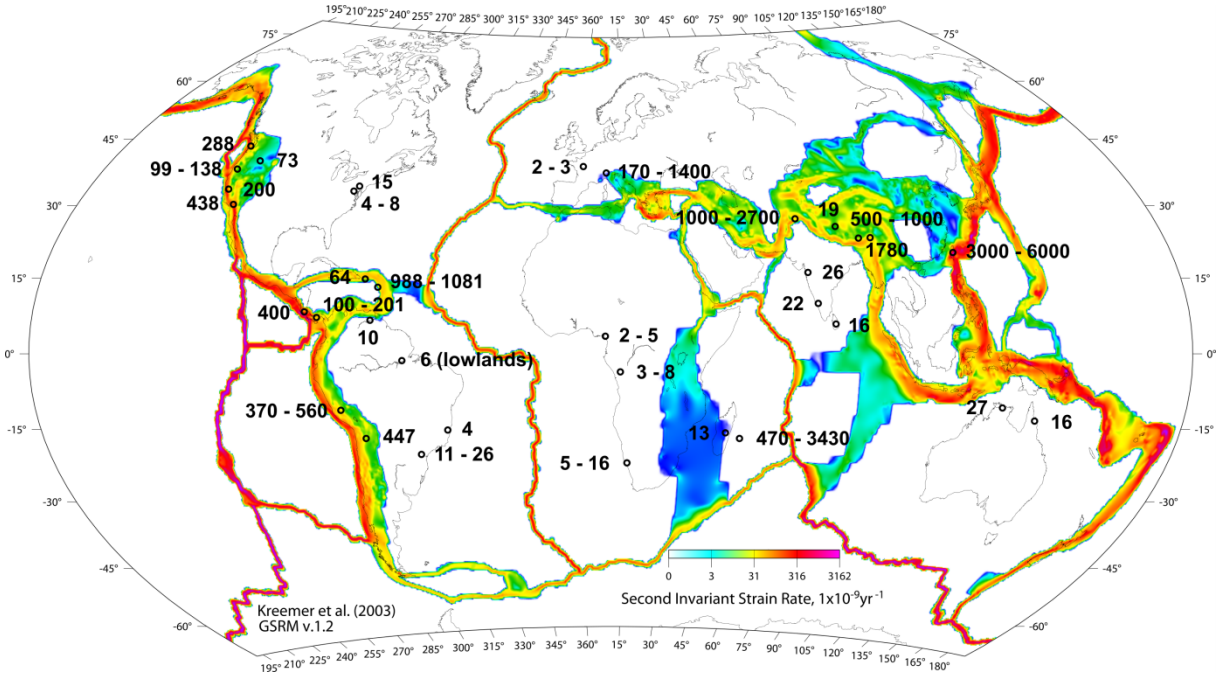

Figure 4.7 Strain rate map with global denudation rates (mm/kyr). References are: Oregon: Heimsath et al. (2001) and Bierman et al. (2001); Idaho: Kirchner et al. (2001); Washington: Belmont et al. (2007); California: Perg et al. (2003) and DiBiase et al. (2010); Virginia: Bacon et al. (2012), Hancock and Kirwan (2007), Price et al. (2008); Pennsylvania: Jin et al. (2010); Puerto Rico: Riebe et al. (2003); Guadeloupe: Dessert et al. (2015); Costa Rica: Sak et al. (2009); Panama: Nichols et al. (2005), Sosa Gonzalez et al. (2016); Guyana Shield: Edmond et al. (1995); Amazonas (lowlands): Gaillardet et al. (1997); Bolivian Andes: Insel et al. (2010), Wittmann et al. (2009); southern Brazil: Barreto et al. (2013), Salgado et al. (2014), Cherem et al. (2012); France: Roy et al. (1999); Swiss Alps: Norton et al. (2011), (2010), (2008), Wittmann et al. (2007); south Cameron: Braun et al. (2012), (2005); Congo: Gaillardet et al. (1995); Namibia: Bierman et al. (2007), (2001); Madagascar: Cox et al. (2009); La Réunion: Louvat and Allègre (1997); Sri Lanka: Hewawasam et al. (2013); India: Braun et al. (2012), (2009), Das and Krishnaswami (2007); Himalaya: Finnegan et al. (2008), Godard et al. (2010), Lal et al. (2003), Scherler et al. (2014), Vance et al. (2003); Taiwan: Dadson et al. (2003); Australia: Heimsath et al. (2009), Nichols et al. (2014); the strain rate map after Kreemer et al. (2003). The list of denudation rates is incomplete and rates were chosen exemplarily.

4.6.1 Tectonic controls

Possibly the most important factor controlling chemical weathering and denudation rates is tectonic activity (Dixon and von Blanckenburg, 2012; Hilley et al., 2010; Riebe et al., 2001; West et al., 2005). To explore this factor, I consider strain as an indicator for tectonic activity. I acknowledge that the World Stress Map by Heidbach et al. (2016) might be a better indicator but concerning visualization issues I chose the strain map to keep it clearly represented. A global strain map is provided in *e.g.* Kreemer et al. (2003). Comparing such a map to published weathering and denudation rates (Fig. 4.7) it is obvious that in regions with low strain, hence tectonic activity, the observed rates are amongst the lowest (Sri Lanka, the Guyana Shield region, Cameroon, Congo, and south-east Brazil, for references see Fig. 4.7). In contrast, catchments in regions with higher strain values exhibit faster weathering rates: for example Guadeloupe, La Réunion, Puerto Rico, Costa Rica, Panama, Bolivian Andes, Himalaya, Alps (for references see Fig. 4.7). Such strain will at some point produce fractures in the bedrock, similar to the oxidative fracturing explored in section 4.4.1, but on a regional scale (Molnar et al., 2007). These fractures provide new fresh weatherable surfaces. Furthermore, in actively uplifting regions and during steady state environments such uplift results in base level lowering. To attain steady state again, rivers will incise deeper in the bedrock channel, thus over-steepening the adjacent slopes. They may become instable once the steepening reaches the critical slope angle and mass wasting such as landslides occurs. On the other hand, after unloading due to preceding uplift, previously closed fractures may open thus providing fresh weatherable surfaces. In regions were no tectonic forcing prevails all fracture surfaces are already attacked by weathering. Another process is needed to produce fresh weatherable surfaces. In Sri Lanka, with its tectonically quiescent nature, a possible processes to account for denudation of the Central Highlands is down-wearing by escarpment retreat, as described in Vanacker et al. (2007b). What is further striking is the fact that, even in similar tectonic and climatic regimes there are differences in denudation rates (Fig. 4.7). Hence, in addition to tectonics there must be other controls such as lithology, mineralogy/chemistry or soil cover, influencing the resistivity for weathering and erosion. These influencing factors will be discussed in more detail in the following sections.

4.6.2 Lithological controls

Based on the results presented in this study I suggest that bedrock chemical and physical characteristics might exert a strong control on the propagation rate of the weathering front and hence on denudation rates. This hypothesis was also raised by Bazilevskaya et al. (2014), Brantley et al. (2017), Goodfellow et al. (2016) and Kim et al. (2017). For example, as bedrock Fe concentrations are low at the Sri Lanka weathering profile, micro-cracks produced during oxidation reactions will form only at slow rates, resulting in slower weathering zone propagation. In the Sri Lanka charnockite, porosity and connected internal surface area of grain boundaries and micro-fractures are below the detection limit of the BET method and He pycnometry. In the case of this coherent bedrock it appears that almost no internal surfaces

are available in the bedrock which could provide contact between minerals and reactive phases. How these observations might explain global findings is envisaged below.

From a general point of view, most of the slow weathering catchments lay above bedrocks of variable lithology: The Nsimi catchment from Cameroon (Braun et al., 2012; Braun et al., 2005) over granodiorite and granite, the Guyana Shield over acidic and calcalkaline igneous and metamorphic (including mafic) bedrocks (Edmond et al., 1995), the Congo Basin over sedimentary rocks (Gaillardet et al., 1995; Henchiri et al., 2016), Amazonian Lowlands with silicate and sediment bedrock (Gaillardet et al., 1997), Shale Hills with shale bedrock (Jin et al., 2010), Canadian Shield with granitoid and metamorphic bedrocks (Millot et al., 2010), Paris Basin in France with sedimentary rocks (Roy et al., 1999). This leads to the suggestion that in addition to the absence of tectonics, weathering in these bedrocks lacks a process that produces fresh weatherable surfaces and pathways at fast rates.

Together with the findings from Sri Lanka, the studies of Bazilevskaya et al. (2013) and (2014) are good examples to explore the mineralogical factors concerning chemical weathering. In these studies diabase and granite weathering profiles from the same region are compared to each other, hence tectonic and climatic regimes are the same. The most striking facts are the low quartz but high plagioclase and pyroxene content in the diabase together with a thin regolith (a few meters), while the granite contains slightly less plagioclase and minor pyroxene but high quartz concentrations and a thick regolith (tens of meters). These findings from Bazilevskaya et al. (2013) are in agreement with other studies on granitic and basaltic lithologies, which all report thinner regolith on mafic but thicker regolith on granitic bedrock (Puerto Rico, Costa Rica, Sierra Nevada in California, Shale Hills, India, the Amazonas, and Cameroon, for references see Fig. 4.7). In the study from Bazilevskaya et al. (2013) they concluded that the regolith thickness is dependent on the style of transport of solutes (*e.g.* protons, O_2) in the bedrock, with diffusive transport in diabase and advective transport in granite. However, my observations of oxidative induced weathering differ from their conclusion and point to other controls on weathering front thicknesses determined stronger by mineralogical factors which in turn control the type of transport *per se*. As an example, in catchments with mafic bedrock (high Fe(II) content), the consumption of O_2 is high and a thin oxidative weathering front exists. This leads to high fragmentation of the bedrock and production of many pathways for reactants. Therefore, mafic bedrock is divided into smaller fragments at much faster rates than *e. g.* low Fe(II)-containing granitic bedrock, a process also in part suggested by Goodfellow et al. (2016). These small fragments provide abundant connected pathways where plagioclase is easily weathered. Hence, thin reaction fronts with enhanced plagioclase weathering and therefore rapid conversion of bedrock to soil can be reached. In steady state theory, soil production equals soil removal and a steady soil thickness is maintained. A high degree of fragmentation produces material that can be removed easily from the regolith. Therefore, in contrast of the studies by Bazilevskaya et al. (2013) and (2014), I conclude that it is not the solute-transport process (diffusive versus advective) that determines the weathering front and regolith thickness but the degree of weathering reactions that exhibit a positive volume change and the rate at which fractures, reactive surfaces and fluid pathways are generated. The dependence of factures on regolith thickness was also

shown in Kim et al. (2017) with thicker regolith above fractured diabase and advective solute-transport properties in contrast to thin regolith above massive, unfractured diabase with diffusive solute-transport properties. I agree with the hypothesis presented in Bazilevskaya et al. (2013) and (2014) that inside the intact bedrock diffusive transport prevails. But as I showed with the feedback model presented in section 4.5, the transport properties of solutes will only have implications on the strength of the feedback between the surface and the weathering front that is dependent on the supply and consumption of O_2. Diffusive solute-transport leads to a stronger feedback while advective solute-transport properties weaken the feedback.

In granitic catchments in contrast, one of the main components is quartz which is inert to weathering. Stable minerals with respect to weathering will hinder the bedrock to easily disintegrate into loose material (Kim et al., 2017). In addition, as explained above for the diabase, but the other way round, low Fe(II) content will lead to slow consumption of O_2 and pathway formation for fluids to reach the easily weatherable minerals is inhibited. Thus a thick weathering front can establish, where at the initial stage diffusion of oxygen is needed to oxidize and fracture the rock, followed by dissolution of plagioclase. Both processes increase the porosity (including micro-fractures) and advective solute-transport establishes. This in turn explains the higher advective solute-transport properties found in granitic bedrock as depicted in Bazilevskaya et al. (2013).

However, I note that such a fragmentation process is not limited to lithologies containing Fe(II) but might also occur in bedrock with no Fe(II) bearing mineral. Hierarchical fracturing can be produced by any replacement reaction with a positive volume change (Jamtveit et al., 2011; Jamtveit et al., 2009; Putnis, 2009; Røyne et al., 2008; Rudge et al., 2010). This aspect of other reactions that produce a positive volume change is missing in the study of oxidative induced biotite weathering of Goodfellow et al. (2016). Therefore I come to the different conclusion that the process of positive volume change induced weathering is a ubiquitous process operating in many different settings and is independent on regolith thickness and climate.

Furthermore, these observations of rocks overall weatherability above fit well with classifications of rocks were the resistance of rock to such fracture processes as described above are considered and *e.g.* tabulated in Hoek and Brown (1997). Similar to the calculation of the oxidational induced fracturing in section 4.4.1, stress-induced strain must overcome a critical point to fracture the rock, independently of the mechanism behind (oxidation, hierarchical fracturing during replacement, etc.). Hoek and Brown (1997) postulated that the effective tensile strength at failure for a given lithology is dependent on two constants: the uniaxial compressive strain σ_{ci} and a constant m_i . Taken together these parameters are higher for granitic than for basaltic intact bedrock and for low fracture density bedrocks (Tables 1 and 2 in Hoek and Brown (1997)). Hence, higher tensile strain is needed the overcome the bedrocks strength and its failure criterion. This holds true also for tectonically induced fracture processes. Therefore, the rock weatherability is lower in such dense bedrock like the

charnockite in Sri Lanka, where many factors add together to provide a setting, where the only process that can produce fresh weatherable surfaces is the oxidation of the lowly contained biotite and pyroxene.

As calculated in section 4.3, oxidation of minerals itself might be relatively fast. However, in Sri Lanka connected porosity is nearly absent in the bedrock, hence reactants that drive a fracture weathering reaction must diffuse along grain boundaries to reach the reaction site. Furthermore, the strain produced by the reaction must reach the criterion threshold, to actually produce a fracture. Hence, if the positive volume change during any of the above mentioned weathering processes is low (either by a low rate or by low concentration of the reactant needed), or the strength of the bedrock is high, the production rate of fresh weatherable surfaces and pathways is low as well.

4.6.3 Profile properties of thick weathering profiles

In addition to the lithological control, another factor in explaining low rates stems from the coupling between the weathering zone advance rate and the O_2 concentration, which at depth is dependent on the regolith thickness (Buss et al., 2008) and on the type of transport of fluids permitted by the regolith, as shown in section 4.5 above. In thick tropical weathering profiles such as those encountered at Hakgala, weathering processes themselves can influence the type of fluid transport. Hydraulic conductivities K_s less than 0.08 cm/h were observed by Lohse and Dietrich (2005) to occur in lower parts of old soils (> 20 cm below the surface) where clay layers hinder the infiltration and shallow sub-surface flows are established. The old soils, mainly composed of kaolinite, and Fe- and Al-(hydr)oxides, show decreasing K_s with high clay contents (Lohse and Dietrich, 2005). Because the results presented in this study also reveal significant amounts of clay minerals and (non)crystalline Fe- and Al-(oxy)(hydr)oxides in the regolith, it is reasonable to infer low hydraulic conductivity throughout the profile at Hakgala. Moreover, overall mass transfer coefficients for Al and Fe ($\tau_{Al,\ Fe}$) are near zero (Hewawasam et al., 2013). Hence, many of the secondary minerals that precipitated from amorphous precursors remain in the profile rather than being dissolved. Therefore, they might maintain the low permeability at least in the lower part of the profile. However, these factors will simply dampen the feedback mechanisms between the profile surface and the weathering front (see discussion about the feedback model in section 4.5). Thus, I showed that even under thick weathering profiles weathering by oxidative induced positive volume change is connected to and controlled by processes at the surface. When a thick profile is present such as investigated at Hakgala, only mechanical disruption might form preferential pathways for fluids and O_2. Such processes are not active at Hakgala because of the absence of tectonically driven landscape rejuvenation (*e.g.,* von Blanckenburg et al. (2004)). The lack of local base level lowering by tectonic movements results in long-term stability of the drainage pattern, leading to low erosion rates (Edmond et al., 1995).

4.6.4 Climatic and biological controls

So far, only abiotic processes are considered in this study to explain low chemical weathering rates in this stable landscape. In addition to tectonic activity, the dense natural vegetation cover exerts a strong control over erosion rate (Istanbulluoglu, 2005; Kirkby, 1995; Vanacker et al., 2007a). During monsoon the soil surface is shielded from rain by the canopy, lowering the velocities of the drops and reducing rain-splash at the surface. Tree leaves also increase evapo-transpiration, thereby reducing the amount of rain that reaches the soil surface. Additionally, the roots of the plants stabilize the soil, decreasing mass movement (Gyssels et al., 2005). Therefore, erosion at the surface is reduced by the dense vegetation cover prevailing up to large-scale deforestation (Hewawasam et al., 2003).

Another biotic driver in weathering reactions are microbes or mycorrhizal hyphae (Bonneville et al., 2011; Bonneville et al., 2009; Gorbushina, 2007; Landeweert et al., 2001; Leake et al., 2008; Smits et al., 2005). In fact, the FIB measurements on plagioclase were driven by the question if the worm-like precipitates in and around them, as observed with the microprobe, may have their origin by biotic weathering. But since the weathering structures in the plagioclase feature planes and not a round worm like appearance in three dimensions, it is more likely that these precipitates rather formed along grain boundaries and intra mineral cracks than being the excretions of microbes or precipitates in tunnels after hyphae retreat. At this point, I would also like to note that I only considered supply of atmospheric O_2 from the surface of the profile. However, Kim et al. (2017) showed that there might be a fundamental source of O_2 by microbial activity in weathering profiles. This biotic supply of O_2 would weaken the strength of the O_2 dependent abiotic weathering feedback between the weathering front and the profile's surface.

Finally, the climate might have implications for under- and oversaturation of the pore fluids with respect to the dissolving minerals. In this case study from Sri Lanka, the weathering profile is exposed to two monsoon seasons, with high precipitation. During this time, outwash and renewal of the pore water occurs. In the remaining year, this pore water might not be exchanged, hence saturation with respect to the dissolving minerals can be reached. In regions with just one monsoon season and without active tectonics this process may be even enhanced. On the other hand, in settings with constant precipitation permanent renewal of the pore water might be present and the pore water stays under-saturated. During under-saturation dissolution of minerals proceed, while during saturation dissolution of minerals will cease.

The combination of all these effects stabilize the mobile layer and provide the conditions to accumulate a thick regolith that slows weathering at depth, until steady-state is reached and low rates of erosion and weathering front advance match. This results in the "soil-shielding" effect where the thick regolith acts as a protecting layer shielding the bedrock from weathering (Goddéris et al., 2008; Hartmann et al., 2014; Stallard, 1995). Although steady-state is actually observed at Hakgala, in settings where even deeper regolith might form the advance of the weathering front might be totally decoupled from erosion at the surface and

regolith might accumulate (Lebedeva et al., 2010). To conclude the findings and to put the entire discussion of section 4.6 in a bigger frame, in contrast to Bazilevskaya et al. (2013) and (2014) I showed that not the solute-transport properties but the mineralogical and bedrock chemical and physical properties exert a strong control on weathering rates and profile thicknesses. In addition, the initiation of weathering by oxidation or other positive volume change reactions is a universally applicable operating process independent of climatic regimes, lithologies and transport properties. Furthermore, by formulating the feedback mechanism dependent of the transport of O_2, I was able to connect processes at the erosional surface with processes at the weathering front in a natural setting at different scales: *in situ* oxidation (mineral scale); spheroidal weathering and disintegration into saprolite (profile scale); and formation of pathways and connected porosity in the bedrock in absence of tectonic activity (regional scale). This implicates that small scale processes are important to understand regional observations in weathering regimes.

5. Conclusions

From the observations at the Hakgala weathering profile in the Central Highlands of Sri Lanka I found that:

(1) The first process initiating weathering of low-porosity charnockite at 10m depth is oxidation of Fe(II)-bearing primary minerals. This reaction begins in the center of the "virtually unweathered" corestone in pyroxene and does not invoke any other significant chemical changes. *In situ* oxidation occurs at relatively fast rates of log J = -11 $mol_{min}/(m^2\ s)$, but occurs only locally along lattice defects. On the corestone-scale, by using Fe-redox measurements of bulk rock from the entire corestone, the oxidation rates are comparable to calculated dissolution rates log R = -13 $mol_{px}/(m^2\ s)$ and log R = -15 $mol_{bt}/(m^2\ s)$. Due to volume increase, this oxidation reaction leads to structural changes in pyroxene and biotite such as dislocations, stacking disorder and lattice spacings. Furthermore, volume-increase-related micro-cracking in the direct vicinity of the primary minerals can be observed. The micro-cracks allow percolation of reactive fluids, promoting further weathering reactions and the subsequent dissolution of plagioclase. At the scale of the corestone, this fracturing is responsible for larger fractures. These larger fractures may connect to each other and separate the corestone from spalled material, the concentric rindlets. In other words, the oxidation reaction is the driver for spheroidal weathering in the Hakgala weathering profile. Hence, oxidation of structural Fe(II) is indeed the rate limiting reaction during weathering as it produces fractures that serve as fresh weatherable surfaces and pathways for reactive fluids.

(2) Primary mineral dissolution is best described with a dissolution – re-precipitation process rather than with leached layer formation. This inference is made from sharp reaction fronts. In contrast, the *in situ* oxidation of structural Fe(II) in pyroxene and biotite is best described with an ion by ion dissolution process that leads to oxidated areas of limited spatial extent.

(3) During weathering further porosity is generated by oxidation-induced fracturing (due to a positive volume change) and by weathering of plagioclase to kaolinite (due to a negative volume change). This porosity allows increased access of reactive fluids, and dissolution of plagioclase is enhanced producing a narrow rindlet zone where bedrock is converted into saprolite. By considering the formation of porosity during weathering bedrock is converted isovolumetrically into saprolite.

(4) Weathering of primary minerals first leads to an amorphous precursor from which secondary clay minerals and crystalline oxides form. During initial stage, these

secondary minerals are poorly crystalline and of nm size. The finding of an amorphous precursor is important regarding the use of reactive transport models at the scale of soil columns, especially in terms of numerical parameters representing secondary phase solubilities and formation rates. The only exception is weathering of biotite to kaolinite where re-arrangement of the tetrahedra and octahedral structure leads to direct transformation. Hence, weathering reactions are most likely conservative with respect to certain minerals. Additional, during most reactions porosity is generated as the amorphous precursor exhibit high internal porosity and only minor amounts of nm-sized secondary clay minerals form. With respect to the secondary clay mineral formation the limiting factor is the availability of excess Al. Aluminum is mainly released by plagioclase dissolution. If it remains dissolved it is transported to the pyroxene and biotite reaction sites core-inwards. However, the availability and transport of such dissolved Al during incipient weathering is low and only low amounts of secondary clay minerals form within the corestone. With further ageing during ongoing weathering in the saprolite, significant amounts of secondary clay minerals (especially kaolinite, but also smectite and gibbsite) and Fe-oxides form, but also decomposition of one secondary clay mineral to another clay mineral or Fe-oxide occurs (smectite to kaolinite and goethite, gibbsite to kaolinite, kaolinite to gibbsite).

(5) The supply of O_2 acts as the main feedback mechanism and the consumption of O_2 at depth is coupled to the supply of atmospheric O_2, which in turn is controlled by erosion at the top of the profile. To recapitulate from section 4.5: at initial steady state the regolith has a certain thickness and a constant O_2 gradient throughout the regolith, with atmospheric O_2 concentration at the top of the profile and consumption of O_2 at the weathering front. An erosion event removes a layer of regolith at the surface, which pushes the system out of steady state. Re-equilibration of O_2 at the surface with the atmosphere results in an increase of O_2. As the transport properties of the regolith are not modified, the O_2 gradient throughout the regolith remains the same. The O_2 concentration at the weathering front increases, too. The increase of O_2 at the weathering front enhances the kinetics of oxidative weathering reactions, ensuing fracturing and downward propagation of the weathering front, resulting in regolith thickening. The system is back at steady state. The "speed" at which the downward propagation of the weathering front occurs after the erosion event, which reflects the "strength" of the feedback, is dependent on the type of transport prevailing in the regolith (advective *vs*. diffusive). While an advective transport component is likely present in the regolith and the corestone zones with significant porosity, in the pristine bedrock O_2 must be transported via grain boundary and intra-mineral diffusion to the reaction sites in pyroxene and biotite. The feedback mechanism is operating at different spatial scales (nm-scale: *in situ* oxidation and micro-fracturing; cm-scale: spheroidal weathering of the corestone), thus it connects processes at the surface with the different weathering features observed at depth: *in situ* oxidation that drives mineral dissolution and spheroidal weathering which converts bedrock to saprolite. Therefore, I conclude that O_2 supply is the rate-limiting factor for weathering advance, and this supply in turn is limited by the erosion rate.

(6) Returning to the questions raised in the introduction: low chemical weathering rates and stable saprolite profiles are promoted on lithologies with low porosity and a low concentration of Fe(II)-bearing primary minerals. Such lithology is prevalent at the Hakgala site in the form of high-grade metamorphosed charnockite. Furthermore, low chemical weathering rates are the result of (a) tectonically quiescent regions (like the Central Highlands of Sri Lanka), where the bedrock and the saprolite profile are not affected by tectonic activity and hence less preconditioned for preferential fluid pathways in form of fractures; (b) lithological parameters like low porosity, minor positive volume-producing mineral reactions and stable minerals with respect to weathering; and (c) regions of dense natural vegetation cover which decreases the amount of rainwater reaching the surface and stabilizes the surface with their roots with respect to erosion. Both influence the regolith transport properties on hill slopes in such a way that the weathering front propagation rate remains low.

6. References

Acker, J.G., Bricker, O.P., 1992. The influence of pH on biotite dissolution and alteration kinetics at low temperature. Geochimica et Cosmochimica Acta 56, 3073-3092.

Armstrong, J.T., 1995. CITZAF - A package of correction programs for the quantitative electron microbeam X-ray-analysis of thick polished materials, thin films, and particles. Microbeam Analyses 4, 177-200.

Bacon, A.R., Richter, D.d., Bierman, P.R., Rood, D.H., 2012. Coupling meteoric 10Be with pedogenic losses of 9Be to improve soil residence time estimates on an ancient North American interfluve. Geology 40, 847-850.

Balan, E., 2006. First-principles study of the OH-stretching modes of gibbsite. American Mineralogist 91, 115-119.

Bandstra, J.Z., Buss, H.L., Campen, R.K., Liermann, L.J., Moore, J., Hausrath, E.M., Navarre-Sitchler, A.K., Jang, J.-H., Brantley, S.L., 2008. Appendix: Compilation of Mineral Dissolution Rates, in: Brantley, S.L., Kubicki, J.D., White, A.F. (Eds.), Kinetics of Water-Rock Interaction. Springer, New York.

Banfield, J.F., Barker, W.W., 1994. Direct observation of reactant-product interfaces formed in natural weathering of exsolved, defective amphibole to smectite: Evidence for episodic, isovolumetric reactions involving structural inheritance. Geochimica et Cosmochimica Acta 58, 1419-1429.

Barreto, H.N., Varajão, C.A.C., Braucher, R., Bourlès, D.L., Salgado, A.A.R., Varajão, A.F.D.C., 2013. Denudation rates of the Southern Espinhaço Range, Minas Gerais, Brazil, determined by in situ-produced cosmogenic beryllium-10. Geomorphology 191, 1-13.

Bazilevskaya, E., Lebedeva, M., Pavich, M., Rother, G., Parkinson, D.Y., Cole, D., Brantley, S.L., 2013. Where fast weathering creates thin regolith and slow weathering creates thick regolith. Earth Surface Processes and Landforms 38, 847-858.

Bazilevskaya, E., Rother, G., Mildner, D.F.R., Pavich, M., Cole, D., Bhatt, M.P., Jin, L., Steefel, C.I., Brantley, S.L., 2014. How Oxidation and Dissolution in Diabase and Granite Control Porosity during Weathering. Soil Science Society of America Journal 79, 55.

Behrens, R., Bouchez, J., Schuessler, J.A., Dultz, S., Hewawasam, T., von Blanckenburg, F., 2015. Mineralogical transformations set slow weathering rates in low-porosity metamorphic bedrock on mountain slopes in a tropical climate. Chemical Geology 411, 283-298.

Belmont, P., Pazzaglia, F.J., Gosse, J.C., 2007. Cosmogenic 10Be as a tracer for hillslope and channel sediment dynamics in the Clearwater River, western Washington State. Earth and Planetary Science Letters 264, 123-135.

Bierman, P.R., Caffee, M., 2001. Slow rates of rock surface erosion and sediment production across the Namib Desert and escarpment, South Africa. American Journal of Science 301, 326-358.

Bierman, P.R., Clapp, E.M., Nichols, K.K., Gillespie, A.R., Caffee, M., 2001. Using cosmogenic nuclide measurements in sediments to understand background rates of erosion and sediment transport, in: Harmon, R.S., Doe, W.M. (Eds.), Landscape Erosion and Evolution Modelling. Kluwer,, New York, pp. 89-116.

Bierman, P.R., Nichols, K.K., Matmon, A., Enzel, Y., Larsen, J., Finkel, R., 2007. 10-Be shows that Namibian drainge basins are slowly, steadily and uniformly eroding. Quaternary International 167-168, 33.

Bonneville, S., Bray, A.W., Benning, L.G., 2016. Structural Fe(II) Oxidation in Biotite by an Ectomycorrhizal Fungi Drives Mechanical Forcing. Environmental science & technology 50, 5589-5596.

Bonneville, S., Morgan, D.J., Schmalenberger, A., Bray, A., Brown, A., Banwart, S.A., Benning, L.G., 2011. Tree-mycorrhiza symbiosis accelerate mineral weathering: Evidences from nanometer-scale elemental fluxes at the hypha–mineral interface. Geochimica et Cosmochimica Acta 75, 6988-7005.

Bonneville, S., Smits, M.M., Brown, A., Harrington, J., Leake, J.R., Brydson, R., Benning, L.G., 2009. Plant-driven fungal weathering: Early stages of mineral alteration at the nanometer scale. Geology 37, 615-618.

Brady, N.C., Weil, R.R., 2007. The nature and properties of soils. 14th ed. Prentice Hall, Upper Saddle River, New Jersey, USA.

Brantley, S.L., Bandstra, J., Moore, J., White, A.F., 2008. Modelling chemical depletion profiles in regolith. Geoderma 145, 494-504.

Brantley, S.L., Chen, Y., 1995. Chemical weathering rates of pyroxenes and amphiboles. Reviews in Mineralogy and Geochemistry 31, 119-172.

Brantley, S.L., Lebedeva, M., 2011. Learning to Read the Chemistry of Regolith to Understand the Critical Zone. Annual Review of Earth and Planetary Sciences 39, 387-416.

Brantley, S.L., Lebedeva, M.I., Balashov, V.N., Singha, K., Sullivan, P.L., Stinchcomb, G., 2017. Toward a conceptual model relating chemical reaction fronts to water flow paths in hills. Geomorphology 277, 100-117.

Braun, J.-J., Descloitres, M., Riotte, J., Fleury, S., Barbiéro, L., Boeglin, J.-L., Violette, A., Lacarce, E., Ruiz, L., Sekhar, M., Mohan Kumar, M.S., Subramanian, S., Dupré, B., 2009. Regolith mass balance inferred from combined mineralogical, geochemical and geophysical studies: Mule Hole gneissic watershed, South India. Geochimica et Cosmochimica Acta 73, 935-961.

Braun, J.-J., Marechal, J.-C., Riotte, J., Boeglin, J.-L., Bedimo Bedimo, J.-P., Ndam Ngoupayou, J.R., Nyeck, B., Robain, H., Sekhar, M., Audry, S., Viers, J., 2012. Elemental weathering fluxes and saprolite production rate in a Central African lateritic terrain (Nsimi, South Cameroon). Geochimica et Cosmochimica Acta 99, 243-270.

Braun, J.-J., Ngoupayou, J.R.N., Viers, J., Dupre, B., Bedimo Bedimo, J.-P., Boeglin, J.-L., Robain, H., Nyeck, B., Freydier, R., Nkamdjou, L.S., Rouiller, J., Muller, J.-P., 2005. Present weathering rates in a humid tropical watershed: Nsimi, South Cameroon. Geochimica et Cosmochimica Acta 69, 357-387.

Bray, A.W., Benning, L.G., Bonneville, S., Oelkers, E.H., 2014. Biotite surface chemistry as a function of aqueous fluid composition. Geochimica et Cosmochimica Acta 128, 58-70.

Brimhall, G.H., Dietrich, W.E., 1987. Constitutive mass balance relations between chemical composition, volume, density, porosity, and strain in metasomatic hydrochemical systems: Results on weathering and pedogenesis. Geochimica et Cosmochimica Acta 51, 567-587.

Brunauer, S., Emmett, P.H., Teller, E., 1938. Adsorption of Gases in Multimolecular Layers. Journal of the American Chemical Society 60, 309-319.

Buss, H.L., Sak, P.B., Webb, S.M., Brantley, S.L., 2008. Weathering of the Rio Blanco quartz diorite, Luquillo Mountains, Puerto Rico: Coupling oxidation, dissolution, and fracturing. Geochimica et Cosmochimica Acta 72, 4488-4507.

Carson, M.A., Kirkby, M.J., 1972. Hillslope form and process. Cambridge University Press, , New York.

Chadwick, O.A., Chorover, J., 2001. The chemistry of pedogenic thresholds. Geoderma 100, 321-353.

Chardon, E.S., Livens, F.R., Vaughan, D.J., 2006. Reactions of feldspar surfaces with aqueous solutions. Earth-Science Reviews 78, 1-26.

Cherem, L.F.S., Varajão, C.A.C., Braucher, R., Bourlés, D., Salgado, A.A.R., Varajão, A.C., 2012. Long-term evolution of denudational escarpments in southeastern Brazil. Geomorphology 173-174, 118-127.

Clarke, B.A., Burbank, D.W., 2011. Quantifying bedrock-fracture patterns within the shallow subsurface: Implications for rock mass strength, bedrock landslides, and erodibility. Journal of Geophysical Research 116.

Colin, F., Nahon, D., Trescases, J.J., Melfi, A.J., 1990. Lateritic Weathering of Pyroxenites at Niquelandia, Goias, Brazil: The Supergene behavior of Nickel. Econommic Geology 85, 1010-1023.

Cox, R., Bierman, P., Jungers, Matthew C., Rakotondrazafy, A.F.M., 2009. Erosion Rates and Sediment Sources in Madagascar Inferred from10Be Analysis of Lavaka, Slope, and River Sediment. The Journal of Geology 117, 363-376.

Dadson, S.J., Hovius, N., Chen, H., Dade, B.W., Hsieh, M.-L., Willett, S.D., Hu, J.-C., Horng, M.-J., Chen, M.-C., Stark, C.P., Lague, D., Lin, J.-C., 2003. Links between erosion, runoff variability and seismicity in the Taiwan orogen. Nature 426, 648-651.

Dahlgren, R.A., Boettinger, J.L., Huntington, G.L., Amundson, R.G., 1997. Soil development along an elevational transect in the western Sierra Nevada, California. Geoderma 78, 207-236.

Das, A., Krishnaswami, S., 2007. Elemental geochemistry of river sediments from the Deccan Traps, India: Implications to sources of elements and their mobility during basalt–water interaction. Chemical Geology 242, 232-254.

Daval, D., Hellmann, R., Corvisier, J., Tisserand, D., Martinez, I., Guyot, F., 2010. Dissolution kinetics of diopside as a function of solution saturation state: Macroscopic measurements and implications for modeling of geological storage of CO2. Geochimica et Cosmochimica Acta 74, 2615-2633.

Daval, D., Hellmann, R., Saldi, G.D., Wirth, R., Knauss, K.G., 2013. Linking nm-scale measurements of the anisotropy of silicate surface reactivity to macroscopic dissolution rate laws: New insights based on diopside. Geochimica et Cosmochimica Acta 107, 121-134.

Delvigne, J., 1983. Micromorphology of the alteration and weathering of pyroxenes in the Koua Bocca ultramafic intrusion, Ivory Coast, Western Africa. Sci. Géol., Mém. 72, 57-68.

Dequincey, O., Chabaux, F., Clauer, N., Liewig, N., Muller, J., 1999. Dating of weathering profiles by radioactive disequilibria: contribution of the study of authigenic mineral fractions. Comptes Rendus de l'Academie des Sciences Series IIA Earth and Planetary Science 328, 679-685.

Dessert, C., Lajeunesse, E., Lloret, E., Clergue, C., Crispi, O., Gorge, C., Quidelleur, X., 2015. Controls on chemical weathering on a mountainous volcanic tropical island: Guadeloupe (French West Indies). Geochimica et Cosmochimica Acta.

DiBiase, R.A., Whipple, K.X., Heimsath, A.M., Ouimet, W.B., 2010. Landscape form and millennial erosion rates in the San Gabriel Mountains, CA. Earth and Planetary Science Letters 289, 134-144.

Dixon, J.L., von Blanckenburg, F., 2012. Soils as pacemakers and limiters of global silicate weathering. Comptes Rendus Geoscience 344, 597-609.

Dong, H., Peacor, D.R., Murphy, S.F., 1998. TEM study of progressive alteration of igneous biotite to kaolinite throughout a weathered soil profile. Geochimica et Cosmochimica Acta 62, 1881-1887.

Edmond, J.M., Palmer, M.R., Measures, C.I., Grant, B., Stallard, R.F., 1995. The fluvial geochemistry and denudation rate of the Guyana Shield in Venezuela, Colombia, and Brazil. Geochimica et Cosmochimica Acta 59, 3301-3325.

Evangelakakis, C., Kroll, H., Voll, G., Wenk, H.-R., Meisheng, H., Köpcke, J., 1993. Low-temperature coherent exsolution in alkali feldspar from high-grade metamorphic rocks in Sri Lanka. Contributions to Mineralogy and Petrology 114, 519-532.

Finnegan, N.J., Hallet, B., Montgomery, D.R., Zeitler, P.K., Stone, J.O., Anders, A.M., Yuping, L., 2008. Coupling of rock uplift and river incision in the Namche Barwa-Gyala Peri massif, Tibet. Geological Society of America Bulletin 120, 142-155.

Fletcher, R., Buss, H., Brantley, S., 2006. A spheroidal weathering model coupling porewater chemistry to soil thicknesses during steady-state denudation. Earth and Planetary Science Letters 244, 444-457.

Gaillardet, J., Dupré, B., Allègre, C.J., 1995. A global geochemical mass budget applied to the Congo Basin rivers: Erosion rates and continental crust composition. Geochmica et Cosmochimica Acta 59, 3469-3485.

Gaillardet, J., Dupré, B., Allègre, C.J., Négrel, P., 1997. Chemical and physical denudation in the Amazon River Basin. Chemical Geology 142, 141-173.

Godard, V., Lavé, J., Carcaillet, J., Cattin, R., Bourlès, D., Zhu, J., 2010. Spatial distribution of denudation in Eastern Tibet and regressive erosion of plateau margins. Tectonophysics 491, 253-274.

Goddéris, Y., Donnadieu, Y., Tombozafy, M., Dessert, C., 2008. Shield effect on continental weathering: Implication for climatic evolution of the Earth at the geological timescale. Geoderma 145, 439-448.

Goddéris, Y., François, L.M., Probst, A., Schott, J., Moncoulon, D., Labat, D., Viville, D., 2006. Modelling weathering processes at the catchment scale: The WITCH numerical model. Geochimica et Cosmochimica Acta 70, 1128-1147.

Goodfellow, B.W., Hilley, G.E., Webb, S.M., Sklar, L.S., Moon, S., Olson, C.A., 2016. The chemical, mechanical, and hydrological evolution of weathering granitoid. J. Geophys. Res. Earth Surf. 121, 1410–1435.

Gorbushina, A.A., 2007. Life on the rocks. Environmental microbiology 9, 1613-1631.

Gunnell, Y., Louchet, A., 2000. The influence of rock hardness and divergent weathering on the interpretation of apatite fission-track denudation rates. Evidence from charnockites in South India and Sri Lanka. Zeitschrift Geomorphologie N. F. 44, 33-57.

Gustafsson, J.P., Bhattacharya, P., Karltun, E., 1999. Mineralogy of poorly crystalline aluminum phases in the B horizon of Podzols in southern Sweden. Applied Geochemistry 14, 707-718.

Gyssels, G., Poesen, J., Bochet, E., Li, Y., 2005. Impact of plant roots on the resistance of soils to erosion by water: a review. Progress in Physical Geography 29, 189-217.

Hancock, G., Kirwan, M., 2007. Summit erosion rates deduced from 10Be: Implications for relief production in the central Appalachians. Geology 35, 89–92.

Harlov, D.E., Förster, H.-J., 2003. Fluid-induced nucleation of (Y+REE)-phosphate minerals within apatite: Nature and experiment. Part II. Fluorapatite. American Mineralogist 88, 1209-1229.

Harlov, D.E., Wirth, R., Förster, H.-J., 2005. An experimental study of dissolution–reprecipitation in fluorapatite: fluid infiltration and the formation of monazite. Contributions to Mineralogy and Petrology 150, 268-286.

Hartmann, J., Moosdorf, N., Lauerwald, R., Hinderer, M., West, A.J., 2014. Global chemical weathering and associated P-release — The role of lithology, temperature and soil properties. Chemical Geology 363, 145-163.

Heidbach, O., Rajabi, M., Reiter, K., Ziegler, M., Team, W., 2016. World Stress Map Database Release 2016. GFZ Data Services.

Heimsath, A.M., Dietrich, W.E., Nishiizumi, K., Finkel, R.C., 1997. The soil production function and landscape equilibrium. Nature 388, 358-361.

Heimsath, A.M., Dietrich, W.E., Nishiizumi, K., Finkel, R.C., 2001. Stochastic processes of soil production and transport; erosion rates, topographic variation and cosmogenic nuclides in the Oregon Coast Range. Earth Surface Processes and Landforms 26, 531–552.

Heimsath, A.M., Fink, D., Hancock, G.R., 2009. The 'humped' soil production function: eroding Arnhem Land, Australia. Earth Surface Processes and Landforms 34, 1674-1684.

Hellmann, R., Cotte, S., Cadel, E., Malladi, S., Karlsson, L.S., Lozano-Perez, S., Cabie, M., Seyeux, A., 2015. Nanometre-scale evidence for interfacial dissolution-reprecipitation control of silicate glass corrosion. Nature materials 14, 307-311.

Hellmann, R., Wirth, R., Daval, D., Barnes, J.-P., Penisson, J.-M., Tisserand, D., Epicier, T., Florin, B., Hervig, R.L., 2012. Unifying natural and laboratory chemical weathering with interfacial dissolution–reprecipitation: A study based on the nanometer-scale chemistry of fluid–silicate interfaces. Chemical Geology 294-295, 203-216.

Henchiri, S., Gaillardet, J., Dellinger, M., Bouchez, J., Spencer, R.G.M., 2016. Riverine dissolved lithium isotopic signatures in low-relief central Africa and their link to weathering regimes. Geophysical Research Letters 43, 4391-4399.

Hewawasam, T., von Blanckenburg, F., Bouchez, J., Dixon, J.L., Schuessler, J.A., Maekeler, R., 2013. Slow advance of the weathering front during deep, supply-limited saprolite formation in the tropical Highlands of Sri Lanka. Geochimica et Cosmochimica Acta 118, 202-230.

Hewawasam, T., von Blanckenburg, F., Schaller, M., Kubik, P., 2003. Increase of human over natural ersosion rates in tropical highlands constrained by cosmogenic nuclides. Geology 31, 597-600.

Hilley, G.E., Chamberlain, C.P., Moon, S., Porder, S., Willett, S.D., 2010. Competition between erosion and reaction kinetics in controlling silicate-weathering rates. Earth and Planetary Science Letters 293, 191-199.

Hoek, E., Brown, E.T., 1997. Practical Estimates of Rock Mass Strength. Int. J. Rock Mech. Min. Sci. 34, 1165-I1186.

Hong, H., Churchman, G.J., Gu, Y., Yin, K., Wang, C., 2012. Kaolinite–smectite mixed-layer clays in the Jiujiang red soils and their climate significance. Geoderma 173-174, 75-83.

Hong, H., Li, Z., Xiao, P., 2009. Clay mineralogy along the laterite profile in Hubei, South China: mineral evolution and evidence for eolian origin. Clays and Clay Minerals 57, 602-615.

Insel, N., Ehlers, T.A., Schaller, M., Barnes, J.B., Tawackoli, S., Poulsen, C.J., 2010. Spatial and temporal variability in denudation across the Bolivian Andes from multiple geochronometers. Geomorphology 122, 65-77.

Istanbulluoglu, E., 2005. Vegetation-modulated landscape evolution: Effects of vegetation on landscape processes, drainage density, and topography. Journal of Geophysical Research 110, 1-19.

Jamtveit, B., Kobchenko, M., Austrheim, H., Malthe-Sørenssen, A., Røyne, A., Svensen, H., 2011. Porosity evolution and crystallization-driven fragmentation during weathering of andesite. Journal of Geophysical Research 116, 1-12.

Jamtveit, B., Putnis, C.V., Malthe-Sørenssen, A., 2009. Reaction induced fracturing during replacement processes. Contributions to Mineralogy and Petrology 157, 127-133.

Jin, L., Ravella, R., Ketchum, B., Bierman, P.R., Heaney, P., White, T., Brantley, S.L., 2010. Mineral weathering and elemental transport during hillslope evolution at the Susquehanna/Shale Hills Critical Zone Observatory. Geochimica et Cosmochimica Acta 74, 3669-3691.

Kalinowski, B.E., Schweda, P., 1996. Kinetics of muscovite, phlogopite, and biotite dissolution and alteration at pH 1-4, room temperature. Geochimica et Cosmochimica Acta 60, 367 385.

Kim, H., Stinchcomb, G., Brantley, S.L., 2017. Feedbacks among O2 and CO2 in deep soil gas, oxidation of ferrous minerals, and fractures: A hypothesis for steady-state regolith thickness. Earth and Planetary Science Letters 460, 29-40.

Kirchner, J.W., Finkel, R.C., Riebe, C.S., Granger, D.E., Clayton, J.L., King, J.G., Megahan, W.F., 2001. Mountain erosion over 10 yr, 10 k.y., and 10 m.y. time scales. Geology 29, 591–594;.

Kirkby, M., 1995. Modelling the links between vegetation and landforms. Geomorphology 13, 319-335.

Koch-Müller, M., Rhede, D., Schulz, R., Wirth, R., 2009. Breakdown of hydrous ringwoodite to pyroxene and spinelloid at high P and T and oxidizing conditions. Physics and Chemistry of Minerals 36, 329-341.

Kourkoumelis, N., 2013. PowDLL: A program for the interconversion of powder diffraction data files, University of Ioannina, Greece. http://users.uoi.gr/nkourkou/powdll/.

Kreemer, C., Holt, W.E., Haines, A.J., 2003. An integrated global model of present-day plate motions and plate boundary deformation. Geophys. J. Int. 154, 8-34.

Kruhl, J.H., Wirth, R., Morales, L.F.G., 2013. Quartz grain boundaries as fluid pathways in metamorphic rocks. Journal of Geophysical Research: Solid Earth 118, 1957-1967.

Lal, D., Harris, N.B.W., Sharma, K.K., Gu, Z., Ding, L., Liu, T., Dong, W., Caffee, M.W., Jull, A.J.T., 2003. Erosion history of the Tibetan Plateau since the last interglacial: constraints from the first studies of cosmogenic 10Be from Tibetan bedrock. Earth and Planetary Science Letters 217, 33-42.

Landeweert, R., Hoffland, E., Finlay, R.D., Kuyper, T.W., van Breemen, N., 2001. Linking plants to rocks: ectomycorrhizal fungi mobilize nutrients from minerals. Trends in Ecology & Evolution 16, 248-254.

Leake, J.R., Duran, A.L., Hardy, K.E., Johnson, I., Beerling, D.J., Banwart, S.A., Smits, M.M., 2008. Biological weathering in soil: the role of symbiotic root-associated fungi biosensing minerals and directing photosynthate-energy into grain-scale mineral weathering. Mineralogical Magazine 72, 85-89.

Lebedeva, M.I., Fletcher, R.C., Balashov, V.N., Brantley, S.L., 2007. A reactive diffusion model describing transformation of bedrock to saprolite. Chemical Geology 244, 624-645.

Lebedeva, M.I., Fletcher, R.C., Brantley, S.L., 2010. A mathematical model for steady-state regolith production at constant erosion rate. Earth Surface Processes and Landforms, 508-524.

Lee, M.R., Hodson, M.E., Parsons, I., 1998. The role of intragranular microtextures and microstructures in chemical mechanical weathering: Direct comparisons of experimentally and naturally weathered alkali feldspars. Geochimica et Cosmochimica Acta 62, 2771-2788.

Lee, M.R., Parsons, I., 1995. Microtextural controls of weathering of perthitic alkali feldspar. Geochimica et Cosmochimica Acta 59, 4465-4488.

Lohse, K.A., Dietrich, W.E., 2005. Contrasting effects of soil development on hydrological properties and flow paths. Water Resources Research 41, 1-17.

Louvat, P., Allègre, C.J., 1997. Present denudation rates on the island of R6union determined by river geochemistry: Basalt weathering and mass budget between chemical and mechanical erosions. Geochimica et Cosmochimica Acta 61, 3645-3669.

Ma, L., Chabaux, F., Pelt, E., Granet, M., Sak, P.B., Gaillardet, J., Lebedeva, M., Brantley, S.L., 2012. The effect of curvature on weathering rind formation: Evidence from Uranium-series isotopes in basaltic andesite weathering clasts in Guadeloupe. Geochimica et Cosmochimica Acta 80, 92-107.

Maher, K., Chamberlain, C.P., 2014. Hydrologic regulation of chemical weathering and the geologic carbon cycle. Science 343, 1502-1504.

Maher, K., Johnson, N.C., Jackson, A., Lammers, L.N., Torchinsky, A.B., Weaver, K.L., Bird, D.K., Brown, G.E., 2016. A spatially resolved surface kinetic model for forsterite dissolution. Geochimica et Cosmochimica Acta 174, 313-334.

Maher, K., Steefel, C.I., White, A.F., Stonestrom, D.A., 2009. The role of reaction affinity and secondary minerals in regulating chemical weathering rates at the Santa Cruz Soil Chronosequence, California. Geochimica et Cosmochimica Acta 73, 2804-2831.

Malmström, M., Banwart, S., 1997. Biotite dissolution at 25°C: The pH dependence of dissolution rate and stoichiometry. Geochimica et Cosmochimica Acta 61, 2779-2799.

Mayes, M.A., Jardine, P.M., Mehlhorn, T.L., Bjornstad, B.N., Ladd, J.L., Zachara, J.M., 2003. Transport of multiple tracers in variably saturated humid region structured soils and semi-arid region laminated sediments. Journal of Hydrology 275, 141-161.

Mehra, O.P., Jackson, M.L., 1960. Iron oxides removal from soils and clays by a dithionite-citrate system buffered with sodium bicarbonate. Clays and Clay Minerals, Proceedings of the 7th National Conference, 317-327.

Merino, E., Nahon, D., Wang, Y., 1993. Kinetics and mass transfer of pseudomorphic replacement: Application to replacement of parent minerals and kaolinite by Al, Fe, and Mn oxides during weathering. American Journal of Science 293, 135-155.

Millot, R., Vigier, N., Gaillardet, J., 2010. Behaviour of lithium and its isotopes during weathering in the Mackenzie Basin, Canada. Geochimica et Cosmochimica Acta 74, 3897-3912.

Molnar, P., Anderson, R.S., Anderson, S.P., 2007. Tectonics, fracturing of rock, and erosion. Journal of Geophysical Research 112.

Moore, D.M., Reynolds, R.C.J., 1997. X-Ray Diffraction and the Identification and Analysis of Clay Minerals, 2 ed. Oxford University Press, Inc., New York.

Moore, J., Lichtner, P.C., White, A.F., Brantley, S.L., 2012. Using a reactive transport model to elucidate differences between laboratory and field dissolution rates in regolith. Geochimica et Cosmochimica Acta 93, 235-261.

Mrosko, M., Lenz, S., McCammon, C.A., Taran, M., Wirth, R., Koch-Muller, M., 2013. Hydrogen incorporation and the oxidation state of iron in ringwoodite: A spectroscopic study. American Mineralogist 98, 629-636.

Murphy, S.F., Brantley, S.L., Blum, A.E., White, A.F., Dong, H., 1998. Chemical weathering in a tropical watershed, Luquillo Mountains, Puerto Rico: II. Rate and mechanism of biotite weathering. Geochimica et Cosmochimica Acta 62, 227-243.

Navarre-Sitchler, A., Steefel, C.I., Sak, P.B., Brantley, S.L., 2011. A reactive-transport model for weathering rind formation on basalt. Geochimica et Cosmochimica Acta 75, 7644-7667.

Navarre-Sitchler, A.K., Cole, D.R., Rother, G., Jin, L., Buss, H.L., Brantley, S.L., 2013. Porosity and surface area evolution during weathering of two igneous rocks. Geochimica et Cosmochimica Acta 109, 400-413.

Nesbitt, H.W., Fedo, C.M., Young, G.M., 1997. Quartz and Feldspar Stability, Steady and Non-steady-State Weathering, and Petrogenesis of Siliciclastic Sands and Muds. The Journal of Geology 105, 173–191.

Nichols, K.K., Bierman, P., Finkel, R., Larsen, J., 2005. Long-Term (10 to 20 kyr) Sediment Generation Rates for the Upper Rio Chagres Basin Based on Cosmogenic 10Be, in: Harmon, R.S. (Ed.), The Rio Chagres: A Multidisciplinary Profile of a Tropical Watershed. Kluwer Academic Publishers, New York.

Nichols, K.K., Bierman, P.R., Rood, D.H., 2014. 10Be constrains the sediment sources and sediment yields to the Great Barrier Reef from the tropical Barron River catchment, Queensland, Australia. Geomorphology 224, 102-110.

Nielsen, L.C., DePaolo, D.J., De Yoreo, J.J., 2012. Self-consistent ion-by-ion growth model for kinetic isotopic fractionation during calcite precipitation. Geochimica et Cosmochimica Acta 86, 166-181.

Noack, Y., Colin, F., Nahon, D., Delvigne, J., Michaux, L., 1993. Secondary-mineral formation during natural weathering of pyroxene: Review and thermodynamic approach. American Journal of Science 293, 111-134.

Norton, K.P., von Blanckenburg, F., DiBiase, R., Schlunegger, F., Kubik, P.W., 2011. Cosmogenic 10Be-derived denudation rates of the Eastern and Southern European Alps. International Journal of Earth Sciences 100, 1163-1179.

Norton, K.P., von Blanckenburg, F., Kubik, P.W., 2010. Cosmogenic nuclide-derived rates of diffusive and episodic erosion in the glacially sculpted upper Rhone Valley, Swiss Alps. Earth Surface Processes and Landforms 35, 651-662.

Norton, K.P., von Blanckenburg, F., Schlunegger, F., Schwab, M., Kubik, P.W., 2008. Cosmogenic nuclide-based investigation of spatial erosion and hillslope channel coupling in the transient foreland of the Swiss Alps. Geomorphology 95, 474-486.

Oelkers, E.H., Schott, J., 2001. An experimental study of enstatite dissolution rates as a function of pH, temperature, and aqueous Mg ans Si concentration, and the mechanism of pyroxene/pyroxenoid dissolution. Geochimica et Cosmochimica Acta 65, 1219-1231.

Palacio, L., Prádanos, P., Calvo, J.I., Hernández, A., 1999. Porosity measurements by a gas penetration method and other techniques applied to membrane characterization. Thin Solid Films 348, 22-29.

Parsons, I., Lee, M.R., 2009. Mutual replacement reactions in alkali feldspars I: microtextures and mechanisms. Contributions to Mineralogy and Petrology 157, 641-661.

Perg, L.A., Anderson, R.S., Finkel, R.C., 2003. Use of cosmogenic radionuclides as a sediment tracer in the Santa Cruz littoral cell, California, United States. Geology 31, 299–302.

Price, J.R., Heitmann, N., Hull, J., Szymanski, D., 2008. Long-term average mineral weathering rates from watershed geochemical mass balance methods: Using mineral modal abundances to solve more equations in more unknowns. Chemical Geology 254, 36-51.

Putnis, A., 2002. Mineral replacement reactions: from macroscopic observations to microscopic mechanisms. Mineralogical Magazine 66, 689-708.

Putnis, A., 2009. Mineral Replacement Reactions. Reviews in Mineralogy and Geochemistry 70, 87-124.

Putnis, A., Austrheim, H., 2010. Fluid-induced processes: metasomatism and metamorphism. Geofluids.

Reis, F.D.A.A., 2015. Modeling the growth of an altered layer in mineral weathering. Geochimica et Cosmochimica Acta 166, 298-311.

Rempe, D.M., Dietrich, W.E., 2014. A bottom-up control on fresh-bedrock topography under landscapes. PNAS 111, 6576-6581.

Riebe, C.S., Kirchner, J.W., Finkel, R.C., 2003. Long-term rates of chemical weathering and physical erosion from cosmogenic nuclides and geochemical mass balance. Geochimica et Cosmochimica Acta 67, 4411-4427.

Riebe, C.S., Kirchner, J.W., Granger, D.E., Finkel, R.C., 2001. Strong tectonic and weak climatic control of long-term chemical weathering rates. Geology 29, 511-514.

Robert, C., Kennett, J.P., 1994. Antartic subtropical humid episode at the Paleocene-Eocene boundary: Clay mineral evidence. Geology 22, 211-214.

Robie, R.A., Hemingway, B.S., 1995. Thermodynamic Properties of Minerals and Related Substances at 298.15 K and 1 Bar (10^5 Pascals) Pressure and at Higher Temperatures. U. S. Geological Survey Bulletin, Washington.

Roy, S., Gaillardet, J., Allègre, C.J., 1999. Geochemistry of dissolved and suspended loads of the Seine river, France: Anthropogenic impact, carbonate and silicate weathering. Geochimica et Cosmochimica Acta 63, 1277-1292.

Røyne, A., Jamtveit, B., Mathiesen, J., Malthe-Sørenssen, A., 2008. Controls on rock weathering rates by reaction-induced hierarchical fracturing. Earth and Planetary Science Letters 275, 364-369.

Rudge, J.F., Kelemen, P.B., Spiegelman, M., 2010. A simple model of reaction-induced cracking applied to serpentinization and carbonation of peridotite. Earth and Planetary Science Letters 291, 215-227.

Ruiz-Agudo, E., King, H.E., Patino-Lopez, L.D., Putnis, C.V., Geisler, T., Rodriguez-Navarro, C., Putnis, A., 2016. Control of silicate weathering by interface-coupled dissolution-precipitation processes at the mineral-solution interface. Geology 44, 567-570.

Ruiz-Agudo, E., Putnis, C.V., Putnis, A., 2014. Coupled dissolution and precipitation at mineral–fluid interfaces. Chemical Geology 383, 132-146.

Ruiz-Agudo, E., Putnis, C.V., Rodriguez-Navarro, C., Putnis, A., 2012. Mechanism of leached layer formation during chemical weathering of silicate minerals. Geology 40, 947-950.

Sak, P.B., Fisher, D.M., Gardner, T.W., Marshall, J.S., LaFemina, P.C., 2009. Rough crust subduction, forearc kinematics, and Quaternary uplift rates, Costa Rican segment of the Middle American Trench. Geological Society of America Bulletin 121, 992-1012.

Sak, P.B., Fisher, D.M., Gardner, T.W., Murphy, K., Brantley, S.L., 2004. Rates of weathering rind formation on Costa Rican basalt. Geochimica et Cosmochimica Acta 68, 1453-1472.

Sak, P.B., Navarre-Sitchler, A.K., Miller, C.E., Daniel, C.C., Gaillardet, J., Buss, H.L., Lebedeva, M.I., Brantley, S.L., 2010. Controls on rind thickness on basaltic andesite clasts weathering in Guadeloupe. Chemical Geology 276, 129-143.

Salgado, A.A.R., Marent, B.R., Cherem, L.F.S., Bourlès, D., Santos, L.J.C., Braucher, R., Barreto, H.N., 2014. Denudation and retreat of the Serra do Mar escarpment in southern Brazil derived from in situ-produced10Be concentration in river sediment. Earth Surface Processes and Landforms 39, 311-319.

Scherler, D., Bookhagen, B., Strecker, M.R., 2014. Tectonic control on10Be-derived erosion rates in the Garhwal Himalaya, India. Journal of Geophysical Research: Earth Surface 119, 83-105.

Schuessler, J.A., Botcharnikov, R.E., Behrens, H., Misiti, V., Freda, C., 2008. Oxidation state of iron in hydrous phono-tephritic melts. American Mineralogist 93, 1493-1504.

Schwertmann, U., 1964. Differenzierung der Eisenoxide des Bodens durch Extraktion mit Ammoniumoxaltat-Lösung. Zeitschrift für Pflanzenernährung, Düngung, Bodenkunde 105, 194-202.

Shelobolina, E., Xu, H., Konishi, H., Kukkadapu, R., Wu, T., Blothe, M., Roden, E., 2012. Microbial lithotrophic oxidation of structural Fe(II) in biotite. Applied and environmental microbiology 78, 5746-5752.

Smits, M.M., Hoffland, E., Jongmans, A.G., van Breemen, N., 2005. Contribution of mineral tunneling to total feldspar weathering. Geoderma 125, 59-69.

Sosa Gonzalez, V., Bierman, P.R., Nichols, K.K., Rood, D.H., 2016. Long-term erosion rates of Panamanian drainage basins determined using in situ 10Be. Geomorphology 275, 1-15.

Stack, A.G., Raiteri, P., Gale, J.D., 2012. Accurate rates of the complex mechanisms for growth and dissolution of minerals using a combination of rare-event theories. J Am Chem Soc 134, 11-14.

Stallard, R.F., 1995. Tectonic, Environmental, and Human Aspects of Weathering and Erosion: A Global Review using a Steady-State Perspective. Annu. Rev. Earth Planet. Sci 23, 11-39.

Steefel, C.I., van Cappellen, P., 1990. A new kinetc approach to modeling water-rock interaction: The role of nucleation, precursors, and Ostwald ripening. Geochimica et Cosmochimica Acta 54, 2657-2677.

Taylor, A.S., Blum, J.D., Lasaga, A.C., McInnis, I.N., 2000. Kinetics of dissolution and Sr release during biotite and phlogopite weathering. Geochimica et Cosmochimica Acta 64, 1191-1208.

Turpault, M.-P., Trotignon, L., 1994. The dissolution of biotite single crystals in dilute HNO3 at 24°C: Evidence of an anisotropic corrosion process of micas in acidic solutions. Geochimica et Cosmochimica Acta 58, 2761-2775.

van Aken, P.A., Liebscher, B., 2002. Quantification of ferrous/ferric ratios in minerals: new evaluation schemes of Fe L2,3 electron energy-loss near-edge spectra.

van Aken, P.A., Liebscher, B., Styrsa, V.J., 1998. Quantitative determination of iton oxidation states in minerals using Fe L2,3-edge electron energy-loss near-edge structure spectroscopy. Phys Chem Minerals 25, 323-327.

van der Marel, H.W., Beutelspacher, H., 1976. Atlas of Infrared Spectroscopy of Clay Minerals and their Admixtures. Elsevier Scientific Publishing Company.

Vanacker, V., von Blanckenburg, F., Govers, G., Molina, A., Poesen, J., Deckers, J., Kubik, P., 2007a. Restoring dense vegetation can slow mountain erosion to near natural benchmark levels. Geology 35, 303-306.

Vanacker, V., von Blanckenburg, F., Hewawasam, T., Kubik, P.W., 2007b. Constraining landscape development of the Sri Lankan escarpment with cosmogenic nuclides in river sediment. Earth and Planetary Science Letters 253, 402-414.

Vance, D., Bickle, M., Ivy-Ochs, S., Kubik, P.W., 2003. Erosion and exhumation in the Himalaya from cosmogenic isotope inventories of river sediments. Earth and Planetary Science Letters 206, 273-288.

Velbel, M.A., 1993. Formation of protectiye surface layers during silicate-mineral weathering under well-leached, oxidizing conditions. American Mineralogist 78, 405-414.

Velbel, M.A., Barker, W.W., 2008. Pyroxene Weathering to Smectite: Conventional and Cryo-Field Emission Scanning Electron Microscopy, Koua Bocca Ultramafic Complex, Ivory Coast. Clays and Clay Minerals 56, 112-127.

von Blanckenburg, F., Hewawasam, T., Kubik, P.W., 2004. Cosmogenic nuclide evidence for low weathering and denudation in the wet, tropical highlands of Sri Lanka. Journal of Geophysical Research 109, 1-22.

Watkins, J.M., Nielsen, L.C., Ryerson, F.J., DePaolo, D.J., 2013. The influence of kinetics on the oxygen isotope composition of calcium carbonate. Earth and Planetary Science Letters 375, 349-360.

West, A., Galy, A., Bickle, M., 2005. Tectonic and climatic controls on silicate weathering. Earth and Planetary Science Letters 235, 211-228.

White, A.F., 2002. Determining mineral weathering rates based on solid and solute weathering gradients and velocities: application to biotite weathering in saprolites. Chemical Geology 190, 69-89.

White, A.F., Brantley, S.L., 2003. The effect of time on the weathering of silicate minerals: why do weathering rates differ in the laboratory and field? Chemical Geology 202, 479-506.

Wilson, M.J., 2004. Weathering of the primary rock-forming minerals: processes, products and rates. Clay Minerals 39, 233-266.

Wirth, R., 2004. Focused Ion Beam (FIB): A novel technology for advanced application of micro- and nanoanalysis in geosciences and applied mineralogy. European Journal of Mineralogy 16, 863-876.

Wirth, R., 2009. Focused Ion Beam (FIB) combined with SEM and TEM: Advanced analytical tools for studies of chemical composition, microstructure and crystal structure in geomaterials on a nanometre scale. Chemical Geology 261, 217-229.

Wirth, R., Morales, L.F., 2012. Combined FIB-SEM Techniques: Advanced tools to resolve microstructures and mineral phases in sedimentary rocks, in: Sylvester, P. (Ed.), Quantitative Mineralogy and Microanalysis of Sediments and Sedimentary Rocks. Mineralogical Association of Canada, pp. 17-34.

Wittmann, H., von Blanckenburg, F., Guyot, J.L., Maurice, L., Kubik, P.W., 2009. From source to sink: Preserving the cosmogenic 10Be-derived denudation rate signal of the Bolivian Andes in sediment of the Beni and Mamoré foreland basins. Earth and Planetary Science Letters 288, 463-474.

Wittmann, H., von Blanckenburg, F., Kruesmann, T., Norton, K.P., Kubik, P.W., 2007. Relation between rock uplift and denudation from cosmogenic nuclides in river sediment in the Central Alps of Switzerland. Journal of Geophysical Research 112.

Yesavage, T., Stinchcomb, G.E., Fantle, M.S., Sak, P.B., Kasznel, A., Brantley, S.L., 2016. Investigation of a diabase-derived regolith profile from Pennsylvania: Mineralogy, chemistry and Fe isotope fractionation. Geoderma 273, 83-97.

Appendix

Appendix A: Electron microprobe analyses

Table A1. Plagioclase

Element-oxides in weight %, n = 48

Comment	Na_2O	FeO	K_2O	Al_2O_3	CaO	SiO_2	MnO	TiO_2	Total
test	8.53	0.06	0.25	24.14	5.41	61.62	0.00	0.00	100.01
Sample-1-Z1	8.41	0.04	0.36	23.46	5.18	61.62	0.00	0.03	99.10
Sample-1-Z1	8.51	0.05	0.33	23.45	5.21	61.22	0.02	0.06	98.86
Sample-1-Z1	8.34	0.03	0.24	23.54	5.34	61.75	0.01	0.00	99.25
Sample-1-Z1	8.30	0.19	0.28	23.44	5.36	61.59	0.02	0.02	99.19
Sample-1-Z1	8.55	0.03	0.29	23.44	5.23	62.07	0.00	0.00	99.61
Sample-1-Z1	8.46	0.04	0.28	23.55	5.20	62.07	0.01	0.00	99.61
Sample-1-Z1	8.49	0.05	0.26	23.79	5.31	62.00	0.00	0.00	99.90
Sample-1-Z1	8.47	0.06	0.24	23.53	5.28	61.71	0.01	0.02	99.32
Sample-1-Z1	8.53	0.02	0.20	23.65	5.26	61.71	0.01	0.00	99.38
Sample-1-Z1	8.40	0.23	0.20	23.49	5.35	61.77	0.01	0.05	99.50
Sample-1-Z1	8.49	0.06	0.25	23.85	5.28	61.97	0.02	0.00	99.93
Sample-1-Z1	8.37	0.04	0.31	23.34	5.25	61.89	0.00	0.03	99.23
Sample-1-Z1	8.54	0.17	0.33	23.53	5.20	62.21	0.00	0.00	99.98
Sample-2-Z2	8.46	0.06	0.21	23.70	5.32	62.02	0.03	0.00	99.80
Sample-2-Z2	8.66	0.04	0.24	23.61	5.24	62.05	0.00	0.00	99.83
Sample-2-Z2	8.56	0.04	0.28	23.71	5.25	61.79	0.02	0.00	99.65
Sample-2-Z2	8.71	0.05	0.22	23.79	5.28	61.90	0.00	0.02	99.98
Sample-2-Z2	8.66	0.04	0.30	23.72	5.18	62.01	0.00	0.00	99.91
Sample-2-Z2	8.55	0.04	0.26	23.63	5.29	61.75	0.01	0.02	99.55
Sample-2-Z2	8.43	0.07	0.24	23.49	5.23	61.97	0.01	0.02	99.46
Sample-2-Z2	8.64	0.08	0.22	23.64	5.23	62.19	0.00	0.01	100.01
Sample-2-Z2	8.55	0.04	0.23	23.61	5.23	61.22	0.00	0.01	98.88
Sample-2-Z2	8.46	0.04	0.21	23.58	5.26	61.08	0.00	0.00	98.63
Sample-3	8.55	0.02	0.28	23.85	5.26	62.16	0.00	0.00	100.11
Sample-3-Z3	8.30	0.09	0.22	23.92	5.44	61.72	0.00	0.03	99.73
Sample-3-Z3	8.29	0.09	0.27	23.75	5.38	61.80	0.02	0.00	99.60
Sample-3-Z3	8.43	0.15	0.22	23.77	5.41	61.66	0.02	0.05	99.70
Sample-3-Z3	8.43	0.01	0.33	23.85	5.21	62.19	0.00	0.03	100.06

Sample-3-Z3	8.52	0.03	0.30	23.63	5.26	61.97	0.01	0.03	99.74
Sample-3-Z3	8.56	0.06	0.35	23.66	5.30	61.91	0.01	0.03	99.87
Sample-3-Z3	8.48	0.06	0.22	23.92	5.36	62.03	0.01	0.03	100.11
Sample-3-Z3	8.40	0.06	0.26	24.00	5.37	62.03	0.00	0.00	100.11
Sample-3-Z3	8.54	0.07	0.31	23.71	5.24	61.94	0.00	0.00	99.81
Sample-3-Z3	8.74	0.01	0.22	23.77	5.31	61.46	0.00	0.00	99.51
Sample-3-Z3	8.63	0.04	0.27	23.93	5.24	61.98	0.00	0.00	100.09
Sample-3-Z3	8.64	0.04	0.25	23.57	5.27	61.99	0.00	0.01	99.77
Sample-3-Z4	8.52	0.02	0.30	23.75	5.20	61.22	0.00	0.00	99.01
Sample-3-Z4	8.45	0.04	0.30	23.73	5.14	61.07	0.00	0.00	98.74
Sample-3-Z4	8.62	0.07	0.19	23.84	5.22	60.99	0.00	0.01	98.94
Sample-3-Z4	8.71	0.06	0.22	23.92	5.21	61.45	0.00	0.04	99.60
Sample-3-Z4	8.75	0.04	0.27	23.84	5.15	61.33	0.00	0.01	99.38
Sample-5-Z4c	8.50	0.04	0.39	23.63	5.20	61.22	0.02	0.01	99.01
Sample-5-Z4c	8.38	0.06	0.39	23.53	5.15	60.99	0.01	0.01	98.51
Sample-5-Z4c	8.37	0.06	0.36	23.57	5.14	61.38	0.00	0.00	98.88
Sample-5-Z4c	8.54	0.03	0.35	23.49	5.21	60.93	0.00	0.00	98.55
Sample-5-Z4c	8.41	0.06	0.34	23.78	5.33	60.47	0.02	0.05	98.45
Sample-5-Z4c	8.67	0.06	0.27	23.54	5.20	60.41	0.00	0.03	98.18

Table A2. K-Feldspar

Element-oxides in weight %, n = 53

Comment	Na_2O	FeO	K_2O	Al_2O_3	CaO	SiO_2	MnO	TiO_2	Total
test	1.45	0.03	14.47	18.88	0.06	64.40	0.00	0.00	99.29
Sample-1-Z1	1.77	0.19	13.99	18.51	0.09	64.46	0.02	0.00	99.03
Sample-1-Z1	1.85	0.04	13.86	18.72	0.08	64.75	0.01	0.00	99.31
Sample-1-Z1	1.40	0.02	14.35	18.50	0.04	64.40	0.01	0.00	98.73
Sample-1-Z1	1.81	0.01	13.68	18.58	0.04	64.88	0.00	0.02	99.03
Sample-1-Z1	1.82	0.08	13.92	18.51	0.05	64.80	0.00	0.00	99.18
Sample-1-Z1	1.66	0.02	13.98	18.67	0.10	64.57	0.00	0.00	99.00
Sample-1-Z1	1.70	0.01	14.05	18.43	0.05	64.40	0.01	0.00	98.65
Sample-1-Z1	1.50	0.00	14.12	18.62	0.06	64.51	0.00	0.00	98.81
Sample-1-Z1	1.48	0.17	14.22	18.37	0.05	64.39	0.00	0.00	98.68
Sample-1-Z1	1.58	0.01	14.30	18.53	0.03	64.52	0.00	0.00	98.97
Sample-1-Z1	1.61	0.01	14.38	18.53	0.02	64.71	0.01	0.00	99.28
Sample-1-Z1	1.64	0.03	14.13	18.50	0.03	64.62	0.00	0.00	98.96
Sample-1-Z1	1.63	0.04	14.14	18.66	0.07	64.34	0.00	0.00	98.88
Sample-1-Z1	1.58	0.00	14.08	18.56	0.06	64.49	0.00	0.00	98.77
Sample-1-Z1	1.48	0.03	14.36	18.51	0.02	64.67	0.00	0.00	99.07
Sample-1-Z1	1.53	0.01	14.47	18.62	0.05	64.29	0.00	0.00	98.97
Sample-2-Z2	1.97	0.00	13.78	18.67	0.05	64.37	0.00	0.00	98.84
Sample-2-Z2	1.75	0.04	13.97	18.60	0.05	64.33	0.00	0.00	98.74
Sample-2-Z2	1.81	0.01	13.96	18.72	0.07	64.67	0.00	0.00	99.24
Sample-2-Z2	1.83	0.00	13.75	18.54	0.07	64.52	0.00	0.07	98.78
Sample-2-Z2	1.76	0.01	13.90	18.70	0.09	64.38	0.00	0.00	98.84
Sample-2-Z2	2.03	0.01	13.51	18.83	0.13	64.50	0.00	0.00	99.01
Sample-2-Z2	1.82	0.03	13.93	18.66	0.06	64.32	0.00	0.00	98.82
Sample-2-Z2	1.73	0.00	13.92	18.55	0.07	64.74	0.02	0.00	99.03
Sample-2-Z2	1.82	0.00	13.80	18.61	0.09	64.61	0.00	0.00	98.93
Sample-2-Z2	1.77	0.00	13.95	18.63	0.05	64.71	0.01	0.00	99.13
Sample-2-Z2	1.28	0.03	14.54	18.51	0.01	64.40	0.00	0.00	98.77
Sample-3	1.34	0.11	14.39	18.81	0.05	64.75	0.00	0.00	99.45
Sample-3-Z3	1.26	0.05	14.68	18.62	0.04	64.12	0.00	0.00	98.78
Sample-3-Z3	1.23	0.42	14.36	18.42	0.08	64.28	0.01	0.00	98.80

Sample-3-Z3	1.15	0.05	14.88	18.62	0.02	64.59	0.00	0.00	99.31
Sample-3-Z3	1.09	0.18	14.76	18.57	0.04	64.55	0.02	0.00	99.21
Sample-3-Z3	1.10	0.05	14.80	18.59	0.03	64.39	0.00	0.00	98.96
Sample-3-Z3	1.79	0.02	13.82	18.70	0.12	64.67	0.00	0.00	99.12
Sample-3-Z3	1.75	0.02	13.85	18.87	0.11	64.47	0.00	0.00	99.07
Sample-3-Z3	2.52	0.08	12.90	18.80	0.10	64.83	0.00	0.00	99.23
Sample-3-Z3	1.88	0.04	13.75	18.75	0.06	64.90	0.02	0.00	99.41
Sample-3-Z3	2.06	0.02	13.49	18.85	0.15	64.75	0.00	0.00	99.33
Sample-3-Z3	1.73	0.04	14.13	18.76	0.05	64.60	0.00	0.00	99.31
Sample-3-Z3	1.56	0.51	13.92	18.62	0.08	64.46	0.00	0.00	99.16
Sample-3-Z3	1.33	0.03	14.62	18.64	0.02	64.69	0.00	0.00	99.33
Sample-3-Z3	1.37	0.27	14.29	18.66	0.06	64.18	0.00	0.00	98.83
Sample-3-Z3	1.39	0.17	14.44	18.69	0.03	64.31	0.00	0.00	99.03
Sample-3-Z4	1.61	0.07	14.22	18.85	0.00	63.51	0.01	0.00	98.26
Sample-3-Z4	1.72	0.02	13.98	18.86	0.03	63.40	0.00	0.00	98.01
Sample-3-Z4	1.90	0.05	13.63	18.93	0.03	63.46	0.00	0.00	98.00
Sample-3-Z4	1.93	0.01	13.76	18.76	0.05	63.80	0.00	0.00	98.31
Sample-3-Z4	1.83	0.02	13.92	18.82	0.10	64.10	0.01	0.00	98.80
Sample-5-Z4c	2.06	0.04	13.81	18.61	0.03	63.58	0.00	0.00	98.14
Sample-5-Z4c	1.97	0.00	13.56	18.58	0.08	63.63	0.01	0.00	97.83
Sample-5-Z4c	2.10	0.03	13.40	18.58	0.10	64.04	0.00	0.00	98.25
Sample-5-Z4c	2.48	0.02	12.99	18.74	0.13	64.01	0.00	0.00	98.37

Table A3. Pyroxene

Element-oxides in weight %, n = 76

Comment	Na_2O	FeO	TiO_2	MgO	CaO	SiO_2	MnO	Cr_2O_3	Al_2O_3	K_2O	Total
test	0.02	33.38	0.11	14.55	0.53	50.86	0.60	0.01	0.82	0.00	100.88
test	0.05	33.32	0.11	14.72	0.49	50.85	0.62	0.01	0.66	0.00	100.84
Sample-1-Z1	0.02	33.02	0.11	14.20	0.54	50.36	0.66	0.00	0.64	0.01	99.54
Sample-1-Z1	0.00	33.19	0.11	14.60	0.54	50.40	0.62	0.02	0.55	0.01	100.04
Sample-1-Z1	0.00	33.63	0.09	14.54	0.55	50.68	0.66	0.02	0.56	0.00	100.74
Sample-1-Z1	0.02	33.48	0.07	14.24	0.56	50.07	0.61	0.00	0.63	0.00	99.69
Sample-1-Z1	0.02	33.24	0.06	14.45	0.55	50.99	0.64	0.00	0.63	0.00	100.59
Sample-1-Z1	0.00	33.28	0.05	14.54	0.55	50.58	0.66	0.00	0.59	0.00	100.26
Sample-1-Z1	0.01	33.35	0.09	14.47	0.54	50.54	0.64	0.01	0.54	0.01	100.19
Sample-1-Z1	0.01	33.70	0.07	14.41	0.54	50.61	0.68	0.01	0.59	0.00	100.64
Sample-1-Z1	0.00	33.16	0.06	14.39	0.47	50.47	0.66	0.02	0.62	0.00	99.85
Sample-1-Z1	0.03	33.56	0.12	14.34	0.53	50.42	0.62	0.00	0.57	0.00	100.18
Sample-1-Z1	0.01	33.01	0.08	14.67	0.51	50.67	0.67	0.02	0.45	0.00	100.08
Sample-1-Z1	0.00	33.12	0.11	14.38	0.49	50.70	0.65	0.00	0.53	0.00	99.98
Sample-1-Z1	0.00	33.66	0.09	14.35	0.49	50.66	0.61	0.01	0.55	0.01	100.43
Sample-1-Z1	0.01	33.18	0.08	14.39	0.53	50.53	0.64	0.00	0.65	0.00	100.02
Sample-1-Z1	0.01	33.25	0.08	14.31	0.53	50.41	0.69	0.00	0.66	0.00	99.94
Sample-1-Z1	0.02	33.13	0.04	14.32	0.55	50.50	0.64	0.01	0.64	0.00	99.83
Sample-1-Z1	0.01	32.95	0.11	14.21	0.56	50.43	0.61	0.00	0.85	0.02	99.76
Sample-1-Z1	0.01	32.59	0.09	14.80	0.52	50.81	0.63	0.02	0.71	0.01	100.19
Sample-1-Z1	0.03	32.54	0.10	14.56	0.51	50.68	0.69	0.01	0.76	0.00	99.88
Sample-1-Z1	0.01	32.73	0.06	14.79	0.47	50.71	0.64	0.00	0.64	0.00	100.06
Sample-2-Z2	0.00	33.41	0.13	14.34	0.53	50.13	0.61	0.03	0.68	0.00	99.85
Sample-2-Z2	0.03	33.16	0.12	14.23	0.51	50.31	0.62	0.00	0.94	0.00	99.91
Sample-2-Z2	0.01	33.58	0.11	14.22	0.49	50.41	0.62	0.01	0.92	0.00	100.38
Sample-2-Z2	0.01	33.44	0.11	14.33	0.55	50.46	0.63	0.02	0.55	0.00	100.09
Sample-2-Z2	0.02	32.97	0.07	14.41	0.54	50.63	0.62	0.00	0.54	0.00	99.79
Sample-2-Z2	0.02	33.54	0.07	14.36	0.58	50.64	0.63	0.00	0.63	0.00	100.47
Sample-2-Z2	0.03	33.19	0.13	14.33	0.56	50.44	0.65	0.01	0.61	0.01	99.96
Sample-2-Z2	0.02	33.07	0.10	14.24	0.54	50.45	0.63	0.01	0.69	0.00	99.75
Sample-2-Z2	0.00	33.34	0.05	14.38	0.51	50.52	0.62	0.00	0.47	0.00	99.90

Sample-2-Z2	0.02	33.48	0.11	14.14	0.56	50.51	0.58	0.00	0.71	0.00	100.11
Sample-2-Z2	0.00	33.19	0.04	14.23	0.51	50.30	0.60	0.02	0.71	0.01	99.61
Sample-2-Z2	0.02	33.11	0.05	14.35	0.46	50.87	0.61	0.01	0.67	0.00	100.14
Sample-2-Z2	0.01	33.27	0.12	14.01	0.48	50.14	0.63	0.01	0.65	0.00	99.33
Sample-2-Z2	0.05	33.56	0.10	14.18	0.49	50.64	0.64	0.01	0.73	0.01	100.41
Sample-2-Z2	0.01	33.42	0.09	14.24	0.53	50.64	0.66	0.00	0.62	0.00	100.21
Sample-2-Z2	0.02	33.59	0.06	14.33	0.53	50.55	0.66	0.01	0.65	0.00	100.40
Sample-2-Z2	0.01	33.64	0.09	14.15	0.51	51.06	0.61	0.00	0.60	0.00	100.67
Sample-2-Z2	0.02	33.52	0.08	14.06	0.50	51.17	0.58	0.00	0.63	0.01	100.57
Sample-2-Z2	0.02	33.33	0.04	14.10	0.50	50.99	0.64	0.02	0.58	0.00	100.24
Sample-3-Z3	0.01	33.45	0.05	14.31	0.46	50.75	0.62	0.00	0.52	0.00	100.16
Sample-3-Z3	0.00	32.85	0.01	14.60	0.46	50.99	0.61	0.00	0.49	0.00	100.01
Sample-3-Z3	0.02	33.22	0.07	14.55	0.47	51.12	0.63	0.02	0.53	0.00	100.64
Sample-3-Z3	0.02	33.23	0.07	14.62	0.45	50.95	0.57	0.01	0.45	0.01	100.39
Sample-3-Z3	0.02	33.18	0.05	14.79	0.50	50.43	0.64	0.02	0.60	0.00	100.23
Sample-3-Z3	0.02	33.10	0.08	14.60	0.51	51.07	0.61	0.00	0.56	0.00	100.55
Sample-3-Z3	0.02	33.58	0.10	14.79	0.52	50.57	0.56	0.00	0.57	0.00	100.71
Sample-3-Z3	0.02	33.27	0.08	14.60	0.51	50.82	0.61	0.01	0.51	0.01	100.44
Sample-3-Z3	0.01	33.03	0.08	14.52	0.51	50.34	0.58	0.00	0.57	0.00	99.64
Sample-3-Z3	0.01	32.78	0.04	14.62	0.49	50.63	0.61	0.00	0.59	0.00	99.78
Sample-3-Z3	0.02	32.96	0.06	14.60	0.46	50.47	0.62	0.01	0.50	0.01	99.71
Sample-3-Z3	0.00	32.87	0.04	14.70	0.47	51.25	0.60	0.02	0.53	0.01	100.49
Sample-3-Z3	0.07	33.30	0.07	14.50	0.49	50.78	0.59	0.01	0.67	0.00	100.50
Sample-3-Z3	0.05	33.18	0.09	14.76	0.49	50.46	0.63	0.00	0.65	0.00	100.30
Sample-3-Z3	0.04	32.70	0.10	14.60	0.49	50.74	0.59	0.00	0.66	0.01	99.93
Sample-3-Z3	0.00	32.82	0.04	14.51	0.41	50.46	0.57	0.03	0.70	0.08	99.63
Sample-3-Z3	0.00	32.55	0.04	14.75	0.43	50.11	0.62	0.00	0.74	0.06	99.31
Sample-3-Z3	0.00	33.04	0.03	14.46	0.53	50.28	0.56	0.01	0.68	0.00	99.60
Sample-3-Z3	0.04	33.25	0.11	14.39	0.55	50.94	0.61	0.03	0.69	0.00	100.61
Sample-3-Z3	0.02	33.40	0.06	14.09	0.54	50.76	0.60	0.01	0.61	0.00	100.10
Sample-3-Z3	0.03	33.33	0.11	13.97	0.53	50.75	0.57	0.01	0.75	0.00	100.05
Sample-3-Z3	0.00	33.66	0.09	14.69	0.47	50.17	0.60	0.00	0.80	0.00	100.49
Sample-3-Z3	0.06	33.20	0.06	14.86	0.46	49.96	0.59	0.00	0.71	0.01	99.92
sample-3-Z4a	0.02	33.15	0.07	14.41	0.47	50.07	0.65	0.01	0.71	0.00	99.55

sample-3-Z4a	0.03	33.34	0.04	14.22	0.45	50.76	0.63	0.00	0.66	0.00	100.12
sample-3-Z4a	0.02	33.30	0.08	14.31	0.49	50.83	0.59	0.00	0.66	0.00	100.28
sample-3-Z4a	0.05	33.35	0.05	14.30	0.50	50.70	0.65	0.01	0.63	0.01	100.24
sample-3-Z4a	0.00	33.54	0.02	14.26	0.45	50.88	0.57	0.01	0.43	0.01	100.16
Sample-5-Z4c	0.04	33.89	0.09	14.15	0.50	50.22	0.55	0.02	0.78	0.00	100.24
Sample-5-Z4c	0.02	34.00	0.07	14.39	0.50	49.86	0.57	0.00	0.75	0.01	100.18
Sample-5-Z4c	0.01	33.26	0.08	14.39	0.45	50.59	0.59	0.00	0.78	0.01	100.18
Sample-5-Z4c	0.02	33.60	0.03	14.49	0.45	49.93	0.56	0.01	0.86	0.00	99.96
Sample-5-Z4c	0.05	33.75	0.05	14.16	0.48	50.39	0.63	0.01	0.78	0.01	100.30
Sample-5-Z4c	0.00	33.14	0.16	13.81	0.47	50.16	0.54	0.00	0.96	0.00	99.24
Sample-5-Z4c	0.03	33.11	0.07	13.88	0.41	50.80	0.56	0.03	0.62	0.01	99.51

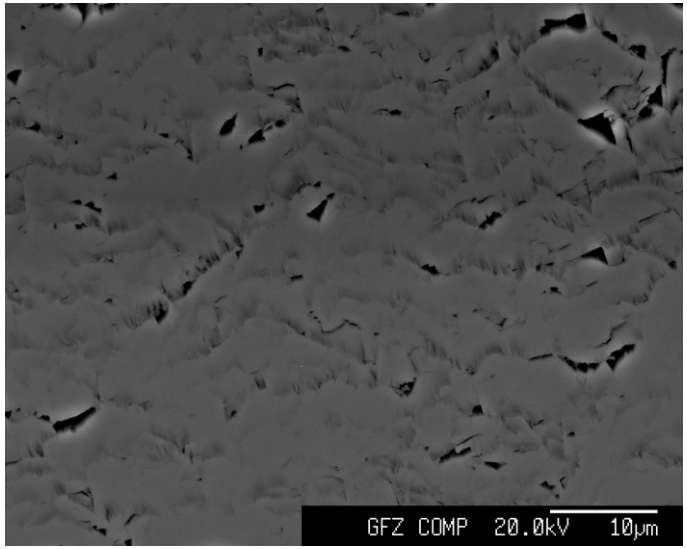

Figure A1. Backscatter image of pyroxene from corestone zone 2 with a rough surface.

Table A4. Biotite

Element-oxides in weight %, n = 65

Comment	F	FeO	K_2O	Na_2O	MnO	Cl	SiO_2	CaO	Al_2O_3	TiO_2	MgO	SrO	Total
test	0.00	19.22	9.15	0.09	0.03	0.13	37.52	0.00	14.01	4.73	12.01	0.14	97.04
test	0.00	19.71	9.01	0.06	0.04	0.11	37.61	0.00	13.79	5.20	11.08	0.13	96.74
sample-1-Z1	0.00	20.01	9.20	0.04	0.09	0.10	37.19	0.00	13.71	6.09	10.87	0.13	97.43
sample-1-Z1	0.00	19.58	9.15	0.06	0.07	0.12	37.23	0.00	13.85	5.56	10.94	0.15	96.71
sample-1-Z1	0.00	19.74	9.24	0.07	0.10	0.11	37.67	0.00	13.57	5.68	10.79	0.13	97.10
sample-1-Z1	0.00	19.63	9.29	0.02	0.07	0.12	37.51	0.00	13.82	5.93	10.74	0.13	97.25
sample-1-Z1	0.00	19.30	9.20	0.05	0.09	0.10	37.59	0.00	13.47	5.60	10.81	0.12	96.34
sample-1-Z1	0.00	19.53	9.25	0.09	0.05	0.11	37.21	0.00	13.71	6.00	10.92	0.12	97.00
sample-1-Z1	0.00	19.53	9.31	0.11	0.09	0.11	37.93	0.00	13.65	5.84	10.62	0.14	97.33
sample-1-Z1	0.00	19.39	9.14	0.03	0.07	0.11	37.23	0.00	13.64	5.62	11.05	0.13	96.42
sample-1-Z1	0.00	19.29	9.31	0.05	0.08	0.11	37.63	0.00	13.50	5.65	10.79	0.15	96.56
sample-1-Z1	0.00	20.68	7.94	0.04	0.10	0.11	37.88	0.10	12.65	5.14	10.93	0.10	95.66
sample-1-Z1	0.00	19.42	9.12	0.07	0.09	0.12	37.75	0.00	13.50	5.74	10.61	0.13	96.55
sample-1-Z1	0.00	19.44	9.08	0.08	0.09	0.10	37.58	0.01	13.67	5.77	10.63	0.15	96.61
sample-1-Z1	0.00	19.85	9.10	0.05	0.06	0.10	37.52	0.00	13.55	6.05	10.71	0.14	97.12
sample-1-Z1	0.00	19.52	9.12	0.07	0.09	0.11	37.16	0.00	13.62	5.94	11.00	0.15	96.78
sample-1-Z1	0.00	19.59	9.35	0.03	0.08	0.10	37.23	0.00	13.65	5.49	11.12	0.11	96.75
sample-1-Z1	0.00	19.78	9.17	0.07	0.08	0.13	37.31	0.00	13.60	5.57	11.07	0.12	96.89
sample-1-Z1	0.00	19.03	9.11	0.06	0.08	0.12	36.87	0.00	13.67	5.23	11.06	0.16	95.38
sample-1-Z1	0.00	20.06	9.27	0.07	0.08	0.11	37.53	0.00	13.62	5.47	11.24	0.13	97.58
sample-2-Z2	0.00	19.64	9.24	0.03	0.06	0.11	38.11	0.00	13.28	4.98	11.51	0.17	97.13
sample-2-Z2	0.00	19.61	9.21	0.08	0.04	0.11	37.62	0.00	13.37	5.13	11.35	0.18	96.70
sample-2-Z2	0.00	19.81	9.00	0.06	0.06	0.11	37.60	0.00	13.72	5.08	11.30	0.14	96.89
sample-2-Z2	0.00	19.43	9.07	0.03	0.05	0.11	37.20	0.00	13.81	5.13	11.43	0.12	96.38
sample-2-Z2	0.00	19.85	9.17	0.06	0.10	0.13	37.76	0.00	13.64	5.33	11.08	0.15	97.26
sample-2-Z2	0.00	19.69	9.24	0.06	0.07	0.11	37.51	0.00	13.69	5.37	10.80	0.12	96.67
sample-2-Z2	0.00	19.92	9.24	0.02	0.08	0.11	37.29	0.00	13.75	5.66	11.09	0.12	97.28
sample-2-Z2	0.00	20.12	9.30	0.06	0.07	0.12	37.43	0.00	13.90	5.57	11.21	0.13	97.91
sample-2-Z2	0.00	20.17	9.22	0.04	0.03	0.11	37.62	0.00	13.69	5.22	10.97	0.14	97.21
sample-2-Z2	0.00	20.05	9.18	0.03	0.09	0.09	37.30	0.00	13.63	5.34	11.07	0.13	96.92
sample-2-Z2	0.00	19.86	9.22	0.02	0.04	0.11	37.06	0.00	13.78	5.32	11.07	0.13	96.61

sample-2-Z2	0.00	19.68	9.01	0.06	0.07	0.11	37.12	0.00	13.73	5.47	10.88	0.15	96.28
sample-2-Z2	0.00	19.39	9.26	0.03	0.08	0.11	37.47	0.00	13.52	5.32	11.12	0.15	96.45
sample-2-Z2	0.00	19.90	9.26	0.03	0.08	0.12	37.11	0.00	13.75	5.56	11.17	0.14	97.13
sample-2-Z2	0.00	19.44	9.22	0.06	0.07	0.12	37.09	0.00	13.90	5.20	11.38	0.13	96.60
sample-3-Z2	0.00	19.43	9.24	0.06	0.06	0.12	37.48	0.00	13.76	5.79	10.96	0.12	97.02
sample-3-Z2	0.00	19.83	9.11	0.04	0.10	0.11	37.48	0.00	13.77	5.81	11.09	0.16	97.51
sample-3-Z2	0.00	19.27	9.15	0.03	0.05	0.10	37.72	0.00	13.94	6.05	11.19	0.13	97.64
sample-3-Z2	0.00	19.45	9.16	0.05	0.06	0.10	37.41	0.00	13.71	6.01	10.93	0.16	97.04
sample-3-Z2	0.00	19.52	9.01	0.09	0.08	0.11	37.42	0.01	13.64	5.69	10.72	0.16	96.44
sample-3-Z2	0.00	19.41	9.19	0.04	0.07	0.11	37.79	0.00	13.77	5.72	11.17	0.13	97.40
sample-3-Z2	0.00	19.00	9.17	0.05	0.04	0.11	37.39	0.00	13.84	5.56	11.13	0.14	96.43
sample-3-Z3	0.00	19.85	9.14	0.07	0.05	0.11	37.27	0.00	14.08	5.18	11.63	0.15	97.54
sample-3-Z3	0.00	20.27	8.98	0.08	0.05	0.09	37.50	0.00	13.74	4.89	11.45	0.14	97.19
sample-3-Z3	0.00	19.81	9.10	0.08	0.06	0.12	37.59	0.00	14.07	5.06	11.57	0.14	97.60
sample-3-Z3	0.00	20.01	8.87	0.08	0.04	0.12	35.29	0.04	14.76	5.14	12.13	0.14	96.61
sample-3-Z3	0.00	19.83	8.85	0.09	0.06	0.11	37.29	0.07	13.45	5.22	11.10	0.14	96.22
sample-3-Z3	0.00	19.87	9.03	0.06	0.05	0.11	37.89	0.00	13.78	5.18	11.34	0.13	97.43
sample-3-Z3	0.00	19.95	9.06	0.09	0.07	0.11	37.78	0.00	13.70	5.12	11.35	0.11	97.34
sample-3-Z3	0.00	19.68	8.99	0.08	0.10	0.11	37.23	0.00	13.98	5.36	11.03	0.13	96.69
sample-3-Z3	0.00	19.71	8.81	0.05	0.10	0.11	37.18	0.07	13.90	5.17	11.29	0.14	96.52
sample-3-Z3	0.00	20.14	9.16	0.05	0.05	0.11	37.27	0.00	13.88	5.29	11.17	0.13	97.25
sample-3-Z3	0.00	20.22	9.10	0.07	0.04	0.10	37.50	0.00	13.96	5.19	11.22	0.13	97.54
sample-3-Z4	0.00	19.33	9.04	0.06	0.04	0.11	36.96	0.00	13.97	5.18	11.25	0.14	96.08
sample-3-Z4	0.00	20.05	9.16	0.08	0.07	0.10	37.14	0.00	13.87	5.23	11.24	0.15	97.08
sample-3-Z4	0.00	20.13	9.23	0.09	0.06	0.11	37.57	0.00	13.74	5.36	11.16	0.14	97.60
sample-3-Z4	0.00	19.42	9.16	0.04	0.05	0.11	37.14	0.00	13.75	5.18	11.16	0.10	96.12
sample-3-Z4	0.00	19.83	9.20	0.06	0.06	0.10	37.12	0.00	14.01	5.24	11.41	0.13	97.16
sample-3-Z4	0.00	19.64	9.19	0.05	0.04	0.11	37.17	0.00	13.83	5.28	11.02	0.13	96.46
sample-5-Z4c	0.00	19.98	9.19	0.10	0.07	0.10	37.60	0.00	13.58	5.71	10.44	0.12	96.89
sample-5-Z4c	0.00	19.80	9.28	0.13	0.08	0.11	37.33	0.00	14.01	5.65	10.79	0.14	97.32
sample-5-Z4c	0.00	19.82	9.37	0.08	0.07	0.10	37.26	0.00	13.90	5.62	10.65	0.11	96.99
sample-5-Z4c	0.00	20.14	9.22	0.08	0.04	0.11	37.30	0.00	13.62	5.31	11.08	0.13	97.03
sample-5-Z4c	0.00	20.05	9.33	0.06	0.06	0.11	37.27	0.00	13.79	5.25	11.11	0.12	97.16
sample-5-Z4c	0.00	19.84	9.29	0.06	0.04	0.11	37.56	0.00	13.61	5.24	10.96	0.13	96.84

Table A5. Ilmenite

Element-oxides in weight %, n = 15

Comment	SiO_2	FeO	TiO2	Al_2O_3	CaO	MnO	HfO_2	MgO	Y_2O_3	ZrO_2	Total
test	0.03	44.48	53.10	0.06	0.01	0.47	0.32	0.82	0.00	0.00	99.31
Sample-1	0.08	45.65	51.19	0.08	0.01	0.48	0.04	1.16	0.00	0.01	98.71
Sample-1	0.06	45.31	51.33	0.07	0.01	0.49	0.00	1.18	0.01	0.00	98.45
Sample-1	0.24	45.26	50.89	0.04	0.01	0.50	0.00	0.70	0.01	0.00	97.65
Sample-1	0.09	45.77	51.67	0.01	0.00	0.54	0.00	0.71	0.00	0.00	98.80
Sample-1	0.54	45.16	50.86	0.23	0.01	0.56	0.04	0.65	0.00	0.00	98.06
Sample-1	0.10	45.98	51.82	0.05	0.00	0.60	0.00	0.32	0.03	0.02	98.93
Sample-1	0.05	46.14	51.38	0.02	0.00	0.59	0.18	0.26	0.00	0.04	98.66
Sample-1-	0.19	45.79	51.35	0.10	0.00	0.72	0.00	0.22	0.00	0.00	98.36
Sample-1-	0.13	45.58	51.14	0.03	0.00	0.57	0.07	1.10	0.00	0.00	98.63
Sample-3	0.40	43.82	52.69	0.05	0.02	0.48	0.00	0.72	0.00	0.00	98.18
Sample-3-Z4a	0.00	44.76	52.11	0.03	0.00	0.65	0.03	0.40	0.00	0.00	97.99
Sample-3-Z4a	0.02	45.00	52.42	0.03	0.01	0.65	0.06	0.41	0.02	0.00	98.62
Sample-3-Z4a	0.15	43.93	53.21	0.13	0.01	0.47	0.00	1.00	0.00	0.00	98.90
Sample-3-Z4a	0.09	43.65	53.61	0.11	0.03	0.48	0.03	0.36	0.00	0.00	98.36

Table A6. Apatite

Element-oxides in weight %, n = 31

Comment	F	Ce_2O_3	P_2O_5	Y_2O_3	CaO	Na_2O	La_2O_3	Cl	SrO	SiO_2	FeO	Pr_2O_3	MnO	Nd_2O_3	SO_3	F=O	Cl=O	Total
Sample-1	3.84	0.41	41.75	0.06	54.68	0.16	0.22	0.09	0.03	0.08	0.03	0.07	0.04	0.23	0.01	1.62	0.02	100.05
Sample-1	3.74	0.55	42.05	0.10	54.43	0.18	0.15	0.10	0.02	0.16	0.04	0.01	0.06	0.30	0.01	1.57	0.02	100.31
Sample-1	3.96	0.46	41.44	0.12	54.48	0.17	0.25	0.09	0.00	0.41	0.14	0.10	0.03	0.23	0.00	1.67	0.02	100.20
Sample-1	3.69	0.21	41.93	0.26	55.05	0.09	0.01	0.07	0.00	0.33	0.16	0.00	0.03	0.14	0.00	1.55	0.01	100.40
Sample-1	3.74	0.21	41.97	0.09	55.38	0.04	0.00	0.05	0.04	0.11	0.09	0.07	0.05	0.16	0.01	1.57	0.01	100.42
Sample-1	3.99	0.39	41.46	0.13	54.72	0.20	0.15	0.09	0.00	0.28	0.04	0.00	0.02	0.25	0.00	1.68	0.02	100.02
Sample-2	3.98	0.15	42.33	0.16	55.10	0.15	0.06	0.09	0.04	0.25	0.08	0.01	0.02	0.14	0.00	1.68	0.02	100.88
Sample-2-test	3.87	0.45	42.34	0.23	54.90	0.14	0.01	0.09	0.00	0.33	0.08	0.10	0.00	0.31	0.01	1.63	0.02	101.21
Sample-2	3.90	0.23	42.49	0.17	54.96	0.06	0.07	0.07	0.03	0.29	0.22	0.08	0.05	0.20	0.02	1.64	0.02	101.19
Sample-2	3.95	0.33	42.12	0.15	54.85	0.10	0.02	0.06	0.00	0.27	0.23	0.05	0.05	0.21	0.00	1.66	0.01	100.72
Sample-2	3.82	0.33	42.11	0.19	55.08	0.12	0.13	0.07	0.01	0.22	0.06	0.12	0.00	0.17	0.00	1.61	0.02	100.81
Sample-2	3.77	0.36	42.01	0.14	54.87	0.08	0.13	0.06	0.04	0.28	0.22	0.00	0.01	0.27	0.00	1.59	0.01	100.63
Sample-2	3.68	0.33	42.07	0.08	55.34	0.10	0.12	0.08	0.03	0.10	0.10	0.03	0.03	0.24	0.00	1.55	0.02	100.77
Sample-3	3.60	0.27	41.71	0.12	54.97	0.12	0.11	0.07	0.03	0.25	0.07	0.00	0.05	0.17	0.00	1.52	0.02	100.02
Sample-3	3.79	0.12	42.12	0.07	55.30	0.11	0.06	0.08	0.06	0.14	0.12	0.12	0.05	0.06	0.02	1.60	0.02	100.60
Sample-3	3.74	0.20	41.97	0.06	55.22	0.12	0.02	0.08	0.03	0.20	0.15	0.06	0.01	0.29	0.01	1.57	0.02	100.57
Sample-3	3.76	0.49	41.16	0.15	54.68	0.20	0.12	0.09	0.03	0.21	0.05	0.14	0.05	0.24	0.00	1.58	0.02	99.75
Sample-3-Z4	4.00	0.47	40.86	0.17	54.78	0.14	0.15	0.09	0.00	0.43	0.08	0.02	0.00	0.39	0.00	1.68	0.02	99.88
Sample-3-Z4	3.72	0.33	41.00	0.21	54.83	0.11	0.14	0.08	0.01	0.37	0.11	0.00	0.02	0.35	0.01	1.57	0.02	99.69
Sample-3-Z4	3.71	0.41	41.66	0.18	55.16	0.09	0.05	0.09	0.03	0.30	0.15	0.13	0.06	0.27	0.02	1.56	0.02	100.74
Sample-3-Z4	3.68	0.33	41.50	0.10	55.39	0.15	0.14	0.08	0.05	0.15	0.10	0.00	0.05	0.20	0.00	1.55	0.02	100.35
Sample-3-Z4	3.84	0.38	40.84	0.25	55.12	0.11	0.10	0.10	0.03	0.37	0.11	0.04	0.02	0.25	0.00	1.62	0.02	99.92
Sample-3-Z4	3.73	0.57	41.85	0.13	54.60	0.19	0.34	0.10	0.02	0.25	0.12	0.13	0.02	0.27	0.00	1.57	0.02	100.73
Sample-5	4.22	0.62	41.57	0.06	54.21	0.18	0.34	0.09	0.03	0.49	0.11	0.04	0.02	0.38	0.00	1.78	0.02	100.58
Sample-5	3.85	0.35	42.21	0.06	55.11	0.11	0.11	0.09	0.04	0.10	0.10	0.01	0.03	0.23	0.01	1.62	0.02	100.77
Sample-5	3.93	0.43	42.01	0.07	55.06	0.19	0.18	0.09	0.04	0.10	0.08	0.15	0.02	0.24	0.00	1.65	0.02	100.91
Sample-5	3.96	0.41	42.51	0.04	54.80	0.19	0.17	0.08	0.02	0.16	0.08	0.07	0.02	0.32	0.01	1.67	0.02	101.15
Sample-5	4.01	0.57	42.44	0.01	54.70	0.27	0.17	0.10	0.01	0.13	0.05	0.00	0.02	0.43	0.02	1.69	0.02	101.23
Sample-5	3.97	0.58	41.78	0.06	54.65	0.23	0.18	0.11	0.06	0.11	0.05	0.09	0.03	0.40	0.04	1.67	0.02	100.63
Sample-5	4.00	0.55	41.86	0.01	54.64	0.18	0.17	0.10	0.01	0.24	0.15	0.07	0.00	0.22	0.00	1.68	0.02	100.52
Sample-5-	3.95	0.16	42.59	0.02	55.41	0.06	0.04	0.05	0.03	0.11	0.09	0.04	0.05	0.09	0.00	1.66	0.01	101.02

Table A7. Zircon

Element-oxides in weight %, n = 5

Comment	SiO_2	FeO	TiO_2	Al_2O_3	CaO	MnO	HfO_2	MgO	Y_2O_3	ZrO_2	Total
test	32.52	0.00	0.03	0.11	0.03	0.03	1.51	0.02	0.00	65.43	99.68
Sample-1	31.98	0.03	0.03	0.02	0.02	0.02	0.90	0.01	0.00	65.86	98.86
Sample-1	32.30	0.15	0.04	0.07	0.01	0.00	1.28	0.04	0.00	65.36	99.26
Sample-1-zir-	32.65	0.12	0.26	0.01	0.01	0.00	2.60	0.01	0.00	64.18	99.85
Sample-1-zir-	32.46	0.03	0.05	0.01	0.00	0.00	1.08	0.00	0.00	65.25	98.87

Table A8. Monazite

Element-oxides in weight %, n = 2

Comment	SiO_2	P_2O_5	CaO	La_2O_3	Ce_2O_3	ThO_2	Pr_2O_3	Nd_2O_3	Gd_2O_3	Sm_2O_3	Total
mona-Th	2.06	26.46	1.01	14.84	28.14	11.18	2.19	10.44	1.38	2.30	100.00
mona- no Th	0.24	29.65	0.65	18.77	33.86	0.00	2.30	10.08	2.11	2.35	100.00

Single point measurement of monazite with Th

```
Group     :
Sample    :   ID# : 0
Comment   :
Condition : Full Scale  : 20KeV(10eV/ch,2Kch)
            Live Time   :  30.000 sec    Aperture #    : 2
            Acc. Volt   : 20.0 KV        Probe Current : 1.992E-08 A
            Stage Point : X=48.149 Y=65.240 Z= 9.791
            Acq. Date   : Mon Apr 16 16:04:20 2012

Element     Mode    Compound   ROI(KeV)    K-ratio(%)  +/-    Net/Background
 Si K      Normal     SiO2    1.49- 2.06     0.5179   0.0005     1009 /     628
  P K      Normal     P2O5    1.75- 2.38    10.0384   0.0076    13022 /     248
 Ca K      Normal      CaO    3.39- 4.30     0.7462   0.0031      834 /     136
 Ag L      Normal     Ag2O    2.34- 4.01     0.0000   0.0000        0 /     138
 La L      Normal    La2O3    3.79- 6.38    10.8414   0.0084     6443 /      92
 Ce L      Normal    Ce2O3    3.95- 6.65    21.6037   0.0098    13210 /      86
 Th M      Normal     ThO2    2.07- 4.38     7.4351   0.0040     5574 /     499
 Pr L      Normal    Pr2O3    4.11- 6.94     1.5038   0.0083      625 /     102
 Nd L      Normal    Nd2O3    4.28- 7.23     8.0948   0.0099     4309 /      77
 Gd L      Normal    Gd2O3    5.00- 8.44     0.8832   0.0054      415 /     168
 Sm L      Normal    Sm2O3    4.63- 7.82     1.5427   0.0070      667 /     224
-------------------------------------------------------------------------------
 Number of Oxygen Atoms = 12           Chi_square =  2.3925

Element Mass%    Cation    ZAF      Z      A      F
  SiO2    2.061  0.2508  1.8095 0.8273 2.1924 0.9976
  P2O5   26.457  2.7254  1.1187 0.9495 1.1786 0.9997
   CaO    1.013  0.1321  0.9437 0.8362 1.1558 0.9765
  Ag2O    0.000  0.0000  1.2548 1.1147 1.1320 0.9944
 La2O3   14.837  0.6658  1.1349 1.0865 1.0462 0.9985
 Ce2O3   28.139  1.2535  1.0816 1.0500 1.0305 0.9996
  ThO2   11.180  0.3096  1.2852 1.2074 1.0645 1.0000
 Pr2O3    2.187  0.0970  1.2088 1.1970 1.0104 0.9995
 Nd2O3   10.444  0.4539  1.0759 1.0521 1.0226 1.0000
 Gd2O3    1.380  0.0557  1.3189 1.2512 1.0541 1.0000
 Sm2O3    2.301  0.0965  1.2511 1.2268 1.0198 1.0000
-------------------------------------------------------------------------------
Total   100.000  6.0403
Normalization factor =  1.0282
```

Single point measurement of monazite without Th

```
Group     :
Sample    :   ID# : 0
Comment   :
Condition : Full Scale   : 20KeV(10eV/ch,2Kch)
            Live Time    :  30.000 sec    Aperture #    : 2
            Acc. Volt    : 20.0 KV        Probe Current : 1.993E-08 A
            Stage Point  : X=44.721 Y=73.570 Z= 9.849
            Acq. Date    : Mon Apr 16 15:37:49 2012

Element     Mode     Compound   ROI(KeV)   K-ratio(%)  +/-    Net/Background
  P K      Normal      P2O5    1.75- 2.38   11.6142   0.0078    15074 /     172
 La L      Normal     La2O3    3.79- 6.38   14.8622   0.0093     8837 /      96
 Ce L      Normal     Ce2O3    3.95- 6.65   28.0789   0.0108    17177 /      76
 Pr L      Normal     Pr2O3    4.11- 6.94    1.7124   0.0089      712 /      90
 Nd L      Normal     Nd2O3    4.28- 7.23    8.4434   0.0105     4497 /     100
 Sm L      Normal     Sm2O3    4.63- 7.82    1.6929   0.0073      732 /     268
 Gd L      Normal     Gd2O3    5.00- 8.44    1.4290   0.0055      672 /     200
 Ca K      Normal       CaO    3.39- 4.30    0.5270   0.0031      590 /     130
 Si K      Normal      SiO2    1.49- 2.06    0.0624   0.0004      122 /     577
-------------------------------------------------------------------------
 Number of Oxygen Atoms = 12           Chi_square =  1.9295

Element Mass%    Cation    ZAF      Z      A      F
  P2O5   29.645  2.9578  1.1501 0.9579 1.2013 0.9995
 La2O3   18.771  0.8159  1.1119 1.0968 1.0159 0.9979
 Ce2O3   33.861  1.4610  1.0630 1.0600 1.0035 0.9993
 Pr2O3    2.296  0.0986  1.1827 1.2085 0.9796 0.9991
 Nd2O3   10.076  0.4241  1.0563 1.0623 0.9944 1.0000
 Sm2O3    2.351  0.0955  1.2365 1.2389 0.9980 1.0000
 Gd2O3    2.109  0.0824  1.3219 1.2638 1.0460 1.0000
   CaO    0.647  0.0817  0.9054 0.8438 1.1099 0.9668
  SiO2    0.244  0.0288  1.8895 0.8346 2.2699 0.9973
-------------------------------------------------------------------------
Total   100.000  6.0457
Normalization factor =  0.9686
```

Appendix B: TEM - EDX measurements, ternary plots and overviews for pyroxene, biotite and plagioclase

Pyroxene

Table B1. Sample 3300, pyroxene from zone 3 (pyroxene and Al-phase)

element	Mg	Al	Si	Ca	Mn	Fe
	atom %					
opx	18.7	1.5	48.3	0.5	0.9	30.1
opx	20.1	1.3	50.2	0.4	0.5	27.4
opx	21.4	1	44.7	0.7	1	31.3
opx	20.7	1.5	49.2	0.3	0.5	27.8
opx	20.7	1.8	49.3	0.4	0.3	27.6
opx	17.8	0.9	47.8	1	0.1	32.4
opx	20.8	1.5	48.4	0.4	0.5	28.3
opx	17.7	1.5	48.5	0.5	1.1	30.8
opx	18	0.4	48.7	0.4	0.5	31.9
opx	20.2	1.2	47.7	0.9	0.7	29.3
opx	21	1.6	49.5	0.5	0.7	26.8
opx	18.9	0.6	49.5	0.6	0.6	29.8
opx	20.4	1.6	48.8	0.4	0.6	28.2
opx	20.3	1.1	50	0.4	0.6	27.6
opx	22.4	1.4	40.6	0.6	0.1	41.5
opx interface	18.8	0.8	49.8	0.5	0.5	29.7
sec. phase interface	3.2	6.3	62.1	1.9	0.3	26.3
sec. phase	1.8	6.6	65.8	2.6	0.1	23.1
sec. phase	0.7	7.7	54.8	1.6	0.4	34.7
sec. phase	2.1	9.1	60.8	1.5	0	26.5
sec. phase	1.5	6.3	67.9	1.6	0	22.8
sec. phase	0.7	17.8	56.1	1.2	0	24.2
sec. phase	2.3	15.6	57.8	1.1	0	23.1
sec. phase	2	6.7	70.1	1.5	0	16.7
sec. phase	2.2	9.3	56.5	1.3	0	30.7
sec. phase	2.5	8.5	57.9	2	0.03	29.2
sec. phase	0	8.1	55.8	2.7	0.2	33.2
sec. phase	2	4.1	64.6	2.5	0.1	26.8
sec. phase	3	7.5	68.1	1.3	0	33.4
sec. phase	2.8	6.1	64.6	2.1	0	24.4
sec. phase	3.4	8	65	1.9	0	21.8
sec. phase	0.7	7.9	57.6	1	0	32.8
sec. phase	1.9	12.5	53.9	2.1	0.8	28.8
sec. phase	1.4	5.9	62.2	1.2	0	29.3
sec. phase	1.1	2.6	47.7	1.4	0	47.2
sec. phase	2.4	2.9	49.8	0.01	0.4	44.4
sec. phase	1.3	2.4	47.3	1.1	0	47.7
sec. phase	2.8	2.9	50	0.4	0	44

Table B2. Sample 3321, pyroxene from zone 3 (pyroxene and Al-phase)

element	Mg	Al	Si	K	Ca	Mn	Fe
	atom %						
opx	20.4	1.3	49.3		0.3	0.4	28.3
opx	19.9	2.7	48.1		1.1	0.6	17.6
sec. phase.	2.1	11	59.9	0	0.6	0	26.5
sec. phase	1.6	9.8	57.3		0.2	0	30
sec. phase	1.1	7.9	66.5	0.2	3	0	21.3
sec. phase	3	15.3	54.9		1.2	0.03	25.6
sec. phase	1.4	11	53.1		2.7	0	31.9

Table B3. Sample 3452, pyroxene from zone 1

element	Mg	Al	Si	Ca	Mn	Fe
	atom %					
opx	19.3	1.2	52.5	0.2	0.4	26.4
opx	21.2	0.4	52	0.3	0.2	25.8
opx	21.4	0.6	51.1	0.2	0.1	26.6
P1	17	8.6	48	1.9	0.2	24.3
P1	15.3	8.8	52.7	1.3	0.0	21.9
P1	19.2	9.7	45.0	1.8	0.0	24.3
P1	15.7	7.6	52.8	2.6	0	21.3
P2	20.7	8	50.3	1.2	0	19.6
P2	22.1	8.5	50.6	1.1	0.0	17.5
P2	18.7	7.9	49.8	1.8	0.0	21.8
P2	21.1	9.3	49.1	1.6	0	18.9
P2 (interface)	20.1	8.3	49.6	1.6	0	20.4

Table B4. Sample 3307, pyroxene from zone 3 (pyroxene and Fe-phase)

element	C	Mg	Al	Si	P	K	Ca	Mn	Fe
	atom %								
opx		21.4	1.2	47.9			0.3	0.8	28.4
interface		18.2	1.2	50.8		0	0.1	0.5	29.2
interface	77.5	4.5	1.4	13.3			0.1	0	3.14
sec. phase		0	1.8	39.4	3.7	0	3.3	0.2	51.6
sec. phase		1.1	2.1	42	0	0	1.4	0.1	53.2
sec. phase		1.4	4.6	54.4	1.1	0.5	0.5	0	37.5
sec. phase		1.1	1.8	46.1	2	1	1.2	0	46.8
sec. phase		1.4	3.3	45	2.3	0.3	1.1	0.1	46.5
sec. phase		0	2.9	40.8	2.1	0.3	1.7	0	52.2
sec. phase		0	1.3	41.9	1.2	0.1	2.6	0	52.8
sec. phase		0	2.5	45.8	0.9	0	2.3	0	48.5
sec. phase		0.2	2.7	45.9	0	0.1	2.3	0	48.8
sec. phase			1.5	39.3	1.4		1.2		56.6
sec. phase			11.4	56.7		1.4			30.4
sec. phase			13.1	57.5		1.5			27.9
sec. phase			2.9	39.2	1.3		2.4		54.2

Biotite

Table B5. Sample 3313, biotite from zone 4c, outer rindlet

element	Mg	Al	Si	K	Ca	Ti	Fe
	atom %						
bt	18.6	16.7	37.8	10.3		3.6	13.0
bt	17.3	16.3	34.6	11.8		4.7	15.3
bt	17.0	18.4	35.1	11.5		3.9	14.1
bt?	15.3	18.8	38.7	10.1		2.6	14.5
sec. phase	1.9	50.8	45.8	0.4		0.0	0.9
sec. phase	3.1	49.3	45.1	0.5		0.2	1.8
sec. phase	3.5	49.6	44.2	0.7		0.0	2.0
sec. phase	1.7	49.3	47.8	0.0		0.0	1.2
sec. phase	0.0	48.2	49.4	0.1		0.0	2.3
sec. phase	1.7	48.2	47.1	0.9		0.0	2.1
sec. phase		50.3	47.4	0.1			2.2
sec. phase	9.2	33.9	41.4	4.4		2.0	9.1
sec. phase	11.6	11.6	24.1	4.9	0.9	2.2	41.7
sec. phase	0.0	17.5	23.2	0.0	0.0	0.0	59.3
sec. phase	0.0	22.4	47.1	0.3	0.2	0.0	30.0
sec. phase	2.6	28.4	44.3	0.0	0.4	0.0	24.3
sec. phase	2.8	26.0	29.5	0.4	0.2	0.0	41.1
sec. phase		51.0	47.9				1.0
sec. phase	0.0	30.6	42.7	0.0	0.3	0.0	26.4
sec. phase	0.0	16.2	24.3	0.0	0.3	0.0	59.2

Table B6. Sample 3396, biotite from zone 2

element	Mg	Al	Si	K	Ca	Ti	Fe
	atom %						
bt	17.5	16.1	34.5	11.1		4.3	16.5
bt	16.4	16.7	34.9	10.9		3.3	17.7
bt	16.4	16.4	36.8	11.1		3.2	15.6
bt	16.7	16.5	35.4	11.6		4.0	15.8
bt	17.6	15.4	35.0	11.9		3.7	16.8
bt	18.3	16.4	35.1	10.7		3.5	16.0
bt	16.4	16.5	36.4	11.9		3.2	15.6
bt	18.9	17.0	34.5	11.4		3.4	14.8
bt	18.6	18.6	35.2	10.3		2.4	14.9
bt	17.1	18.2	35.6	11.5		3.8	13.8
bt	16.1	16.5	36.6	10.9		4.1	15.8
bt	18.6	16.9	34.2	12.2		3.6	14.4
bt	18.7	15.6	36.1	10.6		3.7	15.2
sec. phase	4.2	39.9	51.0	1.3	0.9	0.0	2.7
sec. phase	5.1	36.7	54.1	1.5	0.0	0.0	2.5
sec. phase	5.5	40.3	51.3	0.8	0.2	0.2	1.9

Plagioclase

Table B7. Sample 3320, plagioclase from zone 4c, outer rindlet

element	C	Na	Mg	Al	Si	P	K	Ca	Fe
	atom %								
plag		16.1		24.1	55		0.3	4.6	
plag		16.8		25.5	53.5		0.1	4.1	
plag		12.8		25.1	57.5		0	4.5	
plag		12.7		26.1	56.8		0	4.5	
plag		16.6		27.4	51.7		0.3	3.9	
Al-amorph				38.1	53.7			8.2	
Al-amorph				35.4	57.4			7.2	
Al-amorph			0	61.4	32.3	6.3		0	
Al-amorph			0	61.6	32.5	6.2		1.2	
Al-amorph			2.1	60.7	32.3	4.7		0.3	
Al-amorph			0	64.3	29.2	6		0.5	
Al-amorph		3.4		62.8	26.4	6.2		0.6	
Al-Si rich				52.9	45.9				1.2
Al-Si rich				51.4	48				0.6
Al-Si rich				52.9	45.6				1.5
Fe-rich		0		36.1	39.6	2		0.8	21.5
Fe-rich		0		35.2	48.6	0		0	16.1
Fe-rich		0		33.9	49.7	0.5		0.4	15.4
Fe-rich		3.3		31.3	40.3	2.3		0.8	22
P9 epoxy?	99.2			0.2	0.7				
P5 epoxy?	99.2	0.3		0.1	0.4				
P5 epoxy?	99	0.6			0.5				
P5 epoxy?	100								

Table B8. Sample 3314, plagioclase from zone 3

element	Na	Mg	Al	Si	P	K	Ca	Fe
	atom %							
plag	15.1		26.2	53.1		0.3	5.3	
plag	15.9		25.6	54.3		0.1	4	
plag	15.5		25.3	54.7		0.1	3.9	
interface		1.8	8.1	67.5			1.9	20.7
sec. phase	4.7	3.2	19.9	54.4	0	0	1.4	16.3
sec. phase	0	3.9	29.3	50.8	0	0.5	0.6	15
sec. phase	5.9	0	7.8	61.4	0	0	1.8	23.1
sec. phase	1.2	0.2	3.6	71.1	0	0	1.4	22.5
sec. phase	0	3.5	26.3	50.6	0	0	1.5	18.1
sec. phase	0	2.3	14.1	56.6	0	0	1.5	25.5
sec. phase	0	3.2	25.5	52.6	0.8	0.3	1.3	16.2
sec. phase	0	4.5	25.4	52.6	0	0.1	1	16.5
sec. phase	0	3.4	18.5	54.4	0	0	1	22.7
sec. phase	4.1	2.5	7	63.2	0.8	0	1.6	20.8
sec. phase	0	2.2	6.9	66.2	0	0.1	2	22.6
sec. phase	3.2	2.4	11.2	62.9	0	0.3	1.9	18.2

Appendix C: Calculation of the parameters for the oxidation model (section 4.4.1)

All parameters required to calculate the volume increase by oxidation of iron-bearing minerals in the bedrock, equation (5) in the main text, are presented below. In the following equations each occurrence of "x" can be replaced either by "bt" for biotite or "px" for pyroxene.

We first need to calculate the total amount of FeO lost during weathering between bedrock and the weathered zone j in the corestone, $FeO_{lost,\,j}$ (in moles/kg_{rock}):

$$FeO_{lost,j} = \left(\left([px]_0 - [px]_j\right) * [FeO]_{px} + \left([bt]_0 - [bt]_j\right) * [FeO]_{bt}\right) * \frac{1}{M_{FeO}} \qquad \text{(S1)}$$

Where $[x]_0$ and $[x]_j$ is the concentration of mineral x (kg_x/kg_{rock}) in the bedrock and corestone zone j, respectively (obtained by point-counting and CIPW norm calculation by Hewawasam et al. 2013"). $[FeO]_x$ is the concentration of FeO in mineral x (kg/kg_x), obtained from microprobe measurements (tables above), and M_{FeO} is the molar mass of FeO (kg/mol).

The amount of Fe-bearing mineral in the rock $[x]_0$ is obtained by multiplying the concentration of the mineral in the rock (vol%) with the density of the mineral ρ_x (kg/m^3) divided by the density of the rock ρ_{rock} (kg/m^3):

$$[x]_0 = [x]_{rock} * \frac{\rho_x}{\rho_{rock}} \qquad \text{(S2)}$$

The density of the minerals is taken from literature (Table 4 in the main text, (Robie and Hemingway, 1995)), and the rock density was calculated from the weighed cylinders prepared for He-pycnometry measurements.

As the degree of mineral weathering is comparable to the amount of *in situ* Fe oxidation in the mineral, the amount of the weathered mineral in corestone zone j is evaluated using the mass transfer coefficient ($\tau_{x,\,j}$, Table 5, main text) from Hewawasam et al. (2013). For pyroxene we used τ_{Mn} since nearly all Mn is incorporated in pyroxene. This assumption introduces negligible uncertainties into the full calculation. Biotite depletion τ_{bt} was determined using the biotite loss in the different corestone zones as calculated from Sr isotopes (Hewawasam et al., 2013). Therefore, equation (S1) becomes:

$$FeO_{lost,j} = \left([px]_0 * [FeO]_{px} * \left(-\tau_{px,j}\right) + [bt]_0 * [FeO]_{bt} * \left(-\tau_{bt,j}\right)\right) * \frac{1}{M_{FeO}} \qquad \text{(S3)}$$

In addition to the amount of Fe(II) lost during weathering, the amount of Fe(III) formed during weathering is needed for this calculation (see below). As Fe is immobile in the corestone ($\tau_{Fe} = 0$), $FeO_{lost,\,j}$ (mol/kg_{rock}) must equal the amount of $Fe(OH)_3$ (mol/kg_{rock}) formed during weathering

$$FeO_{lost,j} = Fe(OH)_{3,j} \qquad \text{(S4)}$$

hence the concentration of $[Fe(OH)_3]_j$ in corestone zone j (kg/kg_{rock}) is:

$$[Fe(OH)_3]_j = FeO_{lost,j} * M_{Fe(OH)_3} \quad \text{(S5)}$$

Where $M_{Fe(OH)3}$ is the molar mass of $Fe(OH)_3$ (kg/mol).

The Fe contained in pyroxene and biotite $[Fe]_x$ (kg/kg_{rock}) with respect to the whole rock is obtained by multiplying the concentration of the mineral (kg/kg_{rock}) with the concentration of FeO in the mineral $[FeO]_x$ (kg/kg_x):

$$[Fe]_X = [x]_0 * [FeO]_X \quad \text{(S6)}$$

To derive a value for the fracture criterion for a given layer of our weathering system, we rewrite the elastic strain equation from Fletcher et al. (2006), where the physical change is related to chemical reaction advance:

$$\varepsilon = \frac{\xi f_0}{3} * \left[\frac{V_{Fe(OH)_3} - V_{FeO}}{V_{FeO}}\right] \quad \text{(S7)}$$

To equation (4) in the main text (section 4.2.1).

Worked example for the oxidation model (section 4.2.1)

The parameter for the oxidation model calculations are given in Table 3, main text. Note that we have not included the subscript of the enumerator in the table, but included them in the detailed calculation for the worked sample. The calculation for biotite is worked out for an annite like composition and the max. biotite weathering rate, as given in Hewawasam et al. (2013). The same calculation was done for phlogopite and the min. weathering rate, too. To derive the amount of Fe-bearing mineral in the rock $[x]_0$, we insert the given values in equation (S2) which yield:

$$[px]_0 = 0.04\, {m^3}_{px}/{m^3}_{rock} * \frac{3998\ kg_{px}/{m^3}_{px}}{2700\ kg_{rock}/{m^3}_{rock}} = \mathbf{0.059\ kg_{px}/kg_{rock}}$$

$$[bt]_0 = 0.07\ {m^3}_{bt}/{m^3}_{rock} * \frac{3317\ kg_{bt}/{m^3}_{bt}}{2700\ kg_{rock}/{m^3}_{rock}} = \mathbf{0.086\ kg_{bt}/kg_{rock}}$$

Calculating the Fe contained in pyroxene and biotite $[Fe]_x$ (kg/kg_{rock}) with equation (S6) gives:

$$[Fe]_{px} = 0.059\ kg_{px}/kg_{rock} * 0.33\, kg_{FeO}/kg_{px} = \mathbf{0.020\, kg_{FeO}/kg_{rock}}$$

$$[Fe]_{bt} = 0.086\ kg_{bt}/kg_{rock} * 0.200\, kg_{FeO}/kg_{bt} = \mathbf{0.017\, kg_{FeO}/kg_{rock}}$$

Therefore, *e.g.* in corestone zone 3 $FeO_{lost,\,j}$ becomes (S3):

$$FeO_{lost,j} = \Big(0.059\ kg_{px}/kg_{rock} * 0.33\, kg_{FeO}/kg_{px} * (-0.30) + 0.086\ kg_{bt}/kg_{rock} * 0.200\, kg_{FeO}/kg_{bt} * (-0.13)\Big) * \frac{1}{0.069\, kg/mol}$$

$$= \mathbf{1.17 * 10^{-1}\, mol/kg_{rock}}$$

As this is equal to $[Fe(OH)_3]_j$ we can insert this into equation (S5):

$$[Fe(OH)_3]_j = 1.17 * 10^{-1}\, mol/kg_{rock} * 0.107\, kg/mol = \mathbf{1.25 * 10^{-2}\, kg/kg_{rock}}$$

With these values we can calculate $\Delta\tilde{V}$, equation (5) from the main text:

$$\Delta\tilde{V} = V_{FeO} * \left([Fe]_{bt,0} * \left(1 + \tau_{bt,j}\right) - [Fe]_{bt,0}\right) + V_{FeO} * \left([Fe]_{px,0} * \left(1 + \tau_{px,j}\right) - [Fe]_{px,0}\right) + V_{Fe(OH)_3} * \left([Fe(OH)_3]_j - [Fe(OH)_3]_0\right)$$

$$\Delta\tilde{V} = 1.75 * 10^{-4}\, m^3/kg * (0.017\, kg_{FeO}/kg_{rock} * (1 + (-0.13)) - 0.017\, kg_{FeO}/kg_{rock}) + 1.75 * 10^{-4}\, m^3/kg * (0.020\, kg_{FeO}/kg_{rock} * (1 + (-0.30)) - 0.020\, kg_{FeO}/kg_{rock}) + 1.92 * 10^{-4}\, m^3/kg * (1.25 * 10^{-2}\, kg/kg_{rock} - 0\, kg/kg_{rock})$$

$$= \mathbf{9.90 * 10^{-7}\, m^3/kg_{rock}}$$

For the elastic strain this reveals (equation (4) in the main text):

$$\varepsilon = \frac{1}{3} * \Delta\tilde{V} * \rho_{rock}$$

$$\varepsilon = \frac{1}{3} * 9.90 * 10^{-7}\, m^3/kg_{rock} * 2700\ kg_{rock}/{m^3}_{rock}$$

$$= \mathbf{8.91 * 10^{-4}}$$

Inserting this into equation (3) from the main text:

$$2\Gamma = \frac{E\varepsilon^2}{1-\nu} = U$$

$$U = \frac{1 * 10^{12}\, dyn/cm^2 * (8.91 * 10^{-4})^2}{1 - 0.25} = \mathbf{1.06 * 10^6\, dyn/cm^2}$$

This shows that already in zone 3 the fracturing criterion:

$2\Gamma = 4.0 * 10^5\, dyn/cm^2 < U$ is reached

References

Fletcher, R., Buss, H., Brantley, S., 2006. A spheroidal weathering model coupling porewater chemistry to soil thicknesses during steady-state denudation. Earth and Planetary Science Letters 244, 444-457.

Hewawasam, T., von Blanckenburg, F., Bouchez, J., Dixon, J.L., Schuessler, J.A., Maekeler, R., 2013. Slow advance of the weathering front during deep, supply-limited saprolite formation in the tropical Highlands of Sri Lanka. Geochimica et Cosmochimica Acta 118, 202-230.

Robie, R.A., Hemingway, B.S., 1995. Thermodynamic Properties of Minerals and Related Substances at 298.15 K and 1 Bar (10^5 Pascals) Pressure and at Higher Temperatures. U. S. Geological Survey Bulletin, Washington.